

University of Alberta

Ice-Atmosphere Interactions in the Canadian High Arctic:
Implications for the thermo-mechanical evolution of terrestrial ice masses

by

Trudy M. H. Wohlleben

A thesis submitted to the Faculty of Graduate Studies and Research
in partial fulfillment of the requirements for the degree of

Doctor of Philosophy

Department of Earth and Atmospheric Sciences

©Trudy M. H. Wohlleben

Fall 2009

Edmonton, Alberta

Permission is hereby granted to the University of Alberta Libraries to reproduce single copies of this thesis and to lend or sell such copies for private, scholarly or scientific research purposes only. Where the thesis is converted to, or otherwise made available in digital form, the University of Alberta will advise potential users of the thesis of these terms.

The author reserves all other publication and other rights in association with the copyright in the thesis and, except as herein before provided, neither the thesis nor any substantial portion thereof may be printed or otherwise reproduced in any material form whatsoever without the author's prior written permission.

Examining Committee

Martin Sharp, Department of Earth and Atmospheric Sciences

Andrew Bush, Department of Earth and Atmospheric Sciences

John England, Department of Earth and Atmospheric Sciences

Bruce Sutherland, Departments of Physics and of Earth and Atmospheric Sciences

Gordon Swaters, Department of Mathematical and Statistical Sciences

Greg Flato, Canadian Centre for Climate Modelling and Analysis, Environment Canada, Victoria

Abstract

Canadian High Arctic terrestrial ice masses and the polar atmosphere evolve co-dependently, and interactions between the two systems can lead to feedbacks, positive and negative. The two primary positive cryosphere-atmosphere feedbacks are: 1) The snow/ice-albedo feedback (where area changes in snow and/or ice cause changes in surface albedo and surface air temperatures, leading to further area changes in snow/ice); and 2) The elevation - mass balance feedback (where thickness changes in terrestrial ice masses cause changes to atmospheric circulation and precipitation patterns, leading to further ice thickness changes). In this thesis, numerical experiments are performed to: 1) quantify the magnitudes of the two feedbacks for chosen Canadian High Arctic terrestrial ice masses; and 2) to examine the direct and indirect consequences of surface air temperature changes upon englacial temperatures with implications for ice flow, mass flux divergence, and topographic evolution.

Model results show that: a) for John Evans Glacier, Ellesmere Island, the magnitude of the terrestrial snow/ice-albedo feedback can locally exceed that of sea ice on less than decadal timescales, with implications for glacier response times to climate perturbations; b) although historical air temperature changes might be the direct cause of measured englacial temperature anomalies in various glacier and ice cap accumulation zones, they can also be the indirect cause of their enhanced diffusive loss; c) while the direct result of past air temperature changes has been to cool the interior of John Evans Glacier, and its bed, the indirect result has been to create and maintain warm (pressure melting point) basal temperatures in the ablation zone; and d) for Devon Ice Cap, observed mass gains in the northwest sector of the ice cap would be smaller without orographic precipitation and the mass balance – elevation feedback, supporting the hypothesis that this feedback is playing a role in the evolution of the ice cap.

TABLE OF CONTENTS

page no.

1. Introduction	1
1.1 GENERAL CONTEXT AND AIM OF THE THESIS	1
1.2 THE SNOW/ICE-ALBEDO FEEDBACK	2
1.3 THE MASS BALANCE – ELEVATION FEEDBACK	6
1.3.1 <i>All Spatial Scales: The Lapse-Rate Feedback.</i>	7
1.3.2 <i>Meso- to Synoptic Scales: The Orographic Precipitation Feedback.</i>	7
1.3.3 <i>Synoptic Scales: The Glacier Anticyclone Feedback.</i>	8
1.3.4 <i>Synoptic-Planetary Scales: The Rossby Wave Feedback.</i>	9
1.4 OUTLINE OF THESIS EXPERIMENTS AND THESIS FORMAT	10
1.5 REFERENCES	13
 2. Quantifying the Impact of the Terrestrial Snow/Ice-Albedo Feedback upon a Canadian High Arctic Glacier and its Local Climate.	17
2.0 INTRODUCTION	17
2.1 DEFINITION OF THE CLIMATE SENSITIVITY PARAMETER, λ , AND THE FEEDBACK PARAMETER, f	21
2.2 JOHN EVANS GLACIER	23
2.3 COMPARISON OF THE JEG AND THE JEG-MODEL CLIMATES	25
2.4 JEG MODEL CLIMATE SENSITIVITY TO FIXED AND TIME-VARYING SURFACE ALBEDO	27
2.4.1 <i>ELA Position</i>	28
2.4.2 <i>Melt Season Length</i>	28
2.5 EXPERIMENTAL PROCEDURE	30
2.5.1 <i>Perturbations applied to the model climate</i>	30
2.5.2 <i>“Turning off” the snow/ice-albedo feedback in the model climate</i>	31
2.5.3 <i>Separating the ice-albedo feedback from other feedbacks in the experiments</i>	31
2.5.3.1 SEPARATING THE SNOW/ICE-ALBEDO FEEDBACK FROM THE ELEVATION – MASS BALANCE FEEDBACK	31
2.5.3.2 SEPARATING THE ICE-ALBEDO FEEDBACK FROM THE SNOW-ALBEDO FEEDBACK	31
2.5.4 <i>Choice of model domain for the experiments</i>	32
2.5.5 <i>Choice of model run time for the experiments</i>	33
2.6 SUMMARY OF RESULTS: CALCULATIONS OF f	33
2.6.1 <i>The magnitude of the snow/ice-albedo feedback in the JEG catchment</i>	34
2.7 DISCUSSION	42
2.8 CONCLUSIONS	45
2.9 APPENDIX: THE SURFACE-ATMOSPHERE ENERGY-MASS BALANCE MODEL AND JEG-SPECIFIC PARAMETERIZATIONS	47
2.9.1 <i>Energy Balance</i>	47
2.9.2 <i>Mass Balance</i>	49
2.9.3 <i>Model Integration</i>	50
2.10 REFERENCES	57

3. Little Ice Age – Related Temperature Anomalies within Greenland and Canadian High Arctic Ice Cap Boreholes: the Role of Ice-Atmosphere Feedbacks and the Thermal Memory of the Ice Cap.	62
3.0 INTRODUCTION	62
3.1 THE LITTLE ICE AGE AND MEASURED ICE TEMPERATURE ANOMALIES	65
3.1.1 <i>The Little Ice Age: a Brief Review</i>	65
3.1.2 <i>CHA and GIS Ice Temperature Records of the LIA</i>	66
3.1.3 <i>Reasons for Discrepancies in the Amplitudes of LIA-related Ice Temperature Anomalies</i>	70
3.1.3.1 ATMOSPHERIC CIRCULATION PATTERNS	70
3.1.3.2 SURFACE AND BASAL PROCESSES	70
3.1.3.3 THERMODYNAMIC PROPERTIES	72
3.1.3.4 GEOTHERMAL HEAT FLUX	72
3.1.3.5 ICE-ATMOSPHERE FEEDBACKS	72
3.1.3.6 PRESENCE/ABSENCE OF ADJACENT THERMAL ANOMALIES OF THE OPPOSITE SIGN	74
3.1.4 <i>White Glacier (CHA) versus GRIP (GIS)</i>	75
3.2 AMPLIFICATION OF SAT ANOMALIES BY THE SNOW/ICE-ALBEDO FEEDBACK	76
3.2.1 <i>The Snow/Ice-Albedo Feedback: a Review</i>	77
3.2.2 <i>Calculations of SAT-Anomaly Amplifications by the Snow/Ice Albedo Feedback</i>	78
3.3 THE PRESERVATION OF ICE TEMPERATURE ANOMALIES	80
3.3.1 <i>Model</i>	80
3.3.2 <i>Experiments</i>	82
3.3.3 <i>Results</i>	84
3.4 SUMMARY AND DISCUSSION	88
3.5 CONCLUSIONS	90
3.6 REFERENCES	90
 4. The Influence of Climate on the Thermal Characteristics of a Canadian High Arctic Polythermal Glacier	95
4.0 INTRODUCTION	95
4.1 JOHN EVANS GLACIER	96
4.1.1 <i>Physical Description</i>	96
4.1.2 <i>Measurements and Observations</i>	98
4.1.3 <i>Previous Ice Temperature Modeling of JEG</i>	99
4.2 JEG 2D ICE TEMPERATURE MODEL AND BOUNDARY CONDITIONS	99
4.2.1 <i>Ice Temperature Model</i>	100
4.2.2 <i>Ice Deformation Velocities and Consequent Internal Frictional Heating</i>	100
4.2.3 <i>Ice Thickness</i>	104
4.2.4 <i>Terrain Following Coordinates and Model Integration</i>	104

4.2.5 <i>Model Boundary Conditions</i>	105
4.2.5.1 GLACIER SURFACE	105
4.2.5.2 GLACIER BED	107
4.2.6 <i>A Note Concerning Thermal Conductivity and Volumetric Heat Capacity</i>	109
4.2.6.1 ICE	109
4.2.6.2 BED	109
4.3 JEG 2D ICE TEMPERATURE MODEL EXPERIMENTS AND RESULTS	109
4.3.1 <i>Equilibrium Solutions</i>	110
4.3.1.1 FOR THE MEAN ANNUAL SAT AND GEOTHERMAL HEAT FLUX... ..	110
4.3.1.2 WITH SUPPLEMENTARY SURFACE HEAT FLUXES	111
4.3.1.3 WITH SUPPLEMENTARY BASAL HEAT FLUXES	114
4.3.1.4 SUMMARY OF EQUILIBRIUM EXPERIMENT RESULTS	117
4.3.2 <i>Time-Dependent Experiments</i>	118
4.3.2.1 THE DIRECT IMPACT OF PAST AIR TEMPERATURE CHANGES	119
4.3.2.2 THE INDIRECT IMPACT OF PAST AIR TEMPERATURE CHANGES: ICE THICKNESS CHANGES	125
4.3.2.3 THE INDIRECT IMPACT OF PAST AIR TEMPERATURE CHANGES: ICE THICKNESS CHANGES AND THE BASAL SLIDING FEEDBACK	128
4.3.2.4 THE INDIRECT IMPACT OF PAST AIR TEMPERATURE CHANGES: SURFACE REFREEZING CHANGES	128
4.3.2.5 THE INDIRECT IMPACT OF PAST AIR TEMPERATURE CHANGES: CHANGES IN SUPRAGLACIAL MELTWATER PRODUCTION AND AMOUNTS REACHING THE GLACIER BED	129
4.4 SUMMARY AND DISCUSSION	132
4.5 CONCLUSIONS	133
4.6 APPENDIX: ENGLACIAL TEMPERATURES OF PREDOMINANTLY COLD POLYTHERMAL GLACIERS – A REVIEW	133
4.6.1 <i>Englacial Temperatures: Static versus Deforming Ice</i>	133
4.6.2 <i>Englacial Temperatures and Internal/Basal Feedbacks</i>	136
4.6.3 <i>Englacial Temperatures and Climate Change</i>	136
4.6.4 <i>Englacial Temperatures and Ice-Atmosphere Feedbacks</i>	137
4.7 REFERENCES	139

5. Modelling the Mass Balance – Elevation Feedback: Implications of orographic precipitation for the evolution and geometry of the Devon Ice Cap in the Canadian High Arctic	143
5.0 INTRODUCTION	143
5.1 THE MASS BALANCE – ELEVATION FEEDBACK: A REVIEW	145
5.1.1 <i>The Lapse Rate Feedback</i>	147
5.1.2 <i>The Orographic Precipitation Feedback</i>	147
5.1.3 <i>The Glacier Anticyclone Feedback</i>	151
5.1.4 <i>The Rossby Wave Feedback</i>	153
5.2 DEVON ICE CAP	154
5.2.1 <i>Ice Thickness, Mass Balance, and Flow Observations</i>	154

5.2.2 Evidence for Mass Balance – Elevation Feedbacks	157
5.3 MODELS	160
5.3.1 Atmosphere	160
5.3.2 Ice	164
5.3.3 Coupling the Ice and Atmosphere Models	166
5.4 EXPERIMENTS AND RESULTS	166
5.4.1 Dynamic Ice – Static Atmosphere Experiments	167
5.4.1.1 SETUP OF ICE-ONLY MODEL EXPERIMENTS	167
5.4.1.2 RESULTS OF ICE-ONLY MODEL EXPERIMENTS	169
5.4.1.3 DISCUSSION OF ICE-ONLY MODEL EXPERIMENT RESULTS	172
5.4.2 Dynamic Atmosphere – Static Ice Experiments	173
5.4.2.1 2D ATMOSPHERE-ONLY MODEL EXPERIMENTS: SETUP AND RESULTS	173
5.4.2.2 DISCUSSION OF 2D ATMOSPHERE-ONLY MODEL RESULTS	175
5.4.2.3 1D ATMOSPHERE-ONLY MODEL EXPERIMENTS AND RESULTS	176
5.4.2.4 DISCUSSION OF 1D ATMOSPHERE-ONLY MODEL RESULTS	177
5.4.2.5 COUPLED ATMOSPHERE-(NON-FLOWING)ICE MODEL EXPERIMENTS: SETUP AND RESULTS.....	177
5.4.2.6 DISCUSSION OF ATMOSPHERE-(NON-FLOWING)ICE MODEL RESULTS	179
5.4.3 Coupled Dynamic Atmosphere – Dynamic Ice Experiments	179
5.4.3.1 SETUP OF THE COUPLED ATMOSPHERE-ICE MODEL EXPERIMENTS	179
5.4.3.2 RESULTS OF THE COUPLED MODEL EXPERIMENTS.....	183
5.4.3.3 DISCUSSION OF THE COUPLED MODEL RESULTS.....	185
5.5 SUMMARY AND CONCLUSIONS	185
5.6 REFERENCES	187
6. Conclusions	193
6.1 KEY RESULTS AND CONCLUSIONS	194
6.1.1 Chapter 2	194
6.1.1.1 THE MAGNITUDE OF THE TERRESTRIAL SNOW/ICE-ALBEDO FEEDBACK	194
6.1.1.2 THE CONTRIBUTION OF TERRESTRIAL ICE	195
6.1.1.3 IMPLICATIONS FOR GLACIER RESPONSE TIME	195
6.1.2 Chapter 3	196
6.1.2.1 THE ROLE OF THE SNOW/ICE-ALBEDO FEEDBACK.....	196
6.1.2.2 THE ROLE OF THE THERMAL MEMORY OF THE ICE	197
6.1.3 Chapter 4	197
6.1.3.1 THE EXTENT TO WHICH JEG BASAL ICE TEMPERATURES ARE IN EQUILIBRIUM WITH ITS THERMAL BCs	198
6.1.3.2 THE DIRECT INFLUENCE OF HISTORICAL SAT CHANGES.....	198
6.1.3.3 THE INDIRECT INFLUENCE OF HISTORICAL SAT CHANGES.....	198
6.1.4 Chapter 5	199
6.1.4.1 THE EXTENT TO WHICH DEVON ICE CAP’S OBSERVED MBs AND MFDs ARE IN EQUILIBRIUM	199

6.1.4.2 THE IMPACT OF OROGRAPHIC PRECIPITATION AND THE MASS BALANCE – ELEVATION FEEDBACK.....	200
6.2 SUMMARY AND FUTURE INVESTIGATIONS.....	200
6.3 REFERENCES	202

LIST OF TABLES

page no.

CHAPTER 2

Table 2.1. Calculated values of f , in terms of mean annual area-averaged surface temperatures (TS), atmospheric temperatures (TA) and surface mass balances (MB). 34

Table 2.9.1. Summary of JEG-specific model parameterizations..... 52

Table 2.9.2. Symbol Definitions..... 56

CHAPTER 3

Table 3.1. The magnitudes and depths of LIA-related ice temperature anomalies within five sets of CHA and GIS boreholes. 67

LIST OF FIGURES

page no.

CHAPTER 1

Figure 1.1. The snow/ice - albedo feedback. 2

Figure 1.2. Forms of the mass balance – elevation feedback. a) The lapse-rate feedback, given a static atmosphere. The blue curves indicate 2D ice caps of various sizes. ELA denote the “equilibrium line altitude”, the altitude at which annual snowfall accumulation is balanced by summer melt and runoff. b) The orographic precipitation feedback, given a moist, dynamic atmosphere. Arrows denote forced air flow over the ice cap. Cloud and precipitation form where the air is forced upwards. c) The ice sheet anti-cyclone feedback. “H” denotes high sea level pressure, and black concentric circles are sketches of isobars (which in this case tend to parallel surface elevation contours). Arrows indicate the cold air outflow from the centre of the ice cap and the consequent Northern Hemisphere anticyclonic circulation of the outflow as a result of the coriolis force. “L’s” denote low-pressure storm systems with associated warm fronts (red) and cold fronts (blue) and cloud/precipitation areas. d) The interaction of very large ice sheets with topographically-generated Rossby waves. The red H and blue L denote centres of high and low atmospheric thicknesses (or temperatures), respectively. Black lines are contours of atmospheric thickness. Arrows are upper atmosphere winds (and also indicate the path of the jet stream). “L’s” are surface low-pressure systems as described in c). See text for descriptions of the feedbacks. 6

CHAPTER 2

Figure 2.1 The snow/ice-albedo feedback: a positive feedback that amplifies radiative perturbations. 18

Figure 2.2. John Evans Glacier (Landsat 7 image, July 1999). Three automatic weather stations (WS) are located: 1) near the summit (Upper – UWS); 2) near the equilibrium line (Middle – MWS); and 3) near the snout (Lower – LWS). The area within the gray square outline corresponds to the model domain. 23

Figure 2.3. Model climate (here using a thermal diffusivity parameter $\eta=2.15 \times 10^{-5} \text{ m}^2 \text{ s}^{-1}$): a) mean annual surface temperature; b) mean annual atmospheric temperature; c) surface mass balance; d) model-area averaged surface and atmospheric temperatures ($^{\circ}\text{C}$). The thick black line in panels a), b), and c) is the outline of JEG. 25

Figure 2.4. Model results (black smooth lines) versus 1998-99 observations from the lower weather station (LWS - green variable lines): a) model surface

temperature vs. LWS 2m air temperature (degrees K); b) model mean tropospheric relative humidity vs. LWS ~2m height relative humidity (%); and c) model surface albedo vs. LWS surface albedo. The blue line in a) is the model-calculated atmospheric temperature. 26

Figure 2.5. Model calculated equilibrium line altitudes in metres above sea level for a: 1) time-varying temperature-dependent surface albedo (dashed line); and 2) fixed surface albedo $\alpha=0.9$ (solid line). 29

Figure 2.6. Calculated ice surface temperature at 200m elevation, using a temperature-dependent albedo (blue line) and a fixed surface albedo (black line), where the fixed albedo is 0.9. 29

Figure 2.7. Spatial variations in the snow/ice-albedo feedback parameter f , calculated in terms of mean annual surface temperature, using an atmospheric diffusivity parameter $\eta=2.15 \text{ m}^2 \text{ s}^{-1}$, for a longwave radiative perturbation of -5 W m^{-2} 39

Figure 2.8. Spatial variations in the snow/ice-albedo feedback parameter, f , calculated in terms of surface temperature, using an atmospheric diffusivity parameter $\eta=2.15 \text{ m}^2 \text{ s}^{-1}$, for a shortwave radiation perturbation of $+5 \text{ W m}^{-2}$. Grey areas highlight zones of maximum amplification of surface temperature changes by the feedback for the given radiative perturbation. 40

Figure 2.9.1. Scatter plot of daily averaged surface albedo ($\times 100$) versus 2m air temperatures at the Lower Weather Station, 1998-1999. Surface albedo is measured as the ratio of outgoing to incoming SW radiation during the part of the year when sunlight is available. During the sunless winter months, albedos are assumed fixed at values of 0.9 below the ELA and 0.975 above the ELA. 52

CHAPTER 3

Figure 3.1. a) Sketches of equilibrium solutions to the advective-diffusive temperature equation, for cold and predominantly cold polythermal glaciers, for: 1) downward vertical velocities ($w<0$; thick solid line; typical of glacier accumulation zones); 2) $w=0$ (thin solid line; typical near glacier equilibrium line altitudes, where ice flow is primarily horizontal); and 3) $w>0$ (dashed line; typical in glacier ablation zones). Near the surface of the accumulation zone, annual layers of snow eventually become layers of ice. Submergence (i.e. $w<0$) and mass flux divergence occur to balance this accumulation of ice and, as a result, the vertical temperature gradient near the surface is near zero (i.e. mean annual surface ice temperatures are equal to mean annual surface air temperatures). For real examples of such temperature profiles measured along the entire length of a glacier, see Blatter (1987). b) Sketch of the equilibrium solution (with respect to

present day boundary conditions) for a borehole in a glacier accumulation zone (thick solid line) and the corresponding “measured” temperatures in that borehole (thin solid line). The difference between the two curves produces positive (+) and negative (–) thermal anomalies, which may be related to past climate events. The amplitude of an anomaly is the maximum temperature difference between the measured and equilibrium curves. The depth of the anomaly is the depth at which the maximum temperature difference occurs. 63

Figure 3.2. Map of Greenland and the Canadian High Arctic, showing the locations of the ice temperature measurements cited in Table 3.1. 68

Figure 3.3. a) Air temperature anomaly time series used in time integration experiments (post-LGM time series up to 2000 A.D. after Dahl-Jensen et al., 1998); b) Zoomed in to last 10000 years; c) zoomed in to last 2000 years. 83

Figure 3.4. Equilibrium (dashed line) and time-dependent (solid line) temperature profiles for a hypothetical summit borehole: a) for the full depth of the borehole (3000m); b) for the top 30% (900m) of the borehole, where the temperature anomalies have been shaded (red for positive, blue for negative). 85

Figure 3.5. 1D borehole experiments showing the magnitude and depth of the LIA ice temperature anomaly, for: 1) the full historical SAT-anomaly time series (thick black line); 2) the SAT-anomaly time series without either the CO/MWP or 1930 air temperature maxima (thin black line); 3) the SAT-anomaly time series without the CO/MWP anomalies (blue line); and 4) the SAT-anomaly time series without the 1930 maximum (pink line). The dashed line represents the equilibrium temperature profile computed for the present-day mean SAT. 86

CHAPTER 4

Figure 4.1. John Evans Glacier (79.67°N, 74.5°W). Black squares and circles denote the centre-line velocity / mass balance stake network, where the squares indicate the line that is used in the 2D modelling experiments. The positions and approximate elevations of the Lower, Middle and Upper Weather Stations (LWS, MWS, and UWS) are shown. The grey line passing through the nunatak and MWS follows the 800 m surface elevation contour and represents the approximate post-1963AD mean location of the equilibrium line (based on the elevation distribution of boreholes where the bomb layer can be found – *pers. comm.* Martin Sharp). 97

Figure 4.2. 1999-2000 winter average ice velocities for John Evans Glacier: a) measured surface horizontal velocities; b) calculated englacial ice velocities. The ice in the chosen centre-line flows around a nunatak located approximately

midway down the glacier's length. It also passes to the south of a submerged bedrock ridge or riegel, located approximately 6000m upstream from the glacier snout. The location of the nunatak coincides with the average ELA, separating the accumulation zone from the ablation zone (indicated by light grey bed shading to the right of the nunatak). Temperate basal conditions have been inferred from immediately below the nunatak all the way to just short of the snout, which itself is frozen to the bed. 103

Figure 4.3. Modeled JEG equilibrium ice temperatures under a present-day mean annual air temperature of -15°C and a geothermal heat flux of 0.06 W m^{-2} : glacier cross-section and corresponding depth-profiles. 111

Figure 4.4. Modeled JEG equilibrium ice temperatures under present-day 15m-depth ice temperatures (surface refreezing effects are included): glacier cross-section and corresponding depth-profiles. 113

Figure 4.5. Equilibrium bed temperatures: a) for two different surface BC's; b) for SATs and for various additional basal heat sources; c) for 15m-depth ice temperatures and for various additional basal heat sources. 114

Figure 4.6. a) Ice and bed layers used in the model integrations; b) Subglacial negative LGM-related thermal anomaly in a semi-frozen saturated sand substrate; c) Subglacial negative LGM-related thermal anomaly in solid bedrock. Note that the normalized ice depths in b) and c) represent different actual depths below the ice bed along the length of the glacier, because the bed thickness ($-2 \text{ km a.s.l.} + \text{the bed elevation}$) is greater upstream than it is downstream. For example, at the upstream end of the glacier, 0.5 represents 1700 m below the ice bed, or -300 m a.s.l. At the terminus, 0.5 represents 1050 m below the ice bed, or -950 m a.s.l. 121

Figure 4.7. Modeled JEG 2D ice temperatures: a) equilibrium ice temperatures under a present-day mean SAT of -15.0°C and a geothermal heat flux of 0.06 W m^{-2} ; b) present-day (2000AD) temperatures following a 400 year period of colder than present SATs from 1500-1900AD (experiment 5); and c) the difference between the post-LIA results of experiment 5 and the equilibrium distribution. Ice thickness and velocity were assumed constant in these experiments. 124

Figure 4.8. Time-dependent modeling results: JEG ice bed temperatures for the 4 experiments. 127

Figure 4.9. Time-dependent modeling results: JEG ice bed temperatures for the surface refreezing experiments. 129

Figure 4.10. Modeled JEG 2D ice temperatures: a) equilibrium ice temperatures for present-day 15m ice-depth temperatures and a geothermal heat flux of 0.06 W

m^{-2} ; b) present-day post-LIA temperatures, following a 400 year period of colder than present SATs, 25% thicker than present ice, a 200 m downward shift in ELA and surface refreezing, and accounting for present-day surface and basal meltwater fluxes; and c) the difference between the post-LIA results and the equilibrium distribution. Ice deformation velocities, calculated from present-day winter average values, were assumed to be constant and basal motion was neglected. 131

Figure 4.11. Sketched influence of ice flow (a,d) upon the englacial and basal temperatures (b,e) and the equilibrium vertical temperature profiles (c,f) of predominantly cold, polythermal glaciers: a) – c) for static ice; and d) – f) for deforming ice. T denotes temperature, PMP represents the Pressure Melting Point, and w symbolizes the vertical ice velocity. Sketched contours in (b,e) shade from red (representing the PMP) to dark blue (representing sub-zero surface air temperatures). 135

CHAPTER 5

Figure 5.1. Canadian High Arctic ice caps and ice fields. 143

Figure 5.2. Forms of the mass balance – elevation feedback. a) The lapse-rate feedback, given a static atmosphere. The blue curves indicate ice caps of various sizes, with varying proportions above and below the ELA. ELA denotes the “equilibrium line altitude”, the altitude at which annual snowfall accumulation is balanced by summer melt and runoff. b) The orographic precipitation feedback, given a moist, dynamic atmosphere. Arrows denote forced air flow over the ice cap. Cloud and precipitation form where the air is forced upwards. c) The ice sheet anti-cyclone feedback. “H” denotes high sea level pressure, and black concentric circles are sketches of isobars (which in this case tend to parallel surface elevation contours). Arrows indicate the cold air outflow from the centre of the ice cap and the consequent Northern Hemisphere anticyclonic circulation of the outflow as a result of the Coriolis force. “L’s” denote low-pressure storm systems with associated warm fronts (red) and cold fronts (blue) and cloud/precipitation areas. d) The interaction of very large ice sheets with topographically-generated Rossby waves. The red H and blue L denote centres of high and low atmospheric thicknesses (or temperatures), respectively. Black lines are contours of atmospheric thickness. Arrows are upper atmosphere winds (and also indicate the path of the jet stream). “L’s” are surface low-pressure systems as described in c). See text for descriptions of the feedbacks. 146

Figure 5.3. a) The development of orographic cloud and precipitation under northwesterly winds at the summit of Devon Ice Cap on May 28, 2005. Black and white OLS visible-band and coloured NOAA AVHRR all-band imagery courtesy of Environment Canada. 149

Figure 5.3. b) Hydraulic jump and lee-side roll cloud due to sustained northerly winds passing over the summit of Devon Ice Cap the week of February 19, 2008. Black and white NOAA AVHRR IR image (February 19, 2008), false-colour MODIS visible band image (February 21, 2008), and GEM model wind/pressure plot courtesy of Environment Canada. 150

Figure 5.4. A typical winter sea level surface pressure analysis for Greenland (highlighted in yellow), showing an area of high sea level pressure (or an anticyclone) over the central and northern part of the ice sheet. Atlantic low pressure systems are confined to tracking up the west and east coasts of Greenland. Surface analysis courtesy of Environment Canada (<http://weather.ec.gc.ca>). 152

Figure 5.5. Devon Ice Cap, eastern Devon Island, Canada. Surface elevations are in metres a.s.l. The surface height profiles along the 3 depicted northwest-southeast transects are shown in Figure 5.6. (Source: Canadian Digital Elevation Data, Natural Resources Canada.). 155

Figure 5.6. Three northwest-southeast cross-sections through the Devon Ice Cap, Devon Island, Nunavut (Canadian Digital Elevation Data, Natural Resources Canada). Note that these cross-sections do not follow actual flow lines in the ice. 157

Figure 5.7. The 1975-2000 vertical mean tropospheric wind pattern over the eastern Canadian High Arctic (derived from NCAR gridded monthly data). Mean tropospheric winds are quasi-geostrophic and parallel to atmospheric height contours. Here, mid-tropospheric 500mb height contours are plotted every 10m ranging from 5200 m in the north to greater than 5250 m in the south. 158

Figure 5.8. DIC ice thickness along a NW-SE transect passing through the center of the ice cap. 1 km - resolution surface and bed elevation data courtesy of Dowdeswell et al. (2004). For comparison, 500m-resolution 1959-1960 CDED surface elevations along the same transect are also plotted. The grey area on the left illustrates an area where CDED surface elevation data are available beyond the limit where the Dowdeswell et al. (2004) surface and bed elevation data end. The ice cap terminates at an elevation of ~600m on its northwest side and at an elevation near sea level on its southeast side. 168

Figure 5.9. The three rows represent the three MFD-only ice experiments (Row 1 = case i); Row 2 = case ii); Row 3 = case iii)), while the columns display the surface elevations, horizontal velocities, vertical velocities, and mass flux divergences in each case. Dotted lines represent initial conditions and solid lines represent the solution after 10 ka. The blue line in the first column is a DIC NW-SE transect (from the CDED DEM), plotted for reference. 170

Figure 5.10. Modeled surface elevation in the MB-only experiment. 171

Figure 5.11. The evolution of a dome-shaped ice cap after 2 ka and 10 ka under fixed present-day Devon Ice Cap mass balances and time-evolving mass flux divergences: initial ice dome profile (dashed line), final ice profiles (red and black lines), and 2D transect through the Devon Ice Cap (light blue line). The “peak” on the northwest side of the ice cap is the result of fixing surface elevations at the next left grid-point to a value close to the initial value, given that the actual DIC terminates at ~600m elevation on this side of the ice cap. This forces the deforming ice to bulge upwards as it converges against the invisible “wall”, as in Figure 5.9a. 172

Figure 5.12. DIC anomalous, topographically-generated winds for a mean northwesterly flow of 25 km hr^{-1} (7 m s^{-1}). Top: without annotations. Bottom: with annotations indication areas of accelerated flow, flow divergence and convergence, and anticyclonic and cyclonic flow. The largest arrow over the ice cap summit = 1.0042 m s^{-1} 174

Figure 5.13. Anomalous atmospheric circulation induced by a mean 5 m s^{-1} flow over a Devon-sized dome-shaped ice cap: a) anomalous tropospheric heights about 8000m; b) anomalous tropospheric layer-mean horizontal winds; and c) anomalous lower- to mid-tropospheric vertical winds. 176

Figure 5.14. 5000-year evolution of a static ice cap under orographic precipitation only: a) no topographic - mass balance feedback; b) with the topographic – mass balance feedback. Initial ice profile (dashed line), final ice profile (solid black line), and 2D transect through the Devon Ice Cap (blue line). 179

Figure 5.15. Modeled versus observed surface mass balances: a) for the equilibrium experiments; and b) for the $2\times q$ and $2\times U$ experiments. Note that whereas the mass balance curves presented in Mair et al. (2005) are plotted versus elevation, here they are plotted versus horizontal distance along the NW-SE ice cap transect, thus the slight differences in the shapes of the curves. For a description of the errors in the published mass balance curves (red line), see Mair et al. (2005). 182

Figure 5.16. Results of the coupled ice-atmosphere model experiments: a) model runs to equilibrium; and b) doubled specific humidity and doubled background atmospheric flow experiments. Note that the double-q and double-U experiments yielded identical results because they had an identical effect upon the magnitude of the orographic precipitation. Thus, the red and dark blue curves in b) are plotted one on top of the other. The shaded black and light blue areas represents NW-SE cross-sections of the DIC bed and ice, respectively, taken from the 1km-resolution Dowdeswell et al. (2004) DEM and interpolated to the 10km model grid. 184

List of ABBREVIATIONS, Symbols

Abbreviations

1D	one Dimensional
2D	two Dimensional
3D	three Dimensional
BP	Before Present
CHA	Canadian High Arctic
CO	Climatic Optimum (Holocene)
DIC	Devon Ice Cap
DYE3	one of two DEW Line ice cap stations in Greenland
EBCM	Energy Balance Climate Model
ELA	Equilibrium Line Altitude
GCM	General Circulation Model
GIS	Greenland Ice Sheet
GPS	Geopositioning System (Global)
GRIP	Greenland Icecore Project
IPCC	Intergovernmental Panel on Climate Change
JEG	John Evans Glacier
LGM	Last Glacial Maximum
LIA	Little Ice Age
LIS	Laurentide Ice Sheet
LW	Long Wave
LWS	Lower Weather Station
MB	Mass Balance
MFD	Mass Flux Divergence
m.w.e.	melt water equivalent
MWP	Medieval Warm Period
MWS	Middle Weather Station
NCAR	National Center for Atmospheric Research
PMP	Pressure Melting Point
RH	Relative Humidity
SAT	Surface Air Temperature
SIE	Shallow Ice Equation
SW	Short Wave
SWE	Shallow Water Equation
UWS	Upper Weather Station
WS	Weather Station

Units

Length

cm	centimetre
m	metre
km	kilometre

Time

a	year (annum)
ka	one thousand years
s	second
hr	hour
d	day
t	time
yr	year

Mass/Weight

kg	kilogram
----	----------

Energy/Temperature

°C	degree Celcius
J	Joule
K	Kelvin
W	Watt

Symbols

$^{\circ}\text{N}$	degree North
$^{\circ}\text{W}$	degree West
c	constant (unknown)
c_p	specific heat under constant pressure
c'	anomalous condensation rate
e	surface elevation or topography (same as h_s)
f	feedback parameter
g	gravity
h	thickness or elevation
k	thermal diffusion coefficient
	vertical exchange coefficient for sensible heat (Chapter 2)
n	coefficient in the stress-strain relationship for ice (Glen's Flow Law)
p	precipitation
q	specific humidity
r, r^2	correlation coefficient, correlation coefficient squared
$s(q)$	source/sink of water vapour
t	time
t_R	response time
u	horizontal velocity component (east-west or along-stream direction)
\bar{u}	mean or depth-averaged velocity
v	horizontal velocity component (north-south or cross-stream direction)
w	vertical velocity component
	mixing ratio or water mass (Chapter 2)
x	horizontal distance coordinate (east-west or along-stream direction)
y	horizontal distance coordinate (north-south or cross-stream direction)
z	vertical elevation coordinate
A	Flow parameter in the stress-strain relationship for ice (Glen's Flow Law)
C	Heat capacity
C_D	Drag Coefficient
D	diffusion of water vapour
F	energy flux (atmospheric, oceanic, or surface)
Fr	Froude Number
F_v	meridional flux of water vapour
G	Geothermal heat flux
	Gain
G_{eff}	effective Gain
H	mean thickness or scale height variable
K	thermal conductivity

L	scale variable for length or horizontal distance
L_e	Latent heat of evaporation
L_f	Latent heat of fusion
L_s	Latent heat of sublimation
P	Pressure
	mean precipitation
Pe	Peclet Number
Q	solar constant, daily average, for a given latitude
Q_{net}	radiation balance (incoming/outgoing shortwave and longwave)
R	feedback gain ratio
R_d	Gas constant for dry air
T	Temperature
U	Mean wind or scale variable for wind
X	scale variable for horizontal distance
Z	mean thickness or scale height variable
α	albedo
ε	emissivity of the atmosphere (Chapter 2)
$\dot{\varepsilon}$	strain rate for ice
ϕ	latitude
Φ	internal or basal frictional heating for ice
η	thermal diffusion coefficient for the atmosphere (Chapter 2)
	anomalous atmospheric heights (Chapter 5)
λ	climate sensitivity parameter
μ	molecular viscosity (ice)
ν	bulk or kinematic viscosity (ice)
ρ	density
σ	Stefan-Boltzmann constant (Chapter 2)
	normalized vertical coordinate (Chapter 4)
τ	shear or longitudinal stress in ice
ζ	atmospheric vorticity
Γ	atmospheric lapse rate

Superscripts and Subscripts

a	atmosphere
atm	atmosphere
b	bed or basal
B	Background (atmosphere)
c	condensed (water)
d	deformation (ice)
	dry (Chapter 2)
eff	effective
f	internal friction
i	ice
if	internal friction
l	liquid (water)
net	net
p	at constant pressure
rad	radiation
s	surface
	sliding
sfc	surface
sl	sliding
w	water
x	in the x-direction
y	in the y-direction
xz	in the x-z plane
z	at a given depth or elevation
G	ground
H	horizontal
LH	latent heat due to evaporation/condensation
LW	longwave radiation
MB	mass balance
MF	latent heat due to melting/refreezing
R	response
SH	sensible heat
SW	shortwave radiation
TA	atmospheric temperature
TS	surface temperature
'	anomalous value
—	mean value
↑↓	incoming/outgoing
↔	lateral transfer
0	feedback “off” (Chapter 2)

1. Introduction

1.1 GENERAL CONTEXT AND AIM OF THE THESIS

While no large ice sheets exist in the Canadian High Arctic (CHA) today, many areas remain extensively glaciated and include ice caps tens of thousands of square kilometres in size. Excluding the Greenland Ice Sheet, the CHA ice caps and glaciers collectively contain the largest volume of terrestrial ice within the Northern Hemisphere. These ice masses interact with the polar atmosphere, both by responding to climate changes and by modifying the regional climate.

Because the cryosphere and the atmosphere each impact the other, these systems evolve co-dependently (e.g. Oerlemans, 1986; Dowdeswell et al., 1995; Roe and Lindzen, 2001). For example, variations in air temperature and precipitation lead to changes in glacier temperature, thickness, and flow. Conversely, variations in ice sheet thickness and extent lead to changes in air temperature and atmospheric circulation, and consequently to changes in precipitation patterns. These can lead to feedbacks between the two systems, positive and negative, which can amplify or damp their mutual response to external perturbations.

In this thesis, the impact of two positive feedbacks between the cryosphere and the atmosphere are examined and quantified for present-day CHA land ice systems, through a series of modeling experiments. Positive feedbacks are of interest because of their destabilizing nature – they produce continuing and amplified responses to perturbations and move a system away from its initial state. The primary and secondary positive cryosphere-atmosphere feedbacks are, respectively (e.g. Abe-Ouchi et al., 2007):

- 1) The **snow/ice-albedo feedback** (a thermal feedback, for the most part involving area changes in snow and sea ice on less than centennial-millennial time scales and in terrestrial ice sheets on greater than millennial time scales, but where changes in the extent of land ice may be locally significant at less than centennial time scales); and

- 2) The **elevation-mass balance feedback** (a mechanical feedback, chiefly involving thickness changes in terrestrial ice masses which result from the interaction of their topography with atmospheric circulation patterns).

These two positive feedbacks, reviewed in detail below, further interact with each other and invoke other feedbacks, both positive and negative (e.g. cloud/precipitation feedbacks). To determine their relative importance, the models and experiments in this thesis were designed to isolate the two feedbacks from each other as much as possible.

The aim of this thesis is not only to improve our understanding of glacier-atmosphere interactions and feedbacks within the polar climate system, but to quantify feedback-related amplifications in the response of the terrestrial cryosphere to Arctic climate perturbations and to investigate the consequences of these amplifications. This objective is important because while CHA land ice – atmosphere positive feedbacks likely lead to small modifications of Arctic-wide atmospheric temperatures and circulation on less than centennial time scales, they have the potential to be locally significant and for this reason could appreciably modify the evolution of CHA ice masses themselves. Knowledge of the degree of local amplification of climate perturbations is essential if accurate predictions of cryospheric responses to climate perturbations are to be made. The recent warming trend in Arctic surface air temperatures (SATs – related to natural and anthropogenic radiative forcings – IPCC, 2007) is being amplified in the Arctic primarily via sea ice / snow - albedo feedbacks (Holland and Bitz, 2003). This large amplification is being secondarily amplified/damped by other feedbacks (involving clouds, permafrost, land ice masses, etc. – Curry et al., 1996). Secondary amplifications such as those initiated by CHA land ice masses may or may not be important. It is the goal of this thesis to clarify this issue.

1.2 THE SNOW/ICE-ALBEDO FEEDBACK

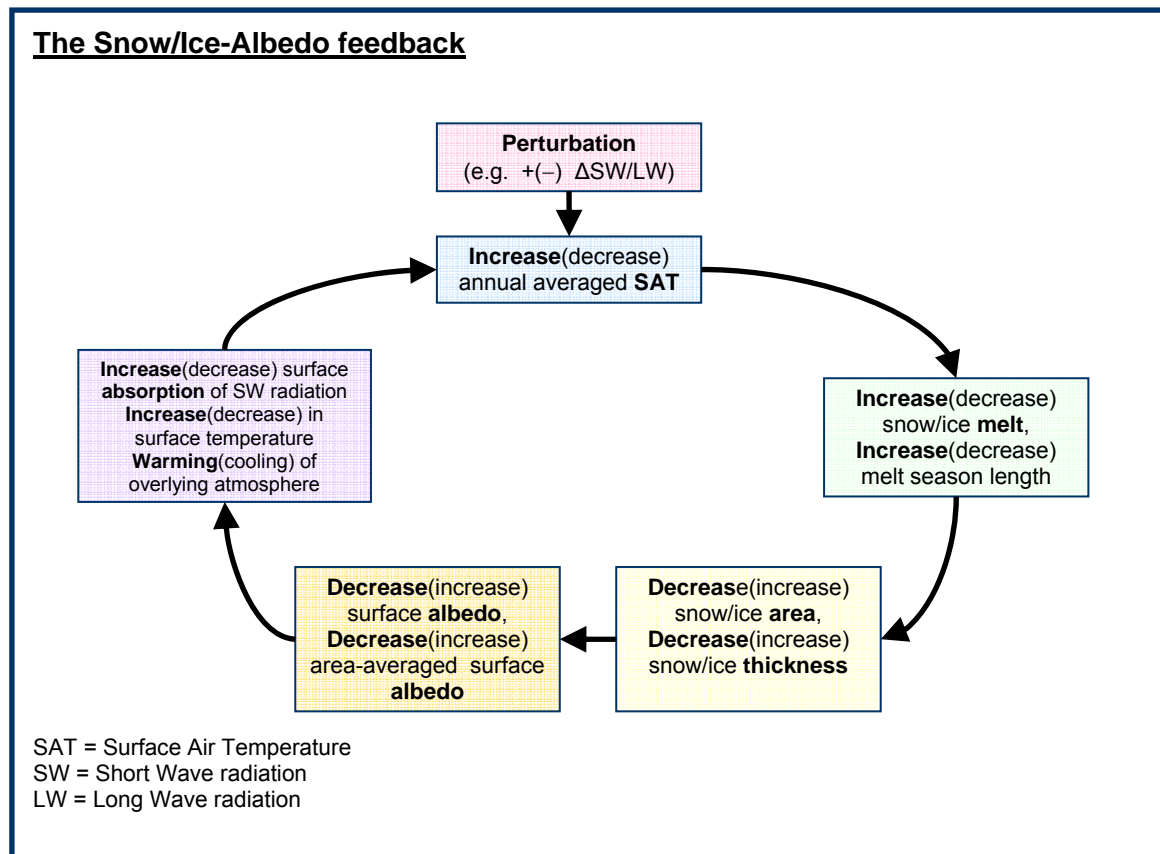


Figure 1.1. The snow/ice - albedo feedback.

The snow/ice - albedo feedback (Figure 1.1) is a positive feedback in that an initial positive radiative perturbation will lead to increasingly positive SAT changes, while an initial negative radiative perturbation will lead to increasingly negative SAT changes. Changes in SAT, snow/ice area and surface albedo, initiated by radiative perturbations, are *amplified* via this feedback. It operates as follows: warmer than normal atmospheric temperatures reduce snow and ice cover, decrease the area-averaged surface albedo (i.e. surface reflectivity), and thereby increase absorption of solar radiation by land surfaces. This results in further warming of the land surface and the overlying atmosphere, further reduction in ice and snow cover, and a further increase in absorption of solar radiation. The mechanism also works in reverse for colder than normal air temperatures, which lead to increased snow and ice cover duration and extent, and even colder temperatures.

It should be noted that this feedback is primarily an *area* feedback. Where global climate is concerned, changes in the areal extent of snow and sea ice have a large impact on the atmosphere (i.e. SATs, and consequently atmospheric circulation/precipitation patterns) at inter-annual and inter-decadal time scales. More slowly changing areal extents of land ice cover will have a lesser impact at shorter time scales but can be significant on longer time scales.

The feedback, in the cases of sea ice and snow, can also be a *thickness* feedback because sea ice and snow albedos are related to their respective thicknesses (for sea ice, see – e.g. Curry et al., 1995; and for snow, see – e.g. Robock, 1983; Fyfe and Flato, 1999; Qu and Hall, 2007). Thin sea ice is grey in colour, while thick sea ice is white. Meltwater ponds on the sea ice surface will also reduce its albedo. Fresh snow has a high albedo while meltwater within a thinning, aging snowpack acts to reduce its albedo. Melting and thinning of snow and/or sea ice leads to lower surface albedo, increased absorption of solar radiation, and further melting and thinning of the snow and/or ice (and vice versa).

The snow/ice-albedo feedback is primarily a thermal (energy) feedback: it involves surface air temperature (SAT) and sensible heat (SH) transfer between the atmosphere and the underlying surface, surface absorption of solar shortwave (SW) radiation, surface temperatures and surface melt/freeze processes. The initial perturbation which triggers this feedback may be a change in solar shortwave (SW) or atmospheric longwave (LW) radiation, changes in atmospheric or oceanic poleward heat transports, or a change in winter precipitation amounts.

The magnitude of the snow/ice-albedo feedback varies in both space and time. It varies with altitude, latitude, and season – operating in those areas where, and at those times when, snow and ice exist and sunlight is available (e.g. see the latitude vs. season plots of Bintanja and Oerlemans, 1995). In the polar regions, sunlight is only available during the summer months. During the polar night (winter), the snow/ice-albedo feedback cannot operate. The magnitude of the snow/ice-albedo

feedback will be greatest in spring in the polar regions, once 24-hour daylight is achieved and prior to the onset of melting when snow/ice albedos are highest (fresh snow having a higher albedo than old, melting snow). The feedback may also peak in the fall, prior to sunset and once the first snows and freezing of sea ice have commenced. Autumn cloudiness, related to maximum end-of-summer open water extents, may reduce sunlight and the magnitude of the snow/ice-albedo feedback, however.

In addition to latitudinal and altitudinal spatial variations, the snow/ice-albedo feedback also varies spatially across an ice mass itself. For example, the feedback cannot operate efficiently at the centre of large ice sheets where surface albedo changes in response to surface air temperature (SAT) changes are small. The feedback will have a larger amplifying effect near the margins of these ice sheets where meltback (growth) of the snow or ice exposes (covers) lower albedo ground, ice or water surfaces, considerably altering the area-averaged surface albedo and the local surface energy balance (e.g. Pritchard et al., 2008). The impacts of any changes to the overlying SATs can be partially advected from the margins towards the center of the snow/ice area by atmospheric winds, but if the snow/ice area is large enough or high enough the enhanced warmer/colder marginal SATs may not penetrate far into the interior.

Climate General Circulation Model (GCM) experiments performed during the 1990's predicted that the snow/ice-albedo feedback would significantly amplify the high-latitude warming response to increasing atmospheric greenhouse gases, although the exact magnitude of this amplification was not well constrained (IPCC, 1996). Because much of the predicted enhanced climate sensitivity at high latitudes arises from the large contribution of sea ice to the snow/ice-albedo feedback in the polar regions (e.g. Bintanja and Oerlemans, 1995; Harvey, 1988; Robock, 1983), sea ice has been the focus of many high latitude numerical and field experiments seeking to quantify the magnitude of the sea ice - albedo feedback (e.g. Curry et al., 2001; Holland and Bitz, 2003). Snow is also a major contributor to the snow/ice-albedo feedback in the mid-latitude and polar regions and much effort has gone into attempting to quantify its global impact as well (e.g. Qu and Hall, 2005; 2006; 2007). However, the impact of the snow-albedo feedback upon global climate is less definite than that of the sea ice - albedo feedback in most models (e.g. Cess et al., 1991).

At decadal time scales and less, when the polar climate system is perturbed (e.g. via changes in surface radiation balance, SAT, or precipitation), snow and sea ice experience large and rapid area changes, leading to large and rapid area-averaged albedo changes. For this reason, polar climate changes on these time scales will be more greatly amplified by the presence of these two components of the cryosphere than by land ice masses which respond more slowly to perturbations (i.e. in terms of ice temperature, ice melt, ice thickness and eventually ice area). In general, no great or rapid area change of land ice has been witnessed on less than century time scales, except where outlet valley glaciers are concerned. For

this reason, the magnitude and significance of the snow/ice-albedo feedback has rarely been examined for high-latitude terrestrial ice caps and glaciers: not only are they smaller in extent than sea ice and snow covers (in the Northern Hemisphere), but they also respond more slowly to climate perturbations. Moreover, the contribution of terrestrial ice is difficult to separate from the contribution of snow, and cloud-albedo effects further complicate the feedback where glaciers and ice sheets are concerned. Consequently, in some comprehensive reviews of climate feedbacks, the contribution of terrestrial ice to the snow/ice-albedo feedback is completely ignored (e.g. Bony et al., 2006). Nevertheless, it is well recognized that at greater than centennial time scales, as ice sheets and ice caps grow and retreat, model experiments confirm a terrestrial ice-albedo feedback with the atmosphere (e.g. the Laurentide Ice Sheet – Abe-Ouchi et al., 2007). Moreover, the glacial anticyclones generally found over large ice sheets (e.g. the Laurentide Ice Sheet – Sweeney et al., 2004), are partly initiated and strengthened by the ice-albedo feedback.

This is not to say that the importance of the terrestrial ice-albedo feedback is always negligible on decadal timescales and less. At the margins of ice caps, significant area changes in outlet or valley glaciers can occur (e.g. Arendt et al., 2002). In these locations, therefore, the land ice-albedo feedback may play a significant role in amplifying such changes (e.g. Paul et al., 2004). In the absence of significant area changes on decadal timescales and less, terrestrial ice may yet play a role in prolonging seasonal snow cover in a glacier catchment, and therefore in prolonging the operation of the snow-albedo feedback throughout the melt season. Although SATs in glaciated catchments tend to be lower than those in non-glaciated catchments, it is possible that *changes* in SATs may be amplified to a greater extent in glaciated valleys as a result of a prolongation of the snow-albedo feedback into the summer season.

Although there have been a number of glacier studies which touch on the subject of snow/ice albedo on decadal timescales and less, most research in this area has focused on modeling the albedo of specific glaciers for energy balance purposes (e.g. Arendt, 1999), and examining how this affects the sensitivity of individual glacier mass balances to climate change (e.g. Zuo and Oerlemans, 1996). Many glacier sensitivity calculations are made by testing a glacier's response to climate perturbations using static glacier models or decoupled atmosphere and ice models with no inherent feedbacks between the ice and the atmosphere (e.g. Hock, Radic, and de Woul, 2007). Others qualitatively examine changes in a model glacier variable without quantifying the ratio of the response to the perturbation, or the feedback-related amplifications (e.g. Arnold, 2005). No numerical studies to date have been performed to quantify the magnitude of the terrestrial snow/ice-albedo feedback for outlet valley glaciers in the CHA using a proper linear feedback analysis (as has been done for snow (e.g. Harvey, 1988) and sea ice (e.g. Curry et al., 2001)).

1.3 THE MASS BALANCE – ELEVATION FEEDBACK

The mass balance - elevation feedback is for the most part a *mechanical* (displacement of mass) feedback, although thermodynamics plays a role as well. It involves forced air flow over/around ice caps, changes in storm tracks and atmospheric temperature / precipitation patterns, and the consequent changes to an ice cap's mass balance and its mass balance - driven geometric evolution. This feedback takes different forms at different scales: it is important at the summits of small ice fields, important at the margins of ice caps, and important over a broader area of large ice sheets. This feedback *amplifies mass balance perturbations* and is triggered by changes in atmospheric moisture availability, radiative changes in SAT, or changes in atmospheric circulation.

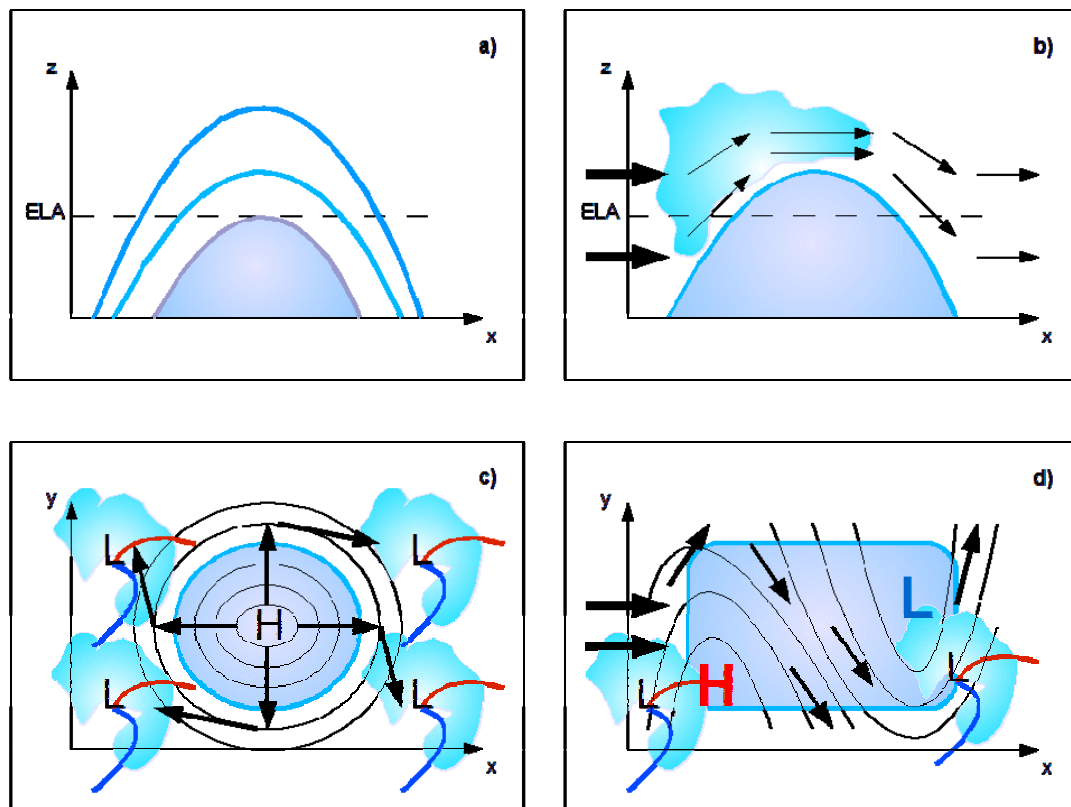


Figure 1.2. Forms of the mass balance - elevation feedback. a) The lapse-rate feedback, given a static atmosphere. The blue curves indicate 2D ice caps of various sizes, with varying proportions above and below the ELA. ELA denote the “equilibrium line altitude”, the altitude at which annual snowfall accumulation is balanced by summer melt and runoff. b) The orographic precipitation feedback, given a moist, dynamic atmosphere. Arrows denote forced air flow over the ice cap. Cloud and precipitation form where the air is forced upwards. c) The ice sheet anticyclone feedback. “H” denotes high sea level pressure, and black concentric circles are sketches of isobars (which in this case tend to parallel surface elevation contours). Arrows indicate the cold air outflow from the centre of the ice cap and the consequent Northern

Hemisphere anticyclonic circulation of the outflow as a result of the coriolis force. “L’s” denote low-pressure storm systems with associated warm fronts (red) and cold fronts (blue) and cloud/precipitation areas. d) The interaction of very large ice sheets with topographically-generated Rossby waves. The red H and blue L denote centres of high and low atmospheric thicknesses (or temperatures), respectively. Black lines are contours of atmospheric thickness. Arrows are upper atmosphere winds (and also indicate the path of the jet stream). “L’s” are surface low-pressure systems as described in c). See text for descriptions of the feedbacks.

1.3.1 All Spatial Scales: The Lapse-Rate Feedback.

Atmospheric temperatures decrease with elevation. Observed environmental lapse rates generally tend to be near $-6^{\circ}\text{C km}^{-1}$. The interaction of growing/shrinking ice caps with this lapse rate can result in a positive surface mass balance feedback, which operates as follows. Thinning of an ice cap or glacier as a result of an increase in equilibrium line altitude (ELA – the altitude at which annual accumulation is balanced by summer melt and runoff) or due to an increase in mass transfer from the accumulation zone to the ablation zone of the ice cap, results in a greater *percentage* of the ice mass lying at lower elevation, below the ELA, where air temperatures are higher. This will lead to increased melt and accelerated ice thinning (Figure 1.2a). This feedback also works in reverse (e.g. Abe-Ouchi et al., 2007).

This positive feedback can be further complicated by: 1) shifts in synoptic-scale atmospheric circulations, associated with climate change, which can lead to changes in regional atmospheric lapse-rates, resulting in further glacier mass balance feedbacks (e.g. Marshall et al., 2007); and 2) a compensating negative feedback if the ice cap is large enough such that its weight is capable of deforming the Earth’s crust beneath it. In this case, a growing ice cap depresses the Earth’s crust below, bringing a larger proportion of the ice cap below the ELA once again, reducing the rate of growth of the ice cap (and vice versa for a shrinking ice cap which leads to isostatic rebound of the Earth’s crust).

1.3.2 Meso- to Synoptic Scales: The Orographic Precipitation Feedback.

At meso- to synoptic scales (horizontal length scales of 10^1 - 10^3 km), the mass balance - elevation feedback is primarily invoked by airflow over mountain ranges, small ice caps or ice fields and involves the resultant orographic precipitation (Figure 1.2b). It has been noted that regional-scale ice caps, such as the ice caps found in the CHA, are capable of generating orographically - enhanced precipitation patterns (e.g. Koerner, 1979). Orographic precipitation can develop when air is forced to flow up and over a mountain or ice cap. As the air rises, it expands and cools adiabatically, and the moisture within it condenses to form cloud and precipitation on the upstream side of the ice cap. Conversely, as the air (now partly depleted of moisture) descends once again on the downstream side of the ice cap, it warms adiabatically, sometimes leading to warm, dry, chinook conditions (Figure 1.2b). In this way, precipitation and winter snowfall accumulation is orographically enhanced on the upstream side of an ice cap or mountain and a “rain shadow” develops on the downstream side. Chinook

winds can also act to dramatically enhance surface melt on the downstream side. This process can act to enhance/suppress precipitation associated with synoptic weather patterns in the area of the ice cap or mountain, or it can act on its own to generate precipitation in the absence of synoptic storms.

Orographic precipitation and lee-side chinooking can lead to a positive mass balance – elevation feedback. A perturbation (e.g. a positive change in upstream atmospheric moisture availability) can lead to amplified changes in summit elevations as air is forced upwards over an ice cap. As the air cools and condenses, it leads to increased snowfall which results in increased surface elevations upstream of and at the summit. Increases in surface elevation mean that the air is forced even higher as it passes over the ice cap, leading to even more cooling/condensing/precipitation, and even further increases in surface elevation upstream of and at the summit. Thus, orographically - enhanced precipitation at high elevations on the windward side of ice caps leads to increased snow/ice accumulation and surface elevations, which in turn further amplifies the orographic precipitation (Figure 1.2b). This feedback also causes the migration of the ice cap summit in an upstream direction (e.g. Hulton and Sugden, 1995; Purves and Hulton, 2000). Alpine ice caps in the Andes, with maritime moisture supplies, have been shown to modify their own mass balances through elevation - precipitation feedbacks (Hulton and Sugden, 1995).

1.3.3 Synoptic Scales: *The Glacier Anticyclone Feedback.*

At synoptic scales (horizontal length scales of 10^2 - 10^3 km), the feedback is primarily invoked by the formation of atmospheric anticyclones over large ice caps and ice sheets (Figure 1.2c). Anticyclones develop because cold, dense air forms over the centre of the ice cap as a result of high surface elevations (and high surface albedo – making this a combined mass balance - elevation and snow/ice-albedo feedback). This results in high surface pressures (when corrected to sea level – e.g. the Greenland climatological High) and a divergent surface outflow of air from the centre of the ice cap towards the edges, known as katabatic winds. This outflow causes atmospheric subsidence over the ice cap, clear skies, and a temperature inversion related to the dry adiabatic warming of the subsiding air. The surface outflow of cold, dense air develops an anticyclonic (clockwise) circulation in the Northern Hemisphere and a cyclonic (counterclockwise) circulation in the Southern Hemisphere due to the Coriolis effect. The outflow also serves to displace clouds and precipitation/snow towards the edges of the ice cap (Figure 1.2c).

Because synoptic-scale ice sheets, such as the present-day Greenland Ice Sheet (GIS), displace storm tracks and shift precipitation patterns towards their margins, they modify their own mass balance, limiting snow accumulation at the centre but causing thickening/expansion at the edges. This can lead to a positive mass balance –elevation feedback which operates as follows.

The displacement of precipitation/snow to the edges of the ice cap means that the ice cap margins will expand outwards and ice near the margins will increase in surface elevation. Expanding/thickening ice cap margins causes the area of high surface atmospheric pressures located over the centre of the ice cap to expand, increasing surface outflow and surface temperature contrasts near the ice cap margins, further enhancing marginal frontal systems and precipitation, displacing precipitation/snowfall even further outwards, and thus causing a continued expansion of the ice cap area.

The migration of the ice edges ever farther outwards will continue (with the help of ice deformation, which causes the ice to flow and spread outwards from central ice divides) until the ice margins either: 1) reach the coastline and the ocean, where the formation of ice shelves and/or calving occurs (e.g. GIS, Antarctica); 2) reach low enough latitudes so that SAT-related melting overwhelms the formation and/or spreading of the ice (e.g. southern extent of the Laurentide Ice Sheet); or 3) reach the limit of available atmospheric moisture such that no significant precipitation and accumulation occurs near the ice cap margins (e.g. where they terminate in the dry interiors of many CHA islands – Koerner 1979; 1989; 2002).

The feedback also operates in the opposite fashion, such that a shrinking ice cap will result in weaker anticyclonic circulation, allowing for the inward invasion of warmer temperatures and precipitation from its edges towards the centre of the ice cap. This results in ice cap thinning, a reduction in the areal extent of the ice cap, and a further reduction of the glacial anticyclone.

1.3.4 Synoptic-Planetary Scales: The Rossby Wave Feedback.

At synoptic-planetary scales (i.e. horizontal length scales of 10^3 km and more), continental scale ice sheets, such as the former Laurentide Ice Sheet (LIS), were capable of amplifying stationary planetary wave patterns in the atmosphere (e.g. Kutzbach et al., 1993; Roe and Lindzen, 2001). This allowed for the southward expansion of the ice sheet over eastern North America (e.g. Roe and Lindzen, 2001). A similar study conducted for the Fennoscandian ice sheet found that the planetary wave pattern forced by the ice sheet led to deviations in the ELA of 500 m (Lindeman and Oerlemans, 1987).

In this case, the feedback primarily involves the interaction of the atmospheric jet stream with the ice sheet's topography (Figure 1.2d). Topographic Rossby or planetary waves are generated by air flow over a step increase in surface elevation, such as occurs when the jet stream crosses the Rocky Mountains range

(e.g. Wallace and Hobbs, 1977) or as occurred when it encountered the Laurentide Ice Sheet (e.g. Roe and Lindzen, 2001). Atmospheric thickness patterns are folded into long waves with high thicknesses (related to warmer air of lower density) in the vicinity of the topographic perturbation and low thicknesses (related to cooler, higher density air sitting atop a surface anti-cyclone or area of high surface pressure) well downstream. The jet stream, which is a thermal wind, will tend to follow lines of equal atmospheric thicknesses.

A synoptic scale ice cap initially growing in northern Canada via the feedback described in section 1.3.3, will also have eventually begun to interact with the topographic Rossby waves generated by the Rocky Mountains and the Cordilleran Ice Sheet. These Rossby waves would have enhanced the southeastwards expansion of the ice sheet into the Great Lakes and Atlantic areas, which would in turn have thermally enhanced the low atmospheric thicknesses downstream of the Cordilleran Ice Sheet, leading to further southeastward expansion of the ice sheet (e.g. Roe and Lindzen, 2001; Kutzbach et al., 1993).

In summary, atmospheric Planetary/Rossby wave modification enhances a downstream surface glacial Anticyclone (i.e. high surface pressures) beneath low atmospheric thicknesses, modifies atmospheric precipitation patterns, modifies ice sheet expansion and geometry, which in turn modifies the atmospheric Planetary/Rossby wave even more.

One of the triggers for this feedback is a change in the strength / incidence angle of the Jet Stream as it reaches the continent from the Pacific, which impacts the amplitude of the topographically generated Rossby waves. A second trigger may be an El Niño event, which thermally enhances the high atmospheric thicknesses and warm temperatures in western North America, and thus enhances the Rossby wave amplitude, leading to a decrease in SATs downstream to the east, which then acts to enhance low thicknesses and cold temperatures in the east. A third trigger for this feedback is an increase/decrease in the surface elevation of the ice cover over the western part of the continent.

1.4 OUTLINE OF THESIS EXPERIMENTS AND THESIS FORMAT

While snow and sea ice in the polar regions are the main factors in the snow/ice-albedo feedback related amplification of present climate change in the Arctic, land ice masses may locally further amplify the changes in a significant way, even on decadal time scales and less. Local amplification in SAT changes as a result of the terrestrial ice-albedo feedback may accelerate changes in outlet glaciers by impacting ice temperatures and eventually ice flow.

Furthermore, although the elevation – mass balance feedback is generally considered to be of secondary importance to the snow/ice-albedo feedback in the co-evolution of ice sheets and the atmosphere, it is nevertheless worth quantifying for CHA ice caps to ascertain its magnitude and impact. The impacts of small

amplifications may “accumulate” over time, so that what appears negligible on decadal time scales may become significant on centennial to millennial time scales.

Studies of CHA terrestrial ice masses are increasing in number, especially with the advent of new remote sensing techniques (e.g. Wang et al., 2005) and with the occasion of the extended International Polar Year (2007-2009). However, much remains to be determined concerning the role of these ice masses in modifying the regional climate, and in modifying their own responses to changes in the regional climate.

To assess whether changes in CHA ice mass temperatures, mass fluxes, and geometries can be amplified by the local interactions of these ice masses with the overlying atmosphere, leading to accelerations in the observed changes, the following must first be determined.

- 1) The magnitude of the snow/ice-albedo feedback for Canadian High Arctic (CHA) terrestrial ice systems, specifically in the vicinity of land ice margins (where outlet valley glaciers are located), should be quantified. If possible, in light of recent climate changes, the specific contribution of land ice to the combined snow/ice-albedo feedback, on less than centennial time scales, should be isolated and the magnitude also quantified;
- 2) The consequences of local snow/ice-albedo feedback amplifications of SAT and ice thickness changes for the evolution of CHA land ice masses (via their marginal valley glaciers) should be examined. SAT and ice thickness (h_{ice}) changes impact internal ice temperatures, which in turn are important to the mass flux divergence of CHA glaciers. As a first step in exploring whether amplified ΔSAT 's/ Δh_{ice} 's are important to a glacier's continuing response to climate perturbations, the climate sensitivity of time-varying internal ice temperatures within CHA land ice masses should be investigated as follows:
 - a) The influence of time-varying SAT changes on the diffusive smoothing of ice temperature anomalies in glacier accumulation zones should be quantified.
 - b) The influence of time-varying SAT and h_{ice} changes upon the basal ice temperatures of glacier ablation zones should be quantified, and implications for ice flow and mass flux divergence analyzed.
- 3) Although considered secondary to the snow/ice-albedo feedback, the impact of mass balance - elevation feedback amplifications of atmospheric moisture perturbations upon the evolution of Holocene CHA ice caps needs to be quantified.

These concerns form the basis of the modeling experiments described in the four core chapters of this thesis. It is hoped that the initial quantifications described in this thesis will form the groundwork for future studies in this area.

In chapter 2, the magnitude of the snow/ice-albedo feedback, on decadal time scales and less, is computed for a CHA outlet valley glacier (John Evans Glacier (JEG), Ellesmere Island). An energy-mass balance ice-atmosphere model of JEG is developed and a linear feedback analysis of the model climate's responses to various radiative perturbations is performed to calculate the magnitude of the snow/ice-albedo feedback's amplification of these perturbations. The model experiments are performed for the JEG valley domain with and without the glacier, to assess the contribution of terrestrial ice to the magnitude of the combined snow/ice-albedo feedback on decadal timescales and less. The implications of the model results for the mass transfer from the accumulation zone to the ablation zone and for the future evolution of JEG's mass flux divergences is examined via a series of glacier response time calculations.

In chapters 3 and 4, the impact of SAT changes and of local albedo-feedback amplifications of SAT changes, on the internal and basal temperatures of CHA land ice masses are investigated. SAT changes associated with the Little Ice Age (LIA), the most recent significant negative perturbation in incoming Holocene solar radiation at the earth's surface, and the subsequent warming to the present day are focused upon in both chapters. In chapter 3, the magnitude of a measured negative ice temperature anomaly, associated with the LIA and found in the accumulation zones of many Arctic glaciers and ice caps, is investigated with a 1D ice borehole temperature model to determine the extent to which its amplitude: 1) was directly affected by local amplifications of the LIA-related Δ SAT perturbation; and/or 2) is being indirectly affected by past and present time-variations in SATs (a function of the ice cap's thickness or thermal memory). In chapter 4, the extensive area of basal ice temperatures inferred to be at the pressure melting point in the ablation zone of JEG, which is in apparent disequilibrium with the glacier's boundary conditions, is investigated. Experiments with a 2D cross-sectional ice temperature model are performed to determine whether ice thickness changes, associated with LIA SAT changes, may have played an indirect role in its creation and maintenance, or whether other, more direct SAT-change related factors such as surface melt-water production were and are more important.

In chapter 5, the impact of mass balance – elevation feedback amplifications of atmospheric moisture perturbations on the evolution of Holocene CHA ice caps is examined. Specifically, this study focuses on whether the mass balance – elevation feedback was important to Devon Ice Cap's surface profile evolution throughout the Holocene and whether it might partially account for the measured 1960's-to-present-day mass gains of the northwest part of the ice cap. To quantify the magnitude of the feedback, a simple linearly viscous Shallow Ice

Equation (SIE) model of Devon Ice Cap was coupled to a simple mechanical slab atmosphere model so that the mass balance – elevation feedback could be simulated in the 10 thousand year model runs. Model mass balances and mass flux divergences were constrained using available present-day observations and measurements. To initiate the feedback, the model mass balance was perturbed by modifying the airflow over the ice cap and by modifying the specific humidity of the atmosphere (to simulate reduced versus increased sea ice - free water fractions to the northwest of the ice cap).

1.5 REFERENCES

Abe-Ouchi, A., T. Segawa and F. Saito, 2007: Climatic conditions for modelling the Northern Hemisphere ice sheets throughout the ice age cycle. *Climate of the Past*, **3**, 423–438.

Arendt, A., 1999: Approaches to modelling the surface albedo of a high arctic glacier. *Geografiska Annaler*, **81 A** (4), 477-487.

Arendt, A. A., K. A. Echelmeyer, W. D. Harrison, C. S. Lingle and V. B. Valentine, 2002: Rapid wastage of Alaska glaciers and their contribution to rising sea level. *Science*, **297**(5580), 382 – 386. DOI: 10.1126/science.1072497 .

Arnold, N. 2005. Investigating the sensitivity of glacier mass-balance/elevation profiles to changing meteorological conditions: model experiments for Haut Glacier D’Arolla, Valais, Switzerland. *Arctic, Antarctic, and Alpine Research*, **37**(2), 139–145.

Bintanja, R., and J. Oerlemans, 1995: The influence of the albedo-temperature feedback on climate sensitivity. *Ann. Glaciol.*, **21**, 353-360.

Bony, S., R. Colman, V.M. Kattsov, R.P. Allan, C.S. Bretherton, J-L. Dufresne, A. Hall, S. Hallegatte, M.M. Holland, W. Ingram, D.A. Randall, B.J. Soden, G. Tselioudis and M.J. Webb. 2006. How well do we understand and evaluate climate change feedback processes? *Journal of Climate*, **19**, 3445-3482.

Cess, R.D., and 32 others, 1991: Interpretation of snow-climate feedback as produced by 17 General Circulation Models. *Science*, **253**, 888-892.

Curry, J. A., J. L. Schramm and E. E. Ebert, 1995: Sea ice-albedo climate feedback mechanism. *Journal of Climate*, **8**, 240-247.

Curry, J. A., W. B. Rossow, D. Randall and J. L. Schramm, 1996: Overview of Arctic cloud and radiation characteristics. *Journal of Climate*, **9**, 1731-1764.

Curry, J.A., J.L. Schramm, D. Petrovich, and J.O. Pinto, 2001: Application of SHEBA/FIRE data to evaluation of sea ice surface albedo parameterizations. *Journal of Geophysical Research*, **106**, 15345-15356.

Dowdeswell, J.A., R. Hodgkins, A.M. Nuttall, J.O. Hagen, and G.S. Hamilton. 1995. Mass balance change as a control on the frequency and occurrence of glacier surges in Svalbard, Norwegian High Arctic. *Geophysical Research Letters*, **22** (21), 2909-2912.

Fyfe, J.C. and G.M. Flato. 1999: Enhanced climate change and its detection over the Rocky Mountains. *Journal of Climate*, **12**, 230-243.

Harvey, L.D.D., 1988: On the role of high latitude ice, snow, and vegetation feedbacks in the climatic response to external forcing changes. *Climatic Change*, **13**(2), 191-224.

Hock, R., V. Radić, M. de Woul, 2007: Climate sensitivity of Storglaciären, Sweden: an intercomparison of mass-balance models using ERA-40 re-analysis and regional climate model data. *Annals of Glaciology*, **46**, 342-348.

Holland, M. M., and C. M. Bitz, 2003: Polar amplification of climate change in coupled models. *Climate Dynamics*, **21**, 221-232.

Hulton, N. R. J. and D. E. Sugden, 1995: Modelling mass balance on former maritime ice caps: a Patagonian example. *Annals of Glaciology*, **21**, 304-310.

IPCC, 1996: *Climate Change 1995: The Science of Climate Change*. Contribution of Working Group 1 to the Second Assessment Report of the IPCC [Houghton, J.T., Meira Filho, L.G., Callander, B.A., Harris, N., Kattenberg, A., and Maskell, K. (eds)]. Cambridge University Press, Cambridge, U.K. 572 pp.

IPCC, 2007: *Climate Change 2007: The Physical Science Basis*. Contribution of Working Group I to the Fourth Assessment Report of the Intergovernmental Panel on Climate Change [Solomon, S., D. Qin, M. Manning, Z. Chen, M. Marquis, K.B. Averyt, M. Tignor and H.L. Miller (eds.)]. Cambridge University Press, Cambridge, United Kingdom and New York, NY, USA, 996 pp.

Koerner, R. M., 1979: Accumulation, ablation, and oxygen isotope variations on the Queen Elizabeth Island ice caps, Canada. *Journal of Glaciology*, **22**(86), 25-41.

Koerner, R.M., 1989: Queen Elizabeth Islands glaciers. *In: Quaternary Geology of Canada and Greenland* (R.J. Fulton, ed.), Geological Survey of Canada, Geology of Canada, no. 1, 464-477.

Koerner, R.M., 2002: Glaciers of North America – Glaciers of Canada, Glaciers of the Arctic Islands, Glaciers of the High Arctic Islands. *In: Satellite Image Atlas of Glaciers of the World* (R.S. Williams, Jr. and J.G. Ferrigno, eds.), U.S. Geological Survey Professional Paper 1386-J-1.

Kutzbach, J.E., P.J. Guetter, P.J. Behling, and R. Selin, 1993: Simulated climatic changes: results of the COHMAP climate-model experiments. *In: Global Climates since the Last Glacial Maximum* (Wright Jr., H.E., J.E. Kutzbach, T. Webb III, W.F. Ruddiman, F.A. Street-Perrott, and P.J. Bartlein, eds.). University of Minnesota Press, Minneapolis and London, 24-93.

Lindeman, M., and J. Oerlemans, 1987: Northern hemisphere ice sheets and planetary waves: a strong feedback mechanism. *International Journal of Climatology*, **7**(2), 109-117. doi:10.1002/joc.3370070202.

Marshall, S. J., M. J. Sharp, D. O. Burgess and F. S. Anslow, 2007: Near-surface-temperature lapse rates on the Prince of Wales Icefield, Ellesmere Island, Canada: implications for regional downscaling of temperature. *International Journal of Climatology*, **27**(3), 385-398. Published online in Wiley InterScience (www.interscience.wiley.com) DOI: 10.1002/joc.1396.

Oerlemans, J., 1986: Glaciers as indicators of a carbon dioxide warming. *Nature*, **320**, 607-609.

Paul, F., A. Kääb, M. Maisch, T. Kellenberger and W. Haeberli, 2004: Rapid disintegration of alpine glaciers observed with satellite data. *Geophysical Research Letters*, **31**, L21402, doi:10.1029/2004GL020816.

Pritchard, M. S., A. B. G. Bush and S. J. Marshall, 2008: Neglecting ice-atmosphere interactions underestimates ice sheet melt in millennial-scale deglaciation simulations. *Geophysical Research Letters*, **35**, L01503, doi: 10.1029/2007GL031738.

Purves, R. S., and N. R. J. Hulton, 2000: Experiments in linking regional climate, ice-sheet models and topography. *Journal of Quaternary Science*, **15**(4), 369–375.

Qu, X., and A. Hall, 2005: Surface contribution to planetary albedo variability in cryosphere regions. *Journal of Climate*, **18**, 5239–5252.

Qu, X., and A. Hall, 2006: Assessing snow albedo feedback in simulated climate change. *Journal of Climate*, **19**, 2617–2630.

Qu, X., and A. Hall, 2007: What Controls the Strength of Snow-Albedo Feedback? *Journal of Climate*, **20**, 3971-3981.

Robock, A., 1983: Ice and snow feedbacks and the latitudinal and seasonal distribution of climate sensitivity. *Journal of the Atmospheric Sciences*, **40**(4), 986-997.

Roe, G.H. and R.S. Lindzen, 2001: The mutual interaction between continental-scale ice sheets and atmospheric stationary waves. *Journal of Climate*, **14**, 1450-1465.

Sweeney, M. R., A. J. Busacca, C. A. Richardson, M. Blinnikov and E. V. McDonald, 2004: Glacial anticyclone recorded in Palouse loess of northwestern United States. *Geology*, **32**(8), 705–708; doi: 10.1130/G20584.1.

Wang, L., M. J. Sharp, B. Rivard, S. Marshall, and D. Burgess, 2005: Melt season duration on Canadian Arctic ice caps, 2000–2004. *Geophysical Research Letters*, **32**, L19502, doi: 10.1029/2005GL023962.

Zuo, Z., and J. Oerlemans, 1996: Modelling albedo and specific balance of the Greenland ice sheet: calculations for the Søndre Strømfjord transect. *Journal of Glaciology*, **42**(141), 305-317.

2. Quantifying the Impact of the Terrestrial Snow/Ice-Albedo Feedback upon a Canadian High Arctic Glacier and its Local Climate.

2.0 INTRODUCTION

Apart from the Greenland Ice Sheet (GIS), Canadian High Arctic (CHA) ice caps, ice fields and glaciers collectively constitute the largest volume of terrestrial ice in the Northern Hemisphere. These ice masses interact with the overlying atmosphere: they both modify, and are modified by, regional climate variations. In some cases, ice-atmosphere interactions result in positive feedbacks between the two systems, which serve to perpetuate and amplify initial climate perturbations. The primary example of such a positive feedback is the snow/ice-albedo feedback, which is well-studied in the cases of sea ice and snow, but often neglected in the case of terrestrial ice on less than centennial to millennial time scales. Although it is generally assumed that terrestrial ice - related feedbacks are less important than sea ice - related feedbacks in terms of recent global climate change, and while this is supported in many model experiments (e.g. Holland and Bitz, 2003), the observations of Paul et al. (2004) and the review of Curry et al. (1996) suggest that the matter is still open to question at local to regional scales. This study, then, seeks to: 1) address the question of whether the terrestrial snow/ice-albedo feedback can be important to the evolution of local climate and ice masses in the CHA on decadal time scales and less; and 2) to isolate the contribution of terrestrial ice to the overall magnitude of climate change amplifications related to the snow/ice-albedo feedback.

The snow/ice-albedo feedback is a positive area feedback that amplifies the response of glaciers and climate to radiative or temperature perturbations. For example, warmer than normal atmospheric temperatures reduce snow and ice cover, decrease the area-averaged surface albedo, and increase the absorption of solar radiation by land surfaces. This results in further warming of the land surface and the overlying atmosphere, further reductions in ice and snow cover, and further absorption of solar radiation (Figure 2.1). This feedback works in reverse for a cooling perturbation.

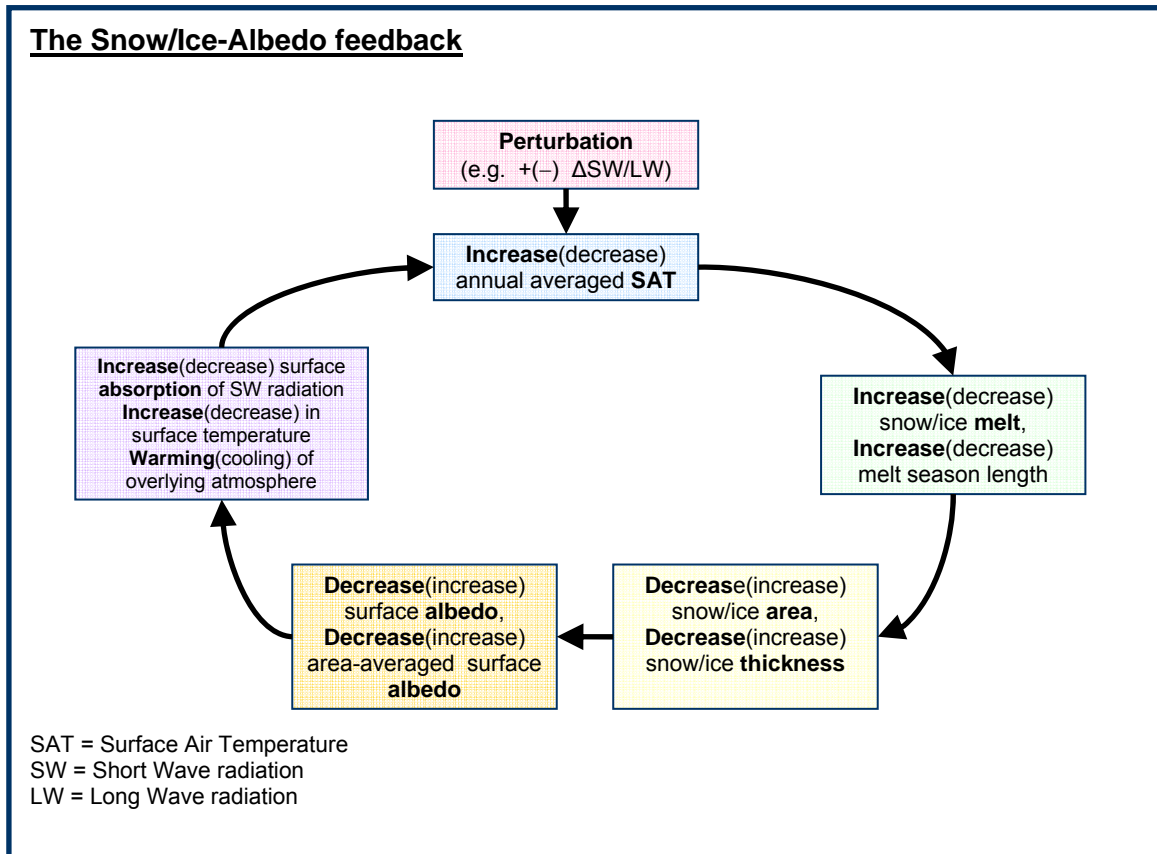


Figure 2.1 The snow/ice-albedo feedback: a positive feedback that amplifies radiative perturbations.

The snow/ice-albedo feedback can also be a thickness feedback, because surface albedo is also correlated with snow/ice thickness and meltwater fraction (for sea ice, see – e.g. Curry et al., 1995; and for snow, see – e.g. Robock, 1983; Fyfe and Flato, 1999; Qu and Hall, 2007). Melting and thinning of snow and/or sea ice leads to lower surface albedo, increased absorption of solar radiation, and further melting and thinning of the snow and/or ice (and vice versa).

The snow/ice-albedo feedback varies in time and space. It is non-zero only in areas where sunlight and snow and/or ice are present. This means that the snow/ice-albedo feedback cannot operate at high-latitudes during the polar night and that the feedback is permanently absent in low-latitude, low-altitude areas which do not experience snow and/or ice. Amplification of climate changes by this feedback will be greatest when sunlight is abundant (i.e. in summer when daylight hours are at a maximum) and when the surface albedo contrast across the snow/ice – no snow/ice boundary is greatest (i.e. after a fresh snowfall or prior to the onset of spring melt). For areas which experience near or complete 24-hour darkness in winter, and which experience complete summer melt of snow and/or sea ice, the feedback can only operate efficiently in the spring and fall (i.e. during

transition seasons). For polar regions with perennial snow and ice cover, the feedback can operate throughout the entire “polar day”.

In addition to latitudinal and altitudinal spatial variations, the snow/ice-albedo feedback also varies spatially across an ice mass itself. For example, the feedback cannot operate efficiently at the centre of large ice sheets where surface albedo changes in response to surface air temperature (SAT) changes are small. The feedback will have a larger amplifying effect near the margins of these ice sheets where meltback or growth of the snow or ice exposes or covers lower albedo ground, ice or water surfaces, considerably altering the area-averaged surface albedo and the local surface energy balance (e.g. Pritchard et al., 2008).

In addition to seasonal variations, the magnitude and nature of the snow/ice-albedo feedback can also vary over different time scales (e.g. decadal versus millennial) and over different historical periods (e.g. early versus late Holocene) because seasonal variations in the feedback themselves can change with time. It cannot be expected that the feedback, triggered by a given radiative perturbation, will produce equivalent amplifications in mean surface air temperature over 100,000 years as it will over 10 years, because over 100,000 years the basic (unperturbed) climate state is not one with simple, regular, annual temperature cycles but one in which temperatures also vary inter-annually, inter-decadally, and on centennial-millennial time scales. Additionally, it cannot automatically be assumed that the magnitude of the snow/ice-albedo feedback, when computed over different timescales, will be significant and comparable to the direct effects of natural external forcings over similar timescales.

During the 1990's, climate General Circulation Model (GCM) experiments predicted that the snow/ice albedo feedback would significantly amplify the warming response of high-latitudes to increases in atmospheric greenhouse gases, although the predicted magnitude of the amplification differed widely between models (IPCC, 1996). Energy Balance Climate Models (EBCMs – e.g. Bintanja and Oerlemans, 1995; Harvey, 1988; Robock, 1983), and various coupled atmosphere-ocean models (e.g. Holland and Bitz, 2003), indicated that sea ice was key to the enhanced climate sensitivity at high latitudes. Although on-going studies have also verified the important contribution of snow to the snow/ice-albedo feedback in the mid-latitude and polar regions (e.g. Qu and Hall, 2005; 2006; 2007), the magnitude of its impact upon global climate is less definite than that of sea ice in most models (e.g. Cess et al., 1991).

When the polar climate system is perturbed (e.g. via changes in surface radiation balance, SAT, or precipitation), snow and sea ice experience large and rapid area changes at decadal time scales and less, leading to large and rapid area-averaged albedo changes. For this reason, polar climate changes on these time scales will be more greatly amplified by the presence of these two components of the cryosphere via the snow/ice-albedo feedback, than by land ice masses which respond more slowly to perturbations (i.e. in terms of ice temperature, ice melt,

ice thickness and eventually ice area). In general, no great or rapid area change of land ice is witnessed on less than century time scales, except where outlet valley glaciers are concerned. For this reason, the magnitude and significance of the snow/ice-albedo feedback has rarely been examined for high-latitude terrestrial ice caps and glaciers: not only are they smaller in extent than sea ice and snow covers (in the Northern Hemisphere), but they also respond more slowly to climate perturbations. Consequently, in some comprehensive reviews of climate feedbacks, the contribution of terrestrial ice to the snow/ice-albedo feedback is completely ignored (e.g. Bony et al., 2005).

This is not to say that the importance of the terrestrial ice-albedo feedback is always negligible. At greater than centennial time scales, as ice sheets and ice caps grow and retreat, model experiments confirm a terrestrial ice-albedo feedback with the atmosphere (e.g. the Laurentide Ice Sheet – Abe-Ouchi et al., 2007). Moreover, the glacial anticyclones generally found over large ice sheets (e.g. the Laurentide Ice Sheet – Sweeney et al., 2004), are partly initiated and strengthened by the ice-albedo feedback.

Furthermore, even on decadal timescales and less, at the margins of ice caps, significant area changes in outlet or valley glaciers can occur (e.g. Arendt et al., 2002). In these locations, therefore, the land ice-albedo feedback may play a significant role in amplifying such changes (e.g. Paul et al., 2004). In the absence of significant area changes on decadal timescales and less, terrestrial ice may yet play a role in prolonging seasonal snow cover in a glacier catchment, and therefore the operation of the snow-albedo feedback throughout the melt season. Although SATs in glaciated catchments tend to be lower than those in non-glaciated catchments, it is hypothesized here that *changes* in SATs may be amplified to a greater extent in glaciated valleys as a result of a prolongation of the operation snow-albedo feedback into the summer season.

Computations of the magnitude of ice-albedo feedback-related climate-change amplifications (using proper linear feedback analysis) are rare, however, on less than centennial time scales and for terrestrial ice masses with less than continental-scale extents. Most research in this area has focused on modeling the surface albedo of specific glaciers for energy balance purposes (e.g. Arendt, 1999), and examining how this affects the sensitivity of individual glacier mass balances to climate change (e.g. Zuo and Oerlemans, 1996). Furthermore, many glacier sensitivity calculations of this sort are made by testing a glacier's response to climate perturbations using static glacier models, or decoupled atmosphere and ice models with no inherent feedbacks between the ice and the atmosphere (e.g. Hock et al., 2007; Bassford et al., 2006). For this reason, the magnitude of the terrestrial ice-albedo feedback is not well known and the degree of further local amplification of radiative perturbations and the impact of this upon an ice mass itself is not well understood.

Knowledge of the magnitude of the terrestrial ice-albedo feedback and understanding of its variations are important, as local amplification of SAT changes on decadal-timescales as a result of the snow/ice-albedo feedback could accelerate changes in outlet and valley glaciers, where glacier thinning (thickening) is related to glacier retreat (advance) (i.e. area changes). Additionally, local SAT-change amplification could impact ice temperatures and eventually ice flow, leading to potentially significant impacts upon the evolution of these marginal outlet or valley glaciers, again on less than century timescales. Changes in surface temperature and in ice thickness will lead to changes in ice velocity and mass flux divergence, in particular where enhanced surface meltwater production is able to reach the glacier bed (e.g. Bingham et al., 2005; Zwally et al., 2002). Ice-albedo feedback enhanced variations in ice cap margins, in turn, could have an important impact upon local/regional SAT and atmospheric pressure patterns, possibly even (eventually) influencing the larger-scale polar and global climate.

The model experiments described in this chapter were performed to assess the local significance of the terrestrial snow/ice-albedo feedback on decadal time scales and less, and to create a foundation for further studies in this area. Because the snow/ice-albedo feedback is most effective near the margins of ice caps, a quantification of the magnitude of the climate-change amplification due to the snow/ice-albedo feedback was performed for a representative CHA outlet glacier. Specifically, this study assessed the impact of the presence of terrestrial ice upon the magnitude of the snow-albedo feedback, as this may be more important than ice area changes on decadal timescales and less. The importance of the determined climate-change amplification for the future evolution of the terrestrial ice mass and its local climate was then explored.

The details of this research are presented in the following manner: 1) the climate sensitivity and feedback parameters, commonly used to quantify the magnitude of climate feedback processes, are defined; 2) John Evans Glacier (JEG), the representative CHA glacier chosen for this study because of its size, location, and for the availability of meteorological and mass balance measurements, is introduced; 3) the experimental procedures and the model perturbation experiments are outlined; 4) the results of the model experiments are presented; 5) the results are discussed; and 6) conclusions are offered. The energy-mass balance model and parameterizations used in the experiments to simulate JEG and its local climate are described in an appendix.

2.1 DEFINITION OF THE CLIMATE SENSITIVITY PARAMETER, λ , AND THE FEEDBACK PARAMETER, f

To quantify the magnitude of the amplification/damping produced by a climate system feedback, the concept of climate sensitivity is used. If the climate system is further assumed to be analogous to an electrical system composed of internal

gains, G , and feedbacks, f , a method for calculating the magnitude of the feedback's effect on the climate system can be developed as described in Peixoto and Oort (1982). This method as applied to the climate system is sometimes referred to as a “Linear Feedback Analysis” (e.g. Harvey, 1988).

The climate sensitivity parameter, λ , is defined as follows (e.g. Harvey, 1988; Cess et al., 1991; Bintanja and Oerlemans, 1995):

$$\lambda = \frac{\Delta T}{\Delta Q} \quad (1)$$

where for our purposes ΔT is the effective change in surface air temperature from the mean climatic state induced by a given radiative perturbation, ΔQ .

The ratio of λ_f (the resultant change in temperature realized when the snow/ice-albedo feedback is in effect) to λ_0 (the resultant change in temperature realized without the snow/ice-albedo feedback) is used to indicate the *gain* in surface air temperature due to the feedback's amplification (e.g. Cess et al., 1991; Curry et al., 2001). This ratio, R , termed the “feedback gain ratio” (Peixoto and Oort, 1982), yields the following equation:

$$R = \frac{\lambda_f}{\lambda_0} = \frac{\Delta T_f}{\Delta T_0} = \frac{G_{\text{eff}}}{G} \quad (2)$$

For a system with no internal gains ($G=1$), R is simply the effective gain, G_{eff} , due to the feedback and $\Delta T_f = G_{\text{eff}} \times \Delta T_0$.

The magnitude of the feedback parameter, f , may be calculated from G_{eff} using:

$$G_{\text{eff}} = \frac{1}{(1-f)} \quad \text{or} \quad f = 1 - \frac{1}{G_{\text{eff}}} \quad (3)$$

(Harvey, 1988; Peixoto and Oort, 1982). Note that in this formulation, f cannot realistically equal or exceed a value of 1 in the positive case. The larger the magnitude of the feedback parameter, f , the larger the effective gain of the system (i.e. the larger the deviation of G_{eff} from a value of 1). For positive f 's, $G_{\text{eff}} > 1$, and the result is an amplification of the system response. For negative f 's, $0 < G_{\text{eff}} < 1$, and the result is a damping of the system response.

The above parameters are used in this study, which seeks to quantify the amplification of climate perturbations by the positive terrestrial snow/ice-albedo feedback in the CHA. An energy - mass balance model is developed for a representative CHA glacier, and the model climate is perturbed with radiative changes to compute the system response and the magnitude of the feedback.

2.2 JOHN EVANS GLACIER

John Evans Glacier (JEG – Figure 2.2) is located on the east coast of Ellesmere Island, Nunavut, Canada (79.67°N, 74.5°W) and provides the main drainage for a small ice field immediately southeast of the Agassiz Ice Cap. It was chosen for this study as a representative example of a CHA outlet/valley glacier, primarily for the reason that it is a non-surging glacier with a length, summit elevation and equilibrium line altitude (ELA – the altitude at which surface mass accumulation equals surface mass ablation) common to many CHA glaciers.

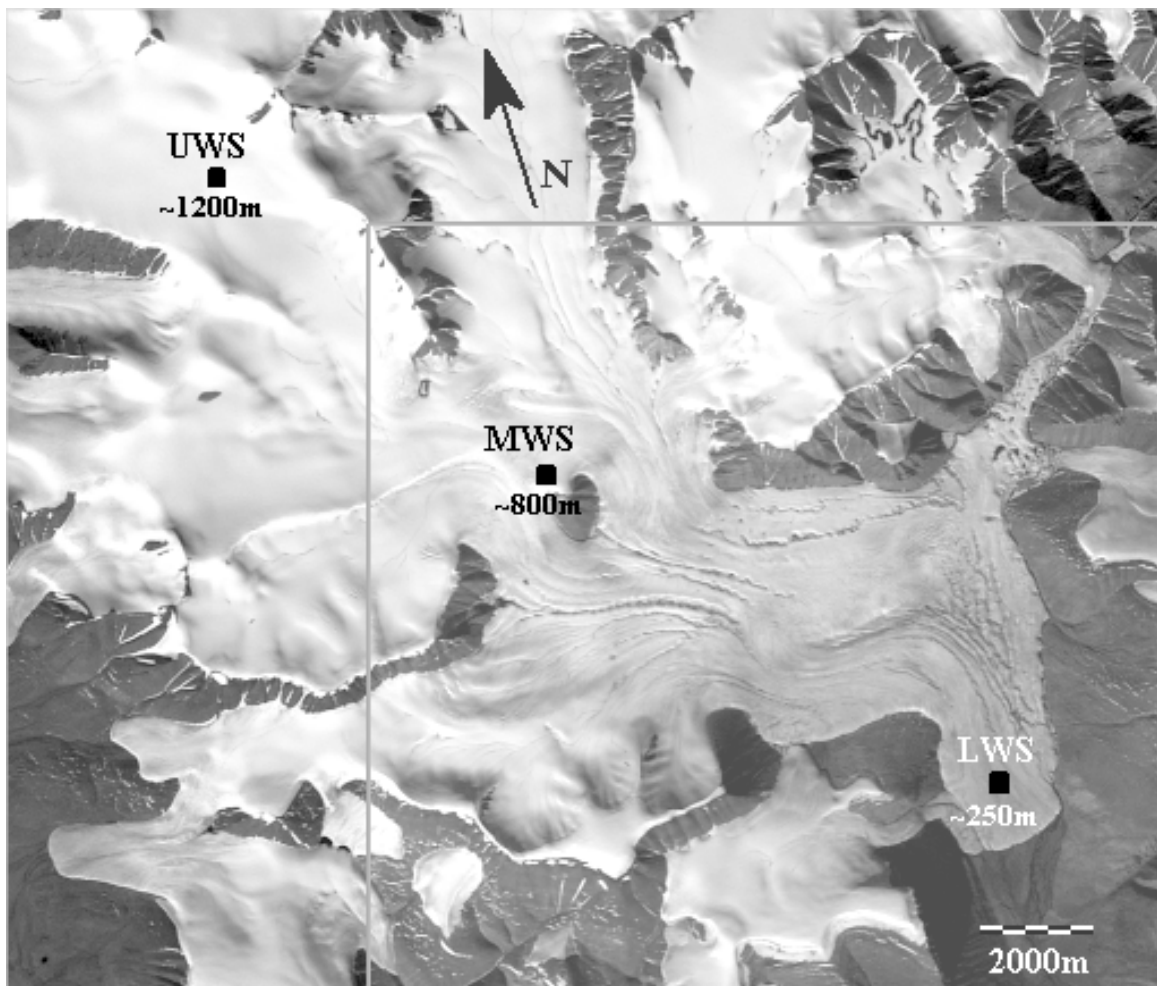


Figure 2.2. John Evans Glacier (Landsat 7 image, July 1999). Three automatic weather stations (WS) are located: 1) near the summit (Upper – UWS); 2) near the equilibrium line (Middle – MWS); and 3) near the snout (Lower – LWS). The area within the gray square outline corresponds to the model domain.

JEG is approximately 20 km long, which makes it a mid-sized CHA glacier. As can readily be seen on topographic maps and satellite imagery covering the CHA, most glaciers in the region are between 10 and 100 km long. JEG's summit

elevation is just under 1500 m, average for ice cap and ice field summits in the CHA which generally range from just over 500 m (e.g. Laika Ice Cap and Glacier: Blatter and Kappenberger, 1988) to near 2000 m (e.g. Devon Ice Cap: Burgess and Sharp, 2004; Prince of Wales Ice Field: Marshall et al., 2007). JEG's mean ELA lies near 800 m a.s.l. (Copland et al., 2003), where other CHA glacier ELAs have been measured at 400–1400 m a.s.l. (e.g. White Glacier: Blatter 1987) and 800–950 m (e.g. Devon Ice Cap: Burgess and Sharp, 2004; Koerner, 1970). JEG also terminates on land near sea level as do many CHA glaciers.

JEG's primary and secondary atmospheric moisture sources are Baffin Bay and the Arctic Ocean, respectively (Koerner, 1979; Alt, 1987). This is typical of most glaciers and ice caps in the eastern part of the CHA (Koerner, 1979), although the Arctic Ocean can become the primary moisture source during certain anomalous seasons or years (Alt, 1987).

In addition to its high Arctic location, average size and ELA, JEG was also chosen for this study because of the availability of meteorological and mass balance data, as well as the availability of surface and bed digital elevation models (DEMs). Three automatic weather stations, erected in 1996 and taken down in 2002, were located on the glacier near the summit (~1180 m elevation), the ELA (~820 m), and close to the snout (~250 m; Figure 2.2), respectively. These stations measured air temperature at a height of ~2 m, relative humidity (RH), wind speed/direction, and incoming/outgoing shortwave and net all-wavelength radiation. Additionally, a centre-line network of up to 34 stakes extended from the glacier summit to the snout during this period, and was used for mass balance measurements.

A surface digital elevation model (DEM) of the JEG catchment was created from stereo-aerial photography of the area, taken during the 1950's and 1960's (available from the National Air Photo Library (NAPL) of Natural Resources Canada (NRCan)), using analytical photogrammetry (*pers. comm.* A. Arendt). Surface DEMs produced in this way have fewer errors than those produced by interpolating from coarser resolution published DEMS (e.g. Cogley and Jung-Rothenhäusler, 2004), such as those derived from the Canadian Digital Elevation Data (CDED). Accuracy of surface DEMs is important when coupling surface processes to atmospheric processes. DEM errors can produce large errors in mesoscale model precipitation and surface mass balances (e.g. as was found in the Patagonian study of Cook et al., 2003, in using the NCAR MM5 mesoscale atmospheric model described by Grell et al., 1994).

JEG ice thicknesses were measured by Copland and Sharp (2001) using radio-echo sounding, and a bed DEM for JEG was developed by subtracting these measurements from the surface DEM. JEG ice thicknesses are found to range between 100–400 m.

2.3 COMPARISON OF THE JEG AND THE JEG–MODEL CLIMATES

The surface-atmosphere energy-mass balance model and the JEG-specific parameterizations used in this study are detailed in the appendix of this chapter. A *qualitative* comparison of the model climate (Figure 2.3) with observations from the weather stations at JEG (e.g. Figure 2.4) indicates that model temperature and albedo simulations adequately reproduce the measured values, although the high frequency day-to-day variability is missing (because layer-average temperatures are calculated over a daily, as opposed to hourly, time-step and as such capture only the seasonal variability – see appendix). The model correctly predicts an inversion ($T_a - T_s > 0$) during late winter and spring for areas adjacent to the glacier, during the spring and summer for areas over the ice, and during spring only when temperatures are averaged over the entire area (Figure 2.3d).

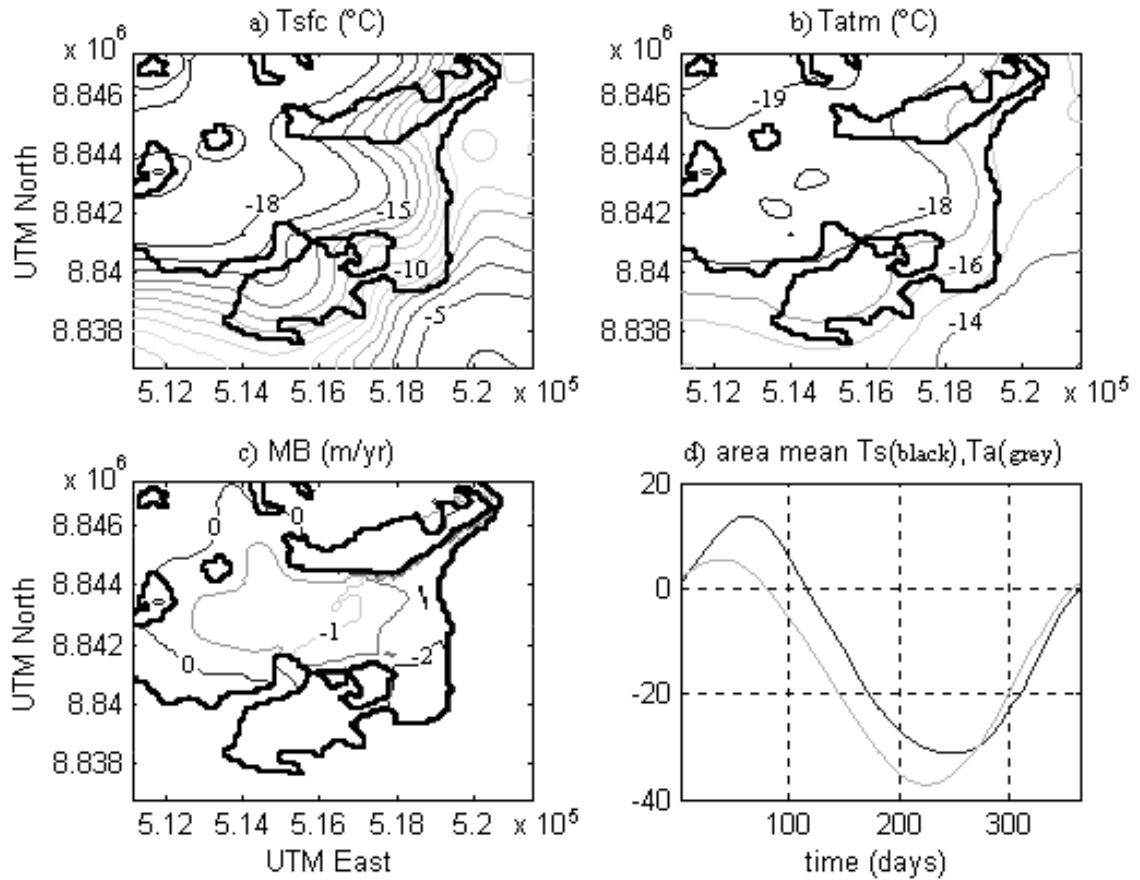


Figure 2.3. Model climate (here using a thermal diffusivity parameter $\eta = 2.15 \times 10^{-5} \text{ m}^2 \text{ s}^{-1}$): a) mean annual surface temperature; b) mean annual atmospheric temperature; c) surface mass balance; d) model-area averaged surface and atmospheric temperatures ($^{\circ}\text{C}$). The thick black line in panels a), b), and c) is the outline of JEG.

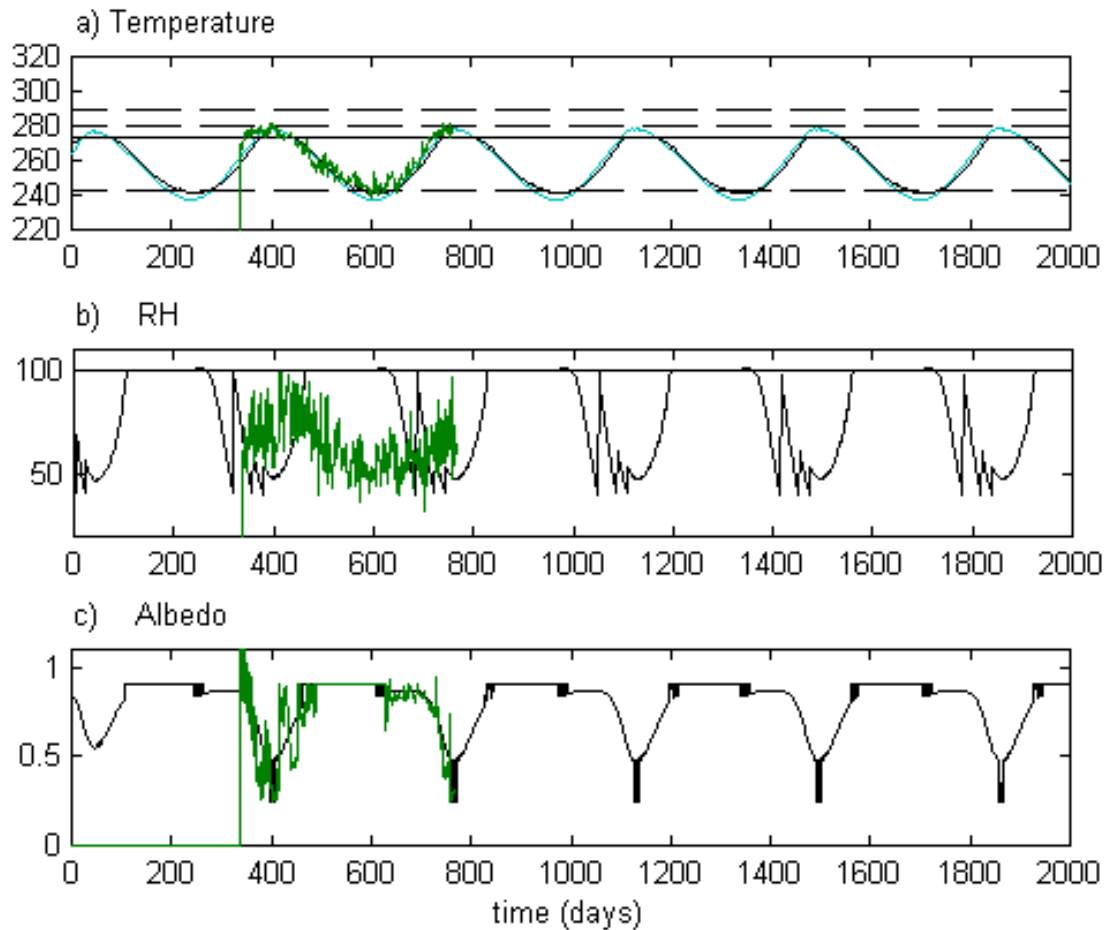


Figure 2.4. Model results (black smooth lines) versus 1998-99 observations from the lower weather station (LWS - green variable lines): a) model surface temperature vs. LWS 2m air temperature (degrees K); b) model mean tropospheric relative humidity vs. LWS ~2m height relative humidity (%); and c) model surface albedo vs. LWS surface albedo. The blue line in a) is the model-calculated atmospheric temperature.

A phase lag of ~ 180 degrees occurs between the observed and modeled daily RH values (Figure 2.7b) because while the weather stations measure the near-surface RH, the model calculates the column averaged RH over the entire troposphere. Measured near-surface RH is high in spring/summer because of spring/summer melt and because the spring-time inversion reduces vertical mixing in the atmosphere. The model column-averaged RH is high in autumn because autumn cooling results in excess atmospheric condensation and precipitation during this time.

A quantitative comparison of model results against observations indicates that the model reasonably reproduces JEG temperatures and mass balances. For a model diffusivity of $\eta = 2.15 \times 10^{-5} \text{ m}^2 \text{ s}^{-1}$, the mean annual area averaged temperatures

predicted by the model are -10.6°C for the surface and -15.3°C for the atmosphere. For a model diffusivity of $\eta=2.15 \text{ m}^2 \text{ s}^{-1}$, the mean annual area averaged temperatures predicted by the model are -10.8°C for the surface and -15.5°C for the atmosphere. The combined annual average of the 3 weather stations' 2m air temperatures is -14.8°C , while JEG 15m-depth ice temperatures (quasi-representative of the annual mean surface air temperature as modified by surface refreezing and firn compaction) range from -8.5°C near the ELA to -15°C near the summit. Note that latent heating associated with the surface refreezing of percolated meltwater tends to peak near the ELA (Paterson, 1994). JEG 15m-depth ice temperatures below the ELA range from -10°C to -13°C . Note also that the value of η does not make much difference to the mean annual area averaged temperatures, since averaging the model temperatures in time and space essentially produces the same result as mixing or stirring the atmosphere (where in this model, thermal advection or mixing by winds was parameterized by enhancing the value of the thermal diffusivity, η – see appendix).

JEG mass balances are well simulated by the model except over the lower-most part of the glacier (Figure 2.6c). For example, the model mass balance at 250 m is -2.25 m yr^{-1} for $\eta=2.15 \times 10^{-5} \text{ m}^2 \text{ s}^{-1}$ (still air) and is -2.275 m yr^{-1} for $\eta=2.15 \text{ m}^2 \text{ s}^{-1}$ (windy or stirred air). These values exceed the observed 1998-99 and 1999-2000 mass balance of $\sim -1.5 \text{ m yr}^{-1}$ at this elevation. A possible reason for the difference between the model and observed mass balance in the lower ablation zone of JEG is the assumption of an instant snow-to-ice density transition at the glacier surface (see appendix). The assumption that all precipitation at sub-zero temperatures is instantly added to the glacier surface as “ice” in terms of density impacts the surface heat capacity and surface melt rates. Again, while this assumption was adopted to simplify the complex snow-firn-ice transition, its impacts should be investigated in future studies.

The model ELA for both the still air and stirred air cases occurs between 800-850 m (e.g. Figure 2.3c). This is slightly higher than the long-term average ELA of $\sim 750\text{-}800 \text{ m}$ determined from ^{137}Cs measurements in boreholes (made by M. Sharp) although the observed annual position of JEG's ELA is variable and has been measured at $\sim 850\text{m}$ in 1996-97 and at $\sim 1100\text{m}$ in 1997-98.

2.4 JEG MODEL CLIMATE SENSITIVITY TO FIXED AND TIME-VARYING SURFACE ALBEDO

Before proceeding to the perturbation experiments which form the crux of this study, a preliminary examination of the model climate's sensitivity to changes in surface albedo is made. The impact of surface albedo upon JEG's mass balance is investigated by comparing the model climate under time-varying and fixed surface albedos. These experiments demonstrate the influence of surface albedo upon the position of the glacier ELA and the length of the melt season.

2.4.1 *ELA Position*

Snow/ice albedos experience significant seasonal variability where high seasonal melt occurs (e.g. Pritchard et al., 2008). The only places and times they do not show significant seasonal variation is near the centres or summits of large ice caps, high in the accumulation zone, or during times of decreased summer snow/ice melt (e.g. during the Little Ice Age (LIA) – e.g. Overpeck et al., 1997). At these places and times, the snow/ice albedo value remains nearly constant, close to the fresh snow value of 0.80 to 0.97 (e.g. Paterson, 1994, p59).

A sensitivity experiment, in which the model's time-varying temperature-dependent surface albedo (related to seasonal snow/ice melt – see appendix) is replaced with a constant albedo of 0.9 over the entire model domain (to simulate year-round snow cover and little seasonal melt), was performed. Results indicate a decrease in the model ELA by 200 m (similar to the ELA decrease determined to have occurred in the region during the LIA from trimline data – Wolken et al., 2008), and a corresponding increase in the area of the accumulation zone (Figure 2.5). To achieve a similar change in the ELA through solar radiation variations alone, keeping the model annual surface albedo cycle fixed (i.e. in the absence of the snow/ice-albedo feedback), would require an unrealistic decrease of $\sim 100 \text{ W m}^{-2}$ in the magnitude of the incoming solar radiation at the top of the model atmosphere. Curry et al. (1995), in their sea ice study, found that similarly large changes in incoming infrared (longwave) radiation were required to achieve a similar year-round-snow-cover threshold for various models, with radiative changes ranging from -23 to -17 W m^{-2} (although these values were computed with the snow/ice-albedo feedback in effect and as a result are not as extreme as the -100 W m^{-2} calculated here). Seasonal variability in surface albedo, therefore, has significant implications for glacier mass balance (see also Pritchard et al., 2008; Arnold, 2005).

2.4.2 *Melt Season Length*

Model results confirm that changes in the mean surface albedo, as well as changes in the temperature dependence of the surface albedo, play a critical role in determining the length of the melt-season of JEG. Fixing the model surface albedo to a constant value of 0.9 results in a significant reduction of the period during which surface temperatures on the glacier are at the melting point (e.g. by ~ 10 -15 days at 200 m elevation; Figure 2.6). This reduction occurs primarily at the beginning of the melt-season, although a few melt days are also lost at the end of the melt-season. Results suggest that winters/springs which experience heavy snowfalls (prolonging the seasonal snow cover and bringing the annual mean albedo closer to a value of 0.9) could reduce the length of the summer melt-season in the lower ablation zone by up to 2 weeks, as could periods of fresh snow during the summer.

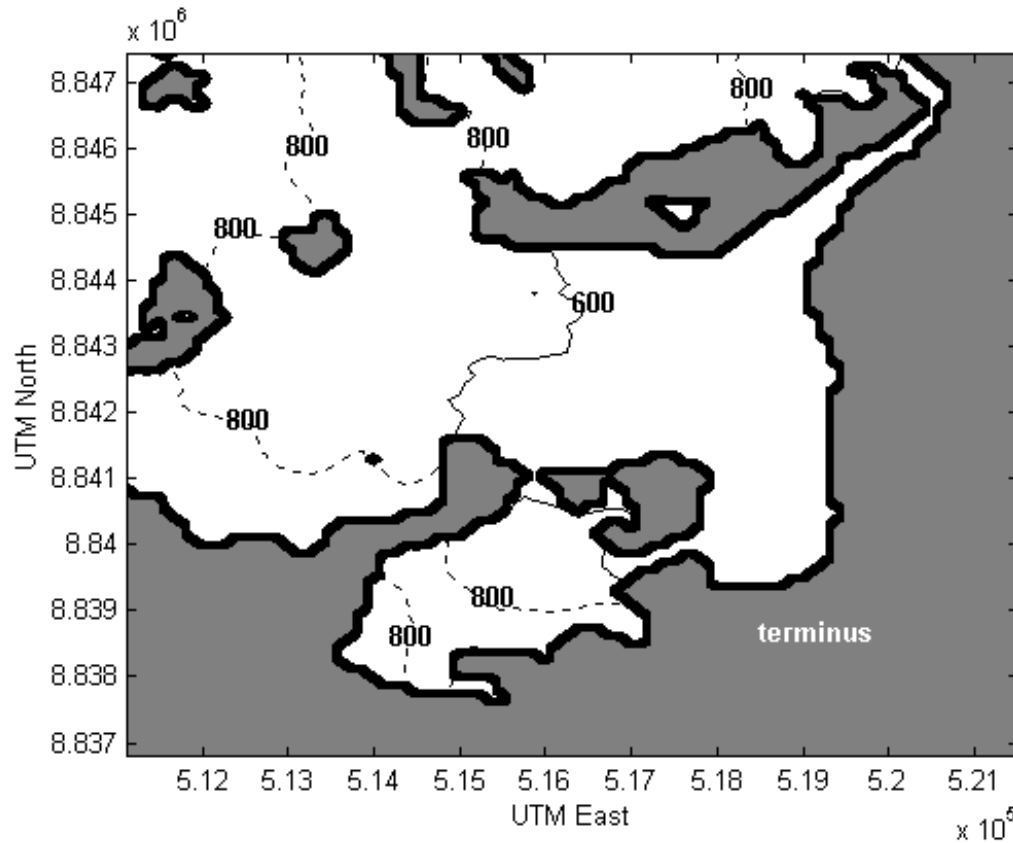


Figure 2.5. Model calculated equilibrium line altitudes in metres above sea level for a: 1) time-varying temperature-dependent surface albedo (dashed line); and 2) fixed surface albedo $\alpha=0.9$ (solid line).

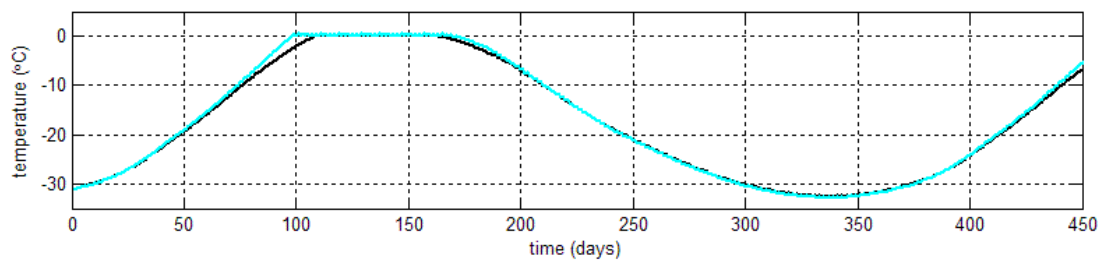


Figure 2.6. Calculated ice surface temperature at 200m elevation, using a temperature-dependent albedo (blue line) and a fixed surface albedo (black line), where the fixed albedo is 0.9.

2.5 EXPERIMENTAL PROCEDURE

To calculate the magnitude of the snow/ice-albedo feedback for the JEG glacier catchment, the model equilibrium climate was perturbed by applying positive and negative changes to the incoming shortwave (SW) and longwave (LW) radiation. The feedback gain ratio “G” and the feedback parameter “f” (described in section 2.1) were then computed in terms of mean annual area-averaged surface temperature, T_s , atmospheric temperature, T_a , and snow/ice thickness, h .

A total of thirteen perturbation experiments were performed. Nine were carried out to examine how f varies with type of radiative perturbation (SW versus LW), sign of perturbation (+ versus –), magnitude of perturbation, and degree of atmospheric thermal mixing (i.e. for a still versus a stirred atmosphere – see appendix). How f computed in terms of area averages differs from f computed at individual model grid points in these experiments was also examined. Four repeat stirred-atmosphere experiments were then performed without a glacier in the model domain, to examine differences in climate change amplifications related to the presence or lack of terrestrial ice, and to separate the snow-only and the snow/ice-albedo feedbacks.

2.5.1 *Perturbations applied to the model climate*

In all but one of the experiments, the incoming SW radiation at the top of the atmosphere and the incoming LW radiation at the surface were perturbed by $\pm 5 \text{ W m}^{-2}$. Perturbation values of 1-2% of the solar constant (i.e. of 3.5 to 7 W m^{-2}) are commonly used in albedo feedback studies using EBCMs (Energy-Balance Climate Models – e.g. Robock, 1983; Harvey, 1988; Bintanja and Oerlemans, 1995). Such perturbations are of the same order of magnitude (i.e. within 10^0 to 10^1 W m^{-2}) as decadal changes in daily average solar irradiance associated with the 11-year sunspot cycle ($\sim 1 \text{ W m}^{-2}$), and longer term changes such as those associated with the Maunder Minimum ($\sim 3.5 \text{ W m}^{-2}$; National Research Council, 1994). Perturbations to the incoming surface LW radiation simulate increased/decreased atmospheric poleward energy transports. The LW experiments were conducted to enable more direct comparisons with the results of Curry et al. (2001; 1995) for sea ice. Curry et al. (2001; 1995) chose to perturb the incoming surface LW radiation in their model by $\pm 5 \text{ W m}^{-2}$, because this value is comparable to the estimated $2 \times \text{CO}_2$ LW radiation forcing of 4 W m^{-2} (e.g. Ramanathan et al., 1989).

Curry et al. (1995) also noted that the magnitude of f in their experiments (i.e. the degree of climate change amplification in their model), depended upon and varied with the size of the radiative perturbation. To examine whether this is also true for the JEG model climate, an additional experiment was performed in which the stirred-atmosphere positive SW perturbation experiment was repeated for a ΔSW value of $+2 \text{ W m}^{-2}$.

2.5.2 “Turning off” the snow/ice-albedo feedback in the model climate

The feedback parameter f is used to quantify the magnitude of the amplification of the JEG system response to given radiative perturbations. To compare the change in model temperature or mass balance produced with the snow/ice-albedo feedback in effect, λ_f , to that produced without the feedback in effect, λ_0 , ΔT_0 in equation (2) must be estimated by removing the snow/ice-albedo feedback from the model before perturbing it. To do this, the albedo at each grid point in the model domain is prescribed to be the seasonally varying albedo of the unperturbed equilibrium model climate and its value is not allowed to respond to temperature changes related to the applied radiative perturbation.

2.5.3 Separating the ice-albedo feedback from other feedbacks in the experiments

2.5.3.1 SEPARATING THE SNOW/ICE-ALBEDO FEEDBACK FROM THE ELEVATION – MASS BALANCE FEEDBACK

The primarily thermal snow/ice-albedo feedback was partially isolated from the primarily mechanical elevation - mass balance feedback by assuming a static atmosphere and static ice in the energy - mass balance model (see appendix). This assumption eliminates atmospheric adiabatic-related feedbacks, where: a) air forced upwards over topography cools and generates orographically-enhanced precipitation/snow, leading to increased summit elevations and even further orographic enhancement of precipitation; and b) air forced down the lee side of glaciers results in adiabatic warming, enhanced surface melt, and even steeper lee-side slopes. Note that while orographic enhancement of precipitation is parameterized in the model (see appendix), there is no orographic precipitation *feedback*. The above assumption also eliminates mass flux divergence feedbacks (where thinning/thickening of the glacier due to ice flow leads to surface elevation gradient changes, changes in ice deformation, and further thinning/thickening of the ice). The “static” assumption cannot eliminate all elevation – mass balance related feedbacks within the model climate, however (e.g. the “lapse rate” feedback, where decreasing/increasing glacier thicknesses results in a larger proportion of the ice lying below/above the equilibrium line altitude, leading to further decreases/increases in overall glacier thickness).

2.5.3.2 SEPARATING THE ICE-ALBEDO FEEDBACK FROM THE SNOW-ALBEDO FEEDBACK

It is difficult to isolate the snow and ice components of the snow/ice-albedo feedback in an energy – mass balance model. Additionally, cloud albedo changes and feedbacks within the model will further impact the true value of the estimated snow/ice-albedo feedback magnitude. Nevertheless, the impact of terrestrial ice upon climate change amplifications related to the snow/ice-albedo feedback can be isolated and estimated by performing the model perturbation experiments with all components present/active (snow, ice, and cloud) and differencing the results

from those obtained by performing the experiments assuming a non-glaciated valley (snow and cloud only). To do this, the stirred-atmosphere perturbation experiments described above were repeated for a catchment area or valley identical to JEG's, but in these cases without a glacier. This was accomplished by substituting those sections of the surface DEM (A. Arendt, *pers. comm.*) which contain glacier ice with the bed DEM for JEG (described in Copland and Sharp, 2001).

2.5.4 Choice of model domain for the experiments

In deciding upon the model domain, or the areal extent over which to perform the experiments and calculations of the snow/ice-albedo feedback parameter f , two factors require consideration. The first involves the choice of variable (e.g. surface temperature, ice thickness, etc.) to use when calculating f . Because the snow/ice-albedo feedback is largely an area-averaged feedback, it is difficult to calculate its magnitude in terms of mass balance when the model domain includes areas which are ice-free and thus have annual mass balances of zero. Surface temperature would therefore appear to better account for the overall impact of the snow/ice-albedo feedback upon the local climate of glacier catchment. However, using mass balance as opposed to surface temperature has been argued to be a better way of determining the climate sensitivity of an ice mass, because surface ice temperatures cannot exceed 273.15 K during the summer melt season (e.g. Curry et al., 2001). Surface (2m) air temperatures are likely the ideal variable to use in calculations of f , as this is the variable most noticeably affected by the feedback (Figure 2.1). However, the energy – mass balance model used in this study computes a single tropospheric-average air temperature at each grid point. For these reasons, in this study, the magnitude of the snow/ice-albedo feedback is examined in terms of all three variables (the mean annual area-averaged surface temperature, atmospheric temperature, and mass balance) over a model domain which covers a major part of the glacier catchment (Figure 2.2).

The second factor which requires consideration in choosing the model domain is the fact that the relative fractions of ice-covered and non-ice-covered areas within the model domain will influence the results and the magnitude of the computed snow/ice-albedo feedback parameter f . For example, if no ice (0% ice) exists within the model domain, the ice-albedo feedback parameter f will equal zero, leaving only the snow-albedo feedback. If the domain is entirely ice covered (100% ice), the area-averaged surface albedo will not change significantly for given radiative perturbations, also leading to small or near-zero computed values of f . The snow/ice-albedo feedback will reach a maximum effectiveness somewhere near the margins of the snow/ice area (Pritchard et al., 2008). Since the point of these experiments is to examine the maximum possible climate change amplification related to the ice-albedo feedback, it would appear best to choose a model domain with nearly equal fractions of ice and bare land, and which includes the glacier margin or terminus. However, if the contribution of terrestrial ice to the snow/ice-albedo feedback on decadal timescales turns out to

be negligible, it may make no difference if an ice-free model domain is chosen. Both scenarios are covered by choosing a model area which contains similar ice-covered (52%) and ice-free (48%) land fractions, (covering $\sim 113 \text{ km}^2$, comprising 84×86 grid points with a $125 \text{ m} \times 125 \text{ m}$ spacing – Figure 2.2), then repeating some of the experiments using this same domain, but without the terrestrial ice. This also accomplishes the separation of the snow/ice- and snow-albedo feedbacks, as described above.

2.5.5 Choice of model run time for the experiments

Because it is observed that the ice-albedo feedback for outlet valley glaciers can be important on decadal timescales and less (e.g. Paul et al., 2004), and because surface mass balances reasonably balance dynamic glacier flow and mass fluxes on these time scales for JEG (justifying the static ice assumption), the model perturbation experiments described above were run for a period of 10 years beyond the point at which annual cycle equilibrium was reached.

2.6 SUMMARY OF RESULTS: CALCULATIONS OF f

The results of the experiments described above are presented here as f -values computed in terms of mean annual area-averaged surface temperatures, atmospheric temperatures, and surface mass balances (Table 2.1). Additionally, the results of two of the experiments are presented as spatial plots of f in terms of mean-annual *non*-area-averaged surface temperatures (Figures 2.7 and 2.8). Positive and negative SW and LW perturbations were used to determine the magnitudes of the snow/ice-albedo and the snow-albedo feedbacks within the JEG model domain. By examining the differences in the results of the snow+ice and snow-only experiments, the contribution of terrestrial ice to local climate change amplifications on decadal time scales is isolated and explored.

2.6.1 The magnitude of the snow/ice-albedo feedback in the JEG catchment

Perturbation	still atmosphere			stirred atmosphere		
	f_{TS}	f_{TA}	f_{MB}	f_{TS}	f_{TA}	f_{MB}
with ice						
SW +5 W m ⁻²	+0.44	+0.35	+0.58	+0.48	+0.39	+0.48
SW -5 W m ⁻²	+0.28	+0.23	+0.37	+0.30	+0.25	+0.17
LW +5 W m ⁻²	+0.24	+0.27	+0.56	+0.30	+0.31	+0.87
LW -5 W m ⁻²	+0.14	+0.17	+0.35	+0.25	+0.27	+0.32
SW +2 W m ⁻²				+0.48	+0.38	
without ice						
SW +5 W m ⁻²				+0.24	+0.21	0
SW -5 W m ⁻²				+0.18	+0.17	0
LW +5 W m ⁻²				+0.25	+0.29	0
LW -5 W m ⁻²				+0.21	+0.24	0

Table 2.1. Calculated values of f , in terms of mean annual area-averaged surface temperatures (TS), atmospheric temperatures (TA) and surface mass balances (MB). Values of f were computed for the JEG valley with and without a glacier, for various radiative perturbations, and for atmospheric thermal diffusive coefficients of $\eta=2.15 \times 10^{-5} \text{ m}^2 \text{ s}^{-1}$ (representative of still air) and $\eta=2.15 \text{ m}^2 \text{ s}^{-1}$ (representative of stirred or mixed air).

Depending upon the perturbation applied, and whether the atmosphere is assumed “still” or “stirred” (i.e. windy), values of the snow/ice-feedback parameter f , calculated in terms of the mean annual area-averaged *surface* temperature, range from $f=+0.14$ to $f=+0.48$, while values of f calculated in terms of the mean annual area-averaged *atmospheric* temperature range from $f=+0.17$ to $f=+0.39$. Values of the snow/ice-albedo feedback parameter f calculated in terms of the mean annual area-averaged surface mass balance range from $f=+0.17$ to $f=+0.87$. The computed magnitudes of the snow-albedo feedback in the non-glaciated valley experiments, in terms of mean annual area-averaged surface and atmospheric temperatures, range from $f=+0.18$ to $f=+0.25$ and $f=+0.17$ to $f=+0.29$, respectively. Not surprisingly, in terms of mass balance, $f_{MB}=0$ in all cases without a glacier in the model domain, as all snow that accumulates in winter melts away in summer in the no-ice cases.

Under the LW perturbations, the range of magnitudes of the computed snow/ice-albedo feedback parameter for JEG, in terms of surface temperature changes ($f_{TS} = +0.14$ to $+0.30$), is comparable to the range of values determined by Curry et al. (2001) for sea ice under similar LW perturbations. However, higher values of f were computed for JEG under the positive perturbation while higher values were computed for sea ice under the negative perturbation. Using an energy-mass-

balance model with a complex spectrally-dependent albedo parameterization, and perturbing the model climate with LW changes of $\pm 5 \text{ W m}^{-2}$, Curry et al. (2001) calculated $f_{TS} = +0.25$ in the positive case, and $f_{TS} = +0.33$ in the negative case (where values of f_{TS} are inferred from their calculated feedback gain ratios). While similar values of f are not necessarily expected, the difference between the studies may also be related to the fact that while cloud and water-vapor feedbacks are inoperative in the model used by Curry et al. (2001; 1995), they are present in the energy-mass balance model used in this study. On the other hand, while care was taken to remove ice thickness changes due to ice mass flux divergences in the JEG model, ice ridging and the formation of leads was allowed in the 1D Lagrangian sea ice model used by Curry et al. (2001; 1995).

In terms of surface and atmospheric temperatures, the computed values of f for the snow-only experiments fall midway within the range of values reported in the climate-model inter-comparison study of Cess et al. (1991; as inferred from their values of λ_T/λ_0 , the feedback gain ratio). The 17 climate models in the study of Cess et al. (1991) provided computed magnitudes for the snow-albedo feedback (in terms of the global mean surface temperature) ranging from $f = -0.1$ to $f = +0.5$ (for sea surface temperature perturbations of $\pm 2 \text{ K}$). Variations in f were attributed to differing model albedo parameterizations and to differing additional model cloud and LW feedbacks. In a separate study, Harvey (1988) used a simpler zonally-averaged ECBM and SW radiative perturbations of $\pm 2 \text{ W m}^{-2}$ to calculate values of the surface (consisting of snow and/or sea ice) albedo feedback in terms of global mean air temperature. His values ranged from $f = +0.082$ (in the positive case) to $f = +0.133$ (in the negative case).

The following points summarize the results of the comparative JEG energy-mass balance model perturbation experiments:

1) *SW versus LW radiative perturbations:* Within the JEG model domain, SW radiative perturbations generally triggered stronger snow/ice-albedo feedback amplifications of temperature changes than did corresponding LW radiative perturbations (for a given sign, positive or negative). However, in the snow-only non-glaciated-catchment experiments, it was the LW radiative perturbations that triggered the stronger snow-albedo feedback amplification of temperature changes. In the case of mass balance changes, on the other hand, the SW radiative perturbations only triggered a stronger snow/ice-albedo feedback amplification in the “still” atmosphere experiments, while the LW perturbations produced greater amplifications of mass balance changes in the “stirred” atmosphere cases. These results are partly related to the complex interaction of the applied radiative perturbations with the model parameterizations of the surface albedo and other processes. Because published studies mainly employ a single type of climate perturbation, comparisons for the above instances are difficult to locate.

SW perturbations trigger stronger temperature amplifications in the combined snow/ice case because incoming solar radiation is more intimately involved with the snow/ice-albedo feedback than is LW radiation. Changes to incoming solar (SW) radiation not only trigger the snow/ice-albedo feedback, but the actual amount of SW radiation reaching and being absorbed by the surface is further impacted by resultant amplified changes in surface albedo. Changes in incoming LW radiation, on the other hand, trigger the feedback but are not directly affected by changes in surface albedo.

2) *Positive versus negative radiative perturbations*: In all experiments, for a catchment with and without a glacier, for still air and for a mixed atmosphere, for both SW and for LW radiative perturbations, the positive perturbations produced higher values of f than did the negative perturbations. This result is partly related to amplified, perturbation-related changes in the relative fractions of snow/ice covered terrain and bare ground within the model domain. Positive perturbations generated climates with decreasing fractions of permanently snow/ice covered terrain within the model domain, while negative perturbations produced climates with increasing fractions of permanently snow/ice covered terrain. These relative fractions can influence results (see section 2.5.6) and the impacts of relative fractions of snow/ice cover will be further discussed at the end of this section. However, differences in model-computed f 's related to the sign of the perturbation may occur for other reasons, perhaps involving the chosen surface albedo parameterization (e.g. for sea ice – Curry et al., 2001).

3) *“Still” atmosphere versus “stirred” atmosphere*: Increasing the model atmospheric thermal diffusivity (to simulate greater thermal advection between model grid points) was found to augment the snow/ice-albedo feedback amplification of perturbation-related surface and atmospheric temperature changes in the JEG model climate. That is, the effectiveness of the feedback in terms of temperature was increased by simulating enhanced horizontal mixing of atmospheric temperature by winds. The opposite, however, was found to be the case regarding the amplification of surface mass balance changes – in general the “still” atmosphere experiments yielded the higher snow/ice-albedo feedback amplification of perturbation-related snow/ice thickness changes (except in the case of the positive LW radiative perturbation).

Where the magnitude of the snow/ice-albedo feedback is computed in terms of temperature, increased atmospheric thermal “advection” can, for example, bring warmer SATs over parts of the model domain which would otherwise remain cool due to the presence of ice, enhancing the snow/ice-albedo feedback's effectiveness in these areas. This is key to the “area” aspect of the snow/ice-albedo feedback. The importance of atmospheric thermal advection has been examined by others (e.g. Oerlemans, 1986), demonstrating that SATs warmed over bare ground near the margins of the glacier can advect over the glacier, enhancing melt where surface temperatures would otherwise remain low. True values of f likely reside within the boundaries provided by the always-windy

stirred-atmosphere ($\eta=2.15 \text{ m}^2 \text{ s}^{-1}$) cases and the never-windy still-atmosphere cases ($\eta=2.15 \times 10^{-5} \text{ m}^2 \text{ s}^{-1}$) presented in this study.

In the case of surface mass balance, because incoming SW radiation, not SAT, plays the dominant role in the surface energy balance, accounting for between 96 and 99% of the melt energy (Arendt, 1999), atmospheric mixing cannot do much to augment these figures and may actually act to diminish them. In the case of the positive LW perturbation, however, increasing the incoming infrared radiation received and absorbed by the glacier surface increases the importance of this component with respect to the SW radiation in the surface energy balance and melt calculation. This then allows for atmospheric mixing to augment the computed value of f as in the cases of the surface and atmospheric temperatures.

4) “ f ” computed in terms of surface temperature versus “ f ” computed in terms of atmospheric temperature: SW perturbations to the JEG model climate resulted in larger magnitudes of the snow/ice-albedo feedback computed in terms of surface temperature than in terms of atmospheric temperature (for the corresponding sign of the perturbation). The opposite was found for LW perturbations, which resulted in larger magnitudes of the computed snow/ice-albedo feedback in terms of atmospheric temperature than in terms of surface temperature. This difference is most likely related to the fact that the Arctic atmosphere absorbs only small amounts of SW radiation (see appendix) and therefore can only be indirectly affected by changes in incoming SW radiation.

5) “ f ” computed in terms of temperature versus “ f ” computed in terms of mass balance: In general, the magnitude of the snow/ice-albedo feedback computed in terms of mean annual area-averaged surface mass balance was found to be larger than the magnitude of the feedback computed in terms of surface or atmospheric temperature (except in the negative SW perturbation experiment). This result was also obtained by others (e.g. Curry et al., 2001, for sea ice), and it is related to the fact that surface temperature cannot exceed 273.15 K over glaciated parts of the model domain during the melt season. For this reason, the snow/ice-albedo feedback can enhance changes in surface melt to a greater degree than it can enhance changes in surface temperature and, as a result, atmospheric temperature.

6) “ $\Delta SW = +2 \text{ W m}^{-2}$ ” versus “ $\Delta SW = +5 \text{ W m}^{-2}$ ”

No significant difference in the degree of surface or atmospheric temperature change amplification was produced by varying the SW perturbation from $+5 \text{ W m}^{-2}$ to $+2 \text{ W m}^{-2}$. That the degree of climate change amplification is found to be independent of the magnitude of the radiative perturbation is logical in a system which does not incur major additional internal feedbacks (recalling that the “amplification” of a temperature change by a feedback process is not the same thing as the actual temperature change incurred, which *will* be dependent on the magnitude of the radiative perturbation). The results of Curry et al. (1995), who noted that the magnitudes of their model-calculated feedback gain ratios (and

therefore f 's) were sensitive to the magnitude of the applied radiative perturbation, were explained by the fact that different magnitudes of LW perturbation caused the sea ice system to approach or retreat from a “transition” in model sea ice behaviour. This is not the case for the JEG energy-mass balance model developed for this study.

7) *The snow/ice-albedo feedback versus the snow-albedo feedback:* In terms of surface and atmospheric temperatures, the computed magnitude of the snow/ice-albedo feedback in the glaciated valley experiment is noticeably larger than (in some cases nearly double) the magnitude of the snow-albedo feedback in the non-glaciated valley experiment.

This result may seem counterintuitive at first, since: a) snow can experience more rapid changes in area at seasonal to decadal time scales than can snow and ice combined; and b) snow - bare ground albedo contrasts, which are greater than snow - bare ice albedo contrasts, will be more prevalent throughout the non-glaciated valley. However, for a non-glaciated valley with predominantly seasonal snow cover, consider that once the snow is gone in summer, there can be no snow-albedo feedback. Since there can neither be a snow-albedo feedback during the darkness of the polar winter months, the snow-albedo feedback on its own can only operate in the spring and autumn of each year.

The actual magnitude of the snow/ice - albedo feedback may be smaller than the snow-albedo feedback on its own at specific times of the year (e.g. spring, autumn) and in specific locations, because the exposure or covering of bare ice as opposed to bare ground results in smaller albedo contrasts across parts of the valley, leading to smaller local SAT change amplifications. However, because the presence of glacier ice can prolong seasonal snow cover, and because the snow/ice-albedo feedback in a glaciated catchment will not disappear during the summer the way the snow-albedo feedback does in a non-glaciated catchment, this can lead to greater annual average SAT change amplifications than can occur when permanent snow-packs or glaciers are absent. As a result the annual average SAT change amplification can be larger in the snow+ice case than in the snow-only case.

8) *“ f ” computed in terms of area averages versus “ f ” computed at individual model grid points:* Grid-point values of f , computed in terms of mean annual *non*-area-averaged surface temperature, display much spatial variability within the JEG model catchment in all experiments (Figures 2.7 and 2.8).

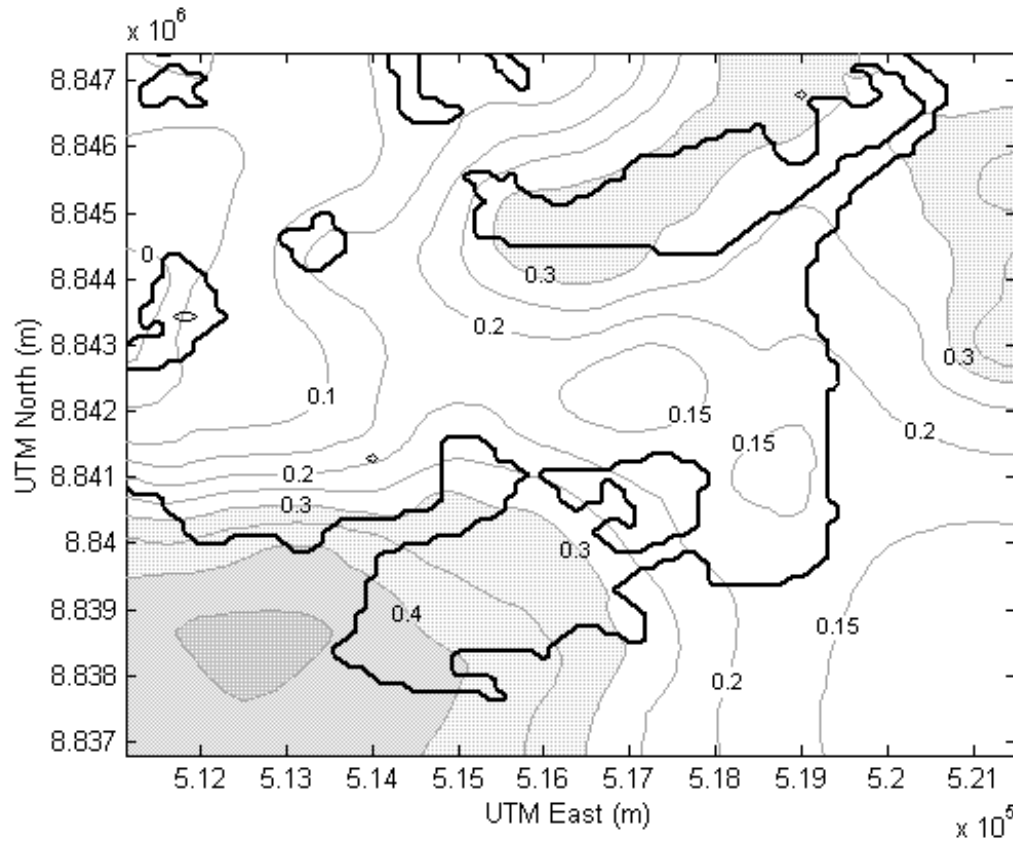


Figure 2.7. Spatial variations in the snow/ice-albedo feedback parameter f , calculated in terms of mean annual surface temperature, using an atmospheric diffusivity parameter $\eta=2.15 \text{ m}^2 \text{ s}^{-1}$, for a longwave radiative perturbation of -5 W m^{-2} . Grey areas highlight zones of maximum amplification of surface temperature changes by the feedback for the given radiative perturbation.

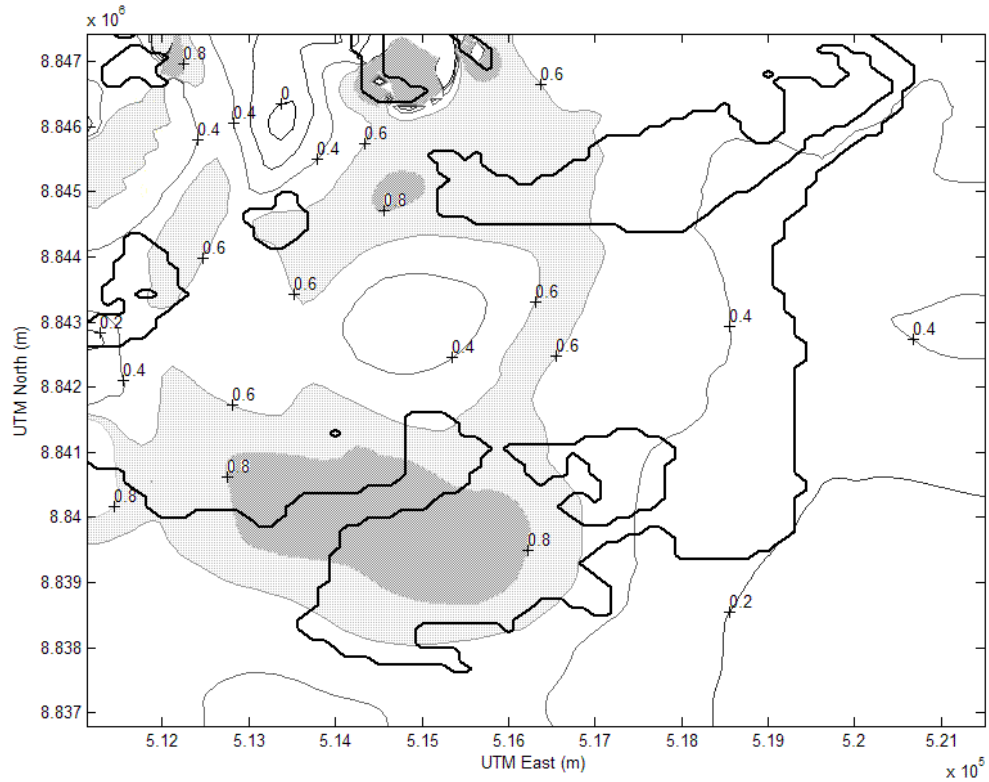


Figure 2.8. Spatial variations in the snow/ice-albedo feedback parameter, f , calculated in terms of surface temperature, using an atmospheric diffusivity parameter $\eta=2.15 \text{ m}^2 \text{ s}^{-1}$, for a shortwave radiation perturbation of $+5 \text{ W m}^{-2}$. Grey areas highlight zones of maximum amplification of surface temperature changes by the feedback for the given radiative perturbation.

Minimum values are generally located on the ice and in the proglacial area, and maximum values are generally located just off the ice along the valley walls (e.g. for $\Delta LW = -5 \text{ W m}^{-2}$, Figure 2.7). These same maxima and minima are present in both the LW and the SW perturbation cases, possessing the more extreme magnitudes in the positive SW case (i.e. for $\Delta SW = +5 \text{ W m}^{-2}$). For example, in the positive SW perturbation experiments, tongues of high values of f_{TS} extend from maxima reaching $+0.8$ and higher, situated near and over non-glaciated areas of the model domain, and intrude over parts of the glacier itself (e.g. Figure 2.8). In addition to the f -maxima computed near the valley walls and in the vicinity of the nunatak located near the ELA, an elongated cross-glacier maximum (associated with the mean polar-day position of the snow - bare ice line) exists in the ablation zone of the glacier (although f -values here are lower than the f -values associated with the maxima located near the ice margins – e.g. Figure 2.8). This linear zone of maximum f 's moves up/down-glacier with the sign (+/–) of the perturbation applied in the experiments and with the mean summer position of the snow - bare ice line (c.f. Figures 2.7 and 2.8, where the $f > 0.15$ zone between the two circular contours over the lower glacier in Figure 2.7 corresponds to the grey-filled cross-glacier zone of $f > 0.6$ in figure 2.8).

Spatial variations in f_{MB} within the model domain (not shown) are similar to those depicted for f_{TS} (Figures 2.7 and 2.8). The f_{MB} -maximum associated with the snow - bare ice line in the ablation zone was also found to move up/down glacier for \pm perturbations.

Spatial variations in f -maxima occur because of the greater contrast in albedo between seasonal snow and bare rock/soil than between seasonal snow and bare ice (e.g. Robock, 1983). This is particularly noticeable in the vicinity of the nunatak and nearby mountains near the ELA, which lose their semi-permanent snow covers in the positive SW experiments, leading to higher and more prolonged albedo contrasts at these elevations than occur normally under non-perturbed conditions.

Because maxima in the computed f -values tend to concentrate along areas of high summer surface albedo contrast (e.g. in the vicinity of nunataks, glacier margins, and in the vicinity of the mean polar day position of the snow - bare ice line in the glacier ablation zone – e.g. Figures 2.7 and 2.8), the calculated average value of f for any given sub-area within the model domain will vary with the relative fractions of ice-covered and non-ice-covered ground. The relative fractions of ice above and below the ELA included in the area-average computations will also influence the magnitudes of area-averaged f -values in the experiments described above. This is because in glacier systems there are not one but three fronts of high-low albedo contrast: 1) a snow/ice - bare ground front near the glacier's terminus and along its margins; 2) a snow - bare ice front in the ablation zone which progresses upward in elevation throughout the melt season; and 3) a snow - bare firn front near or above the ELA at the peak or end of the melt season (see maxima located near/above the nunatak in the positive SW experiment, Figure 2.8). It is near these zones of high contrast in albedo that the snow/ice-albedo feedback can operate most effectively (i.e. where changes in snow or ice cover can lead to the greatest changes in area-averaged surface albedo). The model domain used in this study includes the entire ablation zone of JEG and approximately 50% of the accumulation zone. These fractions were chosen because the lower accumulation zone and the ablation zone are where the ice-albedo feedback will have the most immediate consequences in terms of amplification of changes in snow/ice area.

Of all areas in the JEG model domain, it is clear that the snow/ice-albedo feedback is most effective at and in the vicinity of the ice margins, and that its impacts can significantly amplify the surface temperature changes of this model outlet valley glacier in these locations. This result supports the assertion of others that the snow/ice-albedo feedback is most effective at ice cap and ice sheet margins, where outlet/valley glaciers are located, locally amplifying temperature and ice thickness responses to climate perturbations (e.g. Pritchard et al., 2008).

2.7 DISCUSSION

This study sought to address the question of whether the terrestrial snow/ice-albedo feedback is important to the evolution of local climates and ice masses in the CHA on decadal timescales and less, using model perturbation experiments to quantify the feedback for a representative glacier catchment.

As has been demonstrated by others, computed values of the snow/ice-albedo feedback parameter, f , will vary with the model used, with the surface albedo parameterization used, and with any additional feedbacks operating within the model climate (e.g. Curry et al., 1995; 1996). Within a given model, there exist numerous ways to parameterize processes (not just the surface albedo) and there are numerous justifiable ways to tune a model to reproduce observations. The numerical method chosen to solve the model equations can also have an impact upon the computed model climate. All of these factors affect the feedback processes simulated by the model to some degree. As a result, for the calculated value of the snow/ice-albedo feedback parameter, f , the best that one can do is to determine a realistic range of possible values and examine how values compare to each other within a set of experiments (using either a single model – this study, or a given set of models – Cess et al., 1991).

One of the key findings of this study is that the presence of terrestrial ice can serve to significantly enhance the magnitude of the snow-albedo feedback (or combined snow/ice-albedo feedback) on decadal timescales and less. Terrestrial ice within a catchment or valley contributes to the duration and effectiveness of the snow-albedo feedback by encouraging perennial snow cover in the accumulation zone which serves to prolong the snow-albedo feedback throughout the melt season. Because of this, the magnitude of the combined snow/ice-albedo feedback in terms of mean annual area-averaged surface and atmospheric temperatures can be nearly double that of the snow-albedo feedback on its own. That is, while glaciers may lower the mean annual temperature of a valley, *changes* in mean annual SATs are amplified to a greater extent in glaciated valleys because glaciers also act to prolong the operation and effectiveness of the snow-albedo feedback mechanism into the summer season. The contribution of terrestrial ice to the effectiveness of the snow/ice-albedo feedback on decadal timescales and less is therefore not locally negligible.

This result for terrestrial snow/ice can be placed in context with the results obtained for sea ice in the climate modeling study carried out by Holland and Bitz (2003). They found that: 1) global climate sensitivity is greater when the sea ice extent is larger, because there is more sea ice to lose; 2) the latitude of maximum warming is correlated inversely with sea ice extent; and 3) models with relatively thin ice cover tend to have higher polar amplification because thin ice is more easily melted away, resulting in a stronger surface albedo feedback mechanism. If thin seasonal sea ice cover is thought of as an analogue for seasonal snow cover, and if thicker multi-year sea ice is thought of as an analogue for ice caps

and glaciers, then the results of the two studies are comparable in many ways. Maximum amplification is located near the ice margins; climate change amplification is greater when larger amounts of snow/ice are present because this means that there is more snow/ice to lose; and the snow-albedo feedback, when present, can be larger than the snow/ice-albedo feedback at specific points in time because snow can more readily experience area changes than snow+ice. However, in the case of snow on its own, once the snow is gone in the summer, the feedback-related amplification goes to zero for much of the year. Thicker, permanent areas of snow and ice act to prolong seasonal snow cover and the feedback mechanism. Similarly, areas of thick multi-year sea ice act to prolong and enlarge the area of thinner seasonal sea ice formation, displacing the latitude of maximum warming southwards (in the case of the Northern Hemisphere). Even though thinner ice may produce a larger amplification at any given time (Holland and Bitz, 2003), thicker multi-year sea ice is very likely key to the persistence and enhancement of the sea ice-albedo feedback at longer than seasonal timescales, just as the results of this study have indicated that glaciers are key to the persistence and enhancement of the snow-albedo feedback.

A second key finding of this study is that the magnitude of the terrestrial snow/ice-albedo feedback can locally exceed values computed for sea ice near zones of strong summer surface albedo contrast (e.g. in the vicinity of the ice margins). The following discussion examines the quantitative implications of the ranges of f -values determined in the perturbation experiments in this study.

The ranges of the values computed for the snow/ice-albedo feedback parameter, f , can provide an idea of the gain in, or the amplification of, temperature and mass balance changes, as a result of the presence of the feedback. For example, the magnitude of the computed snow/ice-albedo feedback parameter in terms of mean annual area-averaged surface temperature, for SW radiative perturbations of $\pm 5 \text{ W m}^{-2}$, was found to range from $f_{\text{TS}} = +0.28$ to $f_{\text{TS}} = +0.48$ (for atmospheric thermal diffusivities of $\eta = 2.15 \times 10^{-5} \text{ m}^2 \text{ s}^{-1}$ and $\eta = 2.15 \text{ m}^2 \text{ s}^{-1}$ – table 2.1). From equation (3), $G_{\text{eff}} = 1/(1-f)$, it can be determined that in such a case, effective gains in surface temperature related to the snow/ice-albedo feedback range from 1.39 to 1.92. From equation (2), we obtain $\Delta T_f = G_{\text{eff}} \times \Delta T_0$. This means that SW radiative perturbations in the presence of the snow/ice-albedo feedback result in JEG surface temperature changes of 1.39 \times to 1.92 \times what would be realized without the snow/ice-albedo feedback. Near the glacier margins and nunataks, computed values of f_{TS} for an SW perturbation of $+5 \text{ W m}^{-2}$ (for $\eta = 2.15 \text{ m}^2 \text{ s}^{-1}$) reached values greater than $+0.80$, meaning that temperature gains due to the snow/ice-albedo feedback in these locations could possibly be as high as 5 \times to 10 \times what they would be without the feedback.

Knowing the magnitude of snow/ice-albedo feedback amplifications is particularly important in the study of present-day Arctic glaciers, since increasing concentrations of atmospheric greenhouse gases are likely to act as a large warming perturbation to the polar climate (IPCC, 2007). Holland and Bitz

(2003) found model-simulated polar warming in the Arctic to be 1.5 to 4.5 times the global mean warming, primarily due to sea ice - related feedbacks. Although these authors did not find that terrestrial snow/ice – related feedbacks were important in their relatively coarse-resolution model experiments, the review of Curry et al. (1996) and the results of the experiments performed in this study suggest that the matter is still open to question.

In terms of mean annual area-averaged surface mass balance, the values of f computed in this JEG glacier study were found to be even larger than the values of f computed in terms of temperature (as was also found in the sea ice study of Curry et al., 2001). If the computed values are anywhere near realistic, snow/ice thickness changes could reach $2.4\times$ what they would without the feedback in response to SW radiative perturbations and $7.7\times$ what they would without the feedback in response to LW radiative perturbations.

Mean annual area-averaged surface temperature changes up to $2\times$ what they would be without the snow/ice-albedo feedback and snow/ice thickness changes up to $8\times$ what they would be without the snow/ice-albedo feedback represent substantial amplifications of the response of the model glacier system to radiative perturbations. Such strong local temperature and mass balance amplifications will have serious implications for: 1) the evolution of the glacier; and 2) for its local climate.

Glacier evolution will not only be impacted in terms of melt-season length, ELA position and mass balance, but also in terms of response time, t_R , which can be calculated by dividing the mean total ice thickness, h , by the negative of the mass balance at the snout ($t_R = h/(-MB)$; – Johannesson et al., 1989). Amplified changes in mass balance mean amplified reductions in response time, increasing the sensitivity of the glacier's dynamic response to radiative perturbations (not simulated in this study which uses a static model glacier).

To illustrate how amplified MB changes can lead to amplified reductions in glacier response time, consider the following. If a mean JEG ice thickness of 250 m is chosen and the mass balance near the JEG snout is taken to be $\sim -1.5 \text{ m yr}^{-1}$ (the approximate average of the mass balance observations at the LWS over two years), the JEG response time is found to be $\sim t_R = 250/1.5 = 166.7$ years. If an unamplified change in mass balance were to occur as a result of a given radiative perturbation, reducing the MB at the snout to -3.0 m yr^{-1} , the response time would be cut in half, to 83.3 years. However, the snow/ice-albedo feedback can amplify mass balance changes by up to $8\times$ (as per the results from this study). For an example amplification of $4.5\times$, the mass balance near the snout could actually be further reduced to -13.5 m yr^{-1} , in turn further reducing the normal glacier response time to ~ 18.5 years.

Strong local temperature and mass balance amplifications will also have serious implications for the evolution of the local climate. Although the terrestrial

snow/ice albedo feedback is generally found to be less important than the sea-ice albedo feedback in terms of *global* temperature, in this study it was found to be similar to the magnitude of the sea-ice albedo feedback in terms of *local* temperature. Calculated effective gains in temperature and mass balance due to the snow/ice-albedo feedback in the JEG catchment are comparable to those calculated for sea ice (e.g. Curry et al., 1995; 2001). Thus, while the large areal extent of sea ice makes the sea-ice-albedo feedback a dominant factor in Arctic and global climate sensitivity (e.g. Bintanja and Oerlemans, 1995), the collective importance of the snow/ice-albedo feedback generated by glaciers and ice caps in the CHA may not be negligible – it simply cannot be well resolved with coarse-resolution global climate models using coarse surface DEMs and which use general, non-site specific surface albedo parameterizations (for further insight into global model problems of this sort, see IPCC, 2007 – Technical Summary, Key Uncertainties, p. 86 and p. 91). Also, having a lower heat capacity, land surfaces warm at a faster rate than does the ocean. For this reason, surface temperature changes in the Canadian Arctic Archipelago, amplified by the terrestrial snow/ice-albedo feedback in the CHA as well as by the sea ice - albedo feedback, could lead to significant changes in the regional climate (in terms of temperature, pressure, and circulation patterns). These changes, in turn, could possibly impact the strength of the Northern Annular Mode and consequently the strength and track of the mid-latitude jet stream, because they are a part of this global teleconnection pattern (e.g. IPCC, 2007 – Technical Summary).

2.8 CONCLUSIONS

A surface-atmosphere energy-mass balance model was calibrated to simulate a climate similar to that observed at John Evans Glacier, in the Canadian High Arctic. The model equilibrium climate was then perturbed by applying positive and negative changes to the surface incoming shortwave and longwave radiation, in order to calculate the magnitude of the snow/ice-albedo feedback parameter, f , on decadal timescales and less (using a linear feedback analysis).

The computed magnitude of the snow/ice-albedo feedback parameter, f , was found to vary both with type of perturbation and with sign of perturbation. Reasons for these variations are partly physical and partly due to the model domain and parameterizations used. The degree of atmospheric thermal mixing in the model also influenced the computed f -value, with larger values of f (in terms of temperature) being computed in experiments with enhanced thermal advection between adjacent grid points. This occurred because increased atmospheric thermal advection brings warmer SATs over parts of the model domain which would otherwise remain cool due to the presence of ice, enhancing the snow/ice-albedo feedback's effectiveness in these areas. This is key to the “area” aspect of the snow/ice-albedo feedback.

The computed magnitude of f did not vary with the magnitude of the perturbation, however, which is logical in a system which does not incur major additional internal feedbacks (recalling that the “amplification” of a temperature change by a feedback process is not the same thing as the actual temperature change incurred, which *will* be dependent on the magnitude of the radiative perturbation)

The two most important findings of this study were:

- 1) That f -maxima concentrated along areas of high summer surface albedo contrast (e.g. in the vicinity of nunataks, glacier margins, and in the vicinity of the mean polar day position of the snow - bare ice line in the glacier ablation zone) can be as large or larger than values computed by others for sea ice; and
- 2) That the presence of terrestrial ice prolongs snow cover and enhances the operation and effectiveness of the snow/ice-albedo feedback throughout the summer season, increasing the local-regional amplification of mean area-averaged temperature changes.

These results indicate that the terrestrial ice-albedo feedback is not locally negligible, even at decadal time scales and less. It serves to further amplify mass balance and surface air temperature changes already amplified by sea ice changes in the Arctic region. Secondary amplifications of Arctic regional SAT changes by the terrestrial snow/ice-albedo feedback, after primary Arctic-wide sea ice - related amplifications, can be very large in the vicinity of glaciated CHA valleys.

The presence of a single glacier can result in a significant amplification of the local climate's response to climate perturbations (as a result of the snow/ice-albedo feedback). Collectively, a large number of outlet valley glaciers will be important to the evolution of larger ice caps and ice fields because amplified changes in the response times of these glaciers will amplify changes in the overall ice cap geometry.

Because of the snow/ice-albedo feedback, glaciers such as JEG in the CHA are likely to be extremely sensitive to the current warming temperature trend and to any future changes in climate as a result of increasing concentrations of atmospheric greenhouse gases (as described in IPCC, 2007). These amplifications in glacier response to climate change should not only be taken into account when predicting future changes in glacier extent and behaviour, but also in the interpretations of past air temperature changes derived from proxy data such as internal and basal ice temperature anomalies, terminal moraine positions and trim lines. Further examination into the importance of the terrestrial snow/ice-albedo feedback is needed and encouraged.

2.9 APPENDIX: THE SURFACE-ATMOSPHERE ENERGY–MASS BALANCE MODEL AND JEG-SPECIFIC PARAMETERIZATIONS

The energy balance portion of the model used in this study is similar to energy balance models described elsewhere (e.g. Peixoto and Oort, 1982), whereas the water mass balance part of the model was largely parameterized using JEG meteorological and mass balance data. The model equations are described below and the model parameterizations are summarized in Table 2.9.1. Symbol definitions are presented in Table 2.9.2.

2.9.1 Energy Balance

Local changes in atmospheric and surface temperature, T , are calculated using:

$$\begin{aligned}\frac{\partial T_a}{\partial t} &= \frac{Q_{a_{\text{net}}}}{C_a} - k(T_a - T_s) - \frac{L_e}{c_{p_a}} \frac{dw_a}{dt} + \eta \nabla^2 T_a \\ \frac{\partial T_s}{\partial t} &= \frac{Q_{s_{\text{net}}}}{C_s} + k(T_a - T_s) - \frac{L_s}{c_{p_s}} \frac{dw_c}{dt} - \frac{L_e}{c_{p_s}} \frac{dw_c}{dt} - \frac{L_f}{c_{p_s}} \frac{dw_l}{dt}\end{aligned}\quad (1a,b)$$

(see table 2.9.2 for symbol definitions). The Q_{net}/C terms represent the net radiative balances, the $k(T_a - T_s)$ terms represent the surface-atmosphere sensible heat fluxes, the $(L/c_p)(dw/dt)$ terms represent the latent heat fluxes, and the $\eta \nabla^2 T_a$ term parameterizes horizontal atmospheric mixing.

In a model with a vertically averaged atmosphere, only the radiative fluxes at the top of the atmosphere and at the surface need to be evaluated Bintanja and Oerlemans (1995). The net SW and LW radiation flux balances for the atmosphere and surface layers, respectively, are:

$$\begin{aligned}Q_{a_{\text{net}}}(t) &= \varepsilon_a (\varepsilon_s \sigma T_s^4) - \varepsilon_a \sigma T_a^4 + \varepsilon_a (\varepsilon_B \sigma T_B^4) \\ Q_{s_{\text{net}}}(t) &= (1 - \alpha_a)(1 - \alpha_s)Q(t) - \varepsilon_s \sigma T_s^4 + \varepsilon_s (0.5 \varepsilon_a \sigma T_a^4) + \varepsilon_s (1 - \varepsilon_a)(\varepsilon_B \sigma T_B^4)\end{aligned}\quad (2a,b)$$

The mean thickness of the atmosphere layer in this study is taken to be the scale height of the troposphere. The mean thickness of the ground or ice surface layer is fixed at the commonly used value of $\Delta H_s = 15$ m, and it is assumed that thermal conduction into or from the ice or rock/soil below this depth is negligible on less than decadal time scales (e.g. Arendt, 1999).

As in Oerlemans (1986), it is assumed that $\varepsilon_s = 1.0$ and $\varepsilon_B = 0.8$, and a background atmospheric temperature, T_B , is used to parameterize latitudinal sensible/latent heat transports. It is also similarly assumed that atmospheric absorption of SW radiation is negligible, permissible because Arctic atmospheric specific humidity is low (Peixoto and Oort, 1992). Unlike Oerlemans (1986), it is assumed that: a) the atmosphere, like the surface, behaves as a black body and that $\varepsilon_a = 1.0$; b) SW

inputs/outputs depend upon cloud, as well as surface, albedo, α ; and c) T_B varies cyclically with season, peaking in spring and dipping in autumn (see table 2.9.1). This seasonally varying background temperature simulates spring-time warm air advection from lower latitudes and autumnal cold air advection from the pole and the Beaufort Sea. Note that the impact of atmospheric absorptivity/emissivity changes, due to seasonal changes in RH and cloudiness, are implicitly “incorporated” into this seasonal cycle of the background atmospheric temperature.

A temperature-based JEG surface albedo parameterization (similar to that presented in Bugnion and Stone, 2002; after Kang, 1994) was adopted here, instead of the more complex albedo parameterization employed by Arendt (1999; after van der Wal and Oerlemans, 1994). This was done because complex parameterizations which depend on surface features can give a degraded simulation of surface albedo if the simulation of the surface features is deficient (Curry et al., 2001). This is an important consideration because the magnitude of the computed snow/ice-albedo feedback parameter, f , for sea ice has been shown to be sensitive to the model albedo parameterization used (e.g. Curry et al., 2001). The computed terrestrial snow/ice-albedo feedback is likely to be sensitive to the chosen parameterization as well.

Measured JEG surface albedos exhibit a visible relationship with surface air temperatures. Although much scatter occurs in the data at higher temperatures due to sub-seasonal daily temperature variations, fourth order polynomial regressions were found to best describe albedo-temperature relationships at the three meteorological stations (see Table 2.9.1). Bugnion and Stone (2002), for comparison, used a third order polynomial regression in their parameterization. The derived JEG polynomials have r^2 values of 0.63 above the ELA (in the accumulation zone) and 0.62 below the ELA (in the ablation zone). The correlation coefficients, 0.794 and 0.787 respectively, are significant at the 99% level using the Fisher-z test. Polynomial albedo-temperature relationships eliminate the need to track the exact transition from snow to bare ice or firn during the spring/summer melt season. In the model, albedos are automatically reset to the maximum value after each snowfall event, regardless of new snow depth, and the transition back to pre-snowfall values then follows as per the polynomial equation.

It should be noted that the polynomials were determined using observed surface (2 m) air temperatures, whereas the energy balance model predicts tropospheric-average and ground/ice surface temperatures (1a,b). An average of the surface and atmospheric temperatures was therefore used in the model albedo parameterization. Despite this approximation, model calculations of surface albedo closely reproduce the observed values, although they lack day-to-day variations (see Figure 2.7c in text).

The surface-atmosphere sensible heat fluxes and horizontal atmospheric temperature advection are parameterized in this model because atmospheric winds are not computed (see Table 2.9.1). While a static atmosphere serves the purpose of partially separating the thermal snow/ice-albedo feedback from mechanical feedbacks such as the elevation – mass balance feedback, atmospheric temperature advection is nevertheless important in climate sensitivity calculations and needs to be considered (e.g. Oerlemans, 1986).

2.9.2 Mass Balance

Local changes in atmospheric water vapor and surface snow/ice mass are calculated using:

$$\frac{\partial q}{\partial t} = -\nabla \cdot (q\mathbf{u}_a) + s(q) + D = F_V + s(q) \quad (3)$$

$$\frac{\partial h}{\partial t} = -\nabla_H \cdot (h\mathbf{u}_s) + MB \quad (4)$$

Equation (3) is the local balance equation for atmospheric water vapor mass (e.g. Peixoto and Oort, 1992, p. 275, p. 302). The local change in q is a result of water vapor mass flux divergence (the first term on the right hand side of equation (3)), water vapor sources/sinks, $s(q)$, and molecular/turbulent eddy diffusion of water vapor into the area, D . Sources of water vapor in the atmosphere are surface evaporation or sublimation and sinks are atmospheric condensation and precipitation. The mass flux divergence and the diffusion terms can be combined into a single meridional flux of water vapor, F_V , for the polar regions (e.g. Peixoto and Oort, 1992).

In this study, atmospheric moisture imports and losses are diagnostically determined using calculated surface temperatures, atmospheric temperatures, saturation vapor pressures, and RH values. The atmospheric column receives evaporated/sublimated water mass from the surface (the “source” part of the $s(q)$ term in equation (3)). F_V is parameterized as described in Table 2.9.1. Under this F_V parameterization, most of the moisture advection/diffusion into the model atmospheric column occurs during the spring when atmospheric temperatures are rising and RH values are decreasing towards a summer minimum. This is reasonable as poleward meridional moisture transports reach a maximum near the summer equinox (Peixoto and Oort, 1992, p. 306, figure 12.21). The “sink” part of the $s(q)$ term (i.e. model precipitation) is parameterized as described in Table 2.9.1. Under this parameterization, model precipitation takes place primarily during autumn when atmospheric temperatures are falling and relative humidity is rising. This also agrees with observations, which indicate that 60-70% of the annual precipitation at JEG occurs during autumn (Sharp et al., 2002).

Equation (4) is the local balance/conservation equation for surface snow/ice mass, here expressed as a snow/ice volume, or thickness, h , per unit area (e.g. Paterson, 1994, p. 256). The first term on the right hand side represents the horizontal mass flux divergence (i.e. the accumulation/removal of ice from a point on the earth's surface resulting from glacier deformation and sliding). The second term is the time-dependent surface mass balance (MB), equal to annual snow accumulation plus summer meltwater refreezing minus summer melt/runoff minus surface evaporation/sublimation (Table 2.9.2).

Computed surface accumulation (i.e. model precipitation, Table 2.9.1) is orographically enhanced using an observed JEG MB-elevation relationship (Table 2.9.1). This parameterization is necessary to reproduce observed precipitation amounts at JEG. Water can be lost from the model surface via evaporation, sublimation and/or surface runoff. Surface evaporation/sublimation is calculated from local surface energy budgets, as is surface melt/refreezing. Evaporation and sublimation are also subject to modeled differences between atmospheric and saturation mixing ratios. Surface runoff percentages are parameterized as per Table 2.9.1, and all runoff is assumed lost from the model domain.

Two assumptions are made concerning the model snow/ice mass balance used in this study. The first is that the ice is approximately static on decadal time scales and that the mass flux divergence term in (4) is therefore negligible. This assumption is justified because significant horizontal mass transfer resulting from glacier deformation, in the absence of large-scale sliding, generally takes place over time scales greater than a single decade.

Since the transition from snow to firn to ice can be a complicated process spanning decades to centuries (Paterson, 1994, pp. 12-15), the second assumption concerning the model snow/ice mass balance is that the conversion of precipitated snow into glacier ice occurs immediately. This "ice", however, is assumed to behave as permeable snow when calculating runoff percentages and is assumed to have a temperature-dependent surface albedo during the spring/summer melt period, similar to snow. This assumption will impact the surface layer's heat capacity and the computed daily surface-layer temperatures, because snow and firn have lower densities than ice. However, annual average surface temperatures within the layer will remain close to mean annual surface atmospheric temperatures. This assumption eliminates the need to track the snow-firn-ice transition; however, its impact should be investigated in subsequent studies.

2.9.3 Model Integration

Model grid-point temperatures are integrated forward in time, using a 1-day time step and a square model grid spacing of 125m, by applying an operator splitting method (Press et al., 1992, pp. 847-48). A daily time step is used because sub-daily calculations would require more complex computations of sun angle, etc., without significantly contributing to the seasonal results of interest. The energy

fluxes are first diagnosed from variables within the present time step. A Forward-Time Centred-Space (FTCS) scheme, using the Lax method (Press et al., 1992, pp. 825-29) is then used to compute the temperature changes as a result of the calculated energy fluxes and to integrate them forward by one day. A fully implicit backward time scheme (as recommended by Press et al., 1992, pp. 838-39) was then used to modify the present-day's temperatures as a result of the thermal diffusion part of equation (1a). Mass balance elements were then diagnosed from the present-day surface and atmospheric temperatures as described in section 2.9.2, before moving on to the next time step. Surface elevations used in the model were derived from a surface Digital Elevation Model (DEM) of JEG (*pers. comm.* A. Arendt), and glacier bed elevations (used in the no-ice experiments below) were derived from a bed DEM created by Copland and Sharp (2001). Ice thicknesses were computed by differencing the two DEMs.

Table 2.9.1. Summary of JEG-specific model parameterizations.

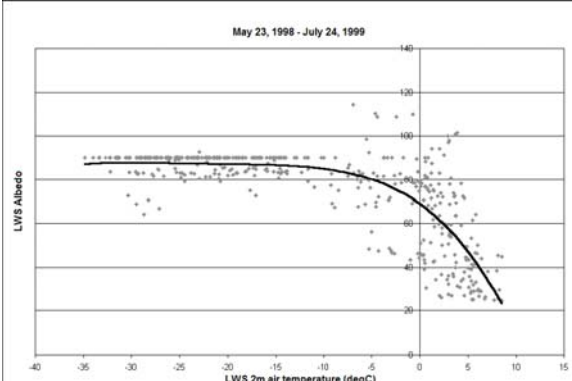
Term	Symbol	Parameterization
1. cloud albedo	α_a	<ul style="list-style-type: none"> thick cloud ($RH \geq 80\%$) $\alpha_c = 0.8$ thin cloud ($60\% \leq RH < 80\%$) $\alpha_c = 0.425$ no cloud ($RH < 60\%$) $\alpha_c = 0.0$ <p>Modeled after values in Gedzelman (1980, p.123); Kondratyev (1969).</p>
2. surface albedo	α_s	<ul style="list-style-type: none"> Fresh snow (above ELA) $\alpha_s = 0.975$ Fresh snow (below ELA) $\alpha_s = 0.90$ $\alpha_s(T_s) = c_1 T_s^4 + c_2 T_s^3 + c_3 T_s^2 + c_4 T_s + c_5$ Bare firn (above ELA) $\alpha_s = 0.50$ Bare ice (below ELA) $\alpha_s = 0.25$ Bare rock/soil (Budyko, 1974) $\alpha_s = 0.10$ <p>(Firn value used above: Paterson, 1994, p58).</p> <p>The polynomial was determined using measured JEG albedo and air temperature data (see figure below). Coefficients c_1 to c_5 differ above/below ELA. Above ELA: $c_1 = -3.2 \times 10^{-5}$, $c_2 = -0.0029$, $c_3 = -0.0935$, $c_4 = -1.745$, $c_5 = +81.52$. Below ELA: $c_1 = -7.0 \times 10^{-5}$, $c_2 = -0.0062$, $c_3 = -0.2084$, $c_4 = -3.147$, $c_5 = +69.00$. This is similar to the third-order polynomial $\alpha_s(T_s)$ parameterization derived for Greenland by Bugnion and Stone (2002); Kang (1994).</p> 

Figure 2.9.1. Scatter plot of daily averaged surface albedo ($\times 100$) versus 2m air temperatures at the Lower Weather Station, 1998-1999. Surface albedo is measured as the ratio of outgoing to incoming SW radiation during the part of the year when sunlight is available. During the sunless winter months, albedos are assumed fixed at values of 0.9 below the ELA and 0.975 above the ELA.

Term	Symbol	Parameterization
3. Background atmospheric temperature (used to parameterize meridional atmospheric sensible and latent heat transports)	T_B	<ul style="list-style-type: none"> Modeled as part of the LW radiation balance by prescribing an empirically-derived seasonally-varying background atmospheric temperature; $T_B(t) = -30.0 \cos(2\pi t / 365.0 - \pi) + 263.15 \text{ K}$; <p>This is a modification of the constant background temperature concept used by Oerlemans (1986), where he chose $T_B = 245 \text{ K}$ for Europe in summer.</p>
4. atmosphere-surface sensible heat exchange	$k(T_a - T_s)$	<ul style="list-style-type: none"> $k = 1.0 \times 10^{-7} \text{ s}^{-1}$ is a vertical exchange coefficient for sensible heat; <p>Parameterized following Oerlemans (1986); Bjornsson and Mysak (2001).</p>
5. atmospheric temperature advection (horizontal heat exchange)	$\eta \nabla^2 T_a$	<ul style="list-style-type: none"> still air $\eta = 2.15 \times 10^{-5} \text{ m}^2 \text{ s}^{-1}$ stirred air $\eta = 2.15 \text{ m}^2 \text{ s}^{-1}$ <p>A diffusive parameterization widely employed in models with no wind calculations (e.g. Bintanja and Oerlemans, 1995; Oerlemans, 1986; Crowley et al., 1986).</p> <p>Values of η for still and stirred air differ by an order of magnitude. Peixoto and Oort (1992, p221): still air ($\eta = 2.15 \times 10^{-5} \text{ m}^2 \text{ s}^{-1}$), stirred air ($\eta = 4.0 \text{ m}^2 \text{ s}^{-1}$). Oerlemans (1986): stirred air ($\eta = 10.0 \text{ m}^2 \text{ s}^{-1}$).</p>
6. atmospheric moisture imports (meridional water vapor flux)	F_v	<ul style="list-style-type: none"> If grid point $RH < 40\%$, then set $RH = 40\%$. (Based on minimum recorded JEG RH's of $\sim 40\%$). This results in atmospheric-column water-mass import values on the order of ~ 0.0001 to $0.001 \text{ kg kg}^{-1} \text{ d}^{-1}$, comparable to the water vapor advection values employed in Beesley and Moritz (1999). If $RH \geq 100\%$, so that precipitation will occur, then empirically add $0.0008 \text{ kg kg}^{-1} \text{ d}^{-1}$ to the atmospheric column. Done to account for cloud and precipitation that was not condensed in situ (that was advected into the model domain during precipitation events).
7. atmospheric moisture losses / surface accumulation (precipitation)	“sink” part of $s(q)$; accumulation part of MB	<ul style="list-style-type: none"> When the atmospheric specific humidity, q, is greater than or equal to the saturation specific humidity, q_s, (i.e. when $RH \geq 100\%$), all water vapor mass in excess of saturation in the column is assumed to condense and precipitate out onto the surface.

Term	Symbol	Parameterization
8a. surface moisture losses / atmospheric moisture gains (evaporation) Note: surface sublimation was neglected for JEG, its magnitude being much smaller than evaporation.	“source” part of $s(q)$ and an ablation term of MB	<ul style="list-style-type: none"> If in a given timestep liquid water exists at the surface <i>and</i> the atmospheric mixing ratio (w_a) is less than the saturation mixing ratio (w_s) for the given air temperature, then evaporation empirically occurs so that $\text{evap (kg)} = (w_s - w_a) \times 0.001 \text{ kg d}^{-1}$, unless “evap” exceeds the available amount of liquid water at the surface in which case only the available amount is evaporated. If no liquid water exists, but ice exists, then as above except using the saturation mixing ratio over ice.
8b. surface moisture losses/gains (melting/refreezing)	Ablation / accumulation terms of MB	<ul style="list-style-type: none"> If in a given timestep ice exists at the surface <i>and</i> the surface temperature is greater than or equal to 273.15K <i>and</i> there is a net positive incoming amount of energy (RHS of equations 1a,b), then the melt rate equals equation (1b) solved for dw_i/dt assuming $\partial T_s / \partial t = 0$. If the melt rate multiplied by the timestep is less than the total amount of available energy, then the remaining energy is used to raise the surface temperature. If in a given timestep the surface temperature is less than 273.15K and liquid water exists at the surface, then all the water that is left after any runoff occurs is assumed to freeze (and latent heat is released).
9. surface accumulation enhancement by the orographic effect		<ul style="list-style-type: none"> $MB_orog(z) = 0.0012 \times z \text{ m w.e. yr}^{-1} \rightarrow 3.3 \times 10^{-6} \times z \text{ m w.e. d}^{-1}$ (per 1-day timestep), where z is elevation. <p>JEG accumulation (Woodward et al., 1997) and mass balance (<i>pers. comm.</i> A. Arendt) are elevation-dependent. Data show $MB(z) \sim 0.0012z - 1.18 \text{ m w.e. yr}^{-1}$. Thus, the mean MB at $z=0$ is enhanced by $0.0012z$ at higher elevations.</p> <p>E.G. At $z=1000\text{m}$, 0.003 m w.e. is added to the surface accumulation during a precipitation event.</p>

Term	Symbol	Parameterization
10. restriction of surface moisture losses (runoff)		<ul style="list-style-type: none"> • Snow is present 60% of melt → runoff • No snow 100% of melt → runoff <p>All meltwater runoff in a given model time step is assumed lost to model domain.</p> <p>Values based on short-term meltwater storage of ~40% in snow and firn, summarized in Jansson et al. (2003, p121).</p>

Table 2.9.2. Symbol definitions.

Symbol	Definition	Symbol	Definition
<i>variables</i>			
T	temperature	h	ice thickness
t	time	MB	Surface mass balance (m yr^{-1}).
Q_{net}	net balance between incoming / outgoing SW and LW radiation fluxes	MB = precipitation rate – evaporation / sublimation rate – melt / runoff rate + refreezing rate.	
SW	ShortWave radiation = $Q(t)$	<i>subscripts</i>	
LW	LongWave radiation = $\varepsilon\sigma T^4$	a	atmosphere
C	model layer heat capacity per unit area ($C=\rho c_p \Delta H$)	s	surface
ΔH	mean layer thickness ($\Delta H_a = R_d T_a / g$), ($\Delta H_s = 15\text{m}$)	B	Background
$Q(t)$	incoming solar SW radiation $Q(t) = (S/4)\cos(\phi_{\text{eff}})$	H	Horizontal
ϕ	latitude ($^\circ$)	<i>constants</i>	
ϕ_{eff}	effective latitude $\phi_{\text{eff}}(t) = \phi + 23.45^\circ \cos(2\pi t / 365.0)$ (23.45° is the tilt angle of the Earth)	g	gravity
ε	absorptivity / emissivity	ρ	density
α	albedo	R_d	gas constant for dry air
$w_a (= q)$	atmospheric water content (mass of water vapor per unit mass of air) in kg kg^{-1} .	σ	Stefan-Boltzmann constant
w_c	total amount of <i>condensed</i> water (kg) which has precipitated to or evaporated/sublimated from the surface, and which is a sum of liquid and frozen water.	L_e	latent heat of evaporation
w_l	the amount of <i>liquid</i> water at the surface	L_s	latent heat of sublimation
$q (= w_a)$	specific humidity in units of kg kg^{-1} (i.e. the mass of water vapor, kg, per unit mass of air, kg)	L_f	latent heat of fusion
RH	Relative Humidity	k	a vertical exchange coefficient for sensible heat
\mathbf{u}	wind or ice velocity vector	c_p	specific heat at constant pressure
D	molecular/turbulent eddy diffusion of water vapor into the area	η	thermal diffusion coefficient
F_v	meridional water vapor flux $F_v = \nabla \cdot (q\mathbf{u}_a) + D$	S	Solar constant
$s(q)$	water vapor sources/sinks		

2.10 REFERENCES

- Abe-Ouchi, A., T. Segawa and F. Saito, 2007: Climatic conditions for modelling the Northern Hemisphere ice sheets throughout the ice age cycle. *Climate of the Past*, **3**, 423–438.
- Alt, B. T., 1987: Developing synoptic analogs for extreme mass balance conditions on Queen Elizabeth Island ice caps. *Journal of Climate and Applied Meteorology*, **26**(12), 1605-1623.
- Arendt, A., 1999: Approaches to modelling the surface albedo of a high arctic glacier. *Geografiska Annalar*, **81 A** (4), 477-487.
- Arendt, A. A., K. A. Echelmeyer, W. D. Harrison, C. S. Lingle and V. B. Valentine, 2002: Rapid wastage of Alaska glaciers and their contribution to rising sea level. *Science*, **297**(5580), 382 – 386. DOI: 10.1126/science.1072497 .
- Arnold, N, 2005: Investigating the sensitivity of glacier mass-balance/elevation profiles to changing meteorological conditions: model experiments for Haut Glacier D’Arolla, Valais, Switzerland. *Arctic, Antarctic, and Alpine Research*, **37**(2), 139–145.
- Bassford, R. P., M. J. Siegert and J. A. Dowdeswell, 2006: Quantifying the mass balance of ice caps on Severnaya Zemlya, Russian High Arctic. III: sensitivity of ice caps in Severnaya Zemlya to future climate change. *Arctic, Antarctic, and Alpine Research*, **38**(1), 21–33.
- Beesley, J. A., and R. E. Moritz, 1999: Toward an Explanation of the Annual Cycle of Cloudiness over the Arctic Ocean. *Journal of Climate*, **12**, 395-415.
- Bingham, R.G., P.W. Nienow, M.J. Sharp, and S. Boon, 2005: Subglacial drainage processes at a High Arctic polythermal valley glacier. *Journal of Glaciology*, **51**, 15-24.
- Bintanja, R., and J. Oerlemans, 1995: The influence of the albedo-temperature feedback on climate sensitivity. *Annals of Glaciology*, **21**, 353-360.
- Bjornsson, H., and L. A. Mysak, 2001: Present-day and Last-Glacial-Maximum ocean thermohaline circulation in a zonally averaged coupled ocean–sea-ice–atmosphere model. *Journal of Climate*, **14**, 1422-1439.
- Blatter, H., 1987: On the thermal regime of an Arctic valley glacier: a study of White Glacier, Axel Heiberg Island, N.W.T., Canada. *Journal of Glaciology*, **33**, 200-211.
- Blatter, H., and G. Kappenberger, 1988: Mass balance and thermal regime of Laika Ice Cap, Coburg Island, N.W.T., Canada. *Journal of Glaciology*, **34**, 102-110.
- Bony, S. R. Colman, V. M. Kattsov, R. P. Allan, C. S. Bretherton, J-L Dufresne, A. Hall, S. Hallegatte, M. M. Holland, W. Ingram, D. A. Randall, B. J. Soden, G. Tselioudis and M. J. Webb, 2006: How Well do we Understand Climate Change Feedback Processes? *Journal of Climate*, **19**(15), 3445-3482.

- Brock, B.W., I. C. Willis and M. J. Sharp, 2000: Measurement and parameterisation of albedo variations at Haut Glacier d'Arolla, Switzerland. *Journal of Glaciology*, **46**(155): 675–688.
- Budyko, M.I., 1974: *Climate and Life*. Academic Press, New York, 508 pp.
- Bugnion, V., and P. H. Stone, 2002: Snowpack model estimates of the mass balance of the Greenland ice sheet and its changes over the twentyfirst century. *Climate Dynamics*, **20**(1), 87-106.
- Burgess, D. O., and M. J. Sharp, 2004: Recent changes in areal extent of the Devon Ice Cap, Nunavut, Canada. *Arctic, Antarctic, and Alpine Research*, **36**(2), 261–271.
- Centre for Topographic Information, 1999: National Topographic Data Base—Edition 3 Simplified User's Guide. NTDB Customer Support Group, Centre for Topographic Information, Natural Resources Canada, Sherbrooke, Quebec. 13 pp.
- Cess, R.D., and 32 others, 1991: Interpretation of snow-climate feedback as produced by 17 General Circulation Models. *Science*, **253**, 888-892.
- Cogley, J. G., and F. Jung-Rothenhäusler, 2004: Uncertainty in Digital Elevation Models of Axel Heiberg Island, Arctic Canada. *Arctic, Antarctic, and Alpine Research*, **36**(2), 249–260
- Cook, K. H., X. Yang, C. M. Carter and B. N. Belcher, 2003: A Modeling System for Studying Climate Controls on Mountain Glaciers with Application to the Patagonian Icefields. *Climatic Change*, **56**(3), 339-367.
- Copland, L., and M. Sharp, 2001: Mapping thermal and hydrological conditions beneath a polythermal glacier with radio-echo sounding. *Journal of Glaciology*, **47**(157), 232-242.
- Copland, L., M. J. Sharp, P. Nienow and R. G. Bingham, 2003: The distribution of basal motion beneath a High Arctic polythermal glacier. *Journal of Glaciology*, **49**(166), 407-414.
- Crowley, T.J., D.A. Short, J.G. Mengel, and G.R. North, 1986: Role of seasonality in the evolution of climate during the last 100 million years. *Science*, **231**, 579-584.
- Curry, J. A., J. L. Schramm and E. E. Ebert, 1995: Sea ice-albedo climate feedback mechanism. *Journal of Climate*, **8**, 240-247.
- Curry, J. A., W. B. Rossow, D. Randall and J. L. Schramm, 1996: Overview of Arctic cloud and radiation characteristics. *Journal of Climate*, **9**, 1731-1764.
- Curry, J.A., J.L. Schramm, D. Petrovich, and J.O. Pinto, 2001: Application of SHEBA/FIRE data to evaluation of sea ice surface albedo parameterizations. *Journal of Geophysical Research*, **106**(D14), 15345-15355.
- Flato, G. M., and R. D. Brown, 1996: Variability and climate sensitivity of landfast Arctic sea ice. *Journal of Geophysical Research*, **101**, 25767-25777.

Fyfe, J.C. and G.M. Flato. 1999: Enhanced climate change and its detection over the Rocky Mountains. *Journal of Climate*, **12**, 230-243.

Gedzelman, S.D., 1980: The Science and Wonders of the Atmosphere. John Wiley & Sons, New York, 535 pp.

Grell, G. A., J. Dudhia and D. R. Stauffer, 1994: A Description of the Fifth- Generation Penn State/ NCAR Mesoscale Model (MM5). *NCAR Technical Note* TN-398 + STR, 121 pp.

Hall, A., and X. Qu, 2006: Using the current seasonal cycle to constrain snow albedo feedback in future climate change. *Geophysical Research Letters*, **33**, L03502, doi:10.1029/2005GL025127.

Harvey, L.D.D., 1988: On the role of high latitude ice, snow, and vegetation feedbacks in the climatic response to external forcing changes. *Climatic Change*, **13**(2), 191-224.

Hock, R., V. Radić, M. de Woul, 2007: Climate sensitivity of Storglaciären, Sweden: an intercomparison of mass-balance models using ERA-40 re-analysis and regional climate model data. *Annals of Glaciology*, **46**, 342-348.

Holland, M. M., and C. M. Bitz, 2003: Polar amplification of climate change in coupled models. *Climate Dynamics*, **21**, 221-232.

IPCC, 1996: *Climate Change 1995: The Science of Climate Change*. Contribution of Working Group 1 to the Second Assessment Report of the IPCC [Houghton, J.T., Meira Filho, L.G., Callander, B.A., Harris, N., Kattenberg, A., and Maskell, K. (eds)]. Cambridge University Press, Cambridge, U.K. 572 pp.

IPCC, 2007: *Climate Change 2007: The Physical Science Basis*. Contribution of Working Group I to the Fourth Assessment Report of the Intergovernmental Panel on Climate Change [Solomon, S., D. Qin, M. Manning, Z. Chen, M. Marquis, K.B. Averyt, M. Tignor and H.L. Miller (eds.)]. Cambridge University Press, Cambridge, United Kingdom and New York, NY, USA, 996 pp.

Jansson, P., R. Hock, and T. Schneider, 2003: The concept of glacier storage: a review. *Journal of Hydrology*, **282**, 116–129.

Johannesson, T., C.F. Raymond, and E.D. Waddington, 1989: A simple method for determining the response time of glaciers. In: *Glacier Fluctuations and Climatic Change* (J. Oerlemans, ed.), Kluwer Academic Publishers, London, 343-352.

Kang, E., 1994: Energy-water-mass balance and hydrologic discharge. *Technical Report 57*, Zürcher Geographische Schriften, ETH, Zürich, 93–94.

Koerner, R. M., 1970: The mass balance of Devon Island ice cap Northwest Territories, Canada, 1961–1966. *Journal of Glaciology*, **9**(57), 325–336.

Koerner, R. M., 1979: Accumulation, ablation, and oxygen isotope variations on the Queen Elizabeth Islands ice caps, Canada. *Journal of Glaciology*, **22**(86), 25-41.

Kondratyev, K. Ya., 1969: Radiation in the Atmosphere. Academic Press, New York, 912 pp.

Marshall, S. J., M. J. Sharp, D. O. Burgess and F. S. Anslow, 2007: Near-surface-temperature lapse rates on the Prince of Wales Icefield, Ellesmere Island, Canada: implications for regional downscaling of temperature. *International Journal of Climatology*, **27**(3), 385-398. Published online in Wiley InterScience (www.interscience.wiley.com) DOI: 10.1002/joc.1396 .

National Research Council: Board on Global Change, 1994: *Solar Influences on Global Change*. National Academy Press, 180pp.
(<http://www.nap.edu/books/0309051487/html/23.html>)

Oerlemans, J., 1986: Glaciers as indicators of a carbon dioxide warming. *Nature*, **320**, 607-609.

Overpeck, J., K. Hughen, D. Hardy, R. Bradley, R. Case, M. Douglas, B. Finney, K. Gajewski, G. Jacoby, A. Jennings, S. Lamoureux, A. Lasca, G. MacDonald, J. Moore, M. Retelle, S. Smith, A. Wolfe, and G. Zielinski, 1997: Arctic Environmental Change of the Last Four Centuries. *Science*, **278**, 1251-1256.
DOI: 10.1126/science.278.5341.1251.

Paterson, W.S.B., 1994: *The Physics of Glaciers*, 3rd ed. Pergamon Press, Oxford, England, 480 pp.

Paul, F., A. Kääb, M. Maisch, T. Kellenberger and W. Haeberli, 2004: Rapid disintegration of alpine glaciers observed with satellite data. *Geophysical Research Letters*, **31**, L21402, doi:10.1029/2004GL020816.

Peixoto, J.P., and A.H. Oort, 1992: *Physics of Climate*. American Institute of Physics, New York, 520 pp.

Press, W. H., S. A. Teukolsky, W.T. Vetterling and B. P. Flannery [eds.], 1992: *Numerical Recipes in Fortran: the Art of Scientific Computing*, 2nd ed. Cambridge University Press, Cambridge, England, 963pp.

Pritchard, M. S., A. B. G. Bush and S. J. Marshall, 2008: Neglecting ice-atmosphere interactions underestimates ice sheet melt in millennial-scale deglaciation simulations. *Geophysical Research Letters*, **35**, L01503, doi: 10.1029/2007GL031738.

Qu, X., and A. Hall, 2005: Surface contribution to planetary albedo variability in cryosphere regions. *Journal of Climate*, **18**, 5239–5252.

Qu, X., and A. Hall, 2006: Assessing snow albedo feedback in simulated climate change. *Journal of Climate*, **19**, 2617–2630.

Qu, X., and A. Hall, 2007: What Controls the Strength of Snow-Albedo Feedback? *Journal of Climate*, **20**, 3971-3981.

- Ramanathan, V., R. D. Cess, E. F. Harrison, P. Minnis, B. R. Barkstrom, E. Ahmad and D. Hartman, 1989: Cloud-radiative forcing and climate: Results from the Earth Radiation Budget Experiment. *Science*, **243**, 57-63.
- Robock, A., 1983: Ice and snow feedbacks and the latitudinal and seasonal distribution of climate sensitivity. *Journal of the Atmospheric Sciences*, **40**(4), 986-997.
- Sharp, M., M. Skidmore, and P. Nienow, 2002: Seasonal and spatial variations in the chemistry of a High Arctic supraglacial snow cover. *Journal of Glaciology*, **48** (160), 149-158.
- Sweeney, M. R., A. J. Busacca, C. A. Richardson, M. Blinnikov and E. V. McDonald, 2004: Glacial anticyclone recorded in Palouse loess of northwestern United States. *Geology*, **32**(8), 705–708; doi: 10.1130/G20584.1.
- Wolken, G. J., J. H. England and A. S. Dyke, 2008: Changes in late Neoglacial perennial snow/ice extent and equilibrium-line altitudes in the Queen Elizabeth Islands, Arctic Canada. *Holocene*, **18**(4), 615-627.
- Woodward, J., M. Sharp and A. Arendt, 1997: The influence of super-imposed ice formation on the sensitivity of glacier mass balance to climate change. *Annals of Glaciology*, **24**, 186-190.
- Zuo, Z., and J. Oerlemans, 1996: Modelling albedo and specific balance of the Greenland ice sheet: calculations for the Søndre Strømfjord transect. *Journal of Glaciology*, **42** (141), 305-317.
- Zwally, H. J., W. Abdalati, T. Herring, K. Larson, J. Saba, and K. Steffen, 2002: Surface melt-induced acceleration of Greenland Ice-Sheet flow, *Science*, **297**, 218-222.

3. Little Ice Age – Related Temperature Anomalies within Greenland and Canadian High Arctic Ice Cap Boreholes: the Role of Ice-Atmosphere Feedbacks and the Thermal Memory of the Ice Cap.

3.0 INTRODUCTION

Terrestrial ice is an important source of quantitative information about past climates. For example, it has long been known that ice-depth-variations in oxygen $^{18}\text{O}/^{16}\text{O}$ isotope ratios (δ 's) are correlated to past surface air temperatures (SATs) (e.g. Paterson et al, 1977). It has also been demonstrated that depth-variations in ice cap borehole temperatures can be used as reliable proxies for SAT histories (e.g. Dahl-Jensen et al., 1998). Historical SAT anomalies are preserved as ice temperature anomalies within the accumulation areas of cold and predominantly cold polythermal ice caps and glaciers. In these places, ice temperatures at depths of 10-15m (the depth at which the seasonal temperature wave is damped out) are equal to the mean annual air temperature at the surface (Paterson, 1994, p. 208). As each layer of ice is buried deeper and deeper by subsequent annual accumulations of snow, it carries with it a “memory” of the SAT from the time of its deposition. Measured ice temperature anomalies, associated with a given climate event, can vary significantly from location to location, however, leading to uncertainties and making the true SAT history of a region difficult to resolve. This chapter examines in greater detail two, often neglected, causes for differences in the amplitudes of Canadian High Arctic (CHA) and Greenland Ice Sheet (GIS) borehole ice temperature anomalies related to a specific climate event: 1) local amplification of SAT anomalies by the snow/ice-albedo feedback; and 2) the influence of adjacent temperature anomalies of the opposite sign within a given borehole. How these factors may partially account for the observed “subdued” Little Ice Age (LIA) signal at the central Greenland summit (e.g. Fischer et al., 1998; Barlow, 2001) is also discussed.

Ice temperature anomalies are defined and detected by differencing a measured ice temperature depth-profile with the computed equilibrium ice temperature depth-profile (i.e. the modeled equilibrium solution to the advective-diffusive temperature equation under present-day surface and basal boundary conditions – Figure 3.1).

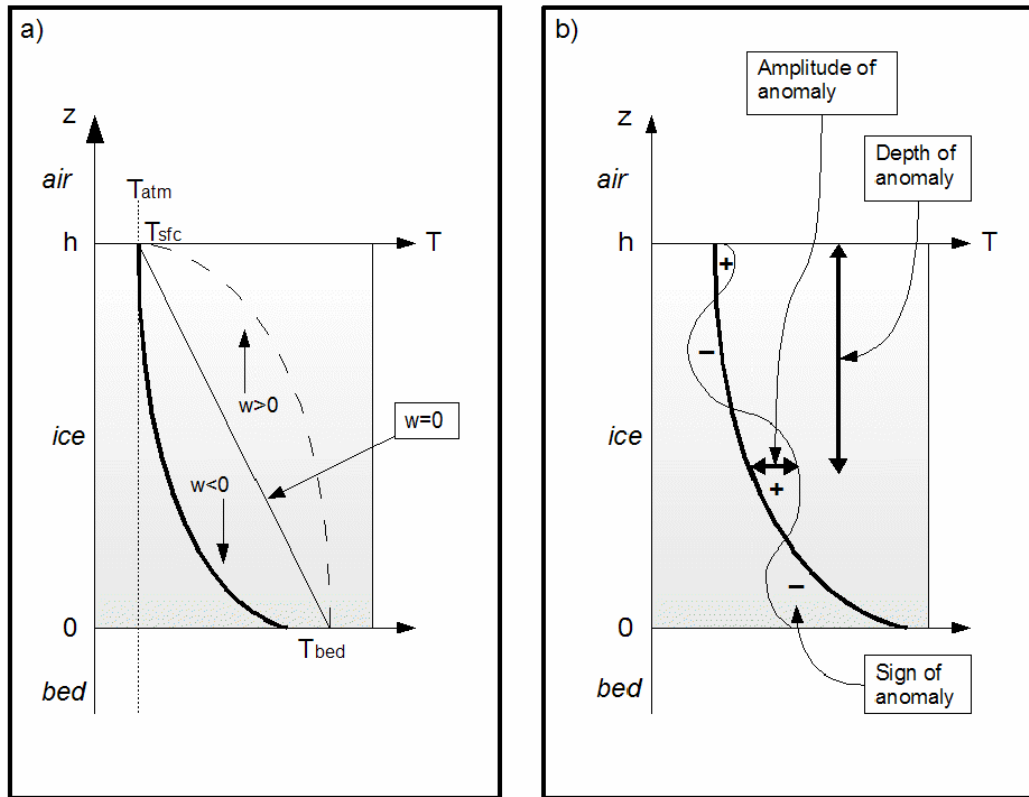


Figure 3.1. a) Sketches of equilibrium solutions to the advective-diffusive temperature equation, for cold and predominantly cold polythermal glaciers, for: 1) downward vertical velocities ($w < 0$; thick solid line; typical of glacier accumulation zones); 2) $w = 0$ (thin solid line; typical near glacier equilibrium line altitudes, where ice flow is primarily horizontal); and 3) $w > 0$ (dashed line; typical in glacier ablation zones). Near the surface of the accumulation zone, annual layers of snow eventually become layers of ice. Submergence (i.e. $w < 0$) and mass flux divergence occur to balance this accumulation of ice and, as a result, the vertical temperature gradient near the surface is near zero (i.e. mean annual surface ice temperatures are equal to mean annual surface air temperatures). For real examples of such temperature profiles measured along the entire length of a glacier, see Blatter (1987). b) Sketch of the equilibrium solution (with respect to present day boundary conditions) for a borehole in a glacier accumulation zone (thick solid line) and the corresponding “measured” temperatures in that borehole (thin solid line). The difference between the two curves produces positive (+) and negative (-) thermal anomalies, which may be related to past climate events. The amplitude of an anomaly is the maximum temperature difference between the measured and equilibrium curves. The depth of the anomaly is the depth at which the maximum temperature difference occurs.

Observed ice temperature anomalies are an indication of the extent to which the ice is out of equilibrium with its current boundary conditions (Blatter and Hutter, 1991; Dahl-Jensen et al., 1998), and they can be inverted to recover information about past air temperatures (e.g. Dahl-Jensen et al., 1998).

Using ice borehole temperature records to recover past SAT-histories has advantages over other methods, such as extracting SAT histories from ice core δ -

profiles and from inverted ground borehole temperature records. To recover SAT histories from ice core δ -profiles, the δ versus temperature relationship must be known (e.g. as discussed in Paterson et al., 1977; Johnsen et al., 1995), but this is not always the case. Extracting SAT-anomaly time series by inverting glacier borehole temperatures is similar, though more complicated due to the deformation of the ice, to extracting SAT histories from ground borehole temperatures (e.g. Taylor, 1991; Beltrami and Taylor, 1995; Beltrami et al., 2003). However, ice temperatures in glacier accumulation zones may better preserve SAT-related temperature anomalies because, in these areas, glacier ice actively incorporates surface snowfall and associated SATs into its own mass. In the case of ground temperatures, snowfall serves to insulate the ground surface from SATs, and can partially obliterate histories of past climate events (e.g. as is the case for one of the ground boreholes described in Taylor, 1991).

Inverting and interpreting ice borehole temperature records to recover past SAT-histories is not problem-free, however. While primarily driven by SAT changes through time, the amplitudes of ice temperature anomalies can be influenced by a variety of other factors, both internal (related to the size, flow, and thermodynamics of the ice mass, as well as latent heat releases associated with the refreezing of meltwater) and external (related to atmospheric circulation patterns and ice-atmosphere feedback processes such as the snow/ice-albedo feedback and the mass balance - surface elevation feedback). For example, in the case of the Greenland Ice Sheet (GIS), ice temperature anomalies measured within the DYE3 borehole are approximately 1.5 times the amplitude of corresponding anomalies measured within the GRIP borehole located 865 km to the north (Dahl-Jensen et al., 1998). The discrepancy is likely related to the different primary sources of the air masses affecting the two locations (North Atlantic maritime versus northeastern Canadian Arctic air masses), and the associated differences in SAT and precipitation rates (Dahl-Jensen et al., 1998).

This study reviews various existing explanations for differences in the amplitudes of CHA and GIS borehole ice temperature anomalies related to a specific climate event, and proposes and examines two additional little-considered, but possibly critical, causes for some of the observed ice temperature anomaly differences. The ice temperature signal associated with the Little Ice Age (LIA) is chosen as the focal SAT-related ice temperature anomaly for this study because CHA ice caps and glaciers, being thinner than the GIS, generally preserve shorter SAT histories which span only the latter part of the Holocene. Through calculations and modeling experiments, attempts are made to determine whether observed differences in the magnitude of LIA-related ice temperature anomalies might also be due to:

- 1) local to regional spatial variations in the amplification of SAT anomalies by the snow/ice-albedo feedback (e.g. as described in Chapter 2 of this thesis); and/or

2) variations in the diffusive smoothing of the anomaly over time as a result of the presence/absence of older, positive ice temperature anomalies associated with the Holocene Climatic Optimum (CO) and the Medieval Warm Period (MWP) (see pp 68-69), which are located below the LIA-related ice temperature anomaly within certain boreholes.

The aim is to determine whether two idealized ice masses, with identical SAT histories and identical ice temperature dynamics, can nevertheless variably record the SAT anomaly, and to investigate the extent to which the observed differences in borehole temperature anomalies may be the result of differences in climate signal strength as a result of local-regional ice-atmosphere feedbacks and/or to preservation-related disparities related to other temperature anomalies within the ice.

This chapter is organized in the following manner: 1) the LIA climate event, measured LIA-signals in various ice cap boreholes, and potential causes for differences in their amplitudes are reviewed; 2) the White Glacier and GRIP borehole temperature anomalies are compared in greater detail and two specific causes are proposed to explain differences in their amplitudes; 3) the snow/ice-albedo feedback, its magnitude and its spatial variations are reviewed, and possible SAT-anomaly amplifications are calculated for White Glacier; 4) a 1D borehole ice temperature model is described, a series of experiments investigating the diffusive smoothing of LIA ice temperature anomalies are performed, and results are presented; 5) the feedback amplification calculations and the ice temperature model results are discussed; and 6) conclusions are offered.

3.1 THE LITTLE ICE AGE AND MEASURED ICE TEMPERATURE ANOMALIES

3.1.1 *The Little Ice Age: a Brief Review*

The LIA was a period of glacial advances and decreasing air temperatures, spanning approximately 400 years, beginning circa 1450 A.D. and culminating circa 1850 A.D (e.g. Jones and Briffa, 2001). Though best documented in Europe, evidence for this climate event has been found in proxy records from North America, Greenland, Asia, the tropics, New Zealand, Africa, South America and Antarctica (Soon and Baliunas, 2003). The beginning and the end of the LIA, however, as well as the degree and timing of maximum cooling, were neither temporally nor spatially synchronous (e.g. Norway versus the European Alps – Nesje and Dahl, 2003; west Greenland versus northern Europe – Barlow, 2001; reconstructed Northern Hemisphere summer temperature anomaly patterns at various times throughout the LIA – Matthews and Briffa, 2005). Additionally, while in some areas the LIA was primarily expressed as low temperatures (e.g. Matthews and Briffa, 2005), in other places it also occurred as an increase in precipitation (e.g. Norway – Nesje and Dahl, 2003; the CHA – Lamoureux et al.,

2001). Proposed causes of the LIA are primarily reduced solar insolation (e.g. as a result of the Maunder Minimum – National Research Council, 1994; Fischer et al., 1998; Mauquoy et al., 2002) and increased atmospheric volcanic aerosols (e.g. Lamoureaux et al., 2001). Modeling studies support both causes to varying degrees (e.g. Liu et al., 2004; Robock, 1979), but suggest that other factors may have also played a role (e.g. vegetation – Liu et al. 2004; dynamic changes in the climate system – Kleinen et al., 2007). It can be argued that the present-day climate is one which is still in the process of emerging from the LIA (e.g. Kreutz et al., 1997).

3.1.2 *CHA and GIS Ice Temperature Records of the LIA*

Few deep borehole temperature records are available for the CHA and the GIS. While surface to bedrock ice cores have been drilled in the GIS (e.g. Dahl-Jensen et al., 1998), in the Agassiz, Devon and Meighen ice caps in the CHA (Koerner, 1989), and in a few glaciers in the CHA (e.g. Blatter, 1987; Blatter and Kappenberger, 1988), not many associated borehole temperature measurements are reported in the published literature. Melt-layers, pollen counts, and δ -profiles are more commonly described. It is hoped that more borehole temperature measurements will be recorded in the future, now that these have been demonstrated to be useful proxies for past SATs (Dahl-Jensen et al., 1998).

The magnitudes and depths of LIA-related ice temperature anomalies within five sets of CHA and GIS boreholes are summarized in Table 3.1 below (see Figure 3.2 for the locations of these boreholes).

BOREHOLE(S) +elevation	Ice Thickness (borehole depth)	LIA Signal: depth	LIA Signal: amplitude
¹ GRIP (72.6N, 37.6W) ~3200 m a.s.l.	3000 m	~ 140 m	SAT ₁₉₉₅ = -31.7°C ΔT _{ice} ≤ -0.1°C ΔSAT ~ -0.5K, -0.7°C
² DYE 3 (65.2N, 43.8W) ~2500 m a.s.l.	2000 m	~ 200 m	SAT ₁₉₉₅ = ~-21°C ΔT _{ice} ~ -0.3°C ΔSAT ~ -1.0K, -1.8°C
³ Devon Ice Cap summit, ~1800 m a.s.l. (2 boreholes)	200-300 m	~ 40-50 m	SAT ₁₉₇₇ = -23°C Negative Inflection ~ ≤ -0.1°C (ΔT _{ice} = positive, due to latent heat of surface refreezing)
⁴ White Glacier summit, ~1000-1500 m a.s.l. (4+ boreholes)	300-400 m	~ 100-150 m	SAT ₁₉₉₂₋₁₉₉₄ = -15.2°C ΔT _{ice} ~ -0.3°C ΔSAT ~ -1.2°C
⁵ Laika Glacier summit ~500 m a.s.l. (1 borehole)	50-100 m	At/below the glacier bed (speculation)	SAT ₁₉₇₂₋₁₉₇₅ = -13°C ΔT _{ice} ~ n/a ΔSAT ~ n/a

Table 3.1. The magnitudes and depths of LIA-related ice temperature anomalies within five sets of CHA and GIS boreholes. After values shown on figures and quoted in: ^{1,2}Dahl-Jensen et al. (1998); ¹Johnsen et al. (1995); ³Paterson and Clarke (1978); ³Paterson et al. (1977); ⁴Blatter (1987); ⁴Doran et al., (1996); ⁴Overpeck et al., (1997); ⁵Blatter and Kappenberger (1988). Amplitudes of ice temperature anomalies and inferred SAT anomalies are with respect to present-day mean SATs.

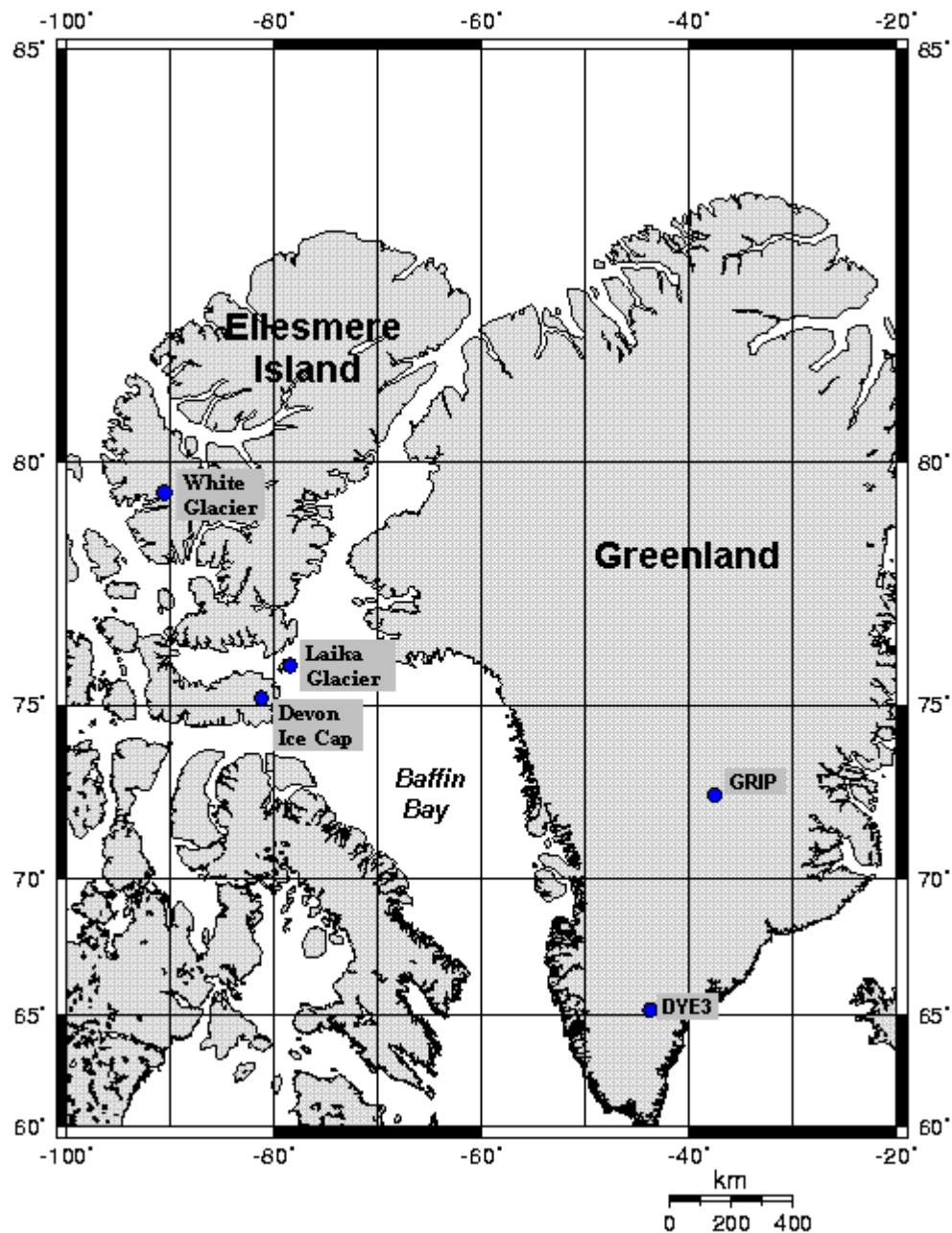


Figure 3.2. Map of Greenland and the Canadian High Arctic, showing the locations of the ice temperature measurements cited in Table 3.1.

The LIA-related ice temperature anomalies within the GRIP and DYE3 boreholes are situated at 140 and 200 m depth, respectively. The differences in these depths are consistent with observations showing that the DYE3 location has the larger mean annual accumulation rate (Dahl-Jensen et al., 1998). Advection of temperature anomalies downward into the ice by negative vertical ice velocities

can enhance the vertical displacement of a temperature anomaly to depths below that which would occur by thermal diffusion processes alone.

The LIA-related ice temperature anomaly within the Devon Ice Cap boreholes is expressed as a *negative inflection* in the thermal depth-profile rather than as an actual negative anomaly, because surface processes have interfered with the upper part of the thermal depth-profile (Paterson and Clarke, 1978). This inflection is situated at 40-50 m depth and agrees with the depth of the minimum LIA-related δ from the associated δ depth-profile (Paterson et al., 1977, their figure 4b). This depth exceeds the product of the present-day mean annual accumulation rate at the Devon Ice Cap summit ($\sim 0.2 \text{ m yr}^{-1}$ – Paterson and Clarke, 1978) when multiplied by 150 years (the approximate time interval since the culmination of the LIA in the CHA), where $0.2 \times 150 = 30 \text{ m}$. This could possibly indicate larger surface accumulation rates at some time during the past 150 years, or reflect the fact that in this location thermal diffusion rates exceed surface accumulation rates (see below).

The LIA-related ice temperature anomaly within the White Glacier summit boreholes is located at a depth of 100 m near the summit of the glacier (where the surface elevation is $\sim 1500 \text{ m}$) and at a depth reaching 150 m approximately 2 km downstream from the summit (where surface elevations are $\sim 1200 \text{ m}$). These depths are similar to the depth of the LIA-signal within the GRIP borehole, indicating a comparable downward movement of the signal over time. The product of the mean annual accumulation rate of 0.23 m yr^{-1} at GRIP (Dahl-Jensen et al., 1998, endnote no. 11) and of $0.15\text{-}0.20 \text{ m yr}^{-1}$ in the vicinity of White Glacier (Koerner, 1979), when multiplied by 150 years (the approximate time interval since the culmination of the LIA in the CHA), cannot explain the measured LIA signal depths of 100-150 m at these sites. This is because the accumulation rates at these sites are less than the diffusive downward propagation rate. The downward propagation rate of a thermal anomaly maximum/minimum by diffusion alone is related to the period of the climate signal and can be calculated as per the equation given in Paterson (1994, pp. 206-207). For a signal with a period of 100 years, the downward diffusion rate is $\sim 2 \text{ m yr}^{-1}$; for a signal with a period of 500 years, the downward diffusion rate is $\sim 0.9 \text{ m yr}^{-1}$; for a signal with a period of 1000 years, the downward diffusion rate is $\sim 0.6 \text{ m yr}^{-1}$. An LIA signal depth of 100-150 m implies a downward propagation rate of $\sim 1 \text{ m yr}^{-1}$, commensurate with a climate event with a period of ~ 500 years.

No negative LIA-related ice temperature anomaly is detected within the accumulation zone of Laika Glacier, however. Since the isotope record from nearby Prince of Wales ice cap has a clear LIA signal (*personal communication* Martin Sharp, 2009), the impact of the LIA event in the vicinity of Laika Glacier almost certainly was not negligible. Likely, given that the glacier is less than 100 m thick, the LIA-signal has by now reached the glacier bed or diffused into the substrate beneath (aided in part by the high snowfall accumulation rates in this part of the CHA – Koerner, 1979; 1989). Another possible reason for the lack of

LIA signal in Laika Glacier is that, being located at very low elevations, latent heat released by the refreezing of percolated meltwater in the summer served to erase the negative ice temperature anomaly before it was able to propagate to a depth below the zone where such surface effects are important.

3.1.3 Reasons for Discrepancies in the Amplitudes of LIA-related Ice Temperature Anomalies

The actual amplitudes of the LIA-related ice temperature anomalies within the various boreholes differ significantly. Here, reasons for these discrepancies as proposed and discussed in the literature are reviewed. Two additional causes are proposed in sections 3.1.3.5 and 3.1.3.6.

3.1.3.1 ATMOSPHERIC CIRCULATION PATTERNS

As discussed by Dahl-Jensen et al. (1998), ice temperature anomalies measured within the DYE3 borehole are 1.5 times the amplitude of the anomalies measured within the GRIP borehole, which is located nearly 1000 km to north (see Table 3.1 and Figure 3.2). It has been proposed that the reason for this discrepancy is the source of the air masses affecting the two sites. The southern DYE3 location is located in an area of high atmospheric variability and is under the influence of maritime air masses from the North Atlantic (Dahl-Jensen et al., 1998). The GRIP site, on the other hand, is located at summit of the GIS, near the centre of the climatological “Greenland High”. It is partially influenced by air masses from northeastern Canada and Baffin Bay (Dahl-Jensen et al., 1998). Different air masses may contain different amplitude SAT anomalies for a given climate event if those air masses interact differently with the land/ocean surface beneath. Additionally, atmospheric modes of spatio-temporal variability, such as the North Atlantic Oscillation (NAO), have been proposed and investigated as a potential cause of the “subdued” central, summit Greenland LIA isotopic signal with respect to signals derived in northern Europe and Iceland (e.g. Barlow, 2001). The NAO may be a factor because it can lead to opposing temperature excursions between Greenland and northern Europe.

3.1.3.2 SURFACE AND BASAL PROCESSES

Glacier surface and basal processes can impact the recording and preservation of an SAT-derived ice temperature anomaly. For example, it has been determined that latent heating due to surface refreezing of summer meltwater has impacted the preservation of the LIA temperature anomaly within the Devon Ice Cap summit boreholes (Paterson and Clarke, 1978). Because of present-day meltwater percolation and refreezing, the measured LIA temperature anomaly in these boreholes is seen only as a negative inflection in the generally positive deviation from modeled equilibrium temperatures for present-day surface temperatures (see Table 3.1).

Surface processes can impact the LIA temperature signal where it has not penetrated the ice mass to any great depth. For example, ice cap summits with very low accumulation rates and/or negative vertical velocities will contain shallower LIA signals (e.g. ~50 m depth, Devon Ice Cap summit boreholes, Table 4.1), while summits with greater accumulation rates and/or mass flux divergences will contain deeper LIA signals (e.g. ~200 m depth, DYE3, Table 3.1). Where the signal is located at shallow enough depths, present-day surface summer melt, percolation, and refreezing can serve to erode the negative temperature anomaly, which was likely initiated during a period of perhaps greater surface accumulation and reduced or no summer melt. In these areas, oxygen-isotope ratio (δ) depth-profiles will better resolve the LIA temperature anomaly than will direct borehole temperature measurements (Paterson and Clarke, 1978; Paterson et al., 1977).

Wind scouring is another surface process which can impact LIA ice temperature records, where these have not penetrated the ice mass to any great depth. Removal of winter snow explains why the annual mean δ depth-profile in an ice core drilled at an ice divide of the Agassiz Ice Cap (~81°N, 73°W) is less negative than it is at an adjacent location ~1 km downslope (Fisher et al., 1983). For the same reason, wind scouring can likely also modify the recording and preservation of associated ice temperature anomalies, by removing layers of low-temperature snow/ice as they are deposited.

Basal processes will affect the amplitudes of LIA temperature anomalies where they have penetrated an ice mass to the glacier bed and into the substrate beneath. For example, no LIA-related negative ice temperature anomaly is found within the measured thermal profile of the Laika ice cap and Laika Glacier summit (Blatter and Kappenberger, 1988). Laika Glacier is a very small, thin glacier, less than 10 km long and less than 100 m thick. Assuming LIA-related ice temperature anomalies found in CHA glaciers generally reach a depth similar to the LIA-signal found within White Glacier (~100-150 m depth – Blatter, 1987; see also Table 4.1), this would place the signal at or below the bed of Laika Glacier. Even if the glacier were 50% thicker during the LIA (150 m; e.g. as proposed by Blatter and Hutter, 1991), the ice temperature anomaly today would still be located at or near the bed, where it would be subject to erosion by frictional heating due to ice deformation and basal sliding where the ice has reached the pressure melting point (PMP). Basal melt/freeze processes may also have an impact upon thermal anomalies near the ice-bed interface.

In general, where surface and/or basal processes are concerned, one can expect that glaciers with the following combination of thickness and flow characteristics will best preserve LIA-related negative ice temperature anomalies: 1) glaciers with accumulation rates and/or advective-diffusive rates great enough to have removed the LIA-related ice-temperature anomaly to a depth below the zone of influence by present-day surface processes (associated with the post-LIA rise in regional ELAs – Wolken et al., 2008a,b); and 2) glaciers that are thick enough so that the LIA-signal will not yet be near/at/below the glacier bed where they can be

significantly influenced by basal frictional heating and/or glacier-permafrost interactions. White Glacier (Blatter, 1987) is an example of a glacier with this combination of characteristics.

3.1.3.3 THERMODYNAMIC PROPERTIES

The thermodynamic properties of an ice mass and its bed (e.g. the density, heat capacity, conductivity and diffusivity of the medium) can also impact borehole thermal profiles and anomalies contained therein. This is especially true where these properties vary with time, such as occurs in the firn compaction layer where surface snow transitions into ice (e.g. Paterson and Clarke, 1978). Different firn compaction rates (and the strain heating produced by this process) might be another important cause for observed differences in LIA-related borehole temperature anomalies. The heat capacity of the subglacial substrate, where it contains permafrost, can also be variable with depth and time. Where the meltwater fraction in the layer is variable, the heat capacity of the subglacial permafrost layer can change by three orders of magnitude (e.g. Bauder et al., 2005). The conductivity of the layer will decrease with increasing meltwater fraction, because the conductivity of ice is greater than the conductivity of water (Johansen et al., 1995). Basal heat capacity and heat conductivity can be important to the evolution of thermal anomalies, especially as they approach the glacier bed.

3.1.3.4 GEOTHERMAL HEAT FLUX

The geothermal heat flux (sometimes called the “heat flow density”) within the subglacial substrate, and its space-time variations, can also impact the measured thermal profile of an ice mass (e.g. Dahl-Jensen et al., 1998). Measured geothermal heat fluxes for Northern Ellesmere Island in the CHA are $\sim 0.06 \text{ W m}^{-2}$ (Beltrami and Taylor, 1995), while those for the GRIP borehole were determined to be $\sim 0.05 \text{ W m}^{-2}$ (Dahl-Jensen et al., 1998). Values for Devon Island geothermal heat fluxes range between 0.04 and 0.05 W m^{-2} (Paterson and Clarke, 1978), whereas measured minimum heat flow densities for the coast of Greenland can be as low as 0.036 to 0.043 W m^{-2} (Sass et al., 1972). Pronounced topography intensifies the geothermal heat flux in deep valleys, by up to 100% in some cases, and attenuates this flux on mountains (van der Veen et al., 2007). Additionally, the availability of this geothermal heat source at the base of a glacier may be reduced if temperature inversions develop within the substrate (e.g. Dyke, 1993). Variations in this subglacial heat flux may cause site-to-site differences in the amplitudes of internal ice temperature anomalies.

3.1.3.5 ICE-ATMOSPHERE FEEDBACKS

SAT anomalies can be locally and/or regionally amplified by positive ice-atmosphere feedbacks, another potential reason for some of the observed differences in borehole temperature anomalies. Two well-known positive ice-

atmosphere feedbacks are the snow/ice-albedo feedback and the mass balance – elevation feedback. The snow/ice-albedo feedback is triggered by radiative, SAT, or snowfall perturbations. In general, increases in SATs lead to increased snow and ice melt, a reduction in snow and ice area and thickness, a reduction in local and area-averaged surface albedo, an increase in the surface absorption of incoming solar radiation, and a further increase in SATs (and vice versa for decreases in SATs). The mass balance – elevation feedback operates primarily as follows: decreases in surface elevation cause an increase in surface temperature and surface melt rates (where atmospheric lapse rates are negative) and a decrease in orographically-enhanced precipitation, leading to further decreases in surface elevation. The opposite occurs for increases in surface elevation. .

While the snow/ice-albedo feedback is widely recognized as the more important of the two feedbacks in terms of global climate and ice sheet evolution (e.g. Abe-Ouchi et al., 2007), it is mainly the mass balance – elevation feedback that has received recognition for its impact upon ice core and ice borehole derived SAT-histories. For example, it has been proposed that changes in surface elevation, related to mass balance – elevation feedbacks involving isostatic depression and uplift of the Earth's crust, contribute up to 40% of the total climatic signal recorded in ice core melt-layers (Koerner and Fisher, 1990). Because of its potential importance, time-dependent isostatic depression/uplift and surface accumulation rates were incorporated into the modeling experiments of Johnsen et al. (1995), which sought to calibrate GRIP ice core δ -profiles in terms of measured borehole ice temperature anomalies.

The snow/ice-albedo feedback, on the other hand, is generally ignored, but could potentially have important implications for local SAT-anomaly histories as well. While the magnitude of this feedback is small at the centres of large ice sheets (e.g. the GIS), where changes in surface albedo in response to radiative/SAT/precipitation perturbations are small, it can be large near ice sheet margins in the vicinity of outlet and valley glaciers (e.g. White Glacier) (Pritchard et al., 2008). Near the lateral margins of outlet glaciers, the feedback can amplify mean annual area-averaged SAT changes by a factor of up to 2, depending on the perturbation (see Chapter 2). Furthermore, CHA ice masses, being closer to sea level and being situated in an archipelago, experience amplified SAT-anomalies via the sea ice – albedo feedback. For example, recent modeling studies have found that temperature gains in the North Polar region are $1.5\times$ to $4.5\times$ the present increases in global mean temperature (Holland and Bitz, 2003). SAT-anomaly amplification by the snow/ice-albedo feedback might therefore partially explain the discrepancies in the LIA borehole signals measured at the GRIP and White Glacier sites (which otherwise have similarly low accumulation rates, negative vertical velocities, and vertical diffusion rates, placing the LIA signal at similar depths within their profiles). It might also partially explain the “subdued” Greenland LIA signal in the vicinity of the GRIP/GISP sites, providing an alternative explanation to the NAO-related one proposed by Barlow (2001). Thus, the extent to which regional differences in LIA cooling (attributed to

differences in the snow/ice-albedo feedback amplification of a regionally coherent forcing – e.g. from decreased incoming solar radiation) exacerbates the problem of deducing and interpreting historical SAT changes from ice borehole temperature profiles is something which requires further examination.

3.1.3.6 PRESENCE/ABSENCE OF ADJACENT THERMAL ANOMALIES OF THE OPPOSITE SIGN

The presence/absence of adjacent thermal anomalies of opposite sign (which may also themselves have once been amplified/damped by ice-atmosphere feedbacks) within a borehole temperature depth-profile might also influence the amplitude of an LIA-related ice temperature anomaly. Older, positive anomalies located below and younger, positive anomalies located above the LIA-related ice temperature anomaly can serve to erode the negative anomaly via vertical thermal (or heat) diffusion.

Thick ice sheets with low mean annual surface accumulation rates will be composed of more annual layers and contain a longer SAT history than will thin ice sheets with high surface accumulation rates. For example, Dahl-Jensen et al. (1998) were able to derive a 50,000-year-long temperature history from the ~3000 m deep GRIP borehole (north-central GIS), but only a 7,000-year-long history from the ~2000 m deep DYE3 borehole (south-central GIS, where the surface accumulation rate is double – Dahl-Jensen et al., 1998, endnote no. 11). CHA ice caps and glaciers, whose thicknesses can locally reach 1000 m but which are generally less than or equal to 500 m thick, can contain temperature histories up to 10,000 years long, but histories spanning 5000 years and less, encompassing only the latter part of the Holocene, are more common (e.g. the Devon Ice Cap summit core temperature histories, Paterson and Clarke, 1978). Thus, the Holocene Climatic Optimum (CO) and Medieval Warm Period (MWP) climate events, periods characterized by positive SAT anomalies prior to the LIA, are detected within the GRIP borehole (Dahl-Jensen et al., 1998) but not within the White Glacier summit boreholes (Blatter, 1987). The presence of these positive temperature anomalies within the GRIP borehole may also partially explain why the LIA signal is weaker within the GRIP thermal depth-profile than it is within the White Glacier borehole temperature profiles.

Dahl-Jensen et al. (1998) implicitly consider the impact of this process, because the 1D ice temperature model used in inverting the GRIP borehole temperatures in order to obtain a history of past SAT-anomalies contains a diffusive as well as an advective term. Its implications, however, are only briefly mentioned in reference to the Younger Dryas climate event, which is not resolved in their GRIP-recovered SAT history.

3.1.4 White Glacier (CHA) versus GRIP (GIS)

The GRIP and the White Glacier summit boreholes have LIA-related temperature anomalies which are located at similar depths within their thermal profiles, indicating that these sites have similar combinations of accumulation rate, diffusion rate, and mass flux divergence. Both sites experience low annual accumulation ($\sim 0.2 \text{ m yr}^{-1}$; Dahl-Jensen et al., 1998, endnote no. 11; Koerner, 1979). The GRIP borehole, located at an elevation of 3200 m a.s.l., sits near the centre of the climatological Greenland High. It receives only limited moisture from Baffin Bay and northeastern Canada (Dahl-Jensen et al., 1998). White Glacier (with a summit elevation near 1800 m a.s.l.) is also situated in an area of minimum annual accumulation (Koerner, 1979). It is located in a trough between the accumulation maxima associated with Baffin Bay and Arctic Ocean moisture sources (Koerner, 1979).

Present-day mean annual SATs at White Glacier are $\sim -15.2^\circ\text{C}$ (e.g. Colour Lake – Doran et al., 1996), while at GRIP they are -31.7°C (Dahl-Jensen et al., 1998). The temperature difference between the two sites, divided by their elevation difference, gives a lapse rate $\Gamma = -16.5/2000 = -0.008^\circ\text{C m}^{-1}$, or -8°C km^{-1} , a value which lies between $\Gamma = -6^\circ\text{C km}^{-1}$ (the environmental lapse rate) and $\Gamma = -10^\circ\text{C km}^{-1}$ (the dry adiabatic lapse rate of the atmosphere), not unreasonable for such semi-arid areas. The two sites, therefore, also have similar present-day sea-level equivalent SATs.

In spite of the climatological similarities between the two sites, however, the amplitude of the LIA-signal in the White Glacier thermal depth-profile is much greater than the amplitude of the signal measured within the GRIP borehole. White Glacier's accumulation zone shows an englacial temperature minimum of $\sim -15.5^\circ\text{C}$ (Blatter, 1987), 0.3°C colder than the present-day mean annual SAT. This is $\sim 3\times$ the measured LIA-related deviation from the equilibrium temperature profile within the GRIP borehole profile (which has an amplitude of $\leq -0.1^\circ\text{C}$ – Johnsen et al, 1995). Note that the actual magnitude of the White Glacier englacial temperature anomaly could be greater than 0.3°C , since equilibrium ice temperatures at depths of 100-150m will be warmer than the present-day mean annual SAT.

Being located at depths of 100-150 m, however, means that neither the White Glacier nor the GRIP LIA-related anomalies are subject to interference by present-day surface or basal processes. Furthermore, geothermal heating is also not a likely explanation for the observed amplitude differences because White Glacier, the site with the higher geothermal heat flux (see section 3.1.3.4), nevertheless has the higher amplitude negative temperature LIA signal. The two remaining possible causes, therefore, for the observed differences in the measured borehole LIA temperature anomalies for these two sites are: 1) ice-atmosphere feedback amplifications of LIA SAT-anomalies; and/or 2) the presence/absence of older, positive thermal anomalies within the borehole temperature profile, which

might serve to partially erode the negative LIA temperature anomaly through heat diffusion.

The hypothesis that these two factors might have played a key role in the observed differences in the amplitudes of the GRIP and White Glacier LIA-signals is further supported by the following points. Firstly, Blatter (1987) was able to model the White Glacier LIA-related englacial temperature minimum using an equilibrium temperature model and an 1880 A.D. SAT of -16.4°C . Differencing this temperature with the present-day mean annual SAT of -15.2°C yields an LIA SAT-anomaly of $\sim -1.2^{\circ}\text{C}$ for this site (a value consistent with those determined via other climate proxies for the CHA – e.g. Overpeck et al., 1997; Wolken et al., 2008b). The associated LIA SAT-anomalies at the GRIP site, on the other hand, derived from the model-inverted ice temperature anomalies, are -0.5°C and -0.7°C . So not only is the White Glacier LIA ice temperature anomaly $\sim 3\times$ greater than that of GRIP, the derived LIA SAT-anomaly at White Glacier is also greater (by $\sim 2\times$) than the calculated LIA SAT-anomaly at the GRIP site. Secondly, the White Glacier LIA-related ice temperature anomaly ($\sim -0.3^{\circ}\text{C}$) is 25% of its associated SAT anomaly ($\sim -1.2^{\circ}\text{C}$). The GRIP ice temperature anomaly ($\leq -0.1^{\circ}\text{C}$), on the other hand, is $\sim 10\%$ of its associated SAT anomalies (-0.5°C , -0.7°C). There therefore appears to have been greater thermal erosion of the borehole signal at the GRIP site than at the White Glacier site over the last ~ 150 years.

The difference in amplitude of the borehole LIA temperature anomaly between the White Glacier and GRIP sites, therefore, appears to be due to the two factors proposed above. Because White Glacier LIA SAT-anomalies were $\sim 2\times$ GRIP LIA SAT anomalies, some local amplification of SATs in that part of the CHA is indicated. Furthermore, because the GRIP borehole LIA ice temperature anomaly constitutes a smaller percentage of the original SAT anomaly at that site, and because the GRIP borehole, being deeper, contains signals associated with the CO and the MWP (Dahl-Jensen et al., 1998), where White Glacier does not (Blatter, 1987), it is possible that enhanced thermal erosion of the negative LIA ice temperature anomaly occurred at GRIP. The implications of these two factors for White Glacier and GRIP are explored in greater depth in the following two sections of this chapter.

3.2 AMPLIFICATION OF SAT ANOMALIES BY THE SNOW/ICE-ALBEDO FEEDBACK

As discussed in section 3.1.3.5, positive ice-atmosphere feedbacks can amplify local to regional scale SAT anomalies to various extents. This can then lead to differences in the amplitudes of associated ice temperature anomalies measured within boreholes at different locations in the CHA and Greenland ice caps. Although the impact of the mass balance – elevation feedback has been considered by others (e.g. Dahl-Jensen et al., 1998), the implications of the

snow/ice-albedo feedback for the interpretation of recovered SAT histories is rarely mentioned in the literature, possibly because the magnitude of this feedback has not been well constrained, especially for terrestrial snow/ice masses, until now (cf. Chapter 2). Nevertheless, an attempt is made here to assess the potential impact of the snow/ice-albedo feedback upon the amplitudes of borehole ice temperature anomalies related to the LIA.

The snow/ice-albedo feedback amplifications described in Chapter 2, computed via model climate perturbation experiments, are first briefly summarized. These are then used in a set of simple, but informative, calculations for White Glacier in the CHA and for the GRIP site in Greenland, to examine whether such SAT-anomaly amplifications can account for a significant proportion of the observed differences in their LIA-related borehole ice temperature anomalies and associated LIA SAT-anomalies (assuming a common background regional SAT anomaly).

3.2.1 *The Snow/Ice-Albedo Feedback: a Review*

As described in section 3.1.3.5, the snow/ice-albedo feedback can be triggered by radiative, SAT, or snowfall (i.e. surface albedo) perturbations. In general, increases in SAT lead to increased snow and ice melt, a reduction in snow and ice area and thickness, a reduction in local and area-averaged surface albedo, an increase in the surface absorption of incoming solar radiation, and a further increase in overlying SATs (and vice versa for decreases in SATs).

Perturbation experiments with an energy – mass balance model for a representative CHA glacier catchment (see Chapter 2, sections 2.6 and 2.7) indicated that positive perturbations to the incoming solar radiation at the top of the atmosphere resulted in the largest amplifications of the mean annual area-averaged atmospheric and surface temperatures by the snow/ice-albedo feedback. Amplifications or gains in mean annual area-averaged *air* temperatures (vertically averaged over the troposphere) ranged from 1.2× to 1.6× for all experiments, which included positive and negative perturbations to the shortwave (SW) and longwave (LW) radiation budget, under both calm and windy conditions, and for both a glaciated and non-glaciated valley. Amplifications or gains in mean annual area-averaged *surface* temperatures ranged from 1.2× to 1.9× for all experiments.

One of the generally accepted causes of the LIA was a reduction in solar output (i.e. the Maunder Minimum, $\sim -3.5 \text{ W m}^{-2}$; National Research Council, 1994). For negative SW perturbations, amplifications of mean annual area-averaged surface temperature changes ranged from 1.2× to 1.4× what would have been realized without the terrestrial snow/ice-albedo feedback in effect within the glacier catchment (see Chapter 2, sections 2.6 and 2.7).

The magnitude of the temperature amplification by the snow/ice-albedo feedback was also found to vary spatially (e.g. Chapter 2, Figures 2.7 and 2.8). For

example, the feedback cannot operate efficiently at the centre of large ice sheets where surface albedo changes in response to SAT changes are small. The feedback will have a larger amplifying effect near the margins of ice sheets, where outlet or valley glaciers are located. Near glacier margins and near the mean summer position of the snow line on the glacier, melt-back or growth of the ice or snow mass exposes or covers low albedo ground or bare ice/firn surfaces, considerably altering the area-averaged surface albedo and the local surface energy balance, and triggering a stronger snow/ice-albedo feedback response.

3.2.2 Calculations of SAT-Anomaly Amplifications by the Snow/Ice Albedo Feedback

As discussed above, the magnitude of the snow/ice-albedo feedback at the GRIP site is likely to be negligible. The SAT anomalies of -0.5K and -0.7K , the two minima for the LIA period recovered by inverting the GRIP borehole temperatures (Dahl-Jensen et al., 1998), may therefore be representative of a general, homogeneous, unmodified LIA SAT anomaly for the CHA - Greenland region north of 70°N , prior to local amplification by feedbacks. If this is true, then feedback-amplification could account for a significant percentage, or all, of the inferred differences in LIA SAT-anomalies from site-to-site within this region.

Inferred White Glacier LIA SAT-anomalies (-1.2°C) were $\sim 2\times$ GRIP LIA SAT anomalies (-0.5°C , -0.7°C), indicating some local amplification of SATs in that part of the CHA. SAT-anomalies in the vicinity of White Glacier, an outlet valley glacier, would have experienced some degree of amplification by the terrestrial snow/ice-albedo feedback, with surface temperature gains ranging from $1.2\times$ to $1.4\times$ in the case of negative SW perturbations of similar magnitude to those inferred for the LIA (Chapter 2). Such snow/ice-albedo feedback gains would have increased the original LIA SAT-anomalies determined at the GRIP site from -0.5°C to $\sim -0.65^\circ\text{C}$, and from -0.7°C to $\sim -0.91^\circ\text{C}$ at White Glacier, accounting for a significant fraction, but not all, of the LIA SAT-anomaly difference between the two sites.

SAT anomalies at the White Glacier site may also have been further amplified by the sea ice – albedo feedback, because the glacier is located in a valley on an island in the Canadian Arctic Archipelago (CAA). Holland and Bitz (2003) estimate sea ice – albedo related gains in mean polar temperatures of $1.5\times$ to $4.5\times$ under the present-day warming, while Curry et al. (2001) estimated a sea ice – albedo feedback gain of $1.5\times$ for a negative LW radiative perturbation, for their albedo parameterization.

If White Glacier LIA SAT-anomalies were further amplified by sea ice – albedo feedback gains of $\sim 1.5\times$ (Curry et al., 2001; Holland and Bitz, 2003), the SAT-anomalies in that part of the CHA would have then been in the range of -0.9°C to -1.47°C , with an average value of -1.2°C . The combined terrestrial snow/ice and sea ice – albedo feedback is therefore capable of accounting for the entire

difference between the White Glacier and GRIP inferred LIA SAT-anomalies. It is possible that the noted “subdued” Greenland summit LIA signal (e.g. Barlow, 2001; Fischer et al., 1998) can be explained by the ineffectiveness of the snow/ice-albedo feedback in this location. That is, it is not so much that the Greenland summit signal has been “subdued”, but rather that the signals of other lower-lying areas (e.g. the CHA, northern Greenland, Norway, etc.) have been amplified to a greater extent by ice-atmosphere feedbacks such as the snow/ice-albedo feedback.

The influence of the snow/ice-albedo feedback demonstrated above is comparable in magnitude to the impact of the mass balance – elevation feedback upon a climate signal at an ice borehole site. Koerner and Fisher (1990) suggest that isostatic recovery over the past 8000 to 9000 years might have contributed to ~40% of the ~2.5°C cooling detected within the Agassiz ice cap ice core between the CO and the LIA. Here, it has been shown that the combined terrestrial snow/ice and sea ice – albedo feedback is able to account for ~50% of the ~1.2°C LIA-related cooling (w.r.t. present-day temperatures) at the White Glacier summit. That is, initial SAT-anomalies of –0.5°C and –0.7°C can readily be amplified by ~2× to ~–1.2°C by the snow/ice-albedo feedback, where the initial SAT-anomalies are assumed to be the result of a decrease in incoming SW radiation at the top of the atmosphere.

It is worth noting that the 40% attributed to isostatic recovery by Koerner and Fisher (1990) may be an exaggerated value, given the distance of the Agassiz core site from the axis of isostatic rebound described in England et al. (2006). From the isobase map of England et al. (2006), the Agassiz core site has a rebound value of ~100m a.s.l., based on the 8.5 14C ka BP shoreline. Using a standard environmental lapse rate of ~–6°C/km, a 100m rise would lead to a 0.6°C cooling, which would represent ~24% of an overall 2.5°C cooling. However, atmospheric lapse rates over ice caps and glaciers are often less than typical environmental values. Atmospheric temperature inversions often prevail from late winter to early summer, balancing the normal lapse rates which prevail during the other half of the year. This can lead to neutral lapse rates in mean annual surface temperatures with height (e.g. John Evans Glacier, described in Chapters 2 and 4, where very little difference in mean annual air temperature is observed between its lower, middle and upper weather stations, which span an elevation range of ~1000m). As such, the percentage described above represents the absolute maximum fraction of the total cooling attributable to isostatic rebound. Isostatic recovery likely accounts for considerably less than 24% of the 2.5°C cooling inferred for the Agassiz ice cap. The White Glacier and Agassiz Ice Cap sites have similar rebound values (England et al. 2006). It is possible that isostatic recovery also played a role in the apparent LIA SAT anomaly in the White Glacier area, but this has been neglected in this study.

3.3 THE PRESERVATION OF ICE TEMPERATURE ANOMALIES

The GRIP borehole LIA ice temperature anomaly constitutes a smaller percentage of the original GRIP SAT anomaly (~10%) than does the White Glacier ice temperature anomaly of its inferred LIA SAT-anomaly (~25%) (see section 4.1.4). Because the GRIP borehole, being deeper, contains signals associated with the CO and the MWP (Dahl-Jensen et al., 1998), where White Glacier does not (Blatter, 1987), it is possible that the negative GRIP LIA ice temperature anomaly was further eroded over time via thermal diffusion processes from these older, positive anomalies. The presence of past and future ice temperature anomalies can affect the “preservation” of a given anomaly within the ice for the reason that, while the vertical velocity and temperature advection are directed downwards at the summit of an ice cap, thermal diffusion acts both upwards and downwards. Thus, while air temperature anomalies are advected sequentially downwards into the ice from the surface, heat diffusing upwards from an older positive ice temperature anomaly would act to modify, or perhaps even erase, a subsequent negative anomaly. For this reason, a relatively short-lived low-amplitude negative air temperature perturbation (such as the LIA), following a longer-term larger-amplitude positive perturbation (such as the CO/MWP), may not be recorded as clearly within the ice as it would be without the influence of the earlier event(s). In this section, the influence of adjacent, positive, ice temperature anomalies upon the preservation of the negative LIA-related anomaly “measured” within a hypothetical 3000 m deep borehole is investigated using a 1-Dimensional (1D) model, similar to that used by Dahl-Jensen et al. (1998) and Blatter (1987).

3.3.1 *Model*

Measured englacial temperatures within the GRIP and White Glacier summit boreholes are well below the pressure melting point (PMP – Dahl-Jensen et al., 1998; Blatter, 1987). Predominantly cold ice masses, such as White Glacier (Blatter, 1987), may reach the PMP near the bed in their ablation zones, but generally not in their accumulation zones (Hutter, 1993). The vertical temperature profiles of cold and predominantly cold ice masses, at any horizontal location, can be represented in 1D by:

$$\frac{\partial T}{\partial t} = -w \frac{\partial T}{\partial z} + k \frac{\partial^2 T}{\partial z^2} + \Phi_f, \quad (1)$$

where T is ice temperature, t is time, z is the vertical coordinate, w is the vertical ice velocity, k is the thermal diffusivity of the ice (assumed here to be constant and equal to $1.15 \times 10^{-6} \text{ m}^2 \text{ s}^{-1}$), and Φ_f is the internal frictional heating term due to the deformation of the ice (calculated as per Paterson, 1994, pp225, 228).

At the surface, in the accumulation zone, where annual snow accumulations are incorporated into the ice and where $w < 0$, the boundary condition (BC) for (1) can

be taken as $T_{\text{sfc}}=T_{\text{atm}}$, where T_{sfc} and T_{atm} are the mean annual ice surface and atmospheric temperatures, respectively (e.g. Hutter, 1993). At the bed, where basal temperatures are below the PMP, the equilibrium basal BC is taken to be $(\partial T/\partial z)_{\text{bed}}=-G/K$, where G is the geothermal heat flux and K is the thermal conductivity of the ice (e.g. Paterson, 1994, p226). Typically, $K=2.16 \text{ W m}^{-1} \text{ K}^{-1}$ for ice (Paterson, 1994) and $G\sim 0.05\text{-}0.06 \text{ W m}^{-2}$ for the Canadian High Arctic and Greenland (Beltrami and Taylor, 1995; Dahl-Jensen et al., 1998). The time-dependent basal BC will depend primarily upon the conductivity and heat capacity (i.e. the thermal diffusivity) of the bed, and the depth at which all climate-related thermal anomalies are damped out. Dahl-Jensen et al. (1998) allowed for 3 km of bedrock beneath the 1D model GRIP borehole in their experiments. Here, because “the property of the earth is to filter high-frequency thermal signals and to integrate the effects of multiple smaller events” (Taylor, 1991), and because the focus of this study primarily concerns the upper 1000 m of a hypothetical ice mass, the bed is assumed to be more or less at equilibrium (i.e. to possess an approximately linear thermal depth-gradient), and the equilibrium basal BC is used. This is also possible here as it is assumed that G is known in the experiments described below, unlike in the Monte Carlo inversion modeling of Dahl-Jensen et al. (1998) where G was treated as an unknown and needed to be determined. Where basal temperatures reach the PMP, the basal BC is fixed at $T_{\text{bed}}=T_{\text{PMP}}$ (Hutter, 1993). Since ice cannot be warmer than the PMP, all additional heating is then assumed to be lost to basal ice melt (e.g. Hutter, 1993), or to the dissipation of subglacial permafrost (e.g. Dyke, 1993).

Latent heating due to surface/basal refreezing is assumed here, for the sake of simplicity, to be negligible in the determination of the internal thermal distributions of the accumulation zones of cold and predominantly cold polythermal High Arctic ice masses. This is not a valid assumption for all ice caps (e.g. Devon Ice Cap, Paterson and Clarke, 1978), but it is valid for the GRIP and White Glacier sites. Although the White Glacier summit is likely experiencing surface refreezing in its accumulation zone at the present day, it likely did not during the LIA (otherwise its englacial LIA-related negative temperature anomaly would have been reduced to an extent similar to that of Devon Ice Cap’s). Furthermore, its LIA-related ice temperature anomaly has reached a sufficient englacial depth, such that it is negligibly impacted by surface processes.

The 3000 m deep model borehole was divided into 100 vertical layers of 30 m each. The vertical ice velocity, representing the inverse of accumulation rates (in units of m yr^{-1}) at equilibrium, was prescribed. The equilibrium solution was obtained by inverting the tri-diagonal matrix for equation (1) for all ice levels (note: the equilibrium form of equation (1) can also be solved analytically – e.g. Hindmarsh, 1999). The time-dependent experiments used finite differences with an explicit forward time-integration (e.g. Blatter, 1987) using a 1-year time step.

3.3.2 Experiments

A series of numerical “summit borehole” experiments were performed to assess the extent to which disparities in the preservation of past air temperature anomalies may be due solely to presence/absence of adjacent thermal anomalies of the opposite sign. The extent to which an ice mass “preserves” a past air temperature anomaly within its temperature distribution is measured in terms of the amplitude of the resultant ice temperature anomaly. An ice temperature anomaly is defined here as the difference between the equilibrium temperature distribution of the ice (the modeled solution for $\partial T/\partial t=0$, under present-day mean annual air temperatures) and the modeled temperature distribution of the ice mass at the end of a time-dependent integration (i.e. at the present day).

Equilibrium solutions to (1) were obtained by using a surface BC of $T_{\text{atm}}=-32^{\circ}\text{C}$ at 3000 m elevation (which matches the present-day mean SAT at the GRIP site – Dahl-Jensen et al., 1998). This also corresponds well to the present-day mean sea-level $T_{\text{atm}}=-15^{\circ}\text{C}$ in the CHA (Phillips, 1990), if an environmental lapse rate of $-6^{\circ}\text{C km}^{-1}$ is assumed, indicating some regional uniformity in mean annual SATs in the Greenland-CHA part of the Arctic.

Time dependent solutions in all experiments were determined using the air temperature anomaly time series inferred by Dahl-Jensen et al. (1998) from the GRIP borehole (Figure 3.3). This time series comprises the period leading up to and including the Last Glacial Maximum (LGM: where the average air temperature anomaly for the period 125 ka to 25 ka Before Present (BP) is $\sim(-23^{\circ}\text{C}-0^{\circ}\text{C})/2=-11.5^{\circ}\text{C}$), the Holocene Climatic Optimum (CO: $+2.5^{\circ}\text{C}$ from 8 to 4.5 ka BP), the Medieval Warm Period (MWP: maximum $+1^{\circ}\text{C}$ at 1000 AD), the LIA (minima of -0.5°C at 1550 AD and -0.7°C at 1850 AD), and the recent warming to current (i.e. 2000 A.D.) air temperatures (which includes a temperature maximum of $+0.5^{\circ}\text{C}$ at 1930 AD).

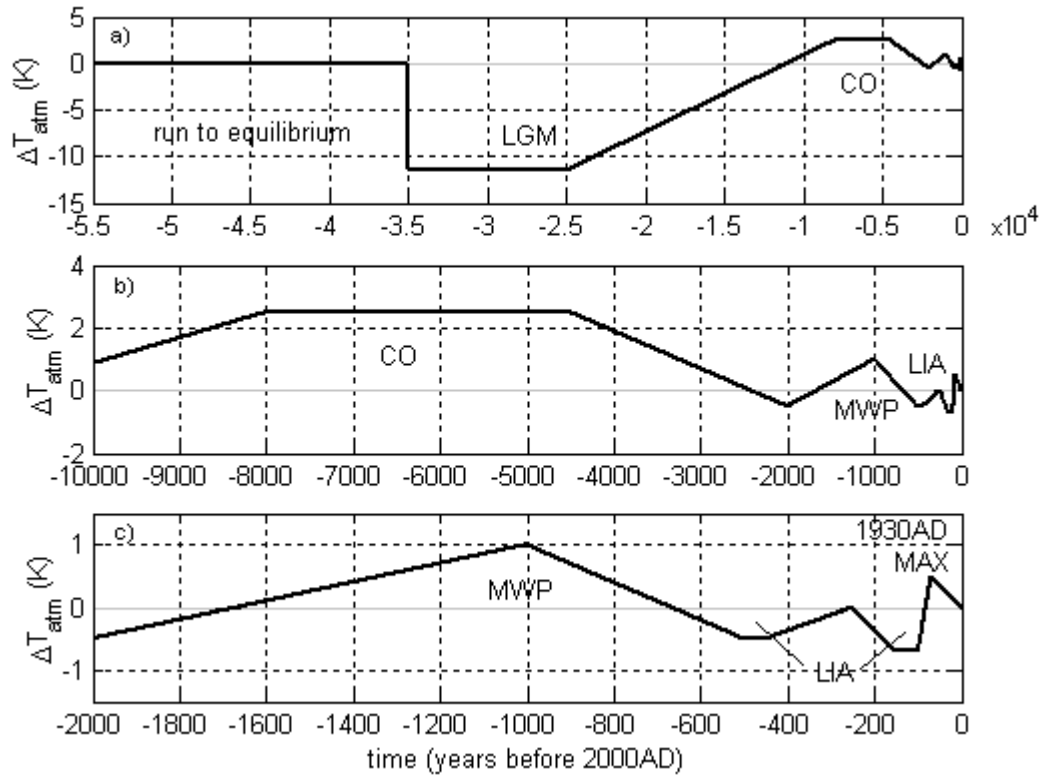


Figure 3.3. a) Air temperature anomaly time series used in time integration experiments (post-LGM time series up to 2000 A.D. after Dahl-Jensen et al., 1998); b) Zoomed in to last 10000 years; c) zoomed in to last 2000 years.

The 1D borehole temperatures were integrated forward in time from the LGM to the present day (i.e. 2000 A.D.). To illustrate that adjacent positive temperature anomalies have an impact upon negative temperature anomalies recorded within the ice, the modeled borehole temperatures were also recomputed omitting:

- 1) the CO and MWP air temperature anomalies;
- 2) the 1930 A.D. air temperature anomaly; and
- 3) both the CO/MWP and 1930 A.D. air temperature anomalies,

from the forcing time series.

In the experiments, the temperature profile of the hypothetical “ice sheet summit borehole” was simulated using mean surface accumulation rates of $0.05\text{--}0.1 \text{ m yr}^{-1}$ (i.e. $w = -0.05$ to -0.1 m yr^{-1}). Results close to the measured GRIP borehole temperatures can be reproduced with the model in this study by assuming $w = -0.05 \text{ m yr}^{-1}$ throughout the LGM and at the present day and by assuming an average $w = -0.11 \text{ m yr}^{-1}$ throughout most of the Holocene (8.5ka to 0.1ka BP). The equation for the downward diffusive propagation of thermal anomalies given in Paterson (1994, p206-207) indicates a rate of $\sim 0.06 \text{ m yr}^{-1}$ for signals with

periods of 100 ka, and rates of 0.2 to 0.6 m yr⁻¹ for signals with periods of 10 ka and 1 ka respectively. Since vertical temperature advection by downward vertical velocities in ice masses is commonly of the same order of magnitude as thermal diffusion rates, the values of w prescribed above were deemed appropriate for this study. A scale analysis of (1) indicates diffusive time scales of H^2/k and advective time scales of H/W , where H is the scale thickness of the ice and W is a characteristic velocity. For vertical ice velocities of order 10⁻¹ m yr⁻¹ (i.e. 10⁻⁹ m s⁻¹), ice diffusivities of 10⁻⁶ s⁻¹, and ice thicknesses of 10³ m, both the diffusive and advective time scales are 10¹² s (~100 ka). Additionally, since actual present-day accumulation rates for the summit of the Greenland Ice Sheet are given as 0.23 m yr⁻¹ (Dahl-Jensen et al., 1998, endnote no. 11), while thickening rates measure 0.016-0.021 m yr⁻¹ (Thomas et al, 2000), the present-day value of w prescribed above is also deemed an appropriate approximation. Note that with depth, vertical velocities in all experiments were decreased exponentially from the surface values discussed above to a value of zero at the glacier bed (because when the ice is frozen to its bed, $w = 0$ m yr⁻¹).

Temporal ice thickness changes at the Greenland summit of up to 200 m were considered by Dahl-Jensen et al. (1998) in their GRIP borehole temperature inversion. However, because such thickness changes constitute a $\leq 7\%$ variability in the overall ice thickness, these were neglected here.

3.3.3 Results

The equilibrium and time dependent solutions to (1) (Figure 3.4) are visually very similar to the equilibrium and measured GRIP borehole temperature profiles presented in Dahl-Jensen et al. (1998; their figure 1). A negative ice temperature anomaly corresponding to the LGM perturbation dominates the bottom of the temperature profile, and above this is located a positive temperature anomaly due to the CO/MWP perturbations. Above this (just below a small positive anomaly near the surface) there exists a negative ice temperature anomaly corresponding to the LIA (-0.06°C located at 120-150m depth). This compares well with the amplitude and depth of the LIA-related ice temperature anomaly within the GRIP borehole (Dahl-Jensen et al., 1998).

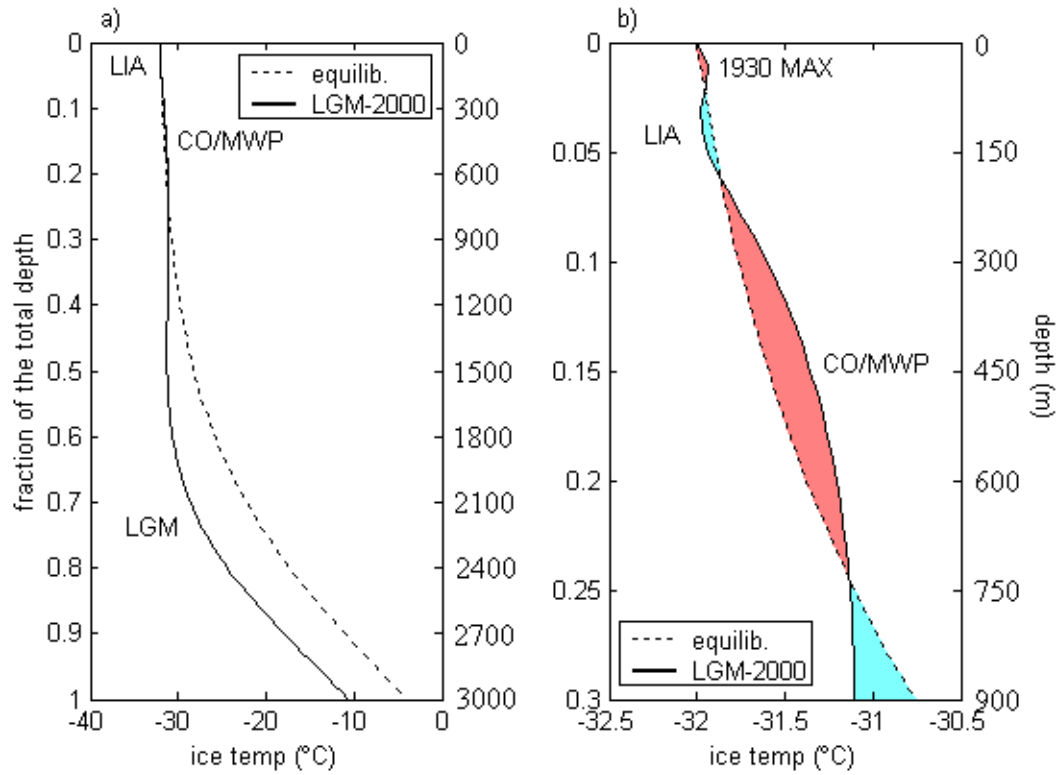


Figure 3.4. Equilibrium (dashed line) and time-dependent (solid line) temperature profiles for a hypothetical summit borehole: a) for the full depth of the borehole (3000m); b) for the top 30% (900m) of the borehole, where the temperature anomalies have been shaded (red for positive, blue for negative).

Results of experiments conducted to investigate the influence of adjacent positive thermal anomalies clearly show that these have an impact upon the amplitude and depth of the recorded negative LIA ice temperature anomaly (Figure 3.5).

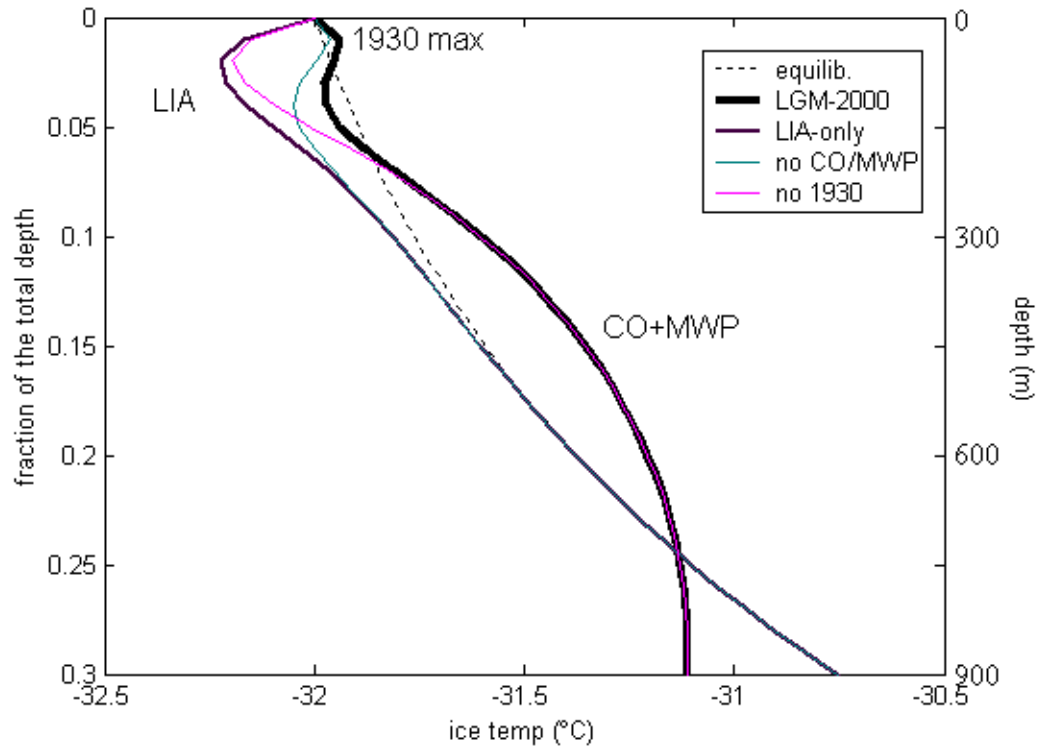


Figure 3.5. 1D borehole experiments showing the magnitude and depth of the LIA ice temperature anomaly, for: 1) the full historical SAT-anomaly time series (thick black line); 2) the SAT-anomaly time series without either the CO/MWP or 1930 air temperature maxima (thin black line); 3) the SAT-anomaly time series without the CO/MWP anomalies (blue line); and 4) the SAT-anomaly time series without the 1930 maximum (pink line). The dashed line represents the equilibrium temperature profile computed for the present-day mean SAT.

Without the CO/MWP anomaly, the LIA anomaly peaks at -0.13°C at 150m depth. In this case, it penetrates much deeper into the ice (spanning down to $\sim 450\text{m}$ depth) than it does in the presence of the CO/MWP anomaly (where the LIA anomaly only reaches to $\sim 215\text{m}$ depth – Figure 3.4). Without the 1930 A.D. anomaly, the LIA anomaly peaks at -0.23°C at 90m depth. Without either positive anomaly, the LIA anomaly peaks at -0.28°C at 90m depth.

Without the CO/MWP signal, the modeled LIA ice temperature anomaly in the hypothetical borehole is augmented from -0.06°C to -0.13°C . Without the CO/MWP signal, 19-26% of the original LIA SAT-anomalies of -0.5°C and -0.7°C are preserved. With the CO/MWP signal, only 9-12% of the original LIA SAT-anomalies are preserved. The presence of the CO/MWP signal reduces the LIA signal by half in these experiments, and might partially account for the observed difference in signal amplitudes of the GRIP and White Glacier borehole LIA-related ice temperature anomalies. Whilst it is probable that White Glacier experienced the CO/MWP SAT anomalies just as the GRIP site did, it is no longer evident in the glacier's ice temperature profiles because the related ice

temperature anomaly has propagated/diffused into the bed at White Glacier. However, regardless of how the CO/MWP anomaly came to be absent (either because the event did not occur or because it has propagated downward through the depth of the glacier into the substrate below and/or because it has diffused away into the larger LGM anomaly beneath), the model results show that a temperature profile in which this positive temperature anomaly is missing will have a stronger LIA-related signal. This is because the older CO/MWP signal, when present as a positive ice temperature anomaly located below the negative LIA anomaly, will serve to erode the LIA-signal via thermal diffusion.

In the model experiments, in addition to the proximity of thermal anomalies of opposite sign, it was found that the choice of w also strongly affected the “preservation” of a given temperature anomaly within the ice. Because w influences the rate of downward propagation or advection of ice temperature anomalies, it can be important to the amplitude of the signal. In the 1D experiments described above, the modeled ice temperature anomaly associated with the CO/MWP is $+0.25^{\circ}\text{C}$ located at 450m depth, while that associated with the LIA is -0.06°C located at 120-150m depth (Figure 3.4). For comparison, the amplitude and location of the CO anomaly in the GRIP borehole temperatures determined by Dahl-Jensen et al. (1998 - their Figure 1a) is $\sim +0.3^{\circ}\text{C}$ at 600m depth, while the GRIP LIA anomaly of $\leq -0.1^{\circ}\text{C}$ is found at 140m depth. Increasing the prescribed w to -0.5 m yr^{-1} at the end of the CO/MWP in the model experiments can be used to place the modeled CO/MWP anomaly at 600m (which matches the depth of the CO anomaly in the GRIP borehole), but then it is found that the magnitude of the modeled anomaly decreases to nearly zero as the positive anomaly propagates into the large LGM-related negative anomaly beneath. Similarly, increasing the prescribed w to -0.5 m yr^{-1} during the LIA causes this ice temperature anomaly to “disappear” into the more slowly moving positive CO/MWP anomaly beneath (because w is assumed to decrease exponentially with depth). Thus, a thermal anomaly (e.g. associated with the LIA) propagating downward into a deeper(older), slower-moving and larger-amplitude anomaly of the opposite sign (e.g. associated with the CO/MWP) will dissipate more rapidly if surface ice velocities increased during the formation of the given anomaly (e.g. LIA). Time-variations of the surface accumulation rate (or the downwards surface vertical velocity), by affecting the downward propagation of a thermal anomaly into the ice, therefore impact its preservation. The rate of diffusive smoothing or information loss of a given thermal signal in the ice is therefore not only a function of its proximity to other thermal anomalies of the opposite sign, but also a function of w (and likely the vertical distance separating successive anomalies). The sensitivity of ice sheet temperature profiles to w can potentially be a problem in model simulations, if w is itself not well modeled (e.g. Hindmarsh, 1999).

The 1D experiments demonstrate that both the thickness of the ice (and thus the length of its thermal “memory”) as well as the vertical velocity of the ice at the summit of an ice cap affect the englacial preservation of past air temperature

anomalies. The englacial preservation of an historical SAT anomaly and its higher-frequency details (i.e. the degree of englacial diffusive smoothing of an historical SAT signal), in turn, will determine the amount (resolution) of the climate information that can be recovered from ice borehole temperature inversions.

3.4 SUMMARY AND DISCUSSION

This study sought to review potential causes for differences in the observed amplitudes of LIA-related temperature signals within ice cap boreholes. It also aimed to determine whether two ice masses, with identical SAT histories and identical ice temperature dynamics, could nevertheless variably record the LIA-related SAT anomaly. It investigated the extent to which the observed differences in borehole temperature anomalies might be the result of: 1) differences in climate signal strength as a result of local-regional ice-atmosphere feedbacks; and/or 2) diffusive-smoothing-related disparities related to the presence of other temperature anomalies within the ice.

It was shown that the LIA SAT-anomalies of -0.5°C and -0.7°C (obtained from GRIP borehole temperatures – Dahl-Jensen et al., 1998) could readily be doubled by the combined terrestrial snow/ice and sea ice – albedo feedbacks, resulting in an LIA SAT-anomaly of $\sim -1.2^{\circ}\text{C}$ (equivalent to that inferred for the White Glacier site – section 3.1.4). It was also shown that where the CO/MWP signal exists within a borehole's thermal depth-profile, only 9-12% of the original LIA SAT-anomalies are preserved, as opposed to 19-26% where the CO/MWP signal is absent. This model result could explain the fact that the White Glacier LIA-related ice temperature anomaly ($\sim -0.3^{\circ}\text{C}$) is 25% of its associated SAT anomaly ($\sim -1.2^{\circ}\text{C}$), while the GRIP ice temperature anomaly ($\leq -0.1^{\circ}\text{C}$), on the other hand, is only $\sim 10\%$ of its associated SAT anomalies (-0.5°C , -0.7°C). Together, therefore, the snow/ice-albedo feedback and the presence/absence of the CO/MWP thermal signal can explain 100% of the observed difference in the amplitudes of the LIA-related ice temperature anomalies within the GRIP and White Glacier summit boreholes.

The snow/ice-albedo feedback calculations performed in this study expand upon the results of Chapter 2. From these, it is suggested that the subdued nature of the central GIS LIA signal, found in its δ and temperature depth-profiles, might not only be due to atmospheric circulation patterns (e.g. Barlow, 2001), but might also be due to a lack of amplification by ice-atmosphere feedbacks such as the snow/ice-albedo feedback. The snow/ice-albedo feedback is likely negligible at the GRIP site, due to its remoteness from the ice cap margins (where this feedback produces the strongest amplification – e.g. Pritchard et al., 2008). On the other hand, the snow/ice-albedo feedback will be important in many areas of the CHA and Norway.

From the above examination of five CHA and GIS borehole temperature profiles and from the 1D model experiments, it appears that smaller CHA ice caps will contain stronger, better preserved LIA signals than thicker ice caps (where these are isolated from surface and/or basal processes). Past thermal anomalies of sufficient magnitude can affect the ice's record of more recent climate changes. A small ice cap, with summit ice thicknesses ~ 400 m or less, will have lost most of the sensible temperature information associated with the CO/MWP, as these will have reached the ice bed and diffused away into the underlying bedrock or sediments. (Recall that even though the actual ice at the bed of an ice cap ≤ 400 m thick may derive from the CO/MWP or even older climate events, vertical thermal diffusion rates mean that the actual measured temperatures of these basal ice layers will no longer correspond to the SAT anomalies of their times of deposition.) Because of this, the amplitude of the LIA signal in a thinner ice cap can be stronger than the signal in a thicker ice cap which contains remnants of ice temperatures associated with the older warm periods.

Prior and subsequent air temperature anomalies recorded in the ice will have an impact not only on the amplitude, but also on the depth and range, of the recorded LIA signal. In the 1D borehole simulations above, because the LIA ice temperature anomaly is located between two positive ice temperature anomalies, not only is the magnitude of the recorded LIA signal significantly reduced, but the vertical range of the anomaly is also smaller, and the maximum temperature difference is displaced to a lower depth. For this reason, the detection and dating of relatively short duration, small amplitude anomalies can be problematic in ice masses with long thermal memories. As a further example of this point, the Younger Dryas cold period (~ 10 -11 ka BP), which would have been bracketed by two relatively large positive thermal anomalies, the Bølling-Allerød (i.e. the end of the LGM) and the early Holocene, can no longer be detected in the measured GISP or GRIP borehole temperature profiles (Cuffey et al., 1995; Dahl-Jensen et al., 1998). This is most likely because the thermal anomaly resulting from this period has diffused away over time (Dahl-Jensen et al., 1998; Alley, 2000). This is plausible, since the diffusion time scale for ice temperature anomalies located 100's of metres apart is of the order of 10^2 to 10^4 years. Thus, although historical SAT changes might be the direct cause of measured englacial temperature anomalies, they can also be the indirect cause of significantly-enhanced diffusive loss of the stored englacial climate information.

Model results show that even for similar SAT anomaly perturbations and ice temperature dynamics, cold and predominantly cold ice masses can variably preserve air-temperature-derived thermal anomalies within their internal temperature distributions. This is an important point which is usually inherently considered in advective-diffusive temperature models but is often neglected in discussions of their results. Spatial variability in SAT forcing due to atmospheric circulation patterns, which also affects the depths and amplitudes of climate-related ice temperature anomalies, can sometimes have a dominating influence upon a borehole's thermal profile (if the resulting SAT variations are sustained for

a sufficiently long period of time), but this may not always be the case. Spatial variability in SATs due to local feedback-amplifications in conjunction with variability in ice thermal memory may be enough to cause significant differences in observed ice temperature anomalies related to a specific climate event.

3.5 CONCLUSIONS

The entire difference between the amplitudes of the GRIP and the White Glacier borehole LIA-related temperature anomalies can be explained via: 1) the snow/ice-albedo feedback amplification of surface air temperatures in the Canadian High Arctic; and 2) the thermal erosion of GRIP's LIA-signal by the Medieval Warm Period and Holocene Climatic Optimum signals located at greater depth in that borehole. This does not definitively rule out other factors such as the mass balance - elevation feedback, the spatial and temporal variability of atmospheric circulation patterns (e.g. the NAO), or surface, basal, or geothermal/thermodynamic processes, but it does suggest that the two factors explored in this study might have been important to the evolution of the englacial temperatures of the Greenland Ice Sheet and White Glacier summits. It is also possible that the "subdued" LIA signal in central Greenland could more accurately be described as one which is: 1) "un-amplified" by ice-atmosphere feedbacks; and 2) damped by the presence of older, positive thermal signals within the ice.

Diffusive loss of climate-signal information over time and with depth will be enhanced in ice caps with long thermal memories (since these will contain a larger number of climate-derived thermal signals, each capable of diffusively modifying those adjacent to it). Estimates of the magnitude of the effect of adjacent ice temperature anomalies, such as those provided in this study, are important as enhanced loss of signal information due to enhanced diffusive smoothing decreases the possible resolution of model-recovered historical SATs.

Englacial temperatures impact the deformation and flow of an ice mass, its volumetric response to climate perturbations and its consequent evolution over time. The impact of ice-atmosphere feedbacks and enhanced/damped thermal diffusive smoothing upon englacial temperatures must therefore be considered when trying to diagnose and/or predict glacier behaviour. The results of this study should also be taken into consideration in the interpretation of existing thermal profiles of Arctic glaciers and ice caps.

3.6 REFERENCES

Abe-Ouchi, A., T. Segawa and F. Saito, 2007: Climatic conditions for modelling the Northern Hemisphere ice sheets throughout the ice age cycle. *Climate of the Past*, **3**, 423–438.

- Alley, R.B., 2000: The Younger Dryas cold interval as viewed from central Greenland. *Quaternary Science Reviews*, **19**, 213-226.
- Barlow, L. K., 2001: The time period A.D. 1400-1980 in central Greenland ice cores in relation to the North Atlantic sector. *Climatic Change*, **48**(1), 101-119.
- Bauder, A., D. M. Mickelson and S. J. Marshall, 2005: Numerical modeling investigations of the subglacial conditions of the southern Laurentide ice sheet. *Annals of Glaciology*, **40**, 219-224.
- Beltrami, H., C. Gosselin and J.C. Mareschal, 2003: Ground surface temperatures in Canada: Spatial and temporal variability. *Geophysical Research Letters*, **30**(10), 1499, doi:10.1029/2003GL017144.
- Beltrami, H., and A.E. Taylor, 1995: Records of climatic change in the Canadian Arctic: towards calibrating oxygen isotope data with geothermal data. *Global and Planetary Change*, **11**, 127-138.
- Blatter, H., 1987: On the thermal regime of an Arctic valley glacier: a study of White Glacier, Axel Heiberg Island, N.W.T., Canada. *Journal of Glaciology*, **33**, 200-211.
- Blatter, H., and K. Hutter, 1991: Polythermal conditions in arctic glaciers. *Journal of Glaciology*, **37**, 261-269.
- Blatter, H., and G. Kappenberger, 1988: Mass balance and thermal regime of Laika Ice Cap, Coburg Island, N.W.T., Canada. *Journal of Glaciology*, **34**, 102-110.
- Curry, J.A., J.L. Schramm, D. Petrovich, and J.O. Pinto, 2001: Application of SHEBA/FIRE data to evaluation of sea ice surface albedo parameterizations. *Journal of Geophysical Research*, **106**(D14), 15345-15355.
- Dahl-Jensen, D., K. Mosegaard, N. Gundestrup, G.D. Clow, S.J. Johnsen, A.W. Hansen, and N. Balling, 1998: Past temperatures directly from the Greenland Ice Sheet. *Science*, **282**, 268-271.
- Doran, P. T., C. P. McKay, W. P. Adams, M. C. English, R. A. Wharton Jr. and M. A. Meyer, 1996: Climate forcing and thermal feedback of residual lake-ice covers in the high Arctic. *Limnology and Oceanography*, **41**(5), 839-848.
- Dyke, A.S., 1993: Landscapes of cold-centred Late Wisconsin ice caps, Arctic Canada. *Progress in Physical Geography*, **17** (2), 223-247.
- Fischer, H., M. Werner, D. Wagenbach, M. Schwager, T. Thorsteinsson, F. Wilhelms, J. Kipfstuhl and S. Sommer, 1998: Little Ice Age clearly recorded in northern Greenland ice cores. *Geophysical Research Letters*, **25**(10), 1749-1752.
- Fisher, D. A., R. M. Koerner, W. S. B. Paterson, W. Dansgaard, N. Gundestrup and N. Reeh, 1983: Effect of wind scouring on climatic records from ice-core oxygen-isotope profiles. *Nature*, **301**, 205-209.

- Hindmarsh, R. C. A., 1999: On the numerical computation of temperature in an ice sheet. *Journal of Glaciology*, **45**(151), 568-574.
- Holland, M. M., and C. M. Bitz, 2003: Polar amplification of climate change in coupled models. *Climate Dynamics*, **21**, 221-232.
- Hutter, K., 1993: Thermo-mechanically coupled ice-sheet response – cold, polythermal, temperate. *Journal of Glaciology*, **39**(131), 65-86.
- Johansen, H., W. Fjeldskaar and J. Mykkeltveit, 1995: The influence of glaciation on the basin temperature regime. *Global and Planetary Change*, **12**, 437-448.
- Johnsen, S. J., D. Dahl-Jensen, W. Dansgaard and N. Gundestrup, 1995: Greenland paleotemperatures derived from GRIP bore hole temperature and ice core isotope profiles. *Tellus B*, **47**, 624-629.
- Jones, P. D., and K. R. Briffa, 2001: The “Little Ice Age”: Local and global perspectives [preface]. *Climatic Change*, **48**(1), 5–8.
- Kleinen, T., T. Osborn and K. Briffa, 2007: Investigation into influences on Little Ice Age climate. *Geophysical Research Abstracts*, **9**, 06909, 2007.
- Koerner, R. M., 1979: Accumulation, ablation, and oxygen isotope variations on the Queen Elizabeth Islands ice caps, Canada. *Journal of Glaciology*, **22**(86), 25-41.
- Koerner, R. M., 1989: Queen Elizabeth Islands glaciers. In: Chapter 6 of Quaternary Geology of Canada and Greenland, R. J. Fulton (ed.), Geological Survey of Canada, Geology of Canada, no. 1. (Also: The Geology of North America, Geological Society of America, **K-1**).
- Koerner, R. M., and D. A. Fisher, 1990: A record of Holocene summer climate from a Canadian high-Arctic ice core. *Nature*, **343**, 630-631.
- Kreutz, K. J., P. A. Mayewski, L. D. Meeker, M. S. Twickler, S. I. Whitlow and I. I. Pittalwala, 1997: Bipolar changes in atmospheric circulation during the Little Ice Age. *Science*, **277**(5330), 1294-1296.
- Lamoureux, S. F., J. H. England, M. J. Sharp and A. B. G. Bush, 2001: A varve record of increased ‘Little Ice Age’ rainfall associated with volcanic activity, Arctic Archipelago, Canada. *The Holocene*, **11**(2), 243–249.
- Liu, J., X. Chen, S. Wang and Y. Zheng, 2004: Palaeoclimate simulation of Little Ice Age. *Progress in Natural Science*, **14**(8), 716-724.
doi: 10.1080/10020070412331344221
- Lowe, J.J., and M.J.C. Walker, 1997: *Reconstructing Quaternary Environments*, 2nd ed. Addison Wesley Longman Ltd., Edinburgh Gate, England.
- Matthews, J. A., and K. R. Briffa, 2005: The ‘Little Ice Age’: re-evaluation of an evolving concept. *Geografiska Annaler*, **87A**, 17-36.

Mauquoy, D., B. van Geel, M. Blaauw and J. van der Plicht, 2002: Evidence from northwest European bogs shows 'Little Ice Age' climatic changes driven by variations in solar activity. *The Holocene*, **12**(1), 1–6.

National Research Council: Board on Global Change, 1994: *Solar Influences on Global Change*. The National Academies Press, 180pp.
(<http://www.nap.edu/books/0309051487/html/23.html>)

Nesje, A., and S. O. Dahl, 2003: The 'Little Ice Age' – only temperature? *The Holocene*, **13**(1), 139-145.

Overpeck, J., K. Hughen, D. Hardy, R. Bradley, R. Case, M. Douglas, B. Finney, K. Gajewski, G. Jacoby, A. Jennings, S. Lamoureux, A. Lasca, G. MacDonald, J. Moore, M. Retelle, S. Smith, A. Wolfe, and G. Zielinski, 1997: Arctic Environmental Change of the Last Four Centuries. *Science*, **278**, 1251-1256.
DOI: 10.1126/science.278.5341.1251.

Paterson, W.S.B., 1994: *The Physics of Glaciers*, 3rd ed. Pergamon Press, Oxford, England, 480 pp.

Paterson, W.S.B. and G.K.C. Clarke, 1978: Comparison of theoretical and observed temperature profiles in Devon Island ice cap, Canada. *Geophys. J. R. astr. Soc.*, **55**, 615-632.

Paterson, W. S. B., R. M. Koerner, D. Fisher, S. I. Johnsen, H. B. Clausen, W. Dansgaard, P. Butcher, and H. Oeschger, 1977: An oxygen isotope climatic record from the Devon Island Ice Cap, Arctic Canada. *Nature*, **266**, 508-511.

Phillips, D., 1990: *The Climates of Canada*, 176 pp, Canadian Government Publishing Centre, Ottawa.

Pritchard, M. S., A. B. G. Bush and S. J. Marshall, 2008: Neglecting ice-atmosphere interactions underestimates ice sheet melt in millennial-scale deglaciation simulations. *Geophysical Research Letters*, **35**, L01503, doi: 10.1029/2007GL031738.

Robock, A., 1979: The "Little Ice Age": Northern Hemisphere Average Observations and Model Calculations. *Science*, **206**(4425), 1402-1404.

Sass, J. H., B. L. Nielsen, H. A. Wollenberg and R. J. Munroe, 1972: Heat flow and surface radioactivity at two sites in South Greenland. *Journal of Geophysical Research*, **77**, 6435–6444.

Soon, W., and S. Baliunas, 2003: Proxy climatic and environmental changes of the past 1000 years. *Climate Research*, **23**, 89–110.

Taylor, A. E., 1991: Holocene paleoenvironmental reconstruction from deep ground temperatures: a comparison with paleoclimate derived from the $\delta^{18}\text{O}$ record in an ice core from the Agassiz Ice Cap, Canadian Arctic Archipelago. *Journal of Glaciology*, **37**(126), 209-219.

Thomas, R., T. Akins, B. Csatho, M. Fahnestock, P. Gogineni, C. Kim, and J. Sonntag, 2000: Mass balance of the Greenland Ice Sheet at high elevations. *Science*, **289**, 426-428.

van der Veen, C. J., T. Leftwich, R. von Frese, B. M. Csatho and J. Li, 2007: Subglacial topography and geothermal heat flux: potential interactions with drainage of the Greenland ice sheet. *Geophysical Research Letters*, **34**, L12501, doi:10.1029/2007GL030046.

Wolken, G. J., J. H. England and A. S. Dyke, 2008a: Changes in late Neoglacial perennial snow/ice extent and equilibrium-line altitudes in the Queen Elizabeth Islands, Arctic Canada. *Holocene*, **18**(4), 615-627.

Wolken, G. J., M. J. Sharp and J. H. England, 2008b: Changes in late Neoglacial climate inferred from former equilibrium-line altitudes in the Queen Elizabeth Islands, Arctic Canada. *Holocene*, **18**(4), 629-641.

4. The Influence of Climate on the Thermal Characteristics of a Canadian High Arctic Polythermal Glacier

4.0 INTRODUCTION

Many glaciers in the Canadian High Arctic (CHA) are polythermal. That is, they are composed primarily of cold ice but their beds, and sometimes a layer of basal ice, reach the pressure melting point (PMP) in the ablation zone. Examples include White Glacier, Axel Heiberg Island (Blatter, 1987), Laika Glacier, Coburg Island (Blatter and Hutter, 1991), John Evans Glacier, Ellesmere Island (Copland and Sharp, 2001) and Stagnation Glacier, Bylot Island (Irvine-Fynn et al., 2006).

It has been suggested that some of these glaciers are not in thermal equilibrium with their present-day boundary conditions (BC's), defined by local surface air temperatures (SATs) or near-surface ice temperatures and by basal geothermal heat fluxes. For example, equilibrium model results indicate that Laika Glacier should not be able to reach the PMP at its bed under its present day BC's because it is too thin (e.g. Blatter and Hutter, 1991). Similarly, Bingham et al. (2008) were unable to reproduce the inferred warm basal temperatures in the ablation zone of John Evans Glacier (JEG), Ellesmere Island, with their model, using its present-day BC's.

Possible reasons for these apparent thermal disequilibria are that the glaciers: 1) have surface, internal, and/or basal heat sources not included in the models; 2) have internal or basal feedbacks that enhance basal heat flow densities; 3) are still responding (geometrically and thermally) to past climatic perturbations; and/or 4) are being influenced by ice-atmosphere interactions which can amplify their thermal responses to past and continuing climate changes by modifying surface and basal BC's. Inadequate knowledge of critical BC's, like the geothermal heat flux, can also be an issue.

It is important that the reasons for the apparent thermal disequilibria of such polythermal glaciers are well understood, because correct modeling of internal ice temperatures is critical to correctly modeling glacier flow and glacier response to climate perturbations. The aim of this study, therefore, is to use modeling experiments to examine the range of possible reasons for the observed thermal disequilibrium of one of these glaciers. While not all polythermal glaciers are identical (Blatter and Hutter, 1991), this study will provide insight into the thermal evolution of predominantly cold glaciers with beds and basal ice layers at the PMP in their ablation zones.

To investigate the possible reasons for its apparent thermal disequilibrium, a 2D cross-sectional ice temperature model is used to simulate the inferred thermal characteristics of JEG, Ellesmere Island. A 2D model was chosen because: 1) below the equilibrium line altitude (ELA), JEG is composed of two primary ice

flow units which do not merge and therefore cannot be treated as a single continuous ice mass; and 2) modeling of this glacier is constrained by the 1D centre-line stake measurement array on the glacier.

While proxy evidence for warm basal temperatures exists for JEG (e.g. from basal meltwater chemistry – Skidmore and Sharp, 1999; from radio echo sounding – Copland and Sharp, 2001; from dye tracing – Bingham et al., 2003), numerical simulations indicate that this glacier should be cold-based under its present BC's (Bingham et al., 2008). An assessment will first be made of the extent to which JEG is in thermal equilibrium with its current BCs. This will then be followed by time-dependent experiments designed to test the continuing impact of past changes in air temperature, ice thickness, amounts of supraglacial meltwater reaching the glacier bed, surface refreezing and equilibrium line altitude upon basal ice temperatures.

This chapter is organized as follows: 1) John Evans Glacier (JEG) and its measured, inferred and previously modeled thermal characteristics are described; 2) the ice temperature model, the ice flow and ice thickness parameterizations, and the application of the boundary conditions (BCs) used in this study are detailed; 3) JEG equilibrium model solutions for present-day BC's are computed and differences between these and measured 15m-depth and inferred basal ice temperatures are presented and discussed; 4) a series of time-dependent model experiments, designed to test the influence of past climates and continuing internal/external feedbacks, are presented; and 5) conclusions are offered. For readers less familiar with the subject, the englacial temperature profiles of predominantly cold polythermal glaciers and the factors which influence them are reviewed in an appendix at the end of the chapter.

4.1 JOHN EVANS GLACIER

4.1.1 *Physical Description*

John Evans Glacier (JEG) is located on the east coast of Ellesmere Island, in the Canadian High Arctic (79.67°N, 74.5°W – Figure 4.1).

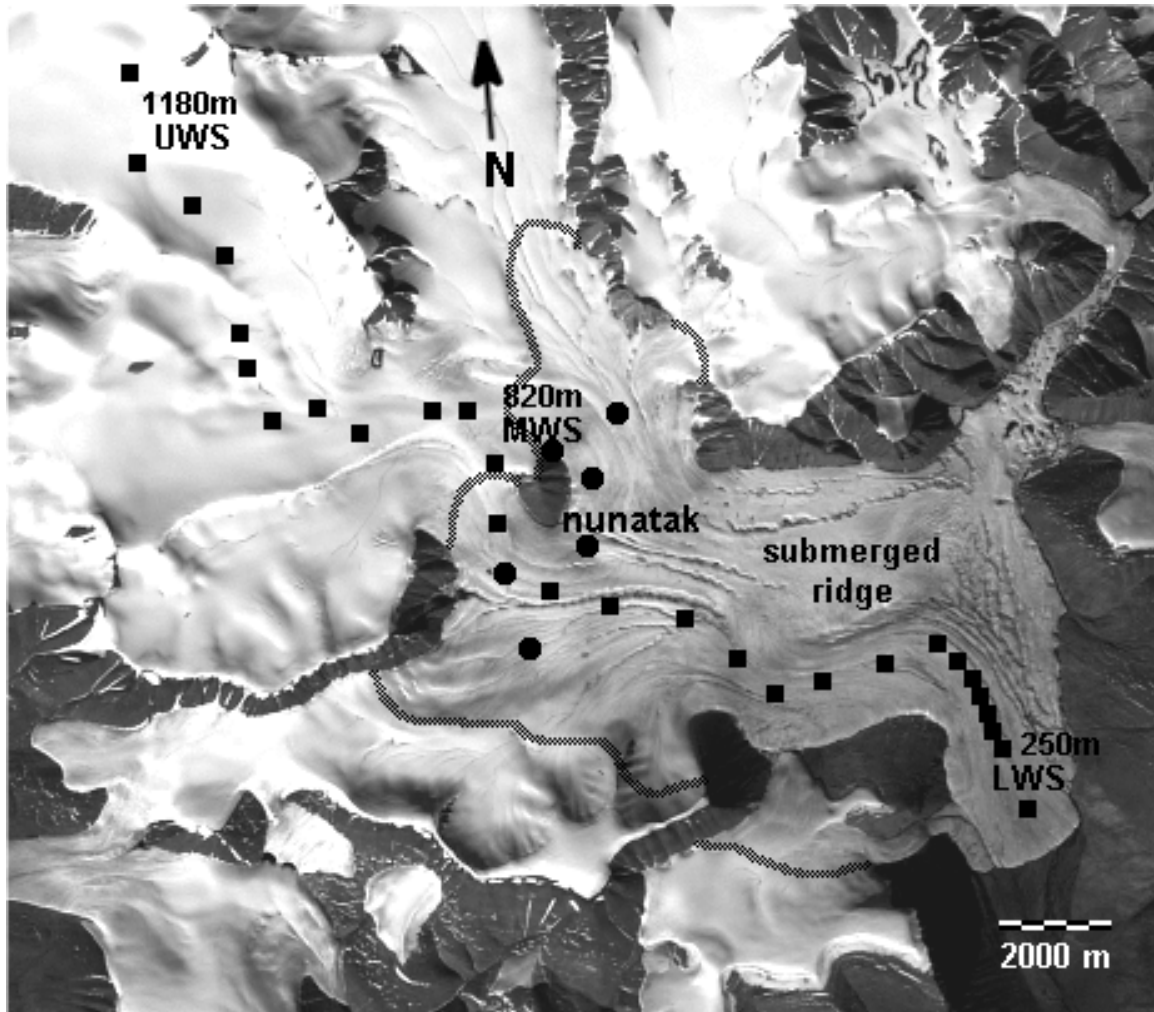


Figure 4.1. John Evans Glacier (79.67°N, 74.5°W). Black squares and circles denote the centre-line velocity / mass balance stake network, where the squares indicate the line that is used in the 2D modelling experiments. The positions and approximate elevations of the Lower, Middle and Upper Weather Stations (LWS, MWS, and UWS) are shown. The grey line passing through the nunatak and MWS follows the 800 m surface elevation contour and represents the approximate post-1963AD mean location of the equilibrium line (based on the elevation distribution of boreholes where the bomb layer can be found – *pers. comm.* Martin Sharp).

JEG is ~18 km long and serves as the main drainage for a small icefield immediately south of the Agassiz ice cap. Ice surface elevations range from ~100 m near the snout to ~1500 m near the summit. Ice thicknesses range from near 400 m immediately upstream and downstream of a nunatak located near the long-term mean equilibrium line altitude (ELA – Figure 4.1), to between 100 and 300 m elsewhere (Copland and Sharp, 2001). The main exception is where it thins as it passes over a submerged ridge downstream from the nunatak and where it nears the snout and glacier margins.

JEG is a polythermal glacier composed primarily of cold ice, but its bed apparently reaches the pressure melting point (PMP) in the ablation zone. While no surface-to-bed borehole temperature measurements exist for this glacier, a

variety of other evidence (presented below) suggests that its internal temperatures are similar to those sketched in Figures 4.10e and 4.10f of the appendix.

4.1.2 Measurements and Observations

Surface air temperatures were measured on JEG between 1996 and 2002 at three automatic weather stations located near the summit (~1200 m elevation), the ELA (~800 m) and close to the snout (~250 m; Figure 4.1). Between 1997 and 1999, measured mean annual 2m air temperatures differed little between these stations, and averaged -14.8°C . The mean annual 2m air temperature at the Middle Weather Station (MWS) averaged -14.6°C between 1997 and 2002.

Near surface (15m depth) ice temperatures on JEG were measured using thermistors drilled into the ice at the three weather stations and at 5 intermediate shallow ice core borehole locations. Average 1998-99 15m ice temperatures ranged from approximately -15°C near the summit to approximately -13.5°C near the snout, with a broad maximum centred about the nunatak and the ELA. Peak observed values within this maximum were found upstream of the nunatak, and reached -8°C to -9.5°C .

An ice temperature of $\sim -11^{\circ}\text{C}$ was measured at 10 cm above the bed in a tunnel drilled into the snout of the glacier, demonstrating that parts of JEG's terminus are frozen to the bed (*personal communication*, Martin Sharp).

Mean annual SATs, 15m ice-depth temperatures, and ice temperature measurements at the snout suggest that the bulk of JEG is likely composed of cold ice below the PMP. However, the following evidence suggests that basal temperatures reach the PMP over large areas of the lower ablation zone:

- 1) Sediment charged artesian fountains on the glacier surface and emergent subglacial streams at the snout indicate contact of englacial water with a sediment bed;
- 2) The ion chemistry and high turbidity of initial melt season outburst floods indicates the prolonged contact of subglacial runoff with the bed during the winter months (Skidmore and Sharp, 1999). As well, ion concentrations of summer subglacial runoff are higher than that of surface runoff (Skidmore and Sharp, 1999);
- 3) Radio-echo sounding measurements show high residual bed reflection power over large parts of the ablation zone (Copland and Sharp, 2001). This is interpreted as evidence of water at the bed and, by inference, of warm basal temperatures;
- 4) Observed seasonal variations in measured ice surface velocity have been attributed to temporally variable basal motion, which is most easily explained as a

response to forcing by seasonal inputs of surface-derived meltwater to the glacier bed (Copland et al., 2003b); and

5) Dye tracing experiments have demonstrated that supraglacial meltwater, which enters crevasses and moulins in the upper ablation area, emerges subglacially at the snout into the proglacial stream network (Bingham et al., 2003; 2005).

The above points assume that water can only exist and flow at the glacier bed if the ice-bed interface is at the PMP. There is always the possibility that if water inputs are large enough, freezing rates might be too low to stop water escaping from the glacier. Supraglacial meltwater reaching the bed may, in such cases, drain over cold beds. However, what freezing does occur would then act as a heat source. Frictional heat released by the flowing water would also serve as a heat source, as would any local sliding of the glacier as a result of the basal water flow. These heat sources would warm the ice-bed interface, eventually bringing them to the PMP.

4.1.3 Previous Ice Temperature Modeling of JEG

Bingham et al. (2008) simulated JEG's measured surface velocities and basal temperatures, using a 3-dimensional thermo-mechanically coupled glacier model. They used the 15m ice-depth thermistor measurements as the surface BC and a spatially-constant geothermal heat flux appropriate for the CHA as the basal BC. Their no-basal-motion control experiments evolved steady-state basal temperature fields with colder basal ice in the accumulation zone than in the ablation zone, similar to what is inferred via radio echo sounding (Copland and Sharp, 2001), but in which the basal temperatures nowhere reach the PMP. They speculate that the reason for this may be that their prescribed geothermal heat flux (0.06 W m^{-2}) was too low, and that possibly it is being augmented by sensible heat transferred by water from the surface to the bed, and the frictional heating that results from en- and subglacial water flow. However, even with the geothermal heat flux increased by a factor of 50% to 0.09 W m^{-2} , nowhere did the bed of JEG attain the PMP under equilibrium conditions.

As with Laika Glacier (Blatter and Hutter, 1991), JEG's internal temperature distribution appears to not be in equilibrium with its present-day BC's. Further time-dependent experiments are required to determine whether it may still be responding to past climatic perturbations.

4.2 JEG 2D ICE TEMPERATURE MODEL AND BOUNDARY CONDITIONS

The model domain represents a vertical cross-section extending the entire length of the glacier, and follows the stake network on the glacier (Figure 4.1). The temperature model used in this study, the numerical integration of the model equations forward in time, and the application of the surface and basal BC's are

described below. Ice thickness changes and ice velocities must be prescribed, modeled, or parameterized in this model and this is also discussed. Glacier length changes, however, were neglected in the model experiments. Even a neoglacial advance and post-neo-glacial retreat of up to 1 km would only represent 5% of the total glacier length (and there is no geomorphological evidence for any such advance/retreat – *personal communication*, Martin Sharp).

4.2.1 Ice Temperature Model

The model used in this study is essentially that described by others (e.g. Hutter, 1993; Funk et al., 1994; Huybrechts, 1996; Marshall and Clark, 2002) for predominantly cold ice masses. Such glaciers may reach the PMP at their beds, but do not develop temperate basal layers of any significant thickness. This characteristic has been established for JEG, where an inferred basal layer of temperate ice in the lower ablation zone averages 20 m thick, or ~10% of the total ice thickness (Copland and Sharp, 2001). For a 2D representation of such a glacier:

$$\frac{\partial T}{\partial t} = -u \frac{\partial T}{\partial x} - w \frac{\partial T}{\partial z} + k \frac{\partial^2 T}{\partial z^2} + \Phi_{if} \quad (1)$$

where T is temperature, t is time, and k is the thermal diffusion coefficient for ice (assumed to be constant here). The horizontal coordinate, x , represents distance in the downstream direction along the centre-line of the glacier, and u represents horizontal velocities along this centre-line. The symbols z and w are the vertical coordinate and vertical velocity, respectively, and Φ_{if} represents an internal frictional heat source which arises from ice deformation and which acts throughout the ice volume.

The horizontal diffusion term has been omitted in (1) because its magnitude is negligible compared to that of the horizontal advection term. Additionally, although k is temperature dependent, the vertical diffusion term $\partial/\partial z(k\partial T/\partial z) = k\partial^2 T/\partial z^2 + (\partial T/\partial z)(\partial k/\partial z)$ is commonly approximated by $k\partial^2 T/\partial z^2$ in models because in general $(\partial T/\partial z)(\partial k/\partial z)$ is negligible except near the base of an ice sheet where temperature gradients are highest and w is small (Paterson, 1994). It is noted that inclusion of the term $(\partial k/\partial z)$ tends to produce slightly lower calculated basal temperatures than if a constant k is assumed, because it reinforces the vertical advection term in the downward direction (Paterson, 1994).

4.2.2 Ice Deformation Velocities and Consequent Internal Frictional Heating

Observed 1999-2000 average winter surface velocities (Figure 4.2a) were used to calculate the present-day englacial distribution of ice deformation flow rates (u, w). JEG surface velocities were measured along a centre-line network of up to 34 stakes extending from the summit to the snout (Figure 4.1). Differential

GPS techniques were used to measure the surface ice motion at the upper 23 of these stakes (Bingham et al., 2003), while electro-optical surveying was used to obtain surface velocity measurements over the lower part of the glacier (Copland et al., 2003a,b).

Englacial ice velocities used in the model were computed from the observed surface velocities using the integrated form of Glen's Flow Law (with exponent $n=3$; Glen, 1955). Thus (e.g. Paterson, 1994, p251):

$$u_z = u_s - \frac{A}{2} \left(\rho g \frac{\partial h_s}{\partial x} \right)^3 (h_s - z)^4 \quad (2)$$

where u_s is the surface horizontal velocity of the ice, ρ is the density of the ice, g is the acceleration due to gravity, and h_s is the elevation of the ice surface. A is the temperature dependent flow parameter (the inverse of viscosity) in the stress-strain relationship $\dot{\epsilon} = A\tau^n$ (Glen's flow law - Glen, 1955), where $\dot{\epsilon}$ is the strain rate, τ is the applied stress, and where n is generally taken as equal to 3 for ice.

The appropriate mean value for A was determined by assuming $u_z=0$ at the bed of the glacier during the winter months and rearranging (2) to read: $A=2(u_s-u_{bed})/((\rho g \partial h_s / \partial x)^3 (h_s-h_b)^4)$. While it is likely that some year-round basal motion occurs at JEG (Copland et al., 2003b; Bingham et al., 2008), its inferred magnitude is model-dependent (Wohlleben, T, M. Sharp and A. Bush: John Evans Glacier, Nunavut, Canada: a Case for Modeling Surface Ice Velocities using a Linearly Viscous Shallow Ice Equation Model *unpublished manuscript*). It is assumed here that this motion is negligible and that winter ice flow is primarily by ice deformation. The values of A so calculated (which range for the most part from $\sim 1.3 \times 10^{-15}$ to $\sim 6.3 \times 10^{-16} \text{ s}^{-1} \text{ kPa}^{-3}$) correspond to a depth-averaged ice temperature near -6°C using the Arrhenius equation (e.g. Paterson, 1994, p86; also p97), although the actual depth-averaged value varies along the length of the glacier flow line.

The vertical velocity of the ice was then diagnosed from the mass continuity equation for an incompressible medium. " w ", at any given depth, was computed from the horizontal velocity divergence integrated from the bed to that depth: $w(z)=w(\text{bed})-\int(\partial u/\partial x)dz$. Assuming that $w=0$ at the glacier bed, then the w 's of all the layers above can be sequentially determined from the horizontal velocity divergence of the layer and the w 's determined from below.

Horizontal ice deformation velocities were augmented by prescribed basal velocities in some model experiments. While the basal velocity, u_b , is assumed to be negligible during the winter months, because this assumption allows for the calculation of the internal deformation ice velocities from the measured over-winter average surface velocities, u_b cannot be assumed to be zero during the summer months. A summer sliding velocity, equal to the difference between

measured summer and winter surface ice velocities (values are given in Copland et al., 2003a,b), can be added to the deformation velocities to assess the impact of the related frictional heating and advective cooling upon englacial and basal ice temperatures. In model experiments which include basal motion, the vertical velocities are recomputed from the new horizontal velocity divergences.

Because the magnitude of time-dependent changes in ice deformation, driven by changes in ice temperature, ($<10 \text{ m yr}^{-1}$ – based on the integrated form of Glen’s Flow Law for various values of A), will be an order of magnitude less than any time-dependent changes in basal motion ($\geq 10 \text{ m yr}^{-1}$ – Copland et al., 2003b), these are neglected in the experiments in this study. As a consequence, a constant value of A is assumed throughout all experiments.

The interior ice deformation velocities modeled using equation (2) (Figure 4.2b), reveal that JEG’s ice flow pattern is not as clean and simple as that of an ideal ice cap or glacier (see appendix – Figure 4.11d), primarily as a result of the nunatak located approximately halfway down its length, near the ELA (Figure 4.1). Because ice must divert around this nunatak, ice flow immediately upstream of this feature must slow down in the x-direction (i.e. ice velocities upstream of the nunatak must converge in the along-stream-direction). Ice is pushed upwards against the upstream flank of the nunatak (Figure 4.2b), such that positive vertical velocities occur where none would otherwise be expected (according to Figure 4.11d). Once the ice has passed around the nunatak, the ice then accelerates (velocities diverge), resulting in downward ice velocities immediately downstream of the nunatak and ELA (Figure 4.2b). Again, in a glacier with a simple geometry, vertical velocities near the ELA generally tend to be close to zero (Figure 4.11d). It can be reasonably expected that JEG’s surface and englacial velocities will have yielded a slightly different 2D englacial temperature profile than that sketched in Figure 4.11e, as a result of these secondary areas of “upwelling” and “subsidence”.

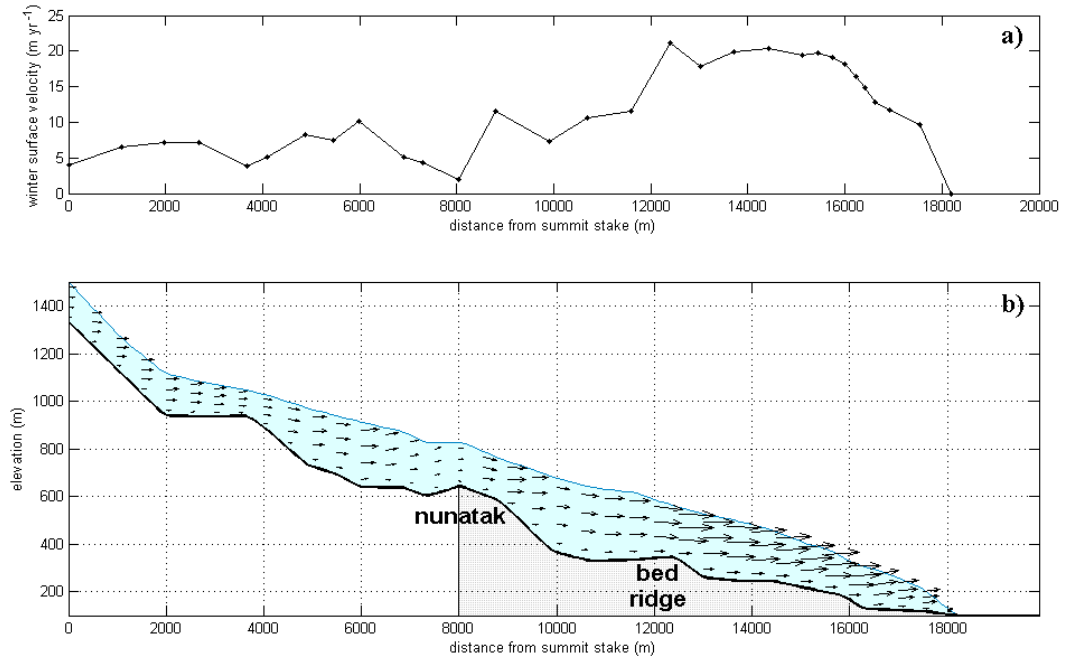


Figure 4.2. 1999-2000 winter average ice velocities for John Evans Glacier: a) measured surface horizontal velocities; b) calculated englacial ice velocities. The ice in the chosen centre-line flows around a nunatak located approximately midway down the glacier's length. It also passes to the south of a submerged bedrock ridge or riegel, located approximately 6000m upstream from the glacier snout. The location of the nunatak coincides with the average ELA, separating the accumulation zone from the ablation zone (indicated by light grey bed shading to the right of the nunatak). Temperate basal conditions have been inferred from immediately below the nunatak all the way to just short of the snout, which itself is frozen to the bed.

Note that the glacier cross-section actually crosses two flow units in the ice: the ice descending from above the nunatak flows around its eastern flank and does not merge with the separate flow unit which passes to the west of the nunatak and which flows all the way to the snout of the glacier (Figure 4.1). This is fortunately accounted for in the model in that the surface horizontal ice velocities, because the ice flow slows down in the along-stream direction as it diverts around the nunatak, reach a minimum value of $\sim 3 \text{ m yr}^{-1}$ immediately upstream of this feature (Figure 4.2a). This minimum in horizontal ice surface velocity effectively divides the 2D model glacier in two, an upper glacier and a lower glacier, which thermally connect only to a very limited extent (since horizontal temperature exchanges are only by advection in this model – Hutter, 1993). Note that the minimum velocity cited here is an extra point based on data from the Middle Weather Station - one not used in the model transect of Copland et al. (2003b).

Heating by internal friction, Φ_{if} , as a result of ice deformation, is determined from (e.g. Fabri et al., 1992; Huybrechts, 1992; Paterson, 1994):

$$\Phi_{\text{if}} = \frac{2\dot{\epsilon}\tau}{\rho c_p}, \quad (3)$$

where $\dot{\epsilon}$ is the strain rate, τ is the shear stress, ρ is the density of the ice, and c_p is the specific heat of the ice at constant pressure. The shear strain rate is $\dot{\epsilon}_{xz} = (1/2)(\partial u/\partial z + \partial w/\partial x)$, where $\partial w/\partial x$ is neglected in this model because it is assumed that $\partial w/\partial x \ll \partial u/\partial z$ (since glacier length scales, X , are so much greater than glacier thickness scales, Z). The values for $\partial u/\partial z$ are computed from the interior velocity profiles calculated from (2). The shear stress, also derived under the same assumption that $X \gg Z$ (such that longitudinal stresses may be neglected), and assuming hydrostatic ice, is $\tau = -\rho g(h_s - z)\partial h_s/\partial x$ (e.g. Paterson, 1994, p.242). Although Φ_{if} is applied at all (x, z) grid points in the model, its effect is primarily “felt” near the bed, where deformation and vertical gradients of horizontal velocity ($\partial u/\partial z$) are greatest.

4.2.3 Ice Thickness

The model domain represents a vertical cross-section extending the entire length of the glacier, and follows the stake network on the glacier (Figures 4.1 and 4.2b). Surface elevations, h_s , for this cross section were derived from a surface digital elevation model (DEM) of the JEG catchment, which was created from stereo-aerial photography of the area taken in 1960 (available from the National Air Photo Library of Natural Resources Canada), using analytical photogrammetric methods (*personal communication*, A. Arendt). Bed elevations, h_b , were derived by subtracting ice thicknesses measured by radio-echo sounding from the glacier surface DEM (Copland and Sharp, 2001).

Changes in h_s are parameterized in some of the time-dependent model experiments below. The different parameterizations applied are described in the pertinent sections.

4.2.4 Terrain Following Coordinates and Model Integration

The model equation (1) is solved on a staggered finite difference grid with a horizontal spacing of 125 m. The vertical z -coordinate is converted to a normalized σ -coordinate by dividing it by the total ice thickness, H , at every point. Thus:

$$\sigma = \frac{h_s - z}{h_s - h_b} = \frac{h_s - z}{H} \quad (4)$$

where again h_s is the surface elevation of the ice, h_b is the bed elevation, and z is any elevation in between. The bed of the glacier is now defined by $\sigma=1$ and the surface of the glacier is defined by $\sigma=0$. Normalizing the vertical coordinate ensures that the model layers follow the glacier topography (e.g. Funk et al., 1994; Huybrechts, 1992; Blatter and Hutter, 1991), and allows the boundary conditions to be more easily implemented. In the experiments that follow, the ice was

divided into 10 equal vertical layers, the thicknesses of which are proportional to H at any horizontal grid point. Approximately identical solutions are achieved with the model regardless of whether the ice is divided into 4 or 10 vertical layers. This indicates that in the JEG case, little improvement would result in using greater than between 4 and 10 equally-spaced layers or an increasingly greater number of non-equally-spaced layers towards the bed where most of the deformation occurs. However, 10 layers are used in the experiments because these provide smoother results and contour plots.

The numerical integration of equation (1), once transformed into σ -coordinates as described in Fabri et al. (1992), uses a finite-difference scheme with centred differences in the vertical and upstream differences in the longitudinal direction (as per Blatter and Hutter, 1991; Funk et al., 1994). Equilibrium solutions are easily obtained by inverting the resultant tridiagonal matrix at each sequential horizontal gridpoint in the downstream direction – assuming zero horizontal advection at the very first horizontal gridpoint at the upstream end of the glacier cross-section. Time-dependent solutions are integrated forward in time as per method 1 described in Blatter (1987), using a one-year time step. This time step satisfies the numerical stability constraints imposed by the grid spacing, the thermal diffusion coefficient and the ice velocities. Equilibrium solutions can also be obtained by integrating (1) forward in time under fixed BC's. A steady-state for JEG is achieved with the model after ~ 2000 years, after which no difference in the results is observed. This agrees with estimated diffusive and advective response time scales for a glacier of this size. For typical glacier thicknesses of order $H \sim 10^2$ m, diffusive time scales are of order $H^2/k = 10^3$ years. For typical ice velocities of order $W \sim 10^0$ m yr⁻¹ and $U \sim 10^1$ m yr⁻¹, and for length scales of order $X \sim 10^4$ m, vertical and horizontal advective time scales are $H/w = 10^2$ years and $X/U = 10^3$ years respectively.

4.2.5 Model Boundary Conditions

4.2.5.1 GLACIER SURFACE

Mean annual SATs are commonly used as the thermal BC at model glacier surfaces, such that $T_{sfc} = T_{atm}$. This is a reasonable assumption above the ELA, in areas where surface refreezing is negligible, where annual snow accumulations are incorporated into the ice, where $w < 0$, and where surface temperature gradients tend towards zero (i.e. where $\partial T / \partial z = 0$ – see Figure 4.11f, leftmost profile).

Below the ELA, on the other hand, where summer melt and runoff remove both winter snow accumulations and surface ice layers and where $w > 0$, surface ice temperatures will not equal T_{atm} . This issue is addressed in some detail in Blatter (1987), and he parameterizes this effect in his ice temperature model via an extrapolation scheme which uses measured 10m-depth temperatures and a modeled temperature gradient. In a different study, Bueler (2002) partially compensates for this effect by including in equation (1) a pseudo-flux across the

ice-surface interface equal to $\omega(T_{\text{atm}} - T)$, where he chooses $\omega = \ln(2)/\Delta t$ (i.e. $e^{-\omega\Delta t} = 1/2$).

In this study, the following simple parameterization is adopted. It is noted that where $w \geq 0$, the surface ice temperature, T_{sfc} , will have a value somewhere between that of the mean surface air temperature, T_{atm} , and that of the temperature of the ice below the 10-15m depth surface layer, T_{below} (the ice depth at which seasonal temperature fluctuations are damped out). Thus, the surface BC where $w \geq 0$ was simply chosen to be $T_{\text{sfc}} = 0.5(T_{\text{atm}} + T_{\text{below}})$. While actual values of T_{sfc} will be closer to T_{atm} where positive w 's are small, and closer to T_{below} where positive w 's are large, this parameterization nevertheless yields results for JEG's modeled surface temperatures that improve upon those computed with the BC $T_{\text{sfc}} = T_{\text{atm}}$, and which are closer to actual measured 15m-depth values. For example, the modeled horizontal distribution of T_{sfc} becomes more realistic when using this surface BC where vertical ice velocities are positive, and it even allows for the partial reproduction of the 15m-depth temperature maximum observed immediately upstream of the nunatak.

To summarize, where supplementary surface heat fluxes such as those associated with surface refreezing are absent: 1) Above the ELA, and where $w < 0$, the surface BC is taken to be $T_{\text{sfc}} = T_{\text{atm}}$; 2) Below the ELA, and where $w \geq 0$, it is noted that $T_{\text{sfc}} \neq T_{\text{atm}}$, but is some value between T_{atm} and T_{below} . In these areas, the surface BC is chosen as $T_{\text{sfc}} = 0.5(T_{\text{atm}} + T_{\text{below}})$.

Supplementary heat fluxes which can impact the thermal BC at the glacier surface are: 1) latent heat released by the refreezing of supraglacial meltwater (e.g. Greuell and Oerlemans, 1989), where this effect is often parameterized in ice models by adding a source term to the surface thermal BC (e.g. Marshall and Clark, 2002); and 2) heat generated by firn compaction in the accumulation zone (Paterson, 1994, p225). In the present study, the impact of these additional heat sources is simulated in the model experiments by replacing the surface BC parameterization described above with the following surface BC: $T_{\text{sfc}} = T_{15\text{m}}$ everywhere, where $T_{15\text{m}}$ are the measured 15m-depth ice temperatures. Measured 15m-depth ice temperatures reflect mean annual air temperatures but are modified by heating due to surface refreezing and firn compaction as well as by heat fluxes to/from the ice below.

For glaciers which experience large changes in surface elevation from summit to snout (e.g. Greenland glaciers), SAT lapse rates can be important. In these cases, the change in SAT with surface elevation needs to be parameterized in the surface BC. JEG, however, which spans an altitude range $\sim 1200\text{m}$, does not experience large changes in mean annual air temperature with elevation (see section 4.1.2). Consequently, a single mean annual SAT is used at all elevations.

4.2.5.2 GLACIER BED

At the ice-bed interface where ice velocities become zero, and in the rock/sediments beneath the ice, the energy balance reduces to:

$$\frac{\partial T}{\partial t} = k \frac{\partial^2 T}{\partial z^2} + \text{basal heat sources} \quad (6)$$

Geothermal heat is the primary basal heat source for predominantly cold polythermal glaciers. Measured geothermal heat fluxes for northern Ellesmere Island in the CHA are $\sim 0.06 \text{ W m}^{-2}$ (e.g. a value of 0.0627 W m^{-2} was determined near the JEG site, immediately west of the Agassiz Ice Cap – Beltrami and Taylor, 1995). Pronounced topography can intensify the geothermal heat flux, especially in deep in-filled structural trenches, and attenuate this flux on mountain summits (van der Veen et al., 2007). Furthermore, the availability of this geothermal heat source at the base of a glacier may be reduced if temperature inversions develop within the substrate (e.g. Dyke, 1993).

In addition to geothermal heating, basal heat sources can include frictional heating due to basal sliding, latent heating due to the refreezing of basal meltwater, frictional heating due to the deformation of subglacial sediments, and heat fluxes related to basal water flow and water flow within subglacial sediments. In the latter case, it was found that enhanced temperature gradients and heat fluxes are generated beneath the ice when liquid water flows through subglacial till or sediments (Echelmeyer, 1987). These additional heat sources are primarily activated when and where temperatures at the glacier bed reach the PMP and basal melting occurs, leading to subglacial water flow (although some basal sliding and sediment deformation may occur at temperatures below the PMP). They may also be initially triggered by supraglacial meltwater reaching the bed via moulins and crevasses.

The equilibrium ($\partial T / \partial t = 0$) thermal BC at the base of the glacier is thus the temperature gradient

$$\left(\frac{\partial T}{\partial z} \right)_{\text{bed}} = - \frac{(G + u_b \tau_b + \rho L_f \dot{m} + \text{other})}{K} \quad (7)$$

(e.g. Christoffersen and Tulaczyk, 2003), where G is the geothermal heat flux, and K is the thermal conductivity of the ice. The terms $u_b \tau_b$ and $\rho L_f \dot{m}$ represent heating due to basal sliding and basal refreezing, respectively, where u_b is the horizontal (sliding) velocity at the bed, τ_b is the basal shear stress, L_f is the latent heat of fusion and \dot{m} is the rate of refreezing in m s^{-1} .

In the time-dependent experiments, following Huybrechts (1996), the BC at the ice-bed interface becomes:

$$\left(\frac{\partial T_{ice}}{\partial z}\right)_{bed} = \left(\frac{K_{rock} \left(\frac{\partial T_{rock}}{\partial z}\right)_{bed} - (u_b \tau_b + \rho L_f \dot{m} + \text{other})}{K_{ice}} \right) \quad (8)$$

and the diffusion-only equation $\partial T_{rock}/\partial t = k_{rock} \partial^2 T_{rock}/\partial z^2$ is solved for the rock/soil layer beneath the glacier. The lithosphere lower BC now becomes $\partial T_{rock}/\partial z = -G/K_{rock}$. The depth of the subglacial rock/soil layer over which the time-dependent calculations are performed is 2km (where, after Huybrechts (1996) and Paterson (1994), at this depth 99% of the amplitude of a thermal wave with a period of 20 ka and 87% of a wave with a period of 100 ka are attenuated). If the rock/soil layer contains permafrost, its thermal conductivity and heat capacity can significantly alter when and where melting occurs (e.g. Bauder et al., 2005). This is discussed further in section 4.3.6 below.

Note that the basal ice BC (7,8) must be modified when the ice reaches the PMP at the bed. For primarily cold glaciers, where basal temperatures can reach the PMP but no significant temperate basal layer develops, basal temperatures are simply not allowed to rise above the PMP in the model solutions (e.g. Huybrechts, 1996; Hutter, 1993; Marshall and Clark, 2002). It is assumed that once the bed reaches the PMP, any/all additional heating is lost to basal ice melt or to the dissipation of subglacial permafrost, and does not contribute to the development of a temperate basal layer. This method was adopted here because the measured thicknesses of JEG's inferred warm basal ice layer (~20 m; Copland and Sharp, 2001) are in general less than or equal to the thickness of the lowest model ice layer. Thus, the basal ice BC (7,8) is applied until the bed reaches the PMP, at which point it is assumed to change from a flux boundary condition to a temperature boundary condition, $T_{bed} = \text{PMP}$. Note that basal temperatures can once again fall below the PMP in the model via temperature advection from the surface of the accumulation zone of the glacier.

For reference, the PMP is calculated as per:

$$T_{PMP} = T_0 - c(P - P_0) \quad (9)$$

where $P(z) = \rho g(h_s - z)$ is the hydrostatic pressure, $c = 7.42 \times 10^{-8} \text{ K Pa}^{-1}$ is the Clausius-Clapeyron constant, and T_0 is the melting point temperature under $P_0 = 1$ atm of pressure (e.g. Hutter, 1993; Calov and Hutter, 1996). Mean ice thicknesses for JEG are generally less than or equal to ~300 m, yielding average melting point depressions of less than ~0.204°C. Thus, average PMP's for JEG are not less than ~-0.2°C.

4.2.6 A Note Concerning Thermal Conductivity and Volumetric Heat Capacity

4.2.6.1 ICE

Thermal conductivity increases with decreases in ice temperature (Paterson, 1994). For example, $K = 2.10 \text{ W K}^{-1} \text{ m}^{-1}$ at 0°C and $K = 2.26 \text{ W K}^{-1} \text{ m}^{-1}$ at -15°C (derived using equation 2, p205, Paterson, 1994). 1D isothermal diffusion-only model tests indicate that large differences in K can lead to basal ice temperature differences of up to 1°C . However, in the experiments conducted below, for simplicity, a constant average value of $2.16 \text{ W K}^{-1} \text{ m}^{-1}$ was used (since K depends on T which in turn depends on K , and no iteration taking this into account is conducted).

4.2.6.2 BED

For the rock/soil beneath the glacier, where permafrost is likely, the fractions of liquid and frozen water contained therein can impact the thermal conductivity, the heat capacity, and consequently the thermal diffusivity of the layer (e.g. Bauder et al., 2005). In most of the experiments conducted in this study, the subglacial substrate was assumed to be composed of saturated sediment with a 40% pore space, and having a constant value of $K = 2.16 \text{ W K}^{-1} \text{ m}^{-1}$ (a value identical to the average ice value noted above). This value is similar to the value for saturated sand with 40% pore space quoted in Peixoto and Oort (1992, p221). It can also be obtained using the equations and values in Bauder et al. (2005), assuming 60% quartz rock and 40% water (of which 60% is frozen and 40% is liquid). The corresponding calculated volumetric heat capacity for this substrate is $C=2.36 \times 10^6 \text{ J m}^{-3} \text{ K}^{-1}$, giving a thermal diffusivity of $k=K/C=0.9 \times 10^{-6} \text{ m}^2 \text{ s}^{-1}$ (while values for ice are $C=2 \times 10^6 \text{ J m}^{-3} \text{ K}^{-1}$ and $k=1 \times 10^{-6} \text{ m}^2 \text{ s}^{-1}$).

4.3 JEG 2D ICE TEMPERATURE MODEL EXPERIMENTS AND RESULTS

Before investigating the possible reasons for JEG's apparent basal thermal disequilibrium in the ablation zone, it must first be established that the glacier is indeed in thermal disequilibrium with its present-day BC's. To do this, the equilibrium state of the glacier under present-day BC's must be modeled as accurately as possible and the degree of thermal disequilibrium established by differencing the equilibrium model solution with observations and any available temperature measurements.

Once the degree of thermal disequilibrium has been established, then the influence of other factors such as climate change (i.e. the continuing response of the glacier's temperatures to past changes in air temperatures and ice thicknesses), and basal, internal and ice-atmosphere feedbacks can be investigated via time-dependent experiments designed specifically to simulate and test them. The numerical results of these time-dependent experiments can then be compared to

present-day field observations to assess the extent to which the model is capable of simulating them.

4.3.1 *Equilibrium Solutions*

The aim of the equilibrium experiments is to determine the extent to which JEG is in equilibrium with its present-day BC's. It must be established that no significant heat sources have been omitted in the model BC's and that a thermal disequilibrium does indeed exist for this glacier.

Before computing the 2D equilibrium temperatures under various surface and basal BCs, though, it is useful to first conduct a few simple 1D test experiments, to get a feel for what to expect and for what is reasonable. Using the present-day mean annual SAT for JEG of $T_{\text{atm}} \sim -15^\circ\text{C}$ as the surface BC, and applying a basal geothermal heat flux of $G = 0.06 \text{ W m}^{-2}$, 1D equilibrium solutions for static-ice (i.e. for ice experiencing thermal diffusion only) indicate that an ice thickness of $\sim 550\text{m}$ is required in order for the bed to reach the PMP. Immediately, this result indicates that reaching the PMP might be problematic for models simulating JEG basal ice temperature, since nowhere do JEG ice thicknesses reach this value.

The thickest ice in the ablation zone of JEG, up to 400m thick, is observed between the nunatak and the submerged bedrock ridge (Figure 4.1). Equilibrium basal ice temperatures, for static ice 300-400m thick, under the BC's given above, range between -4.5°C and -7°C . For ice 300-400m thick, G would need to be increased (or supplemented by other internal/basal heat fluxes) to a value of ~ 0.085 to 0.12 W m^{-2} , in order for the basal ice to reach the PMP under an SAT of -15°C . Alternatively, surface temperatures would need to be increased to values of -8°C to -11°C to achieve temperate basal conditions for static ice 300-400m thick with a basal geothermal heat flux of $G = 0.06 \text{ W m}^{-2}$.

4.3.1.1 FOR THE MEAN ANNUAL SAT AND GEOTHERMAL HEAT FLUX

JEG non-static 2D equilibrium ice temperatures, modeled using equation (1), under the present-day mean annual SAT for JEG of $T_{\text{atm}} \sim -15^\circ\text{C}$ (where the surface BC below the ELA is modified as discussed in section 5.2.5.1) and a basal geothermal heat flux of $G = 0.06 \text{ W m}^{-2}$, are everywhere below the PMP (Figure 4.3).

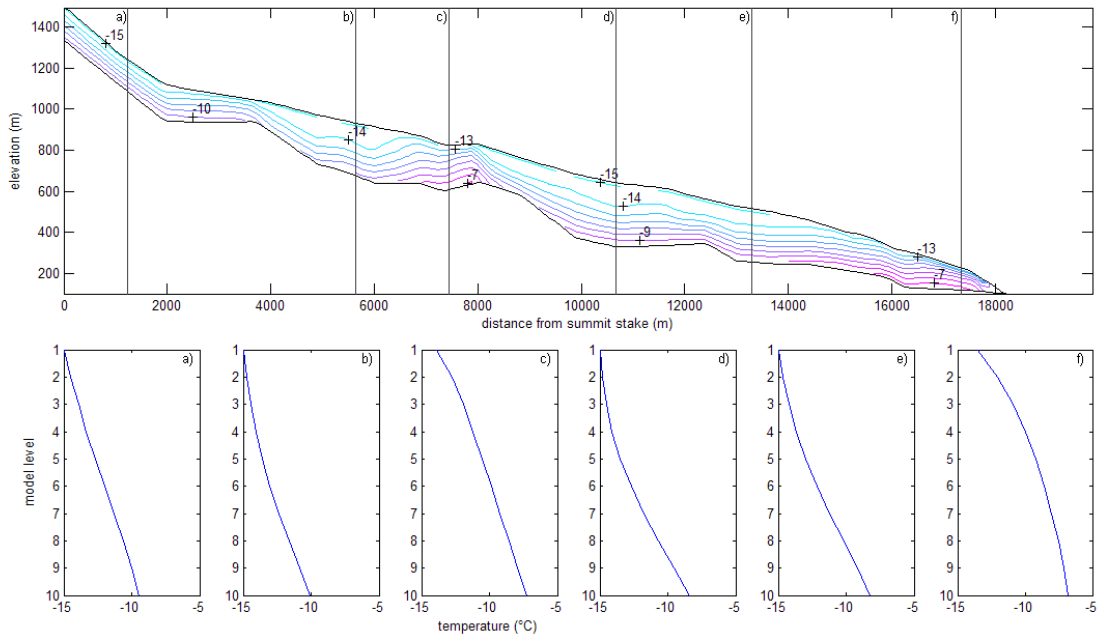


Figure 4.3. Modeled JEG equilibrium ice temperatures under a present-day mean annual air temperature of -15°C and a geothermal heat flux of 0.06 W m^{-2} : glacier cross-section and corresponding depth-profiles.

While modeled equilibrium englacial temperature profiles (Figure 4.3a-f) are commensurate with the derived areas of positive and negative vertical ice velocities (Figure 4.2b), nowhere do basal temperatures exceed -5°C . Advective cooling of the glacier bed is evident immediately downstream of the nunatak, where basal ice temperatures of $\sim -8.5^{\circ}\text{C}$ are computed (whereas 1D modeled static-ice basal temperatures here would range between -4.5°C and -7°C). Frictional warming of the glacier bed is evident near the snout where basal ice temperatures of $\sim -6.5^{\circ}\text{C}$ are computed (whereas 1D modeled static-ice basal temperatures would normally range between -9°C and -12.5°C for ice 100-200m thick).

In this 2D equilibrium experiment, then, geometry-related, forced advective cooling of the ice just below the nunatak more than compensates for internal frictional heating due to ice deformation, and the glacier is predicted to be entirely cold-based. This result would suggest that JEG's inferred warm basal temperatures are indeed out of equilibrium with present-day SATs and basal geothermal heating. Evidence suggests, however, that these BCs are likely supplemented by other sources of heat, both at the surface and at the bed.

4.3.1.2 WITH SUPPLEMENTARY SURFACE HEAT FLUXES

The preliminary 1D static ice experiments described above suggested that an increase in surface temperatures from the mean annual SAT value of -15°C to

between -8°C and -11°C could result in a warm bed for ice 300-400m thick. Possible mechanisms for augmenting surface ice temperatures are latent heating due to surface refreezing, heat generation by firn compaction, and heat fluxes from the ice below where vertical ice velocities are positive.

Except near the summit, measured JEG 15m-depth ice temperatures are warmer than the mean annual SAT. As noted in section 4.1, average 1998-99 15m ice temperatures ranged from approximately -15°C near the summit to approximately -13.5°C near the snout, with a broad maximum centred about the nunatak and the ELA. Peak observed values reached -8°C to -9.5°C immediately upstream of the nunatak.

Given that maximum observed 15m-depth ice temperatures are located immediately upstream of the nunatak, in the vicinity of the ELA, it would appear that the primary additional sources of surface heating for JEG are the positive vertical velocities in this location (Figure 4.2b) and surface refreezing. Surface refreezing and the accumulation of superimposed ice tend to concentrate near and just upstream of the ELA (e.g. Paterson, 1994, p10).

The effect of heat fluxes from below, where $w>0$, is parameterized in the surface BC in the model (as discussed in section 4.2.5.1). In the first 2D equilibrium experiment above, this resulted in near-surface ice temperatures of -13.5°C immediately upstream of the nunatak and of -13°C near the snout (Figure 4.3). However, while near-surface model temperatures are well-simulated as a result of this process near the snout, they fall short of the observed values immediately upstream of the nunatak by 3.5°C to 5°C . This suggests that surface refreezing is a key component of the surface energy balance near the ELA of JEG.

To examine whether surface temperatures modified by refreezing have an important impact upon the basal ice temperature computed with the 2D ice temperature model, JEG equilibrium englacial temperatures were recalculated using the measured 15m-depth ice temperatures as the present-day surface BC, instead of the mean annual SAT. Again, measured mean 15m-depth ice temperatures reflect mean annual air temperatures, modified by surface refreezing, firn compaction, and heat fluxes from the ice below where $w>0$.

Using this alternate surface BC produces warmer, but similarly-shaped, englacial temperature profiles as does using mean annual air temperatures as the surface BC (Figure 4.4). Modeled JEG equilibrium basal temperatures in this experiment are warmer than those achieved when SAT was used as the surface BC, now reaching $\sim 3.5^{\circ}\text{C}$ immediately upstream of the nunatak where heating due to refreezing is maximum and vertical velocities are positive (Figures 4.4c and 4.5a) and reaching $\sim 2.5^{\circ}\text{C}$ between 1 and 3 km upstream from the snout, where vertical velocities are positive and internal frictional heating is significant. Internal frictional heating over the lower part of the glacier is cancelled out to a lesser degree by advective cooling from upstream in this 15m-depth ice temperature BC

experiment than it was in the previous SAT BC experiment (cf. Figures 4.3 and 4.4).

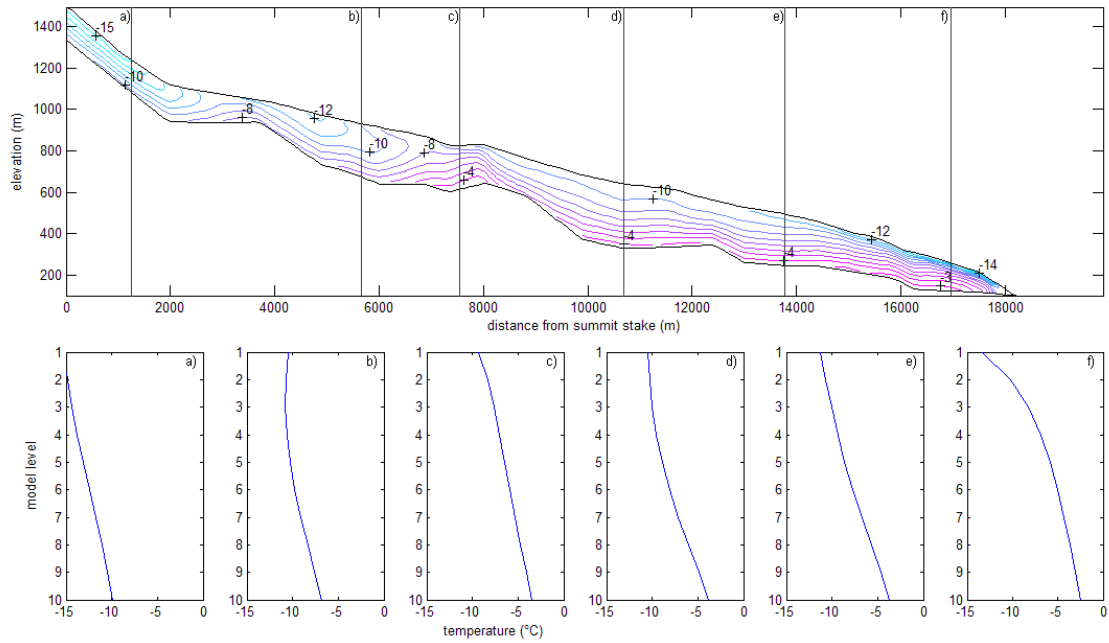


Figure 4.4. Modeled JEG equilibrium ice temperatures under present-day 15m-depth ice temperatures (surface refreezing effects are included): glacier cross-section and corresponding depth-profiles.

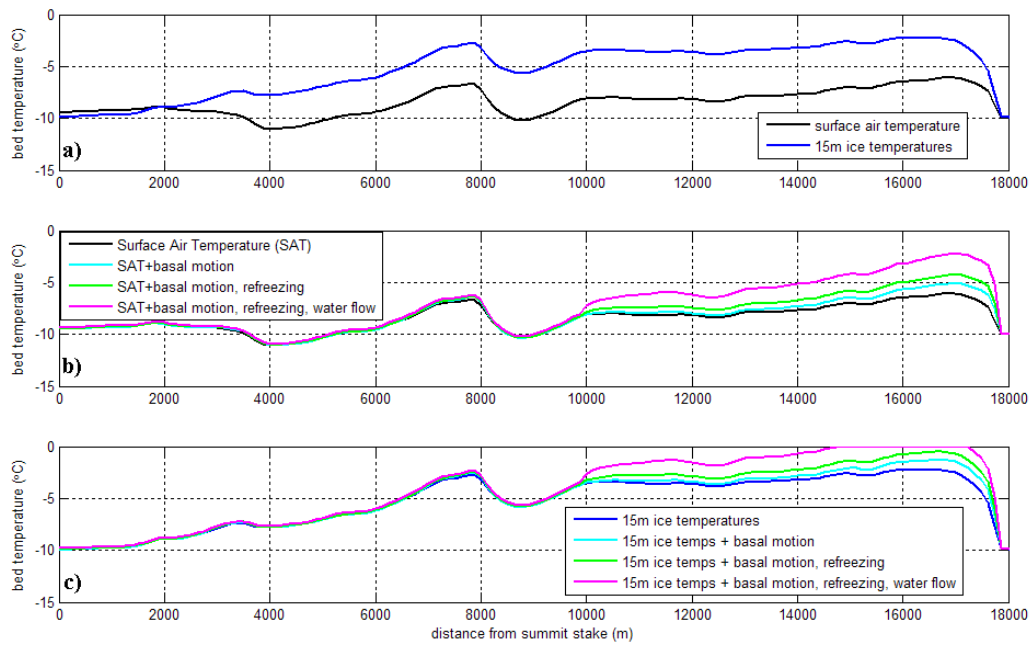


Figure 4.5. Equilibrium bed temperatures: a) for two different surface BC's; b) for SATs and for various additional basal heat sources; c) for 15m-depth ice temperatures and for various additional basal heat sources.

The augmented near-surface temperatures near the ELA significantly modify the advective cooling of the ice downstream from the nunatak, raise surface and basal temperatures by an average of 3-4°C along much of the glacier's length, and allow for warmer basal temperatures near the glacier snout (cf. Figures 4.3 and 4.4; Figure 4.5a). However, again, nowhere is the PMP actually reached (Figures 4.4 and 4.5), although warm basal conditions are inferred from radio-echo sounding measurements (Copland and Sharp, 2001).

It should be noted that the ELA, the zone of surface refreezing, and the observed area of maximum 15m-depth ice temperatures have likely risen in altitude during the past century (given the ice core melt/refreeze-records from the nearby Agassiz Ice Cap – Koerner and Fisher, 1990). Until recently, the refreezing process likely primarily influenced surface ice temperatures below the nunatak and the basal ice temperatures downstream from that location.

4.3.1.3 WITH SUPPLEMENTARY BASAL HEAT FLUXES

The preliminary 1D static-ice experiments described at the beginning of section 4.3.1 suggest that, for ice 300-400m thick, G would need to be increased (or supplemented by other internal/basal heat fluxes) to a value of ~ 0.085 to 0.12 W m^{-2} , in order for the basal ice to reach the PMP under an SAT of -15°C .

In section 4.2.5.2, the magnification of geothermal heat fluxes in deep valleys was discussed, as well as the addition of supplementary basal heat sources to the lower BC, including frictional heating due to basal sliding, latent heating due to refreezing of basal meltwater, frictional heating due to the deformation of subglacial sediments, and heat fluxes related to subglacial water flow and to water flow within subglacial sediments. Here, reasonable maximum values for these supplementary heat fluxes are estimated for JEG, and equilibrium basal temperatures are recomputed to assess the impacts of these.

Topographic Intensification of Geothermal Heat Fluxes: While pronounced topography can intensify the geothermal heat flux in deep subglacial trenches, by up to 100% in some cases (van der Veen et al., 2007), JEG is not located in a particularly deep or narrow valley (Figure 4.1). The subglacial trenches modeled by van der Veen et al. (2007), which had depth-to-width ratios of $\sim 1:10$ and $\sim 1:2$, produced intensifications of $\sim 1.25\times$ to $\sim 2.0\times$, respectively (i.e. the narrower or deeper the subglacial trench, the greater the enhancement). Since no deep subglacial trench comparable to those detected for Petermann Glacier and Jakobshavn Isbrae (van der Veen et al., 2007) was detected in the JEG radio echo sounding transects made by Copland and Sharp (2001), the extent of any intensification of its geothermal heat flux, beyond the area-appropriate value of 0.06 W m^{-2} (Beltrami and Taylor, 1995), is therefore likely negligible. Bingham et al. (2008) experimented with a basal (geothermal) heat flux increased by an extreme factor of 50% in their model, but even so found that nowhere did the bed of their model JEG attain the PMP under equilibrium conditions. In this study, a factor of 50% is considered unrealistic for an assessment of the true extent of JEG's thermal disequilibrium. Any intensification, if it exists at all, will be far less than the 25% ($1.25\times$) calculated for Petermann Glacier (van der Veen et al., 2007). Furthermore, as pointed out in Bingham et al. (2008), "the region's geology and longstanding tectonic stability (Hodgson, 1989) provide no evidence that geothermal heating in this region should be significantly higher." Topographic intensification of the local geothermal heat flux is therefore considered negligible in this study.

Frictional Heating due to Basal Sliding: Where basal melt occurs, or where supraglacial meltwater makes its way to the bed of the glacier, basal sliding may occur. Frictional heating due to this sliding may then contribute to the basal heat fluxes in the lower BC. The magnitude of this heat flux depends on the sliding velocity, which here is estimated by differencing the measured summer and winter JEG ice velocities (as presented in Copland et al., 2003b). Summer velocities in the ablation area of JEG are on average 62% higher than winter velocities, and locally up to double overwinter values (Copland et al., 2003b). While some basal motion is likely during the winter months (Copland et al., 2003b; Bingham et al., 2008), its derived magnitude is model-dependent and is therefore debatable (Wohlleben, T, M. Sharp and A. Bush: John Evans Glacier, Nunavut, Canada: a Case for Modeling Surface Ice Velocities using a Linearly Viscous Shallow Ice Equation Model *unpublished manuscript*). Winter sliding is

therefore neglected here. A maximum summer sliding velocity, u_b , of 10 m yr^{-1} is considered in this calculation. Frictional heating due to sliding is calculated from $u_b \tau_b$, where the basal stress $\tau_b = -\rho g h (\partial h / \partial x)$, where $\rho = 910 \text{ kg m}^{-3}$ is the density of the ice, $g = 9.8 \text{ m s}^{-2}$ is the acceleration due to gravity, $h = 250 \text{ m}$ is approximately the average thickness of the ice, and $\partial h / \partial x = 0.07$ is the average surface slope of the glacier. This gives a maximum summertime basal sliding heat flux of 0.05 W m^{-2} . Because the model uses annual average values in its computations, and since this degree of summertime sliding occurs over a period of only 1-2 months out of the year, the maximum contribution of frictional heat from basal sliding that can be added to the lower model BC is less than 0.01 W m^{-2} . However, given the uncertainties of winter sliding velocities, a heat flux value of 0.01 W m^{-2} is considered here, raising the possible basal heat flux from a geothermal-only value of 0.06 W m^{-2} to 0.07 W m^{-2} . Note that seasonal basal sliding will also increase seasonal horizontal mass flux divergences and consequent advective cooling of the ice. This effect may counteract the basal frictional heating in some locations.

Latent Heating due to Basal Refreezing: Latent heating due to basal refreezing is another possible source of enhancement to the lower BC of the model (see equation 7). Large scale accretion of basal ice from through-flowing water that enters areas of the bed below the PMP may be possible in some areas of the ablation zone. Basal regelation layers are generally a few millimeters to a few centimeters thick (e.g. Paterson, 1994, p400). Assuming a growth rate of $\dot{m} = 0.001 \text{ m yr}^{-1}$, the heat contribution $\rho L_f \dot{m}$ is computed to be $(910 \text{ kg m}^{-3}) \times (3.35 \times 10^5 \text{ J kg}^{-1}) \times 0.001 \text{ m yr}^{-1} / (365 \times 24 \times 3600 \text{ s yr}^{-1}) = 0.01 \text{ W m}^{-2}$, raising the possible total basal heat flux total from 0.07 W m^{-2} to 0.08 W m^{-2} .

Frictional Heating due to Subglacial Sediment Deformation: Frictional heating due to subglacial sediment deformation is another possible basal heat source for the ablation area of JEG. It is likely that the lower portion of JEG is underlain by a layer of sediment, given that the proglacial area is covered in sediment, although its extent and thickness are unknown. Nevertheless, deformation of basal sediments is conceivable for the lower ablation zone of JEG. In their numerical experiments, Thorsteinsson and Raymond (2000) predict a maximum basal warming of $\sim 1^\circ\text{C}$ resulting from sediment deformation, and it is possible that such a warming might be significant to JEG bed temperatures immediately upstream from the terminus. Using equation (3), multiplied by $\rho c_p h$, and applying till-appropriate values, a seasonal heat flux of $\sim 0.05 \text{ W m}^{-2}$ can be obtained for a sediment layer 10m thick during the summer months when the greatest basal motion is observed. Similar to basal sliding, annual average heat fluxes due to sediment deformation are likely less than or equal to 0.01 W m^{-2} . Because basal motion is likely to be either due to basal sliding or to subglacial sediment deformation, but not both, the total possible basal heat flux due to additional basal heat sources so far still remains 0.08 W m^{-2} .

Basal Heat Fluxes Related to Subglacial and Groundwater Flow: Observations and numerical experiments indicate that where there is a flux of groundwater through subglacial sediments, basal temperature gradients can be more than an order of magnitude greater than the commonly chosen basal boundary condition, $\partial T/\partial z = -G/K$ (Clarke et al., 1984; Echelmeyer, 1987). Assuming that this effect can be represented as a basal heat flux (similar to the geothermal heat flux), Clarke et al. (1984) calculate a value of 0.46 W m^{-2} for a small stream through the substrate. Echelmeyer (1987) argued for a value of as much as 0.63 W m^{-2} for glaciers with slopes of 0.3. Assuming that water flows through the sediments underlying JEG's lower ablation zone, and given that the average bed slope of JEG is ~ 0.07 , this would imply an additional heat flux of 0.15 W m^{-2} at the glacier bed during months of high subglacial water flow. Assuming that this heat source is seasonal and related to the amount of supraglacial meltwater reaching the bed, annual average values for this basal heat source are likely less than or equal to 0.025 W m^{-2} , raising the total maximum possible basal heat flux to 0.105 W m^{-2} . Deviations from this average value are considered in the time-dependent experiments in section 4.3.2.

The impacts of these additional basal heat sources upon modeled JEG ablation-zone ice-bed equilibrium temperatures are illustrated in Figures 4.5b and 4.5c, for the two different surface BC's discussed above. Without the combined influence of present-day surface refreezing and significant subglacial water flow, equilibrium basal temperatures nowhere would reach the PMP (as was also found by Bingham et al., 2008). Under both of these influences, JEG model equilibrium basal temperatures are able to reach the PMP over the region between 1 and 3 kilometres upstream from the glacier terminus.

However, since changes in the historical altitude and extent of surface refreezing are unknown, specifically how these may have differed from present during the Little Ice Age (LIA), and since the modeled JEG cross-section requires on the order of 2000 years to reach a thermal equilibrium, it seems prudent to assume that the true equilibrium basal temperatures for JEG lie somewhere between the minimum calculated values (Figure 4.5b) and the maximum calculated values (Figure 4.5c), and that they do not reach the PMP. Furthermore, meltwater-related basal heat sources like those due to sliding, refreezing and subglacial water flow are only activated once the bed reaches the PMP or if a significant amount of supraglacial meltwater is able to force its way to the bed and under the glacier. If the true equilibrium basal temperatures for JEG all lie below the PMP, it is unlikely that they are subject to these additional basal heat sources. However, even if somehow present, these are not enough to bring the bed to the PMP in the absence of the surface refreezing effect.

4.3.1.4 SUMMARY OF EQUILIBRIUM EXPERIMENT RESULTS

It is concluded that JEG's inferred warm basal temperatures, especially those of its upper ablation zone, are not in equilibrium with its present-day BC's. How did

JEG's bed attain the PMP, and how have these warm temperatures persisted to the present-day? As suggested for Laika Glacier by Blatter and Hutter (1991), LIA-related ice thickness changes may be the indirect cause of the observed warm basal temperatures, while basal heat fluxes related to a positive sliding feedback may have served to prolong the existence of the warm basal temperatures to the present-day.

4.3.2 *Time-Dependent Experiments*

The aim of this section is to determine whether past climate, combined with internal and external feedbacks, may have played a role in creating the present-day thermal disequilibrium of JEG. Specifically, the following time-dependent experiments were performed to determine the influence of historical SATs in the development of the present-day thermal disequilibrium of JEG. Both SAT and/or SAT-related BC changes over time could potentially have led to the present-day “warm” glacier bed. For example, JEG bed temperatures may still be responding to:

- 1) past positive SAT perturbations such as those related to the Holocene Climatic Optimum (CO) and the Medieval Warm Period (MWP). However, based on the temperature measurements made for White Glacier (a glacier of similar size and flow to JEG – Blatter, 1987), the temperature anomalies generated by these warm climate events have likely diffused into the subglacial substrate and are no longer significantly impacting ice temperatures.
- 2) past greater ice thicknesses associated with past SAT changes, perhaps related to the Little Ice Age (LIA) which spanned ~1450-1850AD (e.g. Jones and Briffa, 2001). This possibility was raised by Blatter and Hutter (1991) as an explanation for the observed thermal disequilibrium of Laika Glacier.
- 3) a glacier sliding feedback initiated during a time of thicker ice and warmer basal conditions. Again, this was suggested by Blatter and Hutter, 1991, as an explanation for the warm basal temperatures observed for Laika Glacier.
- 4) changes in surface refreezing conditions. Surface refreezing of percolated meltwater may have been greater during the LIA and, because it tends to be localized near the ELA, its maximum would likely have been displaced to lower elevations (to what is now the upper ablation zone of the glacier) during this time.
- 5) changes in supraglacial meltwater production over time, and the amounts reaching the glacier bed.

Furthermore, the historical surface BC changes in these scenarios may have been additionally influenced by surface ice-atmosphere feedbacks, serving to modify and amplify the changes.

4.3.2.1 THE DIRECT IMPACT OF PAST AIR TEMPERATURE CHANGES

The following 2D ice temperature model experiments were conducted to assess the potential (direct) impact of historical SAT changes upon JEG's englacial temperatures. In these experiments, constant ice thicknesses and ice flow through time were assumed, and active supplemental heat sources at the surface and the ice-bed interface were neglected. While this may not appear very realistic, the aim was to isolate as much as possible the direct influence of historical SAT changes upon englacial, basal, and sub-glacial temperatures before additionally considering and examining the impact of ice thickness changes and flow changes over time.

The following five time-dependent ice temperature experiments were performed, starting from an equilibrium state computed under present-day BC's, by applying the historical SAT-anomaly time series derived from inverted GRIP borehole temperatures (Dahl-Jensen et al., 1998):

- 1) spanning 35,000 years, encompassing the Last Glacial Maximum (LGM) to the present day (2000AD), assuming a bed composed of saturated sand;
- 2) spanning 35,000 years, encompassing the LGM to the present day (2000AD), assuming a bed composed of solid bedrock;
- 3) spanning 35,000 years, encompassing the LGM to the present day (2000AD), assuming a saturated-sand bed at constant equilibrium;
- 4) spanning 600 years, encompassing the LIA-onset to the present day (2000AD), assuming a saturated-sand bed at constant equilibrium; and
- 5) spanning 600 years, encompassing the LIA-onset to the present day (2000AD), assuming a saturated-sand bed at constant equilibrium, but with modified LIA SAT-anomalies closer to the $\sim 1.5^{\circ}\text{C}$ Arctic average 19th- to 20th-century warming discussed in Overpeck et al. (1997).

The first two experiments were conducted to determine the impact of the bed conductivity and heat capacity upon subglacial and ice-bed interface temperatures. Experiment 3 was conducted to determine whether a large difference was realized in ice-bed temperatures when full subglacial temperature calculations were replaced with a constant equilibrium temperature gradient at the bed. Experiment 4 was conducted to further investigate whether a large difference in englacial and ice-bed interface temperatures were realized if the model was run from the LIA-onset onwards instead of from the LGM onwards, given that climate signals prior to and including the MWP have likely reached the bed of JEG at the present day and diffused into the subglacial substrate. Finally, the purpose of experiment 5 was to calculate a more realistic impact of LIA temperatures upon JEG's englacial temperatures by replacing GRIP-derived SAT-anomaly values with CHA-appropriate values.

As already mentioned, the historical SATs used as the surface BC in the experiments are the SAT anomalies derived from the inverted GRIP borehole

temperatures (Dahl-Jensen et al. 1998) added to the present-day mean annual SAT for JEG. The GRIP 100+ ka SAT-anomaly time series was chosen because it is one of the longest available published Arctic temperature time series spanning the LGM to the present-day. This time series comprises the period leading up to and including the Last Glacial Maximum (LGM: where the average mean annual air temperature anomaly for the period -125 ka to -25 ka BP is $\sim(-23^{\circ}\text{C}-0^{\circ}\text{C})/2=-11.5^{\circ}\text{C}$), the Holocene Climatic Optimum (CO: $+2.5^{\circ}\text{C}$ from -8 to -4.5 ka BP), the Neoglacial cooling (minimum -0.5°C at -2 ka BP or 0 AD), the Medieval Warm Period (MWP: maximum $+1^{\circ}\text{C}$ at 1000 AD), the LIA (minima of -0.5°C at 1550 AD and -0.7°C at 1850 AD), and the recent warming to current (i.e. 2000 AD) air temperatures (which includes a temperature maximum of $+0.5^{\circ}\text{C}$ at 1930 AD). Note that in experiment 5, the LIA SAT anomalies from GRIP are amplified from -0.5°C at 1550 AD and -0.7°C at 1850 AD, to more CHA-appropriate values of -0.8°C at 1550 AD and -1.2°C at 1850 AD (e.g. Overpeck et al., 1997; see also Chapter 3 of this thesis).

For the long LGM-to-present model runs, which also included a 100 ka spin-up period under fixed BCs to allow the subglacial temperatures down to -2 km a.s.l. to equilibrate, 4 ice layers and 10 basement layers were used in the temperature integrations (Figure 4.6a). For the shorter, ice-only, LIA-to-present model runs, 10 ice layers were used, although, as was discussed previously (section 4.2.4), this increase in resolution makes little difference to the results, other than to smooth them to some extent.

Results of the first two experiments indicate that the LGM signature dominates subglacial temperatures, while the LIA dominates englacial temperatures. These results agree with the results of Johansen et al. (1995) which show that glaciated valley subsurface temperatures are colder than those of non-glaciated valleys, and with the borehole temperature measurements of Blatter (1987) which indicate that the LIA is responsible for a widespread englacial temperature minimum in White Glacier that extends downstream from its accumulation zone.

The depth and magnitude of the LGM signal within the present-day model bed is strongly affected by the thermal conductivity and diffusivity of the bed. Assuming a bed conductivity and diffusivity appropriate for semi-frozen saturated sand with 40% pore space (values similar to those for pure ice – Peixoto and Oort, 1992, p221) results in an LGM-related temperature anomaly (with respect to the equilibrium state) of $\sim-2^{\circ}\text{C}$ between -1360 and -1470 m below the ice bed (Figure 4.6b). Assuming a bed conductivity and diffusivity appropriate for solid generic rock (values approximately double those of semi-frozen saturated sand – e.g. Bauder et al., 2005; Huybrechts, 1996) results in an LGM-related temperature anomaly (with respect to the equilibrium state) of $\leq-5^{\circ}\text{C}$ at ~-3500 m below the ice bed in the upper accumulation zone and at a depth below -2000 m a.s.l. for the rest of the glacier's length (Figure 4.6c).

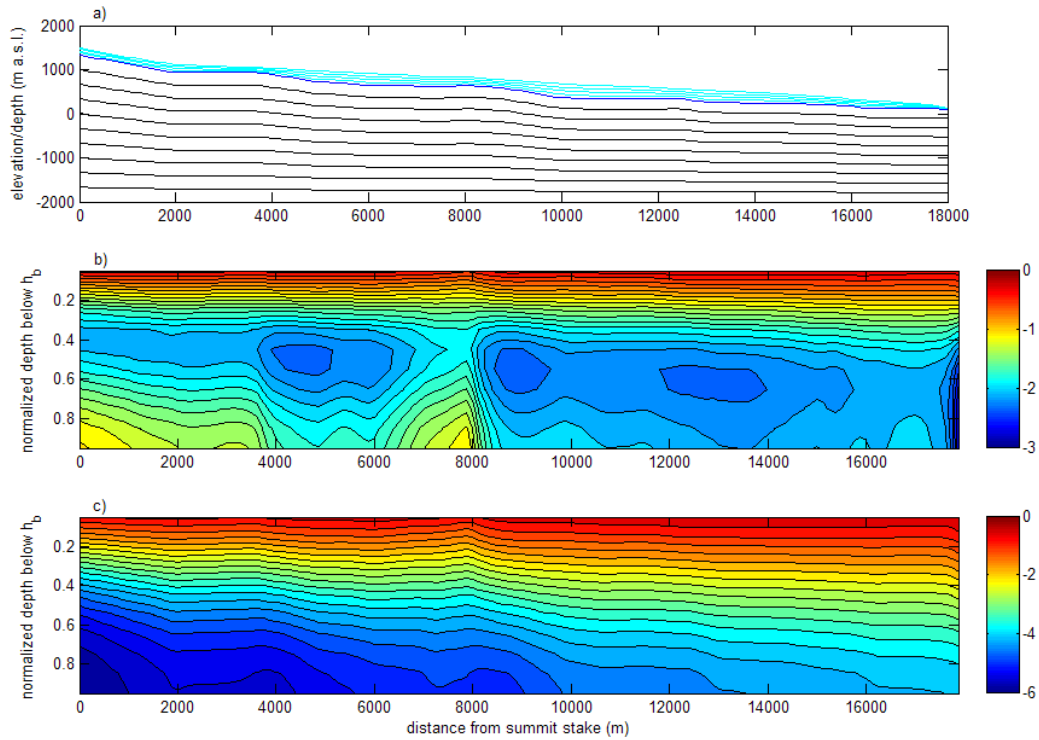


Figure 4.6. a) Ice and bed layers used in the model integrations; b) Subglacial negative LGM-related thermal anomaly in a semi-frozen saturated sand substrate; c) Subglacial negative LGM-related thermal anomaly in solid bedrock. Note that the normalized ice depths in b) and c) represent different actual depths below the ice bed along the length of the glacier, because the bed thickness (-2 km a.s.l. + the bed elevation) is greater upstream than it is downstream. For example, at the upstream end of the glacier, 0.5 represents 1700 m below the ice bed, or -300 m a.s.l. At the terminus, 0.5 represents 1050 m below the ice bed, or -950 m a.s.l.

In the sand bed case, the permafrost ends some 350-450m below the ice bed, while in the solid bedrock case, subsurface temperatures reach 0°C near 700-800m below the ice bed. Permafrost layer thicknesses in the CHA range between 200 and 800 m (Natural Resources Canada, National Permafrost Database – http://gsc.nrcan.gc.ca/permafrost/database_e.php). While thick ice will in most cases result in decreased subglacial permafrost layer thicknesses because it insulates the ground from cold SATs, ice covered areas can also preserve greater subglacial permafrost layer thicknesses by preventing the warming of the ground in the wake of cold events such as the LGM (e.g. Johansen et al., 1995). In the saturated sand case, K , C , and k should be allowed to change as the frozen water fraction decreases to 0%, where $K=1.53 \text{ W K}^{-1} \text{ m}^{-1}$ and $C=2.89 \text{ J m}^{-3} \text{ K}^{-1}$ and $k=0.5 \times 10^{-6} \text{ m}^3 \text{ s}^{-1}$ are the values for 100% liquid water in the pore space. Decreasing frozen water fractions would have the impact of making subglacial temperature gradients shallower with depth, an impact which can be important for subglacial temperature calculations where significant amounts of permafrost exist. However, because subsurface melting and associated complications occur so deep below the ice bed in these historical SAT experiments, the effect of allowing for

changes in K , C , and k near the base of the permafrost layer were not examined here. A full examination may be found in Johansen et al. (1995).

Equilibrium ice-bed temperatures are colder in the solid bedrock experiment than in the semi-frozen saturated sand bed case by $\sim 2^{\circ}\text{C}$ everywhere. For solid bedrock, the time-dependent ice-bed temperatures are colder than the equilibrium ice-bed temperatures by -0.3°C to -0.35°C . For a semi-frozen saturated sand bed, the time-dependent ice-bed temperatures are colder than the equilibrium ice-bed temperatures by -0.2°C to -0.25°C .

In all five of the JEG model experiments in this section, the LIA anomaly is located at the bed of JEG in the higher accumulation zone, where the ice is thin, and lies at a depth of $\sim 150\text{--}230\text{m}$ in the lower accumulation zone and upper ablation zone, where the ice is thicker (e.g. Figure 4.7c). These results concur with the White Glacier borehole temperature measurements of Blatter (1987) which indicate that the LIA is responsible for a widespread englacial temperature minimum that extends downstream from its accumulation zone. Since all five experiments produced very similar-looking englacial thermal patterns, only those of experiment 5 are shown here (Figure 4.7). Note, however, that the magnitude of the LIA anomaly in experiment 5 is greater than that of the other experiments, due to the use of CHA-appropriate LIA SAT-anomalies as opposed to GRIP LIA SAT-anomalies in the experiment. Figure 4.7 will be referred to as an illustration of all the LIA-related results discussed in this section.

The magnitude of the LIA-related englacial ice temperature anomaly is $\sim -0.18^{\circ}\text{C}$ to -0.25°C in the first two experiments, which used GRIP SAT-anomalies. However, in these experiments, the negative englacial temperature anomaly associated with the LIA merges with the subsurface LGM anomaly at the glacier bed, so that it is less distinct than that measured in White Glacier. Note that while differences between time-dependent and equilibrium 2D JEG modeling results show a negative englacial thermal anomaly related to the LIA (which looks similar to the measured minimum in the thermal profile of White Glacier), JEG time dependent results on their own do not show a strong temperature minimum (cf. Figures 4.7b and 4.7c). The visible minimum in measured ice temperatures in the accumulation zone of White Glacier (Blatter, 1987) is therefore likely the result of enhanced present-day warming at the surface, making colder interior temperatures more distinct. This is similar to the surface refreezing case modeled in Figure 4.4 (profile b), and a time-dependent surface refreezing experiment (section 4.3.2.2) further supports this assertion.

In both experiments 1 and 2, the temperature signal associated with the Holocene CO/MWP is absent, having diffused or been absorbed into the larger-amplitude LGM-related negative temperature anomaly below the ice bed. At the glacier surface, in both experiments, positive temperature anomalies associated with the SAT maximum of the 1930's are found, with maxima between $+0.01^{\circ}\text{C}$ and

+0.08°C located upstream and immediately downstream of the nunatak, (see figure 4.7c).

Replacing the time-dependent subsurface calculations in experiments 1 and 2 with an equilibrium basal state for semi-frozen saturated sand has little impact upon the depth and magnitude of the LIA-related ice temperature anomaly in the experiments. The primary difference between experiments 1 and 3 is that the ice-bed interface is $\sim 0.2^\circ\text{C}$ to 0.25°C warmer in experiment 3, because in the time-dependent bed case (experiment 1) some residual of the LGM still exists. As a result, the LIA-related thermal anomaly in the equilibrium bed case (experiment 3) appears slightly more distinct over mid-upper portions of the glacier in 2D profile contour plots of the results (e.g. Figure 4.7c).

Running the time-dependent model experiment from the onset of the LIA to the present day (i.e. 2000AD), assuming subsurface temperatures are at equilibrium, as opposed to running the experiment from -35 ka onwards, also produced negligible differences in the computed englacial and basal temperatures. This is not surprising, as it was already determined that the CO/MWP signals had been eroded by the larger LGM signal at depth and that the LGM residual at the bed was less than $\sim -0.25^\circ\text{C}$.

Based on the results of the first four experiments, it is concluded that SAT anomalies older than the LIA have little direct impact upon the present-day englacial and basal temperatures of JEG. For this reason, all subsequent experiments are performed for a period spanning only the 500 years from the LIA-onset onwards to the present-day, starting from an equilibrium state and using an equilibrium basal BC throughout. This greatly reduces the model integration time.

Experiment 5 is a repeat of experiment 4, except that CHA-appropriate LIA-related SAT-anomalies were used in the time-dependent surface BC. In this case, while the depth of the resultant englacial ice temperature anomaly does not change, the magnitude of the anomaly increases from a range of $\sim -0.18^\circ\text{C}$ to -0.25°C , to a range of $\sim -0.40^\circ\text{C}$ to -0.53°C (Figure 4.7c). This is now greater than the LIA-related englacial thermal anomaly of White Glacier (see Chapter 3). The 1D experiments of Chapter 3 indicated that $\sim 25\%$ of the original LIA SAT-anomaly is preserved when the CO/MWP signal is absent in the ice. For an SAT-anomaly of -1.2°C , this would result in an englacial LIA ice temperature anomaly of -0.3°C . The experiments in Chapter 3 were conducted with very low vertical ice velocities, however, $\leq -0.11 \text{ m yr}^{-1}$, representing conditions near a glacier or ice cap summit. The larger vertical ice velocities of JEG (reaching -1.8 m yr^{-1}) can help protect negative thermal anomalies from subsequent surface warming, by placing them deeper within the glacier than otherwise, over a similar period of time.

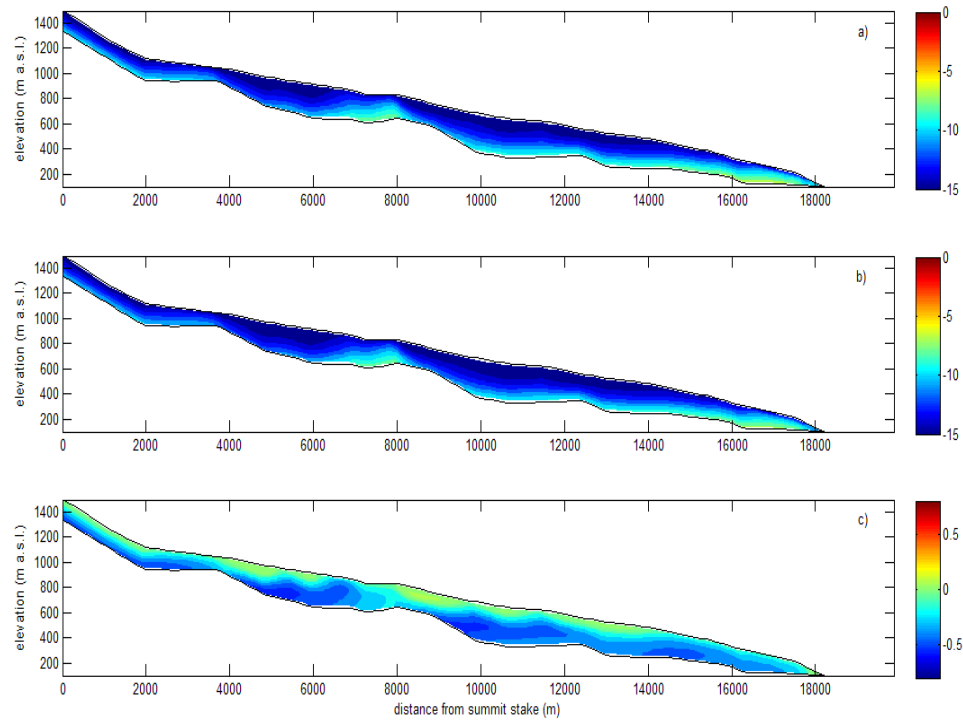


Figure 4.7. Modeled JEG 2D ice temperatures: a) equilibrium ice temperatures under a present-day mean SAT of -15.0°C and a geothermal heat flux of 0.06 W m^{-2} ; b) present-day (2000AD) temperatures following a 400 year period of colder than present SATs from 1500-1900AD (experiment 5); and c) the difference between the post-LIA results of experiment 5 and the equilibrium distribution. Ice thickness and velocity were assumed constant in these experiments.

In summary, the results of all the time-dependent modeling experiments in this section, which allowed for historical SAT changes, but neglected ice thickness and velocity changes, as well as supplementary heat sources at the surface and bed, all indicate that the direct result of past SAT changes has been to cool the ice and its bed. Without invoking other factors such as ice thickness changes and internal/external feedbacks, historical SATs only serve to further increase the degree of disequilibrium between JEG model results and observations.

4.3.2.2 THE INDIRECT IMPACT OF PAST AIR TEMPERATURE CHANGES: ICE THICKNESS CHANGES

The following 2D ice temperature model experiments were conducted to assess the potential (indirect) impact of historical SATs upon JEG's englacial temperatures. SATs can impact ice thicknesses through time by raising and lowering the ELA (i.e. by changing the mass balance and rates of firn compaction), by influencing atmospheric circulation and precipitation patterns, and by directly influencing ice temperatures, ice flow, and consequent mass flux divergences. Historical ice thickness changes, in turn, further influence the evolution of englacial and basal ice temperatures.

In these experiments, which start from an equilibrium state and are run forward in time from the LIA-onset to the present day (i.e. 2000AD), it is assumed that pre-LIA CHA ice thicknesses and glacier extents were similar to those of today and that JEG thickened by up to 50% during the LIA. Geomorphological and geological evidence indicates that by -8 ka to -7 ka BP, the Innuitian Ice Sheet which covered the CHA had retreated into the ice caps of today (e.g. England et al., 2006). Various proxy evidence (summarized in Bradley, 1990) indicates that in many places in the CHA, ice extents during the CO were less than those of the present day. Numerous CHA glaciers experienced a re-advance after the CO, followed by a subsequent recession (Bradley, 1990). While trim lines in the JEG catchment indicate an LIA-related JEG thickening more like ~ 20 - 25% , a thickening of 50% was used here because it corresponds to the 50% thicker ice model experiment of Blatter and Hutter (1991) for Laika Glacier and because it represents a maximum limiting case. As discussed at the beginning of section 4.2, glacier length changes, however, were neglected in the model experiments because even a neoglacial or LIA advance and post-LIA retreat of up to 1 km would only represent 5% of the total glacier length (and there is no geomorphological evidence for any such advance/retreat – *pers. comm.* Martin Sharp).

Starting from an equilibrium state computed under present-day BC's and using the GRIP historical SAT-anomaly time series modified for the CHA as described above, four thickness-change experiments were performed by applying:

- 1) a linear thickening of JEG ice from present-day values to $1.5\times$ these values at the culmination of the LIA, followed by a linear thinning back to present-day ice thicknesses;
- 2) a rapid thickening of JEG ice to $1.5\times$ present-day values at the beginning of the LIA, followed by 400 years at these elevated thicknesses, then followed by a linear thinning from the culmination of the LIA back to present-day ice thicknesses;

3) a rapid thickening of JEG ice to $1.5\times$ present-day values at the beginning of the LIA, followed by 400 years at these elevated thicknesses, then followed by a non-linear exponential thinning from the culmination of the LIA back to present-day ice thicknesses. A rapid initial thickening and a non-linear exponential thinning (i.e. a thinning that doubles or accelerates with time), as opposed to a gradual linear thickening and thinning, may result when ice-atmosphere feedbacks such as the snow/ice-albedo feedback or the elevation – mass balance feedback are active;

4) a repeat of the thickness changes in experiment 3 supplemented with the additional basal heat fluxes described in the Equilibrium Model Solutions section from 1900AD onwards (when supraglacial meltwater production and amounts reaching the bed likely began to increase).

The first three experiments were conducted to determine the impact of ice thickness increases during the LIA upon JEG ice-bed interface temperatures and the persistence of any resultant temperature increases to the present day. The first experiment assumes that peak ice thicknesses were realized near the end of the LIA, and that the prior thickening and subsequent thinning occurred in a generally linear manner. The second and third experiments examine the impact of ice-atmosphere feedbacks upon such a scenario. Experiment 2 assumes a rapid initial thickening of the ice near the beginning of the LIA, then approximately constant ice thicknesses throughout the bulk of the cold period. This scenario is based upon the following reasoning. The cooling SAT trend at the beginning of the LIA, resulting in increasing snow cover and greater ice surface elevations, would have been amplified via the snow/ice-albedo feedback and the elevation – mass balance feedback. Initially this might have led to a rapid increase in seasonal snowfall, but eventually it would have resulted in the creation of an anticyclone over the centre of the CHA and a displacement of extratropical cyclones and associated precipitation further to the south. Increased sea ice cover during the LIA would also have reduced the atmospheric moisture content and precipitation amounts during this period. The third experiment duplicates experiment 2 but further assumes that the thinning from peak-LIA ice thicknesses to present-day values occurred in a non-linear, accelerating fashion. This scenario is based upon the reasoning that ice-atmosphere feedbacks act to amplify SAT and surface mass balance changes in the CHA (see Chapter 2). Amplifications lead to non-linear changes so that, for a chosen amplification of $2.0\times$, an initial -0.1 m yr^{-1} thickness change becomes -0.2 m yr^{-1} over time, which then becomes -0.4 m yr^{-1} , then -0.8 m yr^{-1} and so on. Accelerating, exponential ice thickness changes, as opposed to linear trends or changes, in ice thickness could be important to the evolution of basal temperatures. The non-linear mean annual thickness changes, for 1900-2000AD, at each horizontal grid point in the model were determined by first applying the equation $(1.5h_s - 1.0h_s) = 25\text{yr}(1b) + 25\text{yr}(2b) + 25\text{yr}(4b) + 25\text{yr}(8b)$ at each grid point, in order to determine b , the initial rate of change in ice thickness in m yr^{-1} . This parameter, b , was then doubled every 25 years in the model.

Experiment 4 duplicates experiment 3, but allows for the activation of supplementary basal heat sources, related to basal motion, basal refreezing, and subglacial water flow after 1900AD, in the wake of the LIA. These typically occur whenever and wherever basal temperatures reach the PMP, but can also be initiated by significant amounts of supraglacial meltwater reaching the glacier bed through moulins and crevasses. The maximum annual average values for each of these basal heat sources, determined in section 4.3.1.3, are used in this experiment. However, increases in meltwater production are also considered in subsequent experiments in section 4.3.2.5.

Results of the first 4 experiments indicate that both ice thickness changes and the post-LIA surface meltwater reaching the bed are important to the reproduction of warmer basal temperatures near the snout of JEG (Figure 4.8).

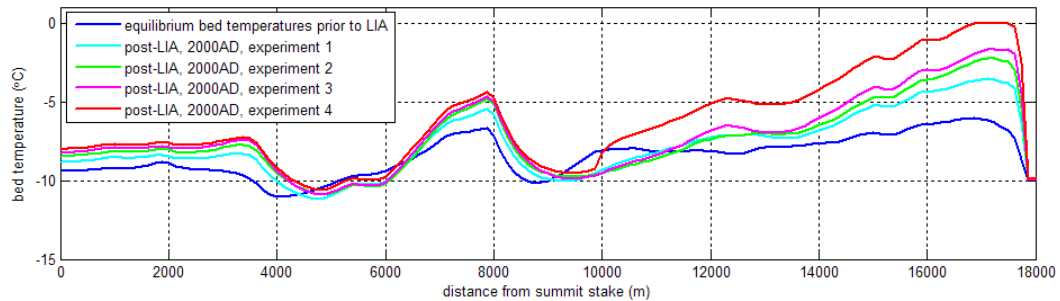


Figure 4.8. Time-dependent modeling results: JEG ice bed temperatures for the 4 experiments.

An increase in ice thickness by 50% during the LIA raises ice bed temperatures by 3.0-4.5°C over the lower two kilometers of the glacier, depending upon how the thickening and thinning are realized (Figure 4.8). Experiments which simulated rapid initial thickening and non-linear post-LIA thinning, related to ice-atmosphere feedbacks, indicate that while such external feedbacks can impact basal temperatures by up to 1.5°C they are not as significant as the bulk thickness change itself in raising basal temperatures. However, while the warmer-than-equilibrium ice temperatures related to past ice thickness changes do persist to the present-day in these experiments, once again nowhere do basal temperatures reach the PMP.

Allowing for additional basal heat sources related to basal motion, basal refreezing and groundwater fluxes in the ablation zone from 1900AD onwards, when supraglacial meltwater production and amounts reaching the bed likely began to increase, further raises JEG model basal temperatures, so that they do reach the PMP over the lower 1km of the glacier (while the snout itself remains frozen to the bed due to significant ice thinning at the terminus, as is observed – Figure 4.8).

4.3.2.3 THE INDIRECT IMPACT OF PAST AIR TEMPERATURE CHANGES: ICE THICKNESS CHANGES AND THE BASAL SLIDING FEEDBACK

Allowing for a basal sliding “feedback” in the experiments described above, as suggested by Blatter and Hutter (1991), whereby a warm lubricated bed allows for increased sliding, increased frictional heating, further basal melting and even further sliding, does not expand the area of warm basal temperatures produced by the JEG model. Repeating the above experiments but this time increasing mean annual surface velocities from present-day winter values to present-day summer values (and even up to 2× present-day winter values) where basal temperatures reach the PMP, results in greater cold advection from the negative englacial LIA ice temperature anomaly located upstream. This more than offsets any temperature increases due to frictional heating, and keeps the area of warm basal temperatures restricted to the last 1 km near the snout.

4.3.2.4 THE INDIRECT IMPACT OF PAST AIR TEMPERATURE CHANGES: SURFACE REFREEZING CHANGES

Observations, however, suggest that most of the bed in the JEG ablation zone is at the PMP (Copland and Sharp, 2001). Other factors than thickness changes and sliding feedbacks must therefore be active in raising basal temperatures and maintaining them at the PMP. To assess the impact of past changes in surface refreezing upon present-day JEG bed temperatures, two constant and one non-constant ice thickness model experiments were performed:

- 1) Assuming no change in surface refreezing amount or location over time (the historical SAT changes were simply applied to the 15m ice-depth temperatures discussed in Equilibrium Model Solutions section).
- 2) Assuming no change in surface refreezing amount, but decreasing the ELA and location of maximum refreezing by 200m in elevation (the LIA-related decrease in ELA determined by Wolken et al., 2008). A 200m elevation change is equivalent to a ~2500m horizontal displacement downstream. In this case the horizontal pattern in the difference between the present-day mean SAT and the 15m ice-depth temperatures was simply shifted downstream by 2500m between 1500AD and 1930AD, then moved back up to its present location. It is noted that this method is inexact, especially because the maximum in JEG 15m ice-depth temperatures above the nunatak is partially due to positive vertical velocities and heat fluxes from below in that location. Nevertheless, it provides an illustration of the thermal impact of such a shift in ELA.
- 3) Assuming a 25% thickness increase and no surface refreezing during the LIA, followed by an exponential glacier thinning after 1900AD and a restoration to present-day refreezing amounts and locations after 1930AD. No surface refreezing prior to 1930AD represents the limiting case for greatly reduced LIA summer surface melt and greatly reduced percolation and refreezing. After

1930AD, the difference between present day 15m ice-depth temperatures and the present-day mean annual SAT was added to the surface BC at each time step.

In the first experiment, modeled 2000AD JEG bed temperatures were everywhere slightly colder than the equilibrium bed temperatures computed using the 15m ice-depth temperatures as the surface BC, as a result of the LIA SAT-related englacial cooling (Figure 4.9). In the second experiment, JEG bed temperatures were noticeably cooler upstream of the nunatak and ELA, because the present-day surface refreezing heat source found in this location was displaced downstream for 400 years during the LIA (Figure 4.9). In this same experiment, bed temperatures below the ELA became only slightly warmer than equilibrium, however, because the resultant increase in surface refreezing due to the ELA-shift was not as drastic as the complete loss of surface refreezing upstream. In the third experiment (not shown), no impact upon basal temperature computations was realized. Less than one hundred years is not a sufficient length of time for the influence of latent heating due to post-LIA surface refreezing to reach and affect basal ice temperatures, especially in light of the past greater ice thicknesses.

In none of the experiments did the modeled 2000AD basal temperatures reach the PMP. A fourth experiment (a repeat of experiment 2) was then performed allowing for the additional basal heat sources described in the Equilibrium Solutions section and allowing for a 25% LIA thickening of the ice. Results of this experiment (Figure 4.9) indicate that such a combination of conditions could explain the warm present-day JEG bed temperatures over the lower ablation zone, but not those inferred for the upper ablation zone.

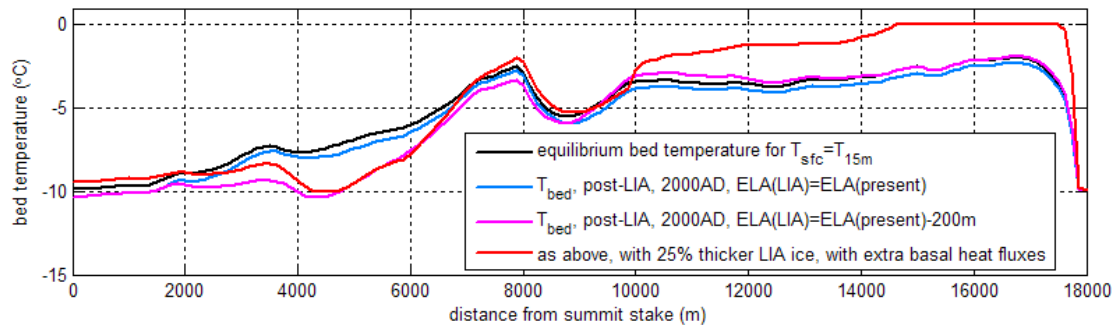


Figure 4.9. Time-dependent modeling results: JEG ice bed temperatures for the surface refreezing experiments.

4.3.2.5 THE INDIRECT IMPACT OF PAST AIR TEMPERATURE CHANGES: CHANGES IN SUPRAGLACIAL MELTWATER PRODUCTION AND AMOUNTS REACHING THE GLACIER BED

The final and most likely possibility for the observation that nearly the entire JEG ablation zone experiences warm basal temperatures at the present day is related to subglacial water flow. To examine whether JEG bed temperatures may have been

influenced by changes in supraglacial meltwater production and the amounts reaching the glacier bed over time, the following was considered. The heating related to subglacial groundwater flow estimated for JEG in section 4.3.1.3 represented the maximum heating based upon the figures given in Echelmeyer (1987). However, present day JEG supraglacial meltwater production is significant, with fluxes during meteorologically-related summer “events” reaching $5\text{--}30 \text{ m}^3 \text{ s}^{-1}$ (Boon et al., 2003). Much of this water reaches the bed and flows along the ice-bed interface during the summer, supplementing the groundwater flow, with residual amounts of liquid water persisting at the bed throughout the winter months (e.g. Bingham et al., 2008). Heat fluxes related to basal water flow can be calculated using:

$$q = -\rho g \frac{Q_w}{W} \frac{\Delta z}{\Delta x} \quad (10)$$

(equation 15 in Echelmeyer, 1987), where q is the heat flux, Q_w is the water flux, and W is the width of the glacier. For average summer basal water fluxes of $1\text{--}5 \text{ m}^3 \text{ s}^{-1}$, assuming an average JEG slope of 0.07 and a glacier width of order 10^3 m , values for average *annual* heat fluxes of 0.12 to 0.58 W m^{-2} are obtained, $10\times$ the value of 0.025 W m^{-2} estimated in the equilibrium section.

The value used in the Equilibrium Solutions section is a reasonable long-term average value if one assumes greatly reduced supraglacial meltwater production during the LIA. For example, $(50 \text{ years} \times \sim 0.3 \text{ W m}^{-2} + 550 \text{ years} \times \sim 0.0 \text{ W m}^{-2}) / 600 \text{ years} = 0.025 \text{ W m}^{-2}$. However, this value underestimates present-day values and also neglects the fact that summer supraglacial meltwater production may have continued throughout the LIA at lower elevations.

Two experiments were performed to examine the impact of: 1) continuous low basal water heat fluxes of 0.025 W m^{-2} in the ablation zone throughout the LIA to the present day; and 2) zero basal water heat fluxes in the ablation zone during the LIA, followed by present-day amounts of 0.35 W m^{-2} from the 1930AD SAT maximum and onwards. In these experiments, it was assumed that JEG was 25% thicker during the LIA and that a 200 m downward shift in ELA and surface refreezing pattern occurred during this period. Ice velocities were assumed constant throughout.

The two experiments gave nearly identical results (Figure 4.10): in the first experiment, basal temperatures reached the PMP from the 12km to the 18 km mark in the ablation zone, while in the second experiment, basal temperatures reached the PMP from the 10km to the 18km mark (i.e. along the entire 8 km length of the glacier ablation zone) (Figure 4.10b). The results of these experiments indicate that basal water fluxes likely played a key role in the evolution of JEG’s basal temperatures. While it is likely that water fluxes have increased over the past 100 years, to the currently observed amounts of $1\text{--}5 \text{ m}^3 \text{ s}^{-1}$, and that supraglacial meltwater production has risen in elevation over time, it is

sufficient that near-present-day amounts reached the bed of the upper ablation zone from ~1930AD onward, regardless of whether significant amounts of supraglacial meltwater reached the bed during the LIA.

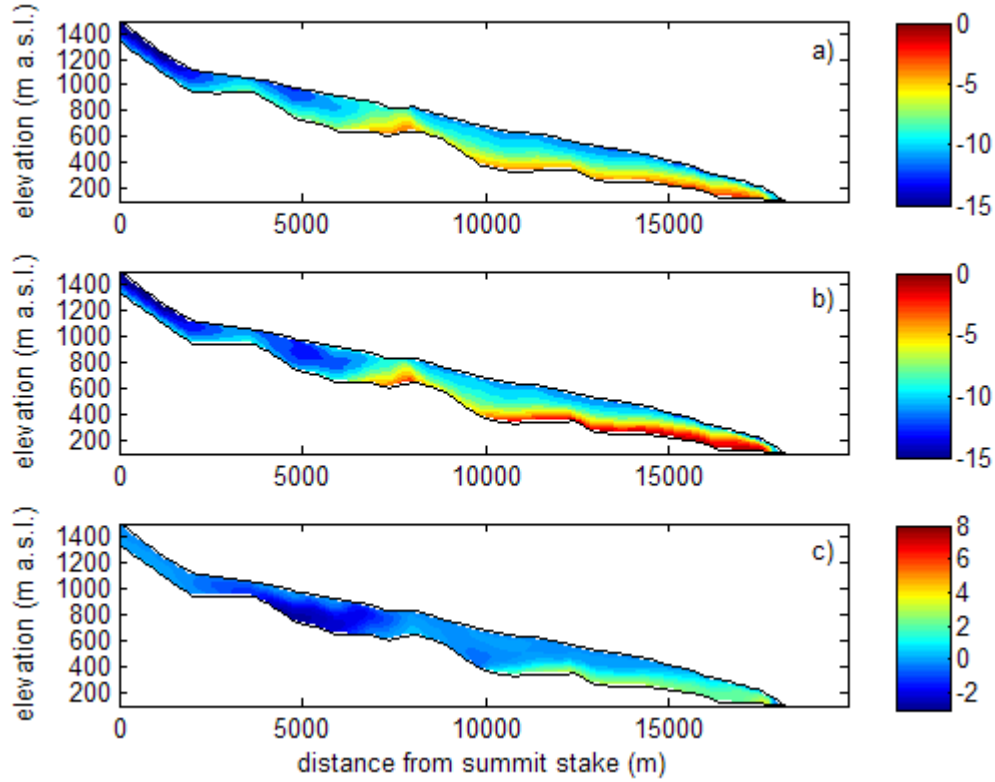


Figure 4.10. Modeled JEG 2D ice temperatures: a) equilibrium ice temperatures for present-day 15m ice-depth temperatures and a geothermal heat flux of 0.06 W m^{-2} ; b) present-day post-LIA temperatures, following a 400 year period of colder than present SATs, 25% thicker than present ice, a 200 m downward shift in ELA and surface refreezing, and accounting for present-day surface and basal meltwater fluxes; and c) the difference between the post-LIA results and the equilibrium distribution. Ice deformation velocities, calculated from present-day winter average values, were assumed to be constant and basal motion was neglected.

As a point of interest, the modeled englacial temperature pattern in the JEG accumulation zone (Figure 4.10b) now very closely resembles the internal ice temperature profiles measured in the White Glacier accumulation zone (Blatter, 1987), with a defined temperature minimum related to the LIA. The basal warming that resulted from the 25% thicker ice during the LIA has the effect of restricting the LIA-related negative ice temperature anomaly of the upper ablation zone to mid-depths, so that it no longer reaches the glacier bed (Figure 4.10b). Furthermore, the post-LIA increase in SAT, and ELA and associated surface refreezing pattern, has the effect of creating an ice temperature inversion near the glacier surface in the accumulation zone (Figure 4.10b).

4.4 SUMMARY AND DISCUSSION

Equilibrium model results suggest that JEG's internal temperature distribution is probably not in equilibrium with present-day atmospheric temperatures and basal heat fluxes. The thermal equilibrium timescale for this glacier is ~2000 years, and one cannot assume that near-present-day surface refreezing amounts and a continuous subglacial water flux persisted throughout the entire LIA period. Since there is much uncertainty regarding the historical changes of JEG's BCs (other than in the historical SAT changes which served to directly cool its interior and bed as a result of the LIA), one cannot conclude with confidence that JEG is in thermal equilibrium with its present-day BCs.

The results of time-dependent modeling experiments which allowed for historical SAT changes, but neglected ice thickness and velocity changes, as well as supplementary basal heat sources, indicate that the direct result of past SAT changes has been to cool the ice and its bed, further increasing the disequilibrium between JEG model results and observations. Model experiments which allowed for ice thickness changes, surface refreezing, and for surface-melt-driven basal water flow confirm that it is the indirect influence of past and continuing SAT changes which has been critical in the evolution of JEG's englacial and basal temperatures. Time-dependent experiments confirm that JEG is still responding thermally to past climatic perturbations.

Ice-atmosphere feedbacks do appear to play a role in determining basal temperatures, although their influence is not large. For example, ice-atmosphere feedback – related rapid ice thickening at the LIA-onset and post-LIA non-linear ice thinning together raised basal ice temperatures by a further 1.5°C over those produced by linear thickening/thinning rates in the experiments. Ice-atmosphere feedbacks such as the snow/ice-albedo feedback may also have served to amplify latter-day surface meltwater production, a critical factor in subglacial heat fluxes.

Englacial temperatures are a critical factor in determining glacier deformation rates, mass flux divergences, and the mass transfer from the accumulation zone to the ablation zone. Past LIA-related SATs have cooled much of the interior of JEG, reducing ice deformation, while latter-day surface meltwater reaching the glacier bed is allowing for warm basal temperatures and seasonal basal motion in the ablation zone. Lower deformation rates upstream of the nunatak and greater basal motion downstream of the nunatak will lead to a slight ice thickening above the ELA and large ice thinning below the nunatak, especially where mass flux divergences are large. Furthermore, at the present time, negative surface mass balances near the snout are more than able to compensate for the mass flux convergence in this area, otherwise some thickening would be evident. If the ELA does not rise any further, this situation will serve to increase JEG surface slopes over time, from the accumulation to the ablation zone, with further implications for ice flow.

4.5 CONCLUSIONS

The following conclusions were drawn from the results of this study:

- 1) JEG's internal and basal temperature distribution in the upper ablation zone is not in equilibrium with present-day SATs and ice thicknesses;
- 2) the *direct* result of past SAT changes has been to cool the ice and its bed, further increasing the disequilibrium between JEG model results and present-day observations;
- 3) the *indirect* influence of past and continuing SAT changes has been critical to the evolution of JEG's englacial and basal temperatures;
- 4) past greater ice thicknesses during the LIA are partially responsible for the elevated basal temperatures in the lower ablation zone of JEG;
- 5) latent heat released by surface refreezing during the LIA is also partially responsible for the elevated basal temperatures in the lower ablation zone of JEG;
- 6) post-LIA supraglacial meltwater reaching the glacier bed is the single most critical heat source responsible for the disequilibrium between present-day observed ice bed temperatures and modeled equilibrium ice bed temperatures under present-day BC's, especially in the upper ablation zone of JEG.

These results should be taken into account when modeling other predominantly cold polythermal glaciers in the Canadian High Arctic. Correct modeling of internal ice temperatures is critical to correctly modeling glacier flow and glacier response to climate perturbations.

4.6 APPENDIX: ENGLACIAL TEMPERATURES OF PREDOMINANTLY COLD POLYTHERMAL GLACIERS – A REVIEW

4.6.1 *Englacial Temperatures: Static versus Deforming Ice*

The internal temperature distributions of predominantly cold, polythermal glaciers are primarily determined by: 1) their boundary conditions or BC's (i.e. their local SATs, surface accumulation/ablation rates, and basal geothermal heat fluxes); 2) the thickness of the glacier (which serves to insulate the ground from SATs); and 3) the flow of the glacier (which serves: a) to entrain cold surface temperatures into the heart of the glacier; and b) as a frictional heat source where shearing and/or basal sliding occur). Other factors such as the thermal conductivity and heat capacity of the ice and the bed will also have an impact. Factors which serve to modify surface and basal BC's, such as the latent heat associated with

refreezing or the frictional heat generated by subglacial water flow, can also be important.

Where ice is static, the equilibrium vertical temperature profile at any horizontal position, x , along a glacier's length is determined primarily by thermal diffusion within the ice (Figures 4.11a to 4.11c). Englacial temperatures decrease linearly from cold SAT values near the surface to warmer temperatures near the bed (Figure 4.11c). Where the ice is thick enough (often nearer the summit in the case of ice caps), basal temperatures may reach the pressure melting point or PMP (Figure 4.11b).

Where the ice is deforming, thermal diffusion, thermal advection and internal and/or basal frictional heating will influence the equilibrium temperature profile at any horizontal position along the length of the glacier (Figures 4.11d to 4.11f). Near the glacier summit, mass flux divergences are positive and resultant vertical ice velocities are negative or downwards (i.e. the ice is subsiding, although equilibrium surface elevations are maintained at a constant level by the surface accumulation of snow and ice – Figure 4.11d). Here, ice flow serves to entrain cold SATs from the surface into the interior of the glacier, cooling the glacier bed locally and downstream (Figures 4.11e and 4.11f). Midway along the glacier's length, mass flux divergences and vertical ice velocities are near zero, and ice flow is primarily horizontal (Figure 4.11d). Here, horizontal ice deformation velocities reach their maximum values, as does any associated internal frictional heating due to basal and lateral shear (in the absence of glacier sliding). Vertical ice temperature profiles at this midway location are determined primarily by vertical thermal diffusion (e.g. Figure 4.11f) and the horizontal advection of cold temperatures from the upstream accumulation zone (which can serve to cancel out the frictional heating effect). Near the glacier terminus, mass flux divergences may be negative (i.e. horizontal velocity convergence may occur), causing vertical ice velocities to be positive or upwards (Figure 4.11d). Under equilibrium conditions, mass flux convergence near the snout serves to balance mass lost by surface ablation. Positive vertical velocities advect warm basal temperatures upward into the ice, allowing the bed to stay warm while restricting cooler englacial temperatures to the near surface, enhancing vertical thermal gradients near the surface (Figures 4.11e and 4.11f). Here basal ice may reach the PMP, if the ice is thick enough. This then allows for basal meltwater to be produced, or for surface meltwater penetrating the ice to the bed to pass through these regions without refreezing. Basal meltwater lubricates the bed and allows for basal sliding (a further frictional heat source which can help to maintain basal temperatures at the PMP). The creation of a significant basal layer of “warm” or “temperate” ice in the ablation zone (i.e. a layer of ice entirely at the PMP) can also serve to soften the ice and further increase the rate of ice deformation (for a given gradient in surface elevation). At the terminus itself, where the ice thins significantly, predominantly cold polythermal glaciers are typically frozen to their beds (e.g. White Glacier – Blatter, 1987; Laika Glacier – Blatter and Kappenberger, 1988; John Evans Glacier – Copland and Sharp, 2001). The

terminus of the glacier can therefore act as a thermal “dam” in some cases, blocking or partially blocking the drainage of accumulated subglacial meltwater. This can result in seasonal (summertime) outburst floods (Skidmore and Sharp, 1999) and the formation of artesian fountains near the snout (Copland and Sharp, 2003a). A glacier terminus frozen to the bed also acts as a dam to ice flow, producing flow convergence at the snout and compressive longitudinal stresses.

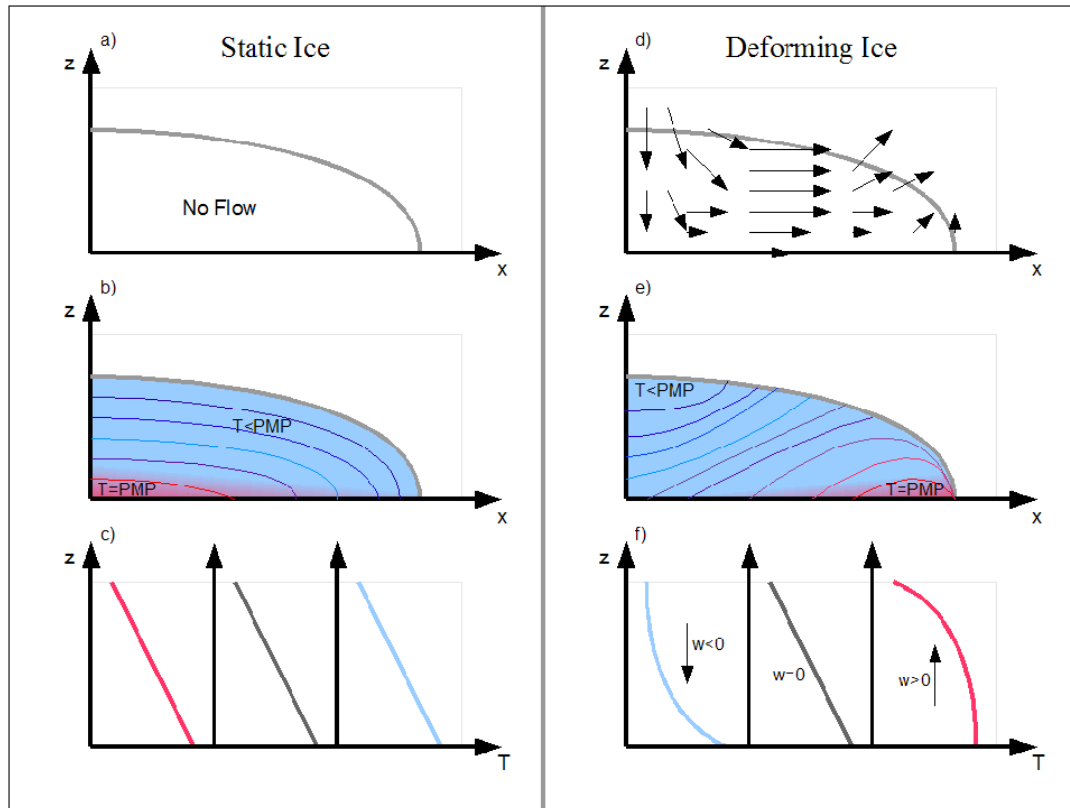


Figure 4.11. Sketched influence of ice flow (a,d) upon the englacial and basal temperatures (b,e) and the equilibrium vertical temperature profiles (c,f) of predominantly cold, polythermal glaciers: a) – c) for static ice; and d) – f) for deforming ice. T denotes temperature, PMP represents the Pressure Melting Point, and w symbolizes the vertical ice velocity. Sketched contours in (b,e) shade from red (representing the PMP) to dark blue (representing sub-zero surface air temperatures).

Real examples of the vertical temperature profiles sketched in Figure 4.11f can be found in the White Glacier study of Blatter (1987). The temperature profiles of numerous boreholes drilled to the bed along the length of this polythermal CHA glacier exhibit the characteristics of the profiles described above.

4.6.2 Englacial Temperatures and Internal/Basal Feedbacks

The thermal evolution of deforming and/or sliding polythermal glaciers is also affected by internal feedbacks between ice thickness, ice flow and ice temperature.

Changes in ice flow feed back on internal ice temperatures by causing changes in thermal advection, changes in ice thickness (due to altered mass flux divergences), changes in internal frictional heating due to deformation, and changes in frictional heating due to basal motion. Speeding up the ice flow increases frictional heating but also increases advective cooling. Crevassing in areas of flow divergence may also affect ice temperatures, both directly by allowing cold air access to the interior of the ice, and indirectly by influencing the ability of surface meltwater to enter the glacier.

Changes in ice temperature, in turn, feed back on ice flow by causing changes in ice viscosity and ice deformation rates, and by facilitating or limiting basal motion. Changes in ice thickness feed back on ice temperature by providing greater or lesser insulation of the ground from Arctic SATS (i.e. by allowing for more or less geothermal heat loss to the colder atmosphere above), and by increasing or decreasing the thermal history of the ice (i.e. the memory of the ice of past climate events). Changes in ice thickness also feedback on ice flow by changing surface elevation slopes and basal pressure gradients or driving stresses.

4.6.3 Englacial Temperatures and Climate Change

SATs and snowfall amounts fluctuate through time, and englacial temperatures respond to changes in SATs and ice thicknesses. However, because most glaciers respond slowly to surface changes, as a result of their high viscosity and large thermal inertia, glaciers today are likely still responding to climate events that occurred hundreds to thousands of years ago (depending on the size and flow properties of the particular glacier).

Changes in SATs over time can cause changes in ice temperatures directly via air-to-ice conduction and via englacial thermal advection and diffusion. They can also (with or without changes in snow accumulation) impact ice temperatures indirectly by causing: 1) ice thickness changes; and 2) variations in supraglacial meltwater production, near-surface refreezing, and basal water flow. Changes in ice thickness (due to changes in SAT and/or precipitation amounts) alter the ability of the ice to insulate the bed from low atmospheric temperatures, which then has implications for ice flow. Supraglacial meltwater can modify englacial and subglacial temperatures if it is able to penetrate the ice and/or reach the bed.

While CHA valley glaciers are generally only a few hundred metres thick, and therefore likely do not contain a thermal “memory” of the entire Holocene, the impacts of the Little Ice Age (LIA), which spanned the period from ~1450 A.D. to

1880 A.D. (e.g. Jones and Briffa, 2001), are still evident within some of these ice masses. Numerical simulations by Blatter (1987) indicate that past air temperatures associated with the peak and culmination of the LIA are directly responsible for the minimum in internal ice temperatures observed in the accumulation zone of White Glacier. On the other hand, numerical simulations by Blatter and Hutter (1991) indicate that historical ice thickness changes and basal feedbacks are likely the indirect cause of the warm basal temperatures observed in the ablation zone of Laika Glacier. The warm basal temperatures of Laika Glacier are not in equilibrium with present-day air temperatures, the glacier being currently too thin to sufficiently insulate the bed from cold atmospheric temperatures (Blatter and Hutter, 1991). For this reason, it was concluded that the glacier must have been thicker in the past, and that the observed warm basal temperatures are a relic of this period (Blatter and Hutter, 1991). It was further postulated, though not tested, that additional basal heat fluxes related to a positive sliding feedback may have served to prolong the existence of the warm basal temperatures to the present-day.

Thus, certain glaciers in the Canadian High Arctic may not be in equilibrium with current climate conditions because they are still responding to conditions that existed during the LIA (e.g. Burgess and Sharp, 2004). Changes in SATs over time, and associated changes in surface mass balance and ice temperature, lead to changes in ice flow and changes in mass flux divergence. In this way, SAT-changes can trigger internal feedbacks such as those discussed above, by leading to further ice thickness changes, which go on to further influence internal temperatures and ice flow.

Because air temperature changes, resultant ice thickness changes, and consequent internal feedbacks are all important to the thermal evolution of such polythermal glaciers, the coupling between these ice masses and their local climates is complex. It is difficult to know which factor plays the dominant role in determining the internal temperature structure of these glaciers.

4.6.4 Englacial Temperatures and Ice-Atmosphere Feedbacks

Changes in SAT and surface mass balance (MB, the surface accumulation rate minus the surface ablation rate), associated with a given climate perturbation, may themselves be amplified by certain cryosphere-atmosphere feedbacks, further complicating the interaction of a glacier with its surface BC's. Three examples of positive ice-atmosphere feedbacks that can amplify changes in SATs and MBs operate as follows:

- 1) *The snow/ice-albedo feedback*: where increased SATs lead to enhanced surface melt, reduced surface albedo, increased absorption of solar radiation, and further increases in surface temperatures and overlying SATs (and vice versa for decreased SATs).

2) *The lapse-rate feedback*: one form of the mass balance – elevation feedback, in which increased SATs lead to increased surface melt and runoff, leading to decreased ice thicknesses and surface elevations, which then lead to further increases in SATs (because SATs are higher near sea level than they are at higher elevations). This feedback works in reverse for decreases in SATs, and can also trigger or interact with the internal feedback described in section 4.6.2, whereby decreases in ice thickness lead to decreases in internal ice temperatures because thinner ice provides less insulation against SATs.

3) *The mass balance – elevation feedback*: another expression of this feedback occurs when precipitation is orographically enhanced near the glacier summit (where air is forced upwards as it passes over the glacier). A positive perturbation in atmospheric moisture could lead to increased snow accumulation, ice thickness and surface elevation, which would then lead to further enhancement of precipitation. This feedback can indirectly impact ice temperatures because ice thickness is intricately connected to ice flow and the englacial thermal evolution of a glacier.

Ice-atmosphere feedbacks, such as those described above, locally modify and amplify regional climate signals. For example, a cooling of $\sim 2.5^{\circ}\text{C}$ between the Holocene Climatic Optimum (CO) and the LIA is detected within the Agassiz ice cap ice cores, however the effects of isostatic uplift over the past 8000 to 9000 years, resulting in greater ice surface elevation, may have contributed to $\sim 40\%$ of this cooling (Koerner and Fisher, 1990). The isostatic-feedback is a variation of the lapse-rate feedback described above. As a second example, it has been shown that the combined terrestrial snow/ice and sea ice – albedo feedback is able to account for $\sim 50\%$ of the $\sim 1.2^{\circ}\text{C}$ LIA-related cooling (w.r.t. present-day temperatures) at the White Glacier summit (based on the calculations and results presented in Chapters 2 and 3).

Amplified surface temperature and glacier thickness changes will lead to nonlinear changes in englacial temperatures, and can also trigger internal feedbacks which then provoke further non-linear thermo-mechanical responses. Such non-linear behaviour could be important to the evolution of basal temperatures and partially explain, or be a factor in, the observed thermal disequilibria of glaciers like Laika Glacier (Blatter and Hutter, 1991) and John Evans Glacier (JEG – Bingham et al., 2008). Accelerating, exponential changes in ice thickness, as opposed to steady linear trends or changes, would have more strongly affected the evolution of englacial temperatures of CHA glaciers throughout the Holocene. Amplified changes in SATs and ice thicknesses during the period extending from the LIA to the present-day may have been of particular significance to currently observed englacial temperatures.

4.7 REFERENCES

- Bauder, A., D. M. Mickelson, and S. J. Marshall, 2005: Numerical modeling investigations of the subglacial conditions of the southern Laurentide ice sheet. *Annals of Glaciology*, **40**, 219-224.
- Beltrami, H., and A. E. Taylor, 1995: Records of climatic change in the Canadian Arctic: towards calibrating oxygen isotope data with geothermal data. *Global and Planetary Change*, **11**, 57-70.
- Bingham, R. G., P.W. Nienow and M. J. Sharp, 2003: Intra-annual and intraseasonal flow dynamics of a High Arctic polythermal valley glacier. *Annals of Glaciology*, **37**, 181-188.
- Bingham R. G., P. W. Nienow, M. J. Sharp and S. Boon, 2005: Subglacial drainage processes at a High Arctic polythermal valley glacier. *Journal of Glaciology*, **51**, 15–24.
- Bingham, R. G., P. W. Nienow, M. J. Sharp and L. Copland, 2006: Hydrology and dynamics of a polythermal (mostly cold) High Arctic glacier. *Earth Surface Processes and Landforms*, **31**, 1463–1479. doi: 10.1002/esp.1374.
- Bingham, R. G., A. L. Hubbard, P. W. Nienow and M. J. Sharp, 2008: An investigation into the mechanisms controlling seasonal speed-up events at a High Arctic glacier. *Journal of Geophysical Research*, **113**, F02006, doi:10.1029/2007JF000832.
- Blatter, H., 1987: On the thermal regime of an Arctic valley glacier: a study of White Glacier, Axel Heiberg Island, N.W.T., Canada. *Journal of Glaciology*, **33** (114), 200-211.
- Blatter, H., and Hutter, K., 1991: Polythermal conditions in Arctic glaciers. *Journal of Glaciology*, **37** (126), 261-269.
- Blatter, H., and Kappenberger, G., 1988: Mass balance and thermal regime of Laika Ice Cap, Coburg Island, N.W.T., Canada. *Journal of Glaciology*, **34** (116), 102-110.
- Boon, S., M. Sharp and P. Nienow, 2003: Impact of an extreme melt event on the runoff and hydrology of a high Arctic glacier. *Hydrological Processes*, **17**, 1051–1072.
doi: 10.1002/hyp.1194 .
- Bradley, R. S., 1990: Holocene paleoclimatology of the Queen Elizabeth Islands, Canadian High Arctic. *Quaternary Science Reviews*, **9**, 365-384.

Bueler, E., 2002: Numerical approximation of a two-dimensional thermomechanical model for ice flow. University of Alaska Fairbanks UAF DMS Technical Report 02-02, 51pp.

Burgess, D. O., and M. J. Sharp, 2004: Recent changes in areal extent of the Devon Ice Cap, Nunavut, Canada. *Arctic, Antarctic, and Alpine Research*, **36**(2), 261-271.

Calov, R., and K. Hutter, 1996: The thermomechanical response of the Greenland ice sheet to various climate scenarios. *Climate Dynamics*, **12**, 243–260.

Christoffersen, P., and S. Tulaczyk, 2003: Thermodynamics of basal freeze-on: predicting basal and subglacial signatures of stopped ice streams and interstream ridges. *Annals of Glaciology*, **36**, 233-250.

Clarke, G. K. C., S. G. Collins, and D. E. Thompson, 1984: Flow, thermal structure, and subglacial conditions of a surge-type glacier. *Canadian Journal of Earth Sciences*, **21**(2), 232-240.

Copland, L. and Sharp, M. 2001: Mapping thermal and hydrological conditions beneath a polythermal glacier with radio-echo sounding. *Journal of Glaciology*, **47**(157), 232-242.

Copland, L., M. Sharp, and P. Nienow (2003a): Links between short-term velocity variations and the subglacial hydrology of a predominantly cold polythermal glacier. *Journal of Glaciology*, **49**, 337-348.

Copland, L., M. J. Sharp, P. W. Nienow, and R. G. Bingham (2003b): The distribution of basal motion beneath a High Arctic polythermal glacier. *Journal of Glaciology*, **49**, 407-414.

Dahl-Jensen, D., K. Mosegaard, N. Gundestrup, G. D. Clow, S. J. Johnsen, A. W. Hansen, and N. Balling, 1998: Past temperatures directly from the Greenland Ice Sheet. *Science*, **282**, 268-271.

Dyke, A. S., 1993: Landscapes of cold-centred Late Wisconsin ice caps, Arctic Canada. *Progress in Physical Geography*, **17** (2), 223-247.

Echelmeyer, K., 1987: Anomalous heat flow and temperatures associated with subglacial water flow. *The Physical Basis of Ice Sheet Modelling* (Proceedings of the Vancouver Symposium, August 1987). IAHS Publ. No. 170.

England, J., N. Atkinson, J. Bednarski, A. S. Dyke, D. A. Hodgson, C. Ó. Cofaigh, 2006: The Innuitian Ice Sheet: configuration, dynamics and chronology. *Quaternary Science Reviews*, **25**, 689-703.

doi:10.1016/j.quascirev.2005.08.007 .

Fabri, K., M. Funk, and A. Iken, 1992: A Sensitivity Study for Modelling Ice Temperatures in Jakobshavns-Isbrae, Greenland. Arbeitsheft Nr. 11, Versuchsanstalt für Wasserbau, Hydrologie und Glaziologie, ETH, Zurich. 118 pp.

Funk, M., Echelmeyer, K., and Iken, A., 1994: Mechanisms of fast flow in Jakobshavns Isbrae, West Greenland: Part II. Modeling of englacial temperatures. *Journal of Glaciology*, **40**(136), 569-585.

Glen, J. W., 1955. The creep of polycrystalline ice. *Proc. R. Soc. Lon. Ser-A*, **228**(1175), 519-538.

Greuell, W., and J. Oerlemans, 1989: The evolution of the englacial temperature distribution in the superimposed ice zone of a polar ice cap during a summer season. Glacier Fluctuations and Climatic Change, (J. Oerlemans, ed.), Kluwer Academic Publishers, p289-303.

Hodgson, D. A., 1989: Quaternary geology of the Queen Elizabeth Islands. In: R.J. Fulton (Ed.), *Quaternary Geology of Canada and Greenland*, pp. 441-478. Geological Survey of Canada, Geology of Canada, No. 1.

Hutter, K., 1993: Thermo-mechanically coupled ice-sheet response – cold, polythermal, temperate. *Journal of Glaciology*, **39**(131), 65-86.

Huybrechts, P., 1992: The Antarctic Ice Sheet and Environmental Change: a Three-Dimensional Modelling Study. *Ph.D. Thesis*. Reports on Polar Research Nr. 99, Alfred Wegener Institute for Polar and Marine Research, Bremerhaven, Germany. 241pp.

Huybrechts, P., 1996: Basal temperature conditions of the Greenland ice sheet during the glacial cycles. *Annals of Glaciology*, **23**, 226-236.

Irvine-Fynn, T. D. L., B. J. Moorman, J. L. M. Williams and F. S. A. Walter, 2006: Seasonal changes in ground-penetrating radar signature observed at a polythermal glacier, Bylot Island, Canada. *Earth Surface Processes and Landforms*, **31**, 892–909.

doi: 10.1002/esp.1299 .

Johansen, H., W. Fjeldskaar and J. Mykkeltveit, 1995: The influence of glaciation on the basin temperature regime. *Global and Planetary Change*, **12**, 437-448.

Jones, P. D., and K. R. Briffa, 2001: The “Little Ice Age”: Local and global perspectives [preface]. *Climatic Change*, **48**(1), 5–8.

Koerner, R. M., and D. A. Fisher, 1990: A record of Holocene summer climate from a Canadian high-Arctic ice core. *Nature*, **343**, 630-631.

Marshall, S. J., and P. U. Clark, 2002: Basal temperature evolution of North American ice sheets and implications for the 100-kyr cycle. *Geophysical Research Letters*, **29**(24), 2214-2217.
doi:10.1029/2002GL015192, 67-1 – 67-4.

Overpeck, J., K. Hughen, D. Hardy, R. Bradley, R. Case, M. Douglas, B. Finney, K. Gajewski, G. Jacoby, A. Jennings, S. Lamoureux, A. Lasca, G. MacDonald, J. Moore, M. Retelle, S. Smith, A. Wolfe and G. Zielinski, 1997: Arctic Environmental Change of the Last Four Centuries. *Science*, **278**, 1251-1256.
DOI: 10.1126/science.278.5341.1251

Paterson, W. S. B., 1994: The Physics of Glaciers, 3rd edition. Pergamon Press, Elsevier Science Inc., New York.

Payne, A. J. 1995. Limit cycles in the basal thermal regime of ice sheets. *Journal of Geophysical Research*, **100**(B3), 4249-4263.

Peixoto, J. P., and A. H. Oort (1992): Physics of Climate. American Institute of Physics, New York.

Skidmore M. L., and Sharp M. J., 1999: Drainage system behaviour of a High-Arctic polythermal glacier. *Annals of Glaciology*, **28**, 209–215.

Thorsteinsson, T., and Raymond, C. F., 2000: Sliding versus till deformation in the fast motion of an ice stream over a viscous till. *Journal of Glaciology*, **46**(155), 633-640.

van der Veen, C. J., T. Leftwich, R. von Frese, B. M. Csatho and J. Li, 2007: Subglacial topography and geothermal heat flux: potential interactions with drainage of the Greenland ice sheet. *Geophysical Research Letters*, **34**, L12501, doi:10.1029/2007GL030046.

Wolken, G. J., J. H. England and A. S. Dyke, 2008: Changes in late Neoglacial perennial snow/ice extent and equilibrium-line altitudes in the Queen Elizabeth Islands, Arctic Canada. *Holocene*, **18**(4), 615-627.

5. Modelling the Mass Balance – Elevation Feedback: Implications of orographic precipitation for the evolution and geometry of the Devon Ice Cap in the Canadian High Arctic

5.0 INTRODUCTION

A number of large ice caps and ice fields exist in the Canadian High Arctic (CHA), with sizes on the order of 10^4 km^2 (e.g. Devon Ice Cap, Agassiz Ice Cap, Prince of Wales Icefield, Manson Icefield, Müller Ice Cap, Sydkap Ice Cap, Penny Ice Cap, Barnes Ice Cap – Figure 5.1). These ice caps interact with the overlying atmosphere, both modifying and being modified by regional atmospheric circulation, temperature, and precipitation patterns. Because ice and atmosphere are interdependent systems that co-evolve over time, feedbacks between the two systems are possible, both positive and negative.

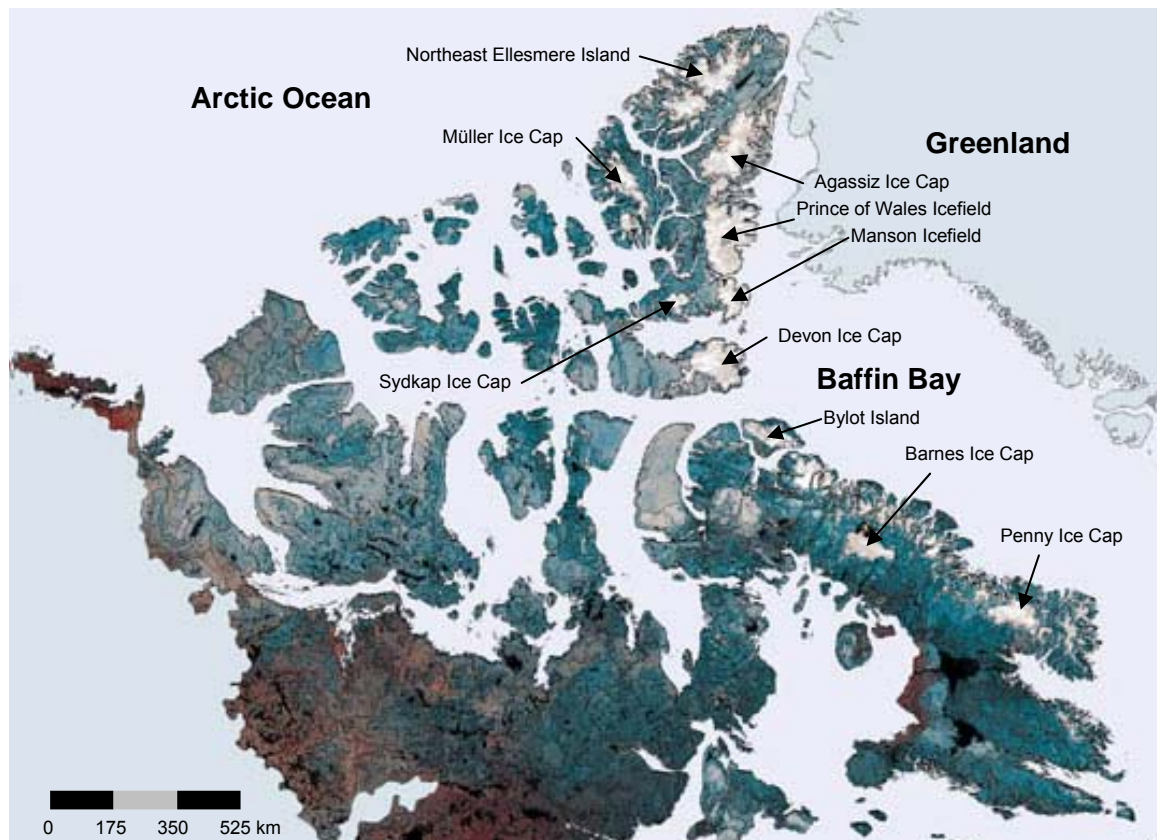


Figure 5.1. Canadian High Arctic ice caps and ice fields.

The two principal positive ice-atmosphere feedbacks are the snow/ice-albedo feedback (described in Chapter 2) and the mass balance – elevation feedback (described in section 5.1). Modeling studies of continental-sized ice sheets (e.g. Abe-Ouchi et al., 2007) indicate that the mass balance – elevation feedback is secondary to the snow/ice-albedo feedback (although it should be noted that the

two feedbacks are often difficult to separate in fully coupled 3D ice-atmosphere models). Whether this is also true for CHA ice caps and ice fields is unknown.

The numerical experiments described in Chapter 2 of this thesis indicated that the snow/ice-albedo feedback may be important in amplifying surface mass balance changes in the CHA at decadal time scales and longer, especially near ice cap margins where outlet valley glaciers are located. The lapse-rate feedback (a form of the mass balance – elevation feedback, see section 5.1) has also been argued by others to be important in some areas of the CHA. For example, Koerner and Fisher (1990) propose that the lapse rate feedback (as initiated by isostatic rebound of the Earth’s crust) may account for up to 40% of the post – Last Glacial Maximum (LGM) climate signal derived from Agassiz Ice Cap ice cores. Furthermore, a recent study of the Prince of Wales icefield suggests lapse rate - synoptic circulation feedbacks may be important to the evolution of CHA ice masses (Marshall et al., 2007). In that study, results suggest “a coherent glacier mass balance feedback to shifts in synoptic conditions that may accompany climate change” (Marshall et al., 2007).

The importance of the mass balance – elevation feedback for the evolution of CHA ice caps (their geometry and flow) therefore merits further investigation. Even if the magnitude of the feedback turns out to be small when compared to that of the snow/ice-albedo feedback, the impacts of small amplifications can accumulate over time, so that what appears negligible on decadal time scales may become significant on centennial to millennial time scales.

Using a coupled atmosphere–ice model, the aim of this chapter is to: 1) investigate where, in the CHA, the mass balance - elevation feedback may be an important component of the long-term averaged surface mass balance; 2) quantify the impact of the feedback in such places; and 3) examine the influence of the feedback’s amplification of atmospheric moisture perturbations on the post–LGM evolution of a CHA ice cap. The model experiments were designed to isolate the mass balance - elevation feedback from the snow/ice-albedo feedback, because the two likely interact and can lead to further feedbacks, both positive and negative. They were also designed to investigate aspects of the mass balance - elevation feedback other than the lapse-rate feedback already partially examined by others. These aspects include the orographic-precipitation feedback and the glacier-anticyclone feedback (see section 5.1).

Devon Ice Cap (DIC) is chosen as the focus for this study because detailed surface and bed elevation Digital Elevation Models (DEMs) exist for this ice cap, as well as mass balance and ice flow measurements. It is also chosen because of its asymmetric northwest-southeast profile along the prevailing wind direction. Purves and Hulton (2000) showed that when model ice sheets were dynamically coupled to climate models, they developed asymmetric profiles as a result of a strong positive mass-balance feedback. The feedback occurs because the evolving ice-sheet topography impacts the atmospheric moisture transport. This, along

with observations of net mass gains in the northwest sector of DIC, while most other sectors are experiencing net mass losses (Shepherd et al., 2007), suggests that a continuing mass balance - elevation feedback may be playing an active role in modifying the long-term mean surface mass balance on the northwest side of the ice cap. The formulation and investigation of this hypothesis forms the basis of this chapter.

This chapter is organized as follows: 1) a review of all aspects of the mass balance – elevation feedback is presented; 2) an overview of Devon Ice Cap ice flow and mass balance measurements is presented; 3) the atmosphere and ice models used in this study and the coupling of these are described; 4) a series of 1D and 2D model experiments, designed to examine the importance of the mass balance – elevation feedback, are performed and results discussed; and 5) conclusions regarding the significance of the mass balance – elevation feedback to the historical and present-day evolution of Devon Ice Cap are offered.

5.1 THE MASS BALANCE – ELEVATION FEEDBACK: A REVIEW

Ice caps interact with the atmosphere directly by modifying atmospheric circulation patterns, which in turn modify surface temperature and precipitation patterns. This interaction with the atmosphere alters the surface mass balance distribution over the ice cap, with consequent implications for ice flow and mass flux divergences, all of which serve to modify the ice cap's profile. The new ice cap profile then initiates further changes in the circulation of the atmosphere. This co-evolution of atmosphere and ice can sometimes take the form of a positive atmosphere-ice feedback, termed the mass balance – elevation feedback in this study.

The mass balance – elevation feedback is for the most part a *mechanical* (displacement of mass) feedback, although thermodynamics plays a role as well. This contrasts with the snow/ice-albedo feedback which is primarily a *thermal energy* feedback. The mass balance – elevation feedback involves forced air flow over/around ice caps, changes in storm tracks and atmospheric temperature/precipitation patterns, and the consequent changes to an ice cap's mass balance and its mass balance – driven geometric evolution. It also involves the accumulation and displacement of ice mass. Where thermodynamics are involved in the atmosphere, it is the adiabatic work term of the first law of thermodynamics which is primarily involved, as opposed to the diabatic radiative/turbulent heating term (which is the important term to the snow/ice-albedo feedback).

This feedback takes different forms at different vertical and horizontal scales (Figure 5.2): it is active at the summits of small ice fields, at the margins of ice caps, and over a broader area of large ice sheets. This feedback *amplifies mass*

balance perturbations and is triggered by changes in atmospheric circulation (temperature and moisture) and by changes in surface mass balance.

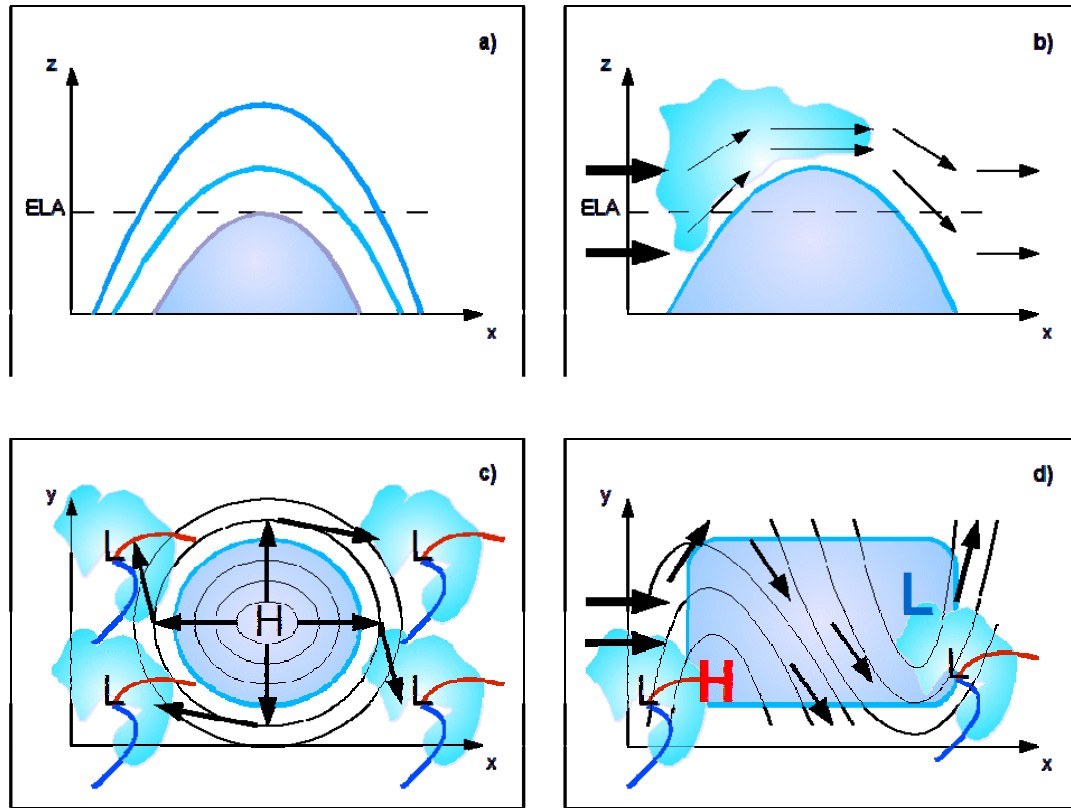


Figure 5.2. Forms of the mass balance – elevation feedback. a) The lapse-rate feedback, given a static atmosphere. The blue curves indicate ice caps of various sizes, with varying proportions above and below the ELA. ELA denotes the “equilibrium line altitude”, the altitude at which annual snowfall accumulation is balanced by summer melt and runoff. b) The orographic precipitation feedback, given a moist, dynamic atmosphere. Arrows denote forced air flow over the ice cap. Cloud and precipitation form where the air is forced upwards. c) The ice sheet anticyclone feedback. “H” denotes high sea level pressure, and black concentric circles are sketches of isobars (which in this case tend to parallel surface elevation contours). Arrows indicate the cold air outflow from the centre of the ice cap and the consequent Northern Hemisphere anticyclonic circulation of the outflow as a result of the Coriolis force. “L’s” denote low-pressure storm systems with associated warm fronts (red) and cold fronts (blue) and cloud/precipitation areas. d) The interaction of very large ice sheets with topographically-generated Rossby waves. The red H and blue L denote centres of high and low atmospheric thicknesses (or temperatures), respectively. Black lines are contours of atmospheric thickness. Arrows are upper atmosphere winds (and also indicate the path of the jet stream). “L’s” are surface low-pressure systems as described in c). See text for descriptions of the feedbacks.

5.1.1 *The Lapse Rate Feedback*

Atmospheric temperatures decrease with elevation. In a dry atmosphere, this lapse rate is equal to $-9.8^{\circ}\text{C km}^{-1}$, but observed environmental lapse rates generally tend to be nearer $-6^{\circ}\text{C km}^{-1}$ as a result of moist atmospheric processes. Over ice-covered surfaces, where summer surface temperatures cannot exceed the melting point, boundary layer inversions may decrease average lapse rates in the lower part of the atmosphere.

The interaction of growing/shrinking ice caps with this lapse rate can result in a positive surface mass balance feedback, which operates as follows. Uniform thinning of an ice cap or glacier as a result of an increase in equilibrium line altitude (ELA – the altitude at which annual accumulation is balanced by summer melt and runoff) or possibly due to an increase in mass transfer from the accumulation zone of the ice cap to the ablation zone of the ice cap, results in a greater percentage of the ice mass lying at lower elevation, below the ELA, where air temperatures are higher. This will lead to increased melt and further ice thinning (Figure 5.2a). This feedback also works in reverse (e.g. Abe-Ouchi et al., 2007).

This positive feedback can be further complicated by shifts in synoptic-scale atmospheric circulations, associated with climate change, which can lead to changes in regional atmospheric lapse-rates, resulting in further glacier mass balance feedbacks. Such a lapse rate - synoptic circulation feedback is proposed to be important for much of the CHA (e.g. Marshall et al., 2007).

This positive feedback can also be further complicated by a compensating negative feedback if the ice cap is large enough that its weight is capable of deforming the Earth's crust beneath it (although note that there are significant time lags involved in any feedback in which isostasy plays a role). In this case, a growing ice cap depresses the Earth's crust below, bringing a larger proportion of the ice cap below the ELA once again, reducing the rate of growth of the ice cap (and vice versa for a shrinking ice cap which leads to isostatic rebound of the Earth's crust). Koerner and Fisher (1990) proposed that isostatic rebound of the Earth's crust accounts for up to 40% of the post-LGM air temperature history inferred from Agassiz Ice Cap ice cores (although they did not consider the possible influence of lapse rate changes over time).

5.1.2 *The Orographic Precipitation Feedback*

Regional-scale ice caps, such as those found in the CHA, are capable of generating orographically - enhanced precipitation patterns (e.g. Koerner, 1979). Orographic precipitation can develop when air is forced to flow up and over a mountain or ice cap. As the air rises, it expands and cools adiabatically, and the moisture within it condenses to form cloud and precipitation on the upstream side of the ice cap. Conversely, as the air (now partly depleted of moisture) descends

once again on the downstream side of the ice cap, it warms adiabatically, sometimes leading to warm, dry, chinook conditions (Figure 5.2b). In this way, precipitation and winter snowfall accumulation are orographically enhanced on the upstream side of an ice cap or mountain and a “rain shadow” develops on the downstream side. Chinook winds can also act to initiate abnormal winter surface melt or to drastically enhance summer surface melt on the downstream side.

This process can act to enhance/suppress precipitation associated with synoptic weather patterns in the area of the ice cap or mountain, or it can act on its own in the absence of synoptic storms to generate windward-side precipitation as well as enhanced lee-side surface melt. An example of orographically-generated cloud/precipitation occurred on May 28, 2005, over the Devon Ice Cap (Figure 5.3a). On this day, a quasi-stationary low in surface pressure, situated beneath a 500 mb low in atmospheric thicknesses, was located to the east of Devon Ice Cap in central Baffin Bay. Cyclonic circulation around these lows produced a north-northwesterly air flow at all atmospheric levels over the Devon Ice Cap. As the air flowed over the ice cap, orographic summit cloud and (possibly) precipitation developed, increasing in extent throughout the day under the sustained northwesterly winds (Figure 5.3a). As indicated by the low-level stratus cloud over Jones Sound in the first 2 panels and by the cloud stream lines in the final panel, the primary moisture source for the orographic cloud and precipitation was the Hell Gate polynya located to the northwest of the ice cap (Figure 5.3a).

An example of Chinook wind conditions occurred on the Devon Ice Cap during the week of February 19, 2008 (Figure 5.3b). During this week, prevailing northerly winds resulted in hydraulic jump conditions over the DIC, with accelerated wind speeds over the summit of the ice cap and the formation of a distinct roll cloud on the lee (south) side of the summit.

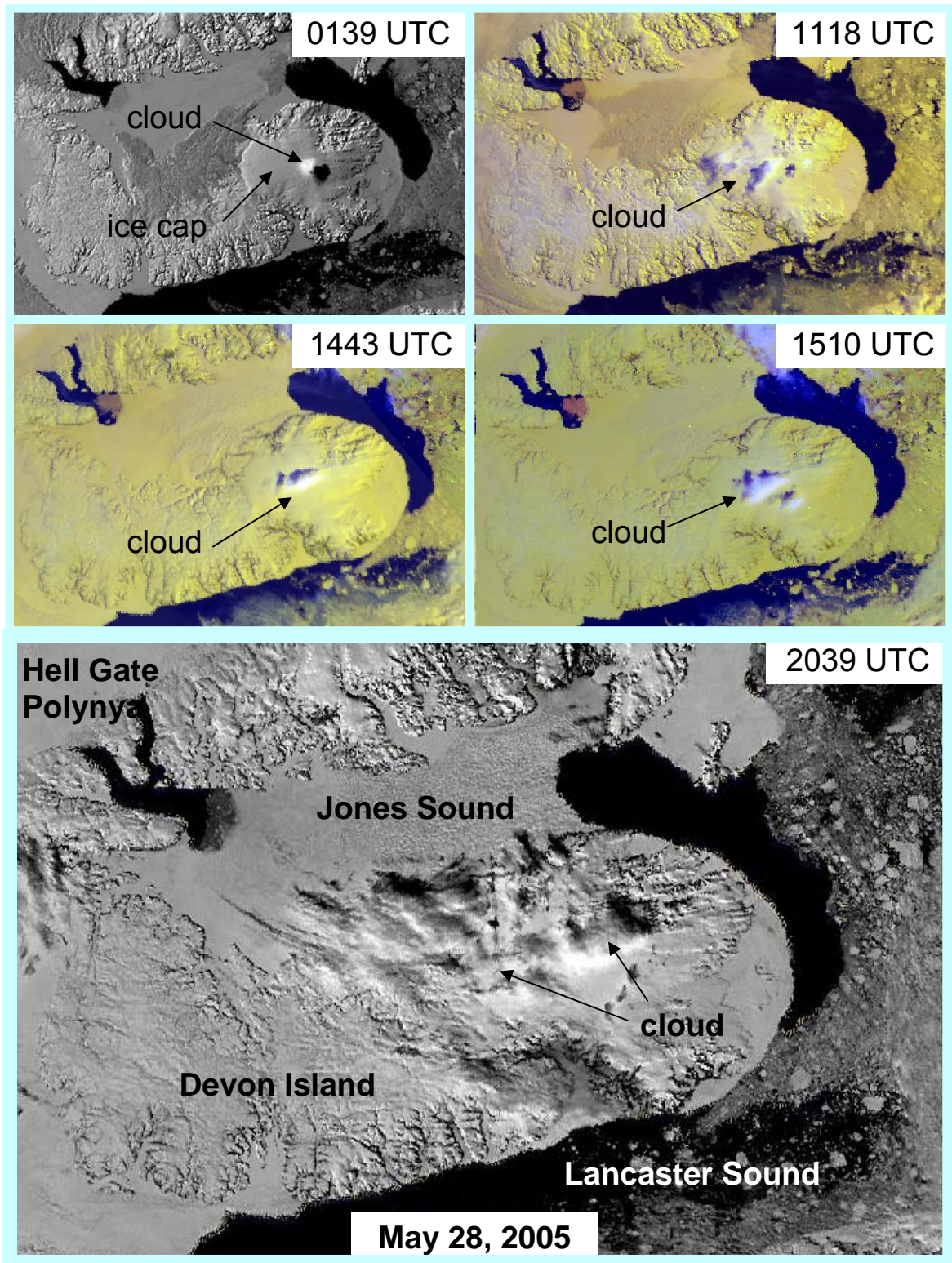


Figure 5.3. a) The development of orographic cloud and precipitation under northwesterly winds at the summit of Devon Ice Cap on May 28, 2005. Black and white OLS visible-band and coloured NOAA AVHRR all-band imagery courtesy of Environment Canada.

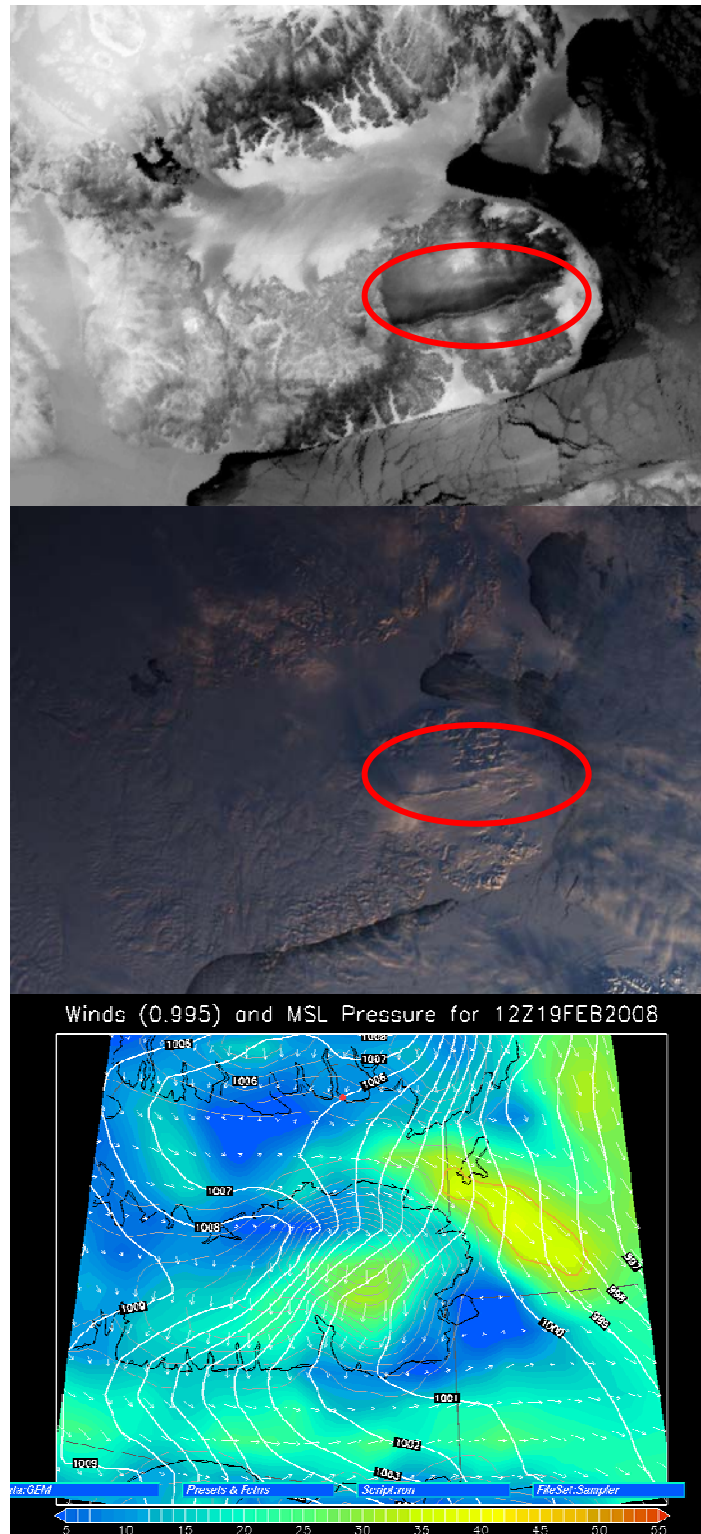


Figure 5.3. b) Hydraulic jump and lee-side roll cloud due to sustained northerly winds passing over the summit of Devon Ice Cap the week of February 19, 2008. Black and white NOAA AVHRR IR image (February 19, 2008), false-colour MODIS visible band image (February 21, 2008), and GEM model wind/pressure plot courtesy of Environment Canada.

Orographic precipitation and lee-side chinooking can lead to a positive mass balance – elevation feedback. A perturbation (e.g. a positive change in upstream atmospheric moisture availability) can lead to amplified changes in summit elevations as air is forced upwards over an ice cap. As the air cools and condenses, it leads to increased snowfall which results in increased surface elevations upstream of and at the summit. Increases in surface elevation mean that the air is forced even higher as it passes over the ice cap (unless ice cap growth alters the circulation pattern around the ice cap – see section 5.1.3), leading to even more cooling/condensing/precipitation, and even further increases in surface elevation upstream of and at the summit. Thus, orographically - enhanced precipitation at high elevations on the windward side of the ice caps leads to increased snow/ice accumulation and surface elevations, which in turn further amplifies the orographic precipitation (Figure 5.2b). This feedback will also cause the migration of the ice cap summit in an upstream direction (e.g. Hulton and Sugden, 1995; Purves and Hulton, 2000). Alpine ice caps in the Andes, with maritime moisture supplies, have been shown to modify their own mass balances through elevation - precipitation feedbacks (Hulton and Sugden, 1995).

On the lee side of the ice cap, Chinook winds may enhance ice melt, helping to decrease (or slow the increase of) surface elevations over time. If surface elevation decreases are realized and enhanced, this will allow for even stronger and warmer Chinook winds when atmospheric conditions allow, and a positive mass balance – elevation feedback.

Note that changes in ice surface slopes as a result of this process will eventually lead to adjustments in ice flow and mass fluxes, providing a compensating negative feedback. However, because atmospheric adjustment time scales are so much shorter than ice adjustment time scales (discussed further in section 5.3.3), the orographic precipitation feedback can likely operate for some time before an adjustment in ice flow occurs.

5.1.3 The Glacier Anticyclone Feedback

Atmospheric anticyclones tend to form over large ice caps and ice sheets (Figure 5.2c). This is because cold, dense air forms over the centre of the ice cap as a result of high surface elevations (and high surface albedo – making this a combined mass balance - elevation and snow/ice-albedo feedback). This results in high surface pressures (when corrected to sea level – e.g. the Greenland climatological High – Figure 5.4) and a divergent surface outflow of air from the centre of the ice cap towards the edges, known as katabatic winds. This outflow causes atmospheric subsidence over the ice cap, clear skies, and an atmospheric inversion related to the dry adiabatic warming of the subsiding air. The surface outflow of cold, dense air will develop a clockwise circulation in the Northern Hemisphere and a counter-clockwise circulation in the Southern Hemisphere due

to the Coriolis effect. The outflow also serves to displace clouds and precipitation/snow towards the edges of the ice cap (Figure 5.2c and Figure 5.4).

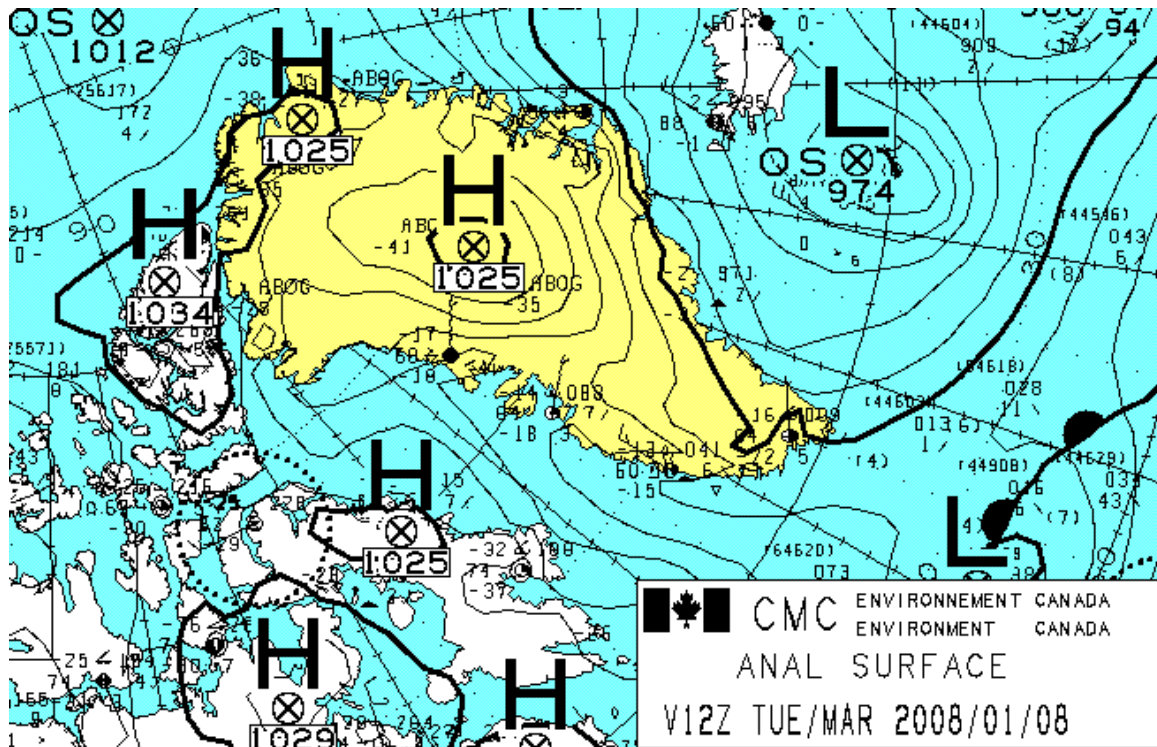


Figure 5.4. A typical winter sea level surface pressure analysis for Greenland (highlighted in yellow), showing an area of high sea level pressure (or an anticyclone) over the central and northern part of the ice sheet. Atlantic low pressure systems are confined to tracking up the west and east coasts of Greenland. Surface analysis courtesy of Environment Canada (<http://weather.ec.gc.ca>).

Because synoptic-scale (i.e. horizontal length scales of 10^2 - 10^3 km) ice sheets, such as the present-day Greenland Ice Sheet (GIS), displace storm tracks and shift precipitation patterns towards their margins, this modifies the mass balance of the ice sheet, limiting snow accumulation at the centre but causing thickening/expansion at the edges. This can lead to a positive mass balance – elevation feedback which operates as follows.

The displacement of precipitation/snow to the edges of the ice cap means that the ice cap margins will expand outwards and the margins will increase in surface elevation. Thickening ice cap margins will cause the area of high surface atmospheric pressures located over the centre of the ice cap to expand, increasing surface outflow and surface temperature contrasts near the ice cap margins, further enhancing marginal frontal systems and precipitation, and displacing precipitation/snowfall even further outwards, thus causing the ice cap itself to grow even further outwards.

The migration of the ice edges ever further outwards will continue (with the help of ice deformation, which causes the ice to flow and spread outwards from central ice divides) until the ice margins either: 1) reach the coastline and the ocean, where the formation of ice shelves and/or iceberg calving occur (e.g. GIS, Antarctica); 2) reach low enough latitudes that SAT-related melting overwhelms the formation and/or spreading of the ice (e.g. southern extent of the former Laurentide Ice Sheet); or 3) reach the limit of available atmospheric moisture such that no significant precipitation and accumulation occur near the ice cap margins (e.g. where they terminate in the dry interiors of many CHA islands – Koerner 1979; 1989; 2002).

The feedback also operates in the opposite fashion, such that a shrinking ice cap will result in weaker anti-cyclonic circulation, allowing for the inward invasion of warmer temperatures and precipitation from the edges towards the centre of the ice cap. This results in ice cap thinning, a reduction in the areal extent of the ice cap, and a further reduction of the glacial anticyclone.

5.1.4 *The Rossby Wave Feedback*

At synoptic-planetary scales (i.e. horizontal length scales of 10^3 km and more), continental scale ice sheets, such as the former Laurentide Ice Sheet (LIS), were capable of amplifying stationary planetary wave patterns in the atmosphere (e.g. Kutzbach et al., 1993; Roe and Lindzen, 2001). This allowed for the southward expansion of the ice sheet over eastern North America (e.g. Roe and Lindzen, 2001). A similar study conducted for the Fennoscandian ice sheet found that the planetary wave pattern forced by the ice sheet led to deviations in the ELA of 500 m on the eastern side of the ice sheet (Lindeman and Oerlemans, 1987).

In this case, the feedback primarily involves the interaction of the atmospheric jet stream with the ice sheet's topography (Figure 5.2d). Topographic Rossby or planetary waves are generated by air flow over regions where there is a step increase in surface elevation, such as occurs when the jet stream crosses the Rocky Mountains (e.g. Wallace and Hobbs, 1977) or as occurred when it encountered the Laurentide Ice Sheet (e.g. Roe and Lindzen – 2001). Atmospheric thickness patterns are folded into long waves with high thicknesses (related to warmer air of lower density) in the vicinity of the topographic perturbation and low thicknesses (related to cooler, higher density air sitting atop a surface anti-cyclone or area of high surface pressure) well downstream. The jet stream, which is a thermal wind, will tend to follow lines of equal atmospheric thicknesses, flowing up over the western thickness ridge then southeastwards across the centre of the continent, then turning back northeastwards across the eastern-most part of the continental-scale ice sheet (Figure 5.2d).

A synoptic-scale ice sheet initially growing in northern Canada via the feedback described in section 5.1.3, will also have eventually begun to interact with the topographic Rossby waves generated by the Rocky Mountains and the Cordilleran

Ice Sheet. These Rossby Waves would have enhanced the southeastwards expansion of the ice sheet into the Great Lakes and Atlantic areas, which would in turn have thermally enhanced the low atmospheric thicknesses downstream of the Cordilleran Ice Sheet, leading to further southeastwards expansion of the ice sheet (e.g. Roe and Lindzen, 2001; Kutzbach, 1993).

In summary, atmospheric Planetary/Rossby wave modification enhances a downstream surface glacial Anticyclone (i.e. high surface pressures) beneath low atmospheric thicknesses, modifies atmospheric precipitation patterns, modifies ice sheet expansion and geometry, which in turn modifies the atmospheric Planetary/Rossby waves even more.

One of the triggers for this feedback is a change in the strength / incidence angle of the Jet Stream as it reaches the continent from the Pacific, which impacts the amplitude of the topographically generated Rossby Waves. A second trigger may be an El Niño event, which thermally enhances the high thicknesses and warm temperatures in western North America, and thus enhances the Rossby wave amplitude, leading to a decrease in SATs downstream to the east, which then acts to enhance low thicknesses and cold temperatures in the east. A third trigger for this feedback is an increase/decrease in the surface elevation of the western part of the continent (as a result of significant accumulation/loss of glacier ice in the cordillera).

5.2 DEVON ICE CAP

5.2.1 Ice Thickness, Mass Balance, and Flow Observations

Devon Ice Cap (DIC) is located in the CHA, centred near 75°N and 82°W (Figure 5.1). Except for a south-westerly extension or arm, it is roughly circular or dome-shaped, with a diameter of ~150 km and a summit elevation near 2000 m. DIC was chosen for this study because of the availability of ice thickness, mass balance and ice flow measurements.

A digital elevation model (DEM) of DIC surface elevations was created from aerial photographs taken by the Canadian Government in 1959/60 (a subset of the Canadian Digital Elevation Dataset – CDED – Figure 5.5). This has recently been supplemented with a new DEM created from airborne radar measurements (Dowdeswell et al., 2004) and a second DEM created using satellite radar interferometry (Shepherd et al., 2007). A DEM of DIC bed elevations has also been created at a 1 km horizontal resolution from airborne ice-penetrating radar measurements (Dowdeswell et al., 2004). DIC ice thicknesses are therefore now well established, and range from up to 100 m in the southwest arm to 600+ m in places in the interior and in the upper accumulation zones of some of the larger southeastern outlet glaciers (Dowdeswell et al., 2004).

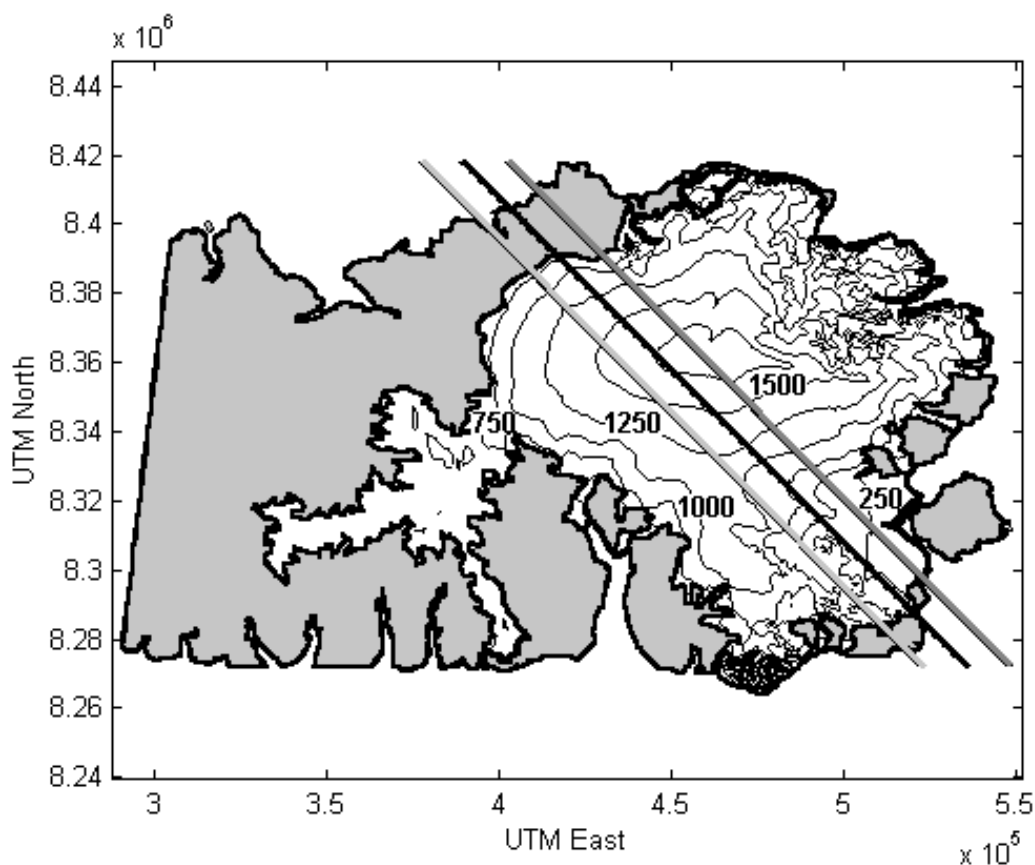


Figure 5.5. Devon Ice Cap, eastern Devon Island, Canada. Surface elevations are in metres a.s.l. The surface height profiles along the 3 depicted northwest-southeast transects are shown in Figure 5.6. (Source: Canadian Digital Elevation Data, Natural Resources Canada.).

Historical changes in the extent and thickness of the DIC have been inferred from geomorphological evidence (e.g. Dyke and Prest, 1987; Dyke, 1999; England et al., 2006; Wolken et al., 2008a). Maximum DIC ice thicknesses and extents occurred during the LGM, associated with a secondary divide of the Innuitian Ice Sheet located over Devon Island (England et al., 2006). The DIC then thinned and retreated to nearly present-day values by 7000 years B.P (Dyke and Prest, 1987; Dyke, 1999; England et al., 2006). Evidence from glacier trim lines indicates that following the Holocene Climatic Optimum (CO), the DIC thickened and expanded during the Little Ice Age (LIA: ~1500-1850 A.D.) then thinned once again to present-day extents (Wolken et al., 2008a). Records of historical surface air temperature (SAT) anomalies have also been inferred from oxygen-isotope data within DIC summit ice cores (Paterson et al., 1977) and from the distribution of melt features and layers detected within an ice core (Koerner, 1977).

The present-day DIC is characterised by an east-west contrast in surface accumulation and ablation amounts, surface profile (i.e. convex upwards vs. concave upwards surface slopes – Figure 5.6) and ice flow dynamics. Surface accumulation is highest in the east-southeast part of the ice cap, which is directly affected by Baffin Bay cyclones (Koerner, 1966) and lowest in the west-northwest

part of the ice cap. In spite of this, the mean net balance in the southeast is similar to that of the rest of the ice cap (Koerner, 1970). This is because surface ablation is also greater in the southeast of DIC than it is in the northwest (Koerner, 1970).

Although ELAs are slightly higher (by ~150m) in the northwest than in the southeast (Koerner, 1970; 1979), the northwest sector is advancing slightly and gaining mass while all other sectors of the ice cap are retreating and losing mass (Burgess and Sharp, 2004; Shepherd et al., 2007). This is partly related to the hypsometry of the ice cap profiles: larger percentages of the ice cap area lie above the ELA in northern and western parts of the DIC than in the south-eastern sections (Burgess and Sharp, 2004). It is also related to the rate of transfer of mass from the accumulation zone above the ELA to the ablation zone below.

Northwest-to-southeast cross-sections of the DIC reveal steeper, convex upwards surface slopes on the northwest side and less-steep, concave upwards surface slopes on the southeast side (Figure 5.6). Steeper surface slopes generally occur where ice caps terminate inland in broad, slow-moving tongues, while gentler slopes exist where ice is channeled through valleys towards the ocean (Koerner, 2002). This is true for the DIC: its western margin terminates on land at 300-500m a.s.l., while its northern, eastern and southern margins terminate in a number of outlet valley glaciers, many of which terminate at sea level and calve into the surrounding bays and sounds.

Ice flow in the interior and western half of the ice cap is primarily by deformation, whereas the flow of the eastern outlet valley glaciers is also influenced by basal motion (sliding or subglacial sediment deformation) (Dowdeswell et al., 2004; Burgess et al., 2005). Because of this, ice flow in the outlet glaciers of Devon Ice Cap can be ~5-10 times faster than in the areas of undifferentiated flow on the western side of the ice cap (Dowdeswell et al., 2004; Burgess et al., 2005; Shepherd et al., 2007). Recent satellite-derived ice velocity patterns (Dowdeswell et al., 2004; Burgess et al., 2005; Shepherd et al., 2007) confirm earlier ice flow measurements made in the ablation zones of tidewater Devon outlet glaciers (e.g. Cress and Wyness, 1961), and also confirm the northwest side ice velocity measurements discussed in Doake et al. (1976) and Wolff and Doake (1986).

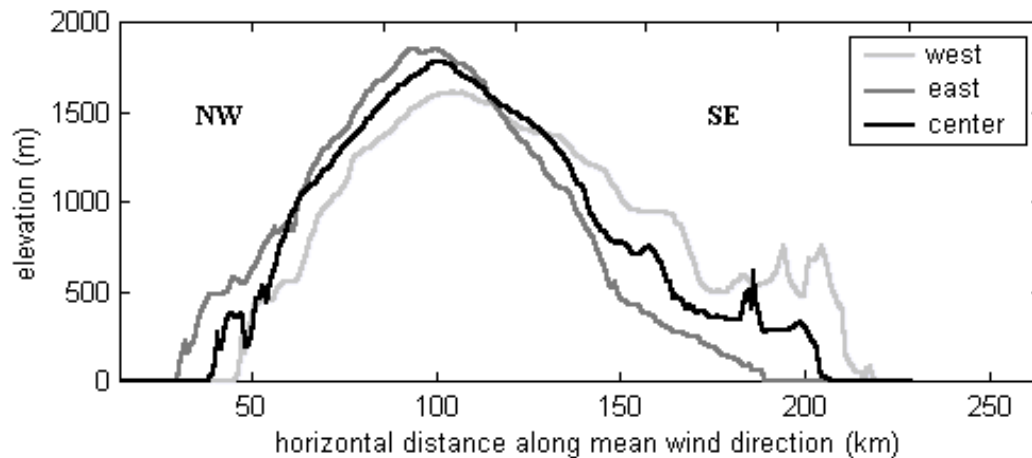


Figure 5.6. Three northwest-southeast cross-sections through the Devon Ice Cap, Devon Island, Nunavut (Canadian Digital Elevation Data, Natural Resources Canada). Note that these cross-sections do not follow actual flow lines in the ice.

5.2.2 Evidence for Mass Balance – Elevation Feedbacks

Contrasting ice flow on either side of the ice cap's divides (Koerner, 1989) and the importance of subglacial topographic controls (Koerner, 1989, 2002) were proposed early on as one of the primary reasons for DIC's asymmetric NW-SE ice cap profiles. However, while ice flow and subglacial topographic controls are clearly important to the present-day observed geometry of the DIC, it is possible that ice-atmosphere interactions and feedbacks have played an historical role as well. Purves and Hulton (2000) used numerical experiments to show how an ice sheet's evolution differs when: a) under a constant imposed climate; and b) dynamically coupled to a climate model. Ice sheets that developed under the dynamically linked models were shown to be asymmetric as a result of a strong positive mass-balance feedback. The feedback occurs because the evolving ice-sheet topography impacts the atmospheric moisture transport.

Evidence of orographically-generated precipitation on DIC has already been presented (Figure 5.3a). While orographically-generated precipitation on its own and/or the orographic enhancement of synoptic system precipitation can potentially occur on any side of the DIC, a sustained orographic-precipitation feedback (as opposed to simple orographic precipitation with no mass balance feedback) is most likely in the northwest sector because annual mean tropospheric winds are from the northwest (Figure 5.7). This is in spite of the fact that the dominant moisture sources are located on the southeast side of the ice cap.

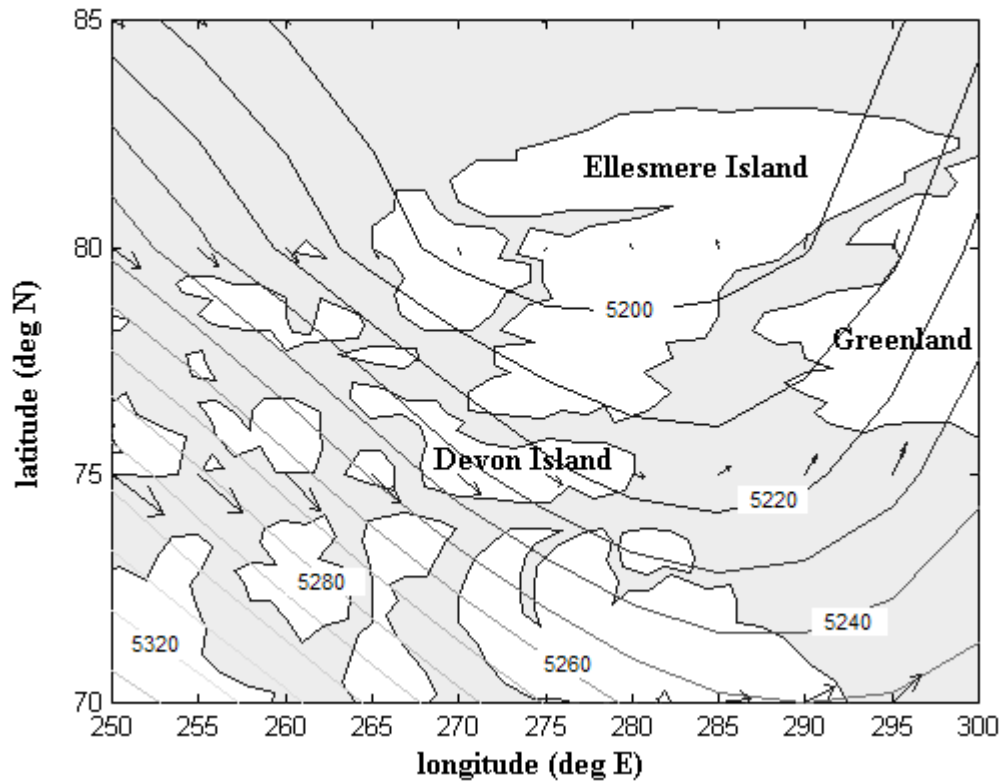


Figure 5.7. The 1975-2000 vertical mean tropospheric wind pattern over the eastern Canadian High Arctic (derived from NCAR gridded monthly data). Mean tropospheric winds are quasi-geostrophic and parallel to atmospheric height contours. Here, mid-tropospheric 500mb height contours are plotted every 10m ranging from 5200 m in the north to greater than 5250 m in the south.

It is important to distinguish between the following: 1) actual precipitation amounts and the magnitude of any inherent orographic enhancement; and 2) the magnitude of the orographic-precipitation *feedback*. While observed precipitation amounts are greatest on the southeast side of DIC (Koerner, 1966; Shepherd et al., 2007), and while orographic enhancement of precipitation is likely also to be greater on the southeast side during episodes of easterly and southeasterly winds (as a result of atmospheric moisture availability related to summertime non-ice covered waters in Baffin Bay), the magnitude of the orographic-precipitation *feedback* is likely to be greatest on the northwest side (in the sense of increasing surface elevations) because most of the time winds are from the northwest (Figure 5.7). It is also important to distinguish between: 1) the *potential* for the orographic-precipitation feedback (which is presumed to exist for DIC); and 2) the actual occurrence of the orographic-precipitation feedback (which is uncertain and one of the subjects of this study). That the orographic-precipitation feedback is actually occurring or that it is having a significant impact on mass balances is not a foregone conclusion.

Prevailing northwesterly winds will also allow for the feedback to operate in reverse on the southeast side, with descending air flow suppressing the precipitation and enhancing surface melt, leading to more negative mass balances, lower surface elevations, and subsequently even greater down-slope wind magnitudes. Evidence of sustained south side chinooking has been observed for DIC during the winter (Figure 5.3b). On the southeast side of DIC, this reverse form of the feedback (in the sense of down-slope winds and decreasing surface elevations), which can arise as a result of the prevailing northwesterly winds, will compete with and oppose the forward form of the feedback (in the sense of upslope winds and increasing surface elevations) which may arise during transient episodes of easterly winds during months of ice-free water in Baffin Bay. On the northwest side of DIC, the forward form of the mass balance - elevation feedback is largely unopposed because conditions for the formation of a hydraulic jump (which would require prolonged and strong vertically averaged winds from the southeast) do not exist.

For the northwest part of DIC, atmospheric moisture and precipitation can be supplemented by year-round polynyas located upstream, such as Hell Gate polynya (Figure 5.3a). Such an atmospheric moisture perturbation in a sustained northwesterly flow could trigger an orographic-precipitation feedback and may partially account for the convexity of the northwestern DIC profiles (Figure 5.6). Surface melt can also be affected by the presence or absence of low orographically-generated cloud in northwestern parts of the DIC (Koerner, 2005), possibly further enhancing the above orographic-accumulation feedback. Alt (1978) discovered that northwestern DIC surface melt is much greater under clear sky anticyclonic conditions than it is under synoptic cloud covered conditions. Anticyclonic conditions also produce atmospheric inversions, as descending air warms adiabatically. This could result in higher-than-normal temperatures and increased melt-rates at higher elevations.

A thickening of $\sim 0.20 \text{ m yr}^{-1}$ of the DIC high elevation areas of the central and northwestern sectors between 1995 and 2000 A.D. (e.g. Abdalati et al. 2004), calculated northwest sector mass gains of ~ 0.03 to 0.04 Gt a^{-1} (Shepherd et al., 2007), and an advance of the western margin of $\sim 130 \text{ m}$ between 1960 and 1999 A.D. (Burgess et al., 2004) have been measured. While the short-term 1995-2000 thickening was unlikely to have been accumulation related as proposed by Abdalati et al. (2004), given the decrease in net accumulations over that period inferred from ice core data (Colgan and Sharp, 2008), longer-term (40 years and greater) mass gains may be a continuing or delayed dynamic response to historical climate conditions and positive mass balance associated with the LIA (e.g. Burgess et al., 2004; Colgan and Sharp, 2008). It is also possible that the mass balance – elevation feedback has had an influence on the longer-term surface mass balances on the northwest side of DIC, increasing the imbalance between surface mass balances and mass flux divergences.

Evidence that the glacier-anticyclone feedback might be important to the evolution of the DIC is found in Koerner (1966), in which it is shown that katabatic winds tend to displace snowfall accumulations to 100-200m below summit. Koerner (1979) suggested that the DIC's own circulation may be sufficiently strong above 900m a.s.l. to restrict the effects of Baffin Bay cyclones. At larger than single-ice-cap scales, a CHA-scale anticyclone has been shown to be important to the mass balance of DIC. Alt (1978; 1987) showed that a season in which a CHA-scale anticyclone dominates the evolution of the mass balance of DIC (as opposed to Baffin Bay cyclones or cyclones tracking southeastwards from the Arctic Ocean) can erase the positive mass balance of 5 seasons dominated by the Baffin Bay cyclone. This is because the anticyclone restricts summertime precipitation and accumulation, and also restricts the associated cloudy skies which suppress melt. Wolken et al. (2008b) also found that high sea level pressures dominated the CHA and Greenland during their chosen "warm decade" in the 20th century (1953-62 A.D.), and that a much weaker CHA-wide anticyclone dominated during their "cold decade" (1965-74 A.D.). This is related to the dynamics of the summer polar vortex and its effect on the occurrence of ridging over the CHA (Gardner and Sharp, 2007) which shows that Alt's (1987) explanations for interannual variability in ice cap mass balance remain valid over longer time scales as well.

Finally, numerical simulations of the post-LGM retreat of North American ice sheets have so far had difficulty in simulating the geomorphologically-inferred post-LGM ice thinning and retreat in the CHA (e.g. Marshall, 2000; 2002). It has been suggested that this may be due to a poor understanding of glaciological processes, but it may equally be due to a poor understanding of ice-atmosphere coupling processes and resultant feedbacks between these two systems.

5.3 MODELS

To examine the importance of the mass balance – elevation feedback to the evolution of the DIC, specifically the orographic-precipitation feedback and the glacier-anticyclone feedback, the following "mechanical" atmosphere and ice models are developed and coupled. By "mechanical", it is meant that thermal and surface energy calculations are omitted so that the mass balance – elevation feedback is isolated from the snow/ice-albedo feedback. This also means therefore the lapse-rate feedback form of the mass balance – elevation feedback cannot be explicitly examined.

5.3.1 *Atmosphere*

The atmospheric model used in this study is very similar to the simple slab models for orographic precipitation used by others (e.g. Jiang, 2003; Hulton and Sugden, 1995; Sanberg and Oerlemans, 1983). In slab models, the local precipitation rate, p , over the windward slope is calculated using:

$$p = \epsilon \rho_a q_0 U \cdot \nabla h \quad (1)$$

where ϵ is the constant precipitation efficiency, ρ_a is the air density, q_0 is the water vapor mixing ratio at the ground, U represents the un-sheared incoming horizontal air flow, and ∇h is the local terrain slope (Jiang, 2003). Slab models have been shown to be successful at predicting orographic precipitation amounts, especially in the statistical sense, because for low mountains, precipitation is proportional to ascent (Jiang, 2003). Jiang (2003) concluded that slab models of this type can provide a reasonable estimate of the condensation and the distribution of orographic-related precipitation in wintertime mid-latitude areas as long as the mountain height was not so high as to force the air to flow around it instead of over it. A model of this type was also used by Sanberg and Oerlemans (1983) to examine the effect of upslope precipitation on Pleistocene European ice sheets.

The linear dependence of orographic precipitation upon mountain height eventually breaks down, however, as the mountain becomes too high and air flow is forced around rather than over the peak or moisture in the air has been precipitated out and depleted at lower elevations (according to experiments using a more physically realistic mesoscale atmospheric model; Jiang, 2003). Beyond certain critical mountain heights (which ranged anywhere between 1000 to 3500 m a.s.l. in Jiang's (2003) experiments) the local precipitation rates no longer increase with mountain height and even begin to decrease (Jiang, 2003). Because of this, and to improve upon simply multiplying the background flow by the surface slope of the ice cap to obtain the topographically-generated vertical winds, the vertical winds were computed in this study using a shallow water equation model.

Assuming a hydrostatic atmosphere of constant density, the non-linearized, inviscid, shallow water momentum and mass continuity equations are:

$$\frac{\partial u'}{\partial t} + u \frac{\partial u'}{\partial x} + v \frac{\partial u'}{\partial y} - fv = -g \frac{\partial \eta}{\partial x} \quad (2)$$

$$\frac{\partial v'}{\partial t} + u \frac{\partial v'}{\partial x} + v \frac{\partial v'}{\partial y} + fu = -g \frac{\partial \eta}{\partial y} \quad (3)$$

$$\frac{\partial \eta}{\partial t} = -\nabla \cdot (h\mathbf{u}) = -u \frac{\partial (\eta - e)}{\partial x} - v \frac{\partial (\eta - e)}{\partial y} - h \frac{\partial u'}{\partial x} - h \frac{\partial v'}{\partial y} \quad (4)$$

Here, the thickness of the atmospheric layer, $h=H+\eta-e$, is equal to the mean layer thickness, H , plus the amplitude of topographically-generated waves which form at the upper free surface of this layer, η , minus the elevation of the surface topography at the base of this layer, e . Note that e in this model corresponds to

the surface elevation of the ice cap, h_s in the ice model described below. The letter g denotes the acceleration due to gravity, and t represents time. Horizontal distance is represented by the east-west x -coordinate and the north-south y -coordinate, and the horizontal wind is represented by u in the east-west direction and v in the north-south direction. The vector \mathbf{u} represents the total horizontal wind. Note that \mathbf{u} is a vertically-averaged horizontal wind for the atmospheric layer. The total horizontal wind, $\mathbf{u}=\mathbf{U}+\mathbf{u}'$, is composed of the mean climatological wind, \mathbf{U} , plus an anomalous, topographically-generated component, \mathbf{u}' .

The mean atmospheric state, as represented by \mathbf{U} and H , is prescribed such that it is constant in time and space. The horizontal divergence of \mathbf{U} and the horizontal gradient of H are therefore zero. Equations (2) and (3) thus become the horizontal momentum equations for the anomalous wind components, and equation (4), the incompressible mass continuity equation integrated over the single atmospheric layer, becomes a prognostic equation for η .

The inviscid assumption is made because frictional effects can generally be neglected for synoptic-scale motions above the planetary boundary layer (e.g Peixoto and Oort, 1992, pp37-38). It was further assumed that the Coriolis parameter, $f\sim 1\times 10^{-4} \text{ s}^{-1}$, is constant in equations (2) and (3) because f varies little over latitude spans of a few degrees.

Most of the model experiments in this chapter are conducted in 1D. In these experiments, the Coriolis force is neglected, partly because the cross-flow is not computed, and partly because the relatively small diameter of the DIC means that this effect is minor. This can be demonstrated by computing the Rossby deformation radius, the ratio of the speed of shallow water waves in the atmosphere to the coriolis parameter. For a troposphere 10 km thick and a coriolis parameter of $f\sim 10^{-4} \text{ s}^{-1}$, the Rossby deformation radius is $\sim 3000\text{km}$. Thus, the deflection of shallow water waves (with amplitude η) by the coriolis force over distances of much less than 3000km will be minimal. However, for gradient wind situations (as will be discussed on p. 164), where the centripetal force becomes an important component, the radius of curvature is now the ratio of the wind speed to the coriolis parameter f (Holton, 1979, p. 59). For DIC, where mean winds are typically $\sim 1\text{-}10 \text{ m s}^{-1}$, this radius of curvature is $\sim 100\text{km}$. In gradient wind situations, neglecting the coriolis force for DIC is therefore less justifiable. In summary, the Coriolis force is neglected in the 1D experiments, although it is noted that its influence begins to achieve comparable importance to the inertial and pressure gradient terms at length scales greater than 100km when and where centripetal forces are important. Although not a factor in the 1D experiments, neglecting the Coriolis force in 2D simulations would lead to a slight under-estimation of the strength of the mechanically-generated anticyclone at the ice cap surface.

The 1D shallow water equations for the atmosphere are:

$$\frac{\partial u'}{\partial t} + u \frac{\partial u'}{\partial x} = -g \frac{\partial \eta}{\partial x} \quad (5)$$

$$\frac{\partial \eta}{\partial t} = -\frac{\partial(hu)}{\partial x} = -u \frac{\partial(\eta - e)}{\partial x} - h \frac{\partial u'}{\partial x}. \quad (6)$$

where the x and u now represent the upstream-downstream horizontal coordinate and wind, respectively.

Since no mean vertical motion is prescribed, model vertical winds exist purely as anomalous winds, $w=w'$ (such as those generated by atmospheric flow over an obstacle). At the upper free surface of the atmosphere, w at any specific point is equal to $d\eta/dt$ and is related to the velocity divergence within the atmosphere. Thus, from $\partial u'/\partial x + \partial w'/\partial z = 0$ (assuming an incompressible atmosphere) – the uninterated form of the mass continuity equation (6) – if $\partial u'/\partial x$ is not zero, then $\partial w'/\partial z$ cannot be zero. Even when $w=0$ at the top of the atmosphere, it cannot be zero at all levels within the atmosphere (i.e. w' cannot be zero within the atmospheric layer) if and where horizontal velocity divergences/convergences exist. For this reason, $\partial u'/\partial x + \partial w'/\partial z = 0$ was used to calculate w' within the atmospheric layer in this study. If the vertical wind is further assumed to be zero at the earth's surface and at atmospheric mid-levels, w then varies linearly with z , being positive in the lower atmosphere and negative in the upper atmosphere where horizontal divergences in u are positive (and vice versa where horizontal divergences in u are negative).

The model precipitation rate, p , is the sum of a prescribed annual mean background precipitation, \bar{P} (implicit within the surface mass balance term), and an anomalous precipitation component, p' , which is generated by vertical movement in the atmosphere. If it is assumed that any positive w' results in complete saturation and 100% precipitation of all available atmospheric moisture (as is assumed in some of the preliminary experiments in this study and which is similar to the slab_100 model experimented with in Jiang, 2003), equation (1) now becomes:

$$p' = \rho_a \times q_0 \times w' \quad (7)$$

where ρ_a is taken to be $\sim 1 \text{ kg m}^{-3}$ and where q_0 , here the annual mean specific humidity, has a CHA-appropriate value less than or equal to 0.001 kg kg^{-1} (e.g. Peixoto and Oort, 1992, p165-168, p279-281). The corresponding surface accumulation rate (in m s^{-1}), is then calculated by dividing (7) by the density of snow (or ice, if snow to firn transitions are neglected as is the case with this model). Enhanced orographic precipitation occurs where vertical velocities are positive; suppressed precipitation occurs where vertical velocities are negative. Note that specific humidity (the ratio of water vapour mass to total air mass) and mixing ratio (the ratio of water vapour mass to dry air mass) are not exactly the

same thing although both are expressed in kg kg^{-1} (e.g. Rogers, 1979, p18-19). Specific humidity was used in this study in place of mixing ratios, however, because most data sources are expressed in this form (e.g. Peixoto and Oort, 1992, p279-284). Also note that precipitation efficiencies were not taken to be 100% in all experiments in this study. A discussion of appropriate precipitation efficiencies can be found in section 5.4.2.4.

5.3.2 *Ice*

In this study, ice cap cross-sections were modeled as isothermal Newtonian (linearly-viscous), hydrostatic fluids. Assuming a linear stress-strain rate constitutive relationship simplifies the inclusion of the longitudinal stresses in the momentum equation, and is justified in many areas of a deforming ice cap (e.g. near divides – Mangeney et al., 1996; Mangeney and Califano, 1998; at ice depths shallower than 115m – Marshall et al., 2002; in all regions of low deviatoric stress – Pettit and Waddington, 2003; and in regions of diffusional flow – Goldsby and Kohlstedt, 2001). A linear constitutive relationship has even been derived directly from observations for parts of the DIC (Wolff and Doake, 1986). While a non-linear constitutive relation better describes ice deformation at depths near the ice bed, where basal shear stresses are higher, a linear constitutive relationship with an exponent of $n=1$ is just as valid or invalid as a non-linear one with an exponent of $n=3$, when modelling an entire ice cap in the absence of a mixed flow law (e.g. such as those proposed by Goldsby and Kohlstedt, 2001, and Mangeney and Califano, 1998). Additionally, most simulations of glacier flow are based on the assumption that ice has an isotropic viscosity (Mangeney et al., 1996). While this is reasonable near the surface of an ice sheet, it is not reasonable at greater depths. In anisotropic ice, the shear stresses are relaxed while the longitudinal stresses are significantly increased (Mangeney et al., 1996). Mangeney et al. (1996) argue that $n=1$ should prevail in ice sheets.

The shallow ice assumption (that glacier length scales greatly exceed thickness scales) was also made, allowing the ice to be modeled as a single layer. This simplifies the mass continuity equation but then requires that part of the shear stresses in the momentum equation be parameterized. A quadratic bottom friction viscous drag term is commonly used to do this (e.g. Garrett, 2004; Grubišić et al., 1995). Note that the shallow ice assumption is commonly used as a rationale for neglecting the longitudinal stresses in ice flow models, but this was not done here. Longitudinal stresses become important in areas of spatially varying ice convergence and divergence (such as near the margins and summit of an ice cap), and including these stresses in the model equations is essential in order to obtain realistic horizontal velocity distributions (e.g. Hubbard, 2000).

Under the above assumptions, the ice model equations reduce from 2D to the following 1D equations:

$$0 = \frac{1}{\rho} \left(-\frac{\partial P}{\partial x} + \frac{\partial \tau_{xx}}{\partial x} + \frac{\partial \tau_{xz}}{\partial z} \right) \Rightarrow$$

$$0 = -g \frac{\partial h_s}{\partial x} + \nu \frac{\partial^2 \bar{u}}{\partial x^2} + \frac{C_D}{h} |\bar{u}| \bar{u} \quad (8)$$

$$\frac{\partial u}{\partial x} + \frac{\partial w}{\partial z} = 0 \Rightarrow$$

$$\frac{\partial h_s}{\partial t} = -\frac{\partial(h\bar{u})}{\partial x} + \dot{b} \quad (9)$$

where ρ is the density of the ice (assumed constant), g is the acceleration due to gravity, P is the hydrostatic pressure, x and z are the horizontal and vertical coordinates, respectively, and u and w are the horizontal and vertical ice velocities, respectively. τ_{xx} and τ_{xz} are the deviatoric longitudinal and shear stresses, respectively, and t represents time. The thickness of the ice layer, h , is equal to the surface elevation, h_s , minus the bed elevation, h_b . C_D is a non-dimensional basal drag coefficient, ν is the kinematic viscosity of the ice (proportional to the inverse of A , the flow parameter in Glen's Flow Law for polycrystalline ice – Glen, 1955), and \bar{u} is the depth-averaged velocity of the ice at any given horizontal grid point in the model. The time-dependent surface mass balance of the ice, \dot{b} , is equal to the accumulation rate (of snow/ice) minus the ablation rate (snow/ice melt lost via runoff, or mass lost via iceberg calving at the margins) at any given horizontal grid point. Note that the inertial terms and the Coriolis term are neglected in equation (8) because for ice flow these terms are orders of magnitude smaller than the stress balance terms.

The momentum equation (8) in some experiments was further simplified to:

$$0 = -g \frac{\partial h_s}{\partial x} + \nu_e \frac{\partial^2 \bar{u}}{\partial x^2}, \quad (10)$$

where ν_e is an enhanced kinematic viscosity, because experiments indicate that enhancing the viscosity of the ice adequately accounts for the frictional effects related to viscous basal drag. That is, assuming that the effects of the third (parameterized vertical shear) term on the right hand side of equation (8) can be included in the equation by enhancing the viscosity of the second term on the right hand side was found to make little difference to the results. It should be noted, however, that this formulation of the equation precludes a $\bar{u}(x)=\text{constant}$ solution and is therefore not strictly realistic.

In the model runs, the ice cap margins may be fixed by setting $\bar{u}=0$ at the edges, to simulate negligibly-moving inland margins or margins frozen to the bed.

Decoupling of the ice margins from the bed, and/or calving if ice flowing across the margin is assumed lost, may be simulated by setting $\partial\bar{u}/\partial x=0$ at the edges.

Enhanced ice flow as a result of basal motion, important in the outlet glaciers on the east side of the DIC (Dowdeswell et al., 2004; Burgess et al., 2005), was simulated in the experiments by locally modifying the basal drag coefficient in (8) or the layer-average ice viscosity in (10).

5.3.3 Coupling the Ice and Atmosphere Models

In some experiments, a coupled ice-atmosphere model is used to investigate the joint impacts of time-evolving surface mass balances (as modified by the feedback) and time-evolving mass flux divergences (as modified by surface slope changes) upon the topographic evolution of an initially dome-shaped ice cap.

The ice-atmosphere model is constructed by asynchronously coupling the 1D ice and atmosphere models described above. Asynchronous coupling of the two models is necessary because the dynamic response times of the ice and the atmosphere are so different (decades-millennia versus seconds-hours, respectively). Response times may be taken to be of order L/U (length/velocity, from the mass continuity equation). Typical length scales for Arctic ice caps are 10's to 100's of kilometres, while typical deformational ice velocities are on the order of 1's to 10's of m yr^{-1} . These values yield response times of 10^2 to 10^5 years for an entire ice cap, although these times may be an order of magnitude shorter for individual outlet glaciers. For similar length scales in the atmosphere, typical wind velocities of 1 to 10 m s^{-1} yield response times of 10's of minutes to 10's of hours. Thus, for a given mean atmospheric flow over a specified ice surface topography, the 1D atmosphere adjusts to a new equilibrium in a very short time compared to the response time of the ice cap. Furthermore, this atmospheric equilibrium remains approximately constant for decades-millennia in the model, because the ice surface beneath changes so slowly.

Given the above, the surface mass balance in the model is assumed to remain fixed for 50 years following the calculation of an atmospheric equilibrium state. Ice flow, which also changes slowly, is assumed to remain fixed throughout these 50 years as well. Under these fixed mass balance and ice flux conditions, ice thicknesses are then integrated forward in time over 5×10 -year time steps (i.e. over 50 years), by means of forward-time centred-space finite differencing (using a LAX method) on a grid with a horizontal spacing of 10 km. At the end of each 50 year period, the atmospheric flow, mass balance, the equilibrium ice flow, and ice flux divergence are recomputed.

5.4 EXPERIMENTS AND RESULTS

The model experiments in this study aim to quantify the impact of the mass balance – elevation feedback for the DIC summit and northwest sector (i.e. the orographic-precipitation feedback and the mechanical part of the glacier-anticyclone feedback). Specifically, the goal of the experiments is to examine the feedback-related amplification of atmospheric flow or moisture perturbations and its influence upon the post-LGM evolution of a CHA ice cap (i.e. the DIC). The experiments were divided into three groups: 1) dynamic ice / static atmosphere experiments which use the ice-model only; 2) static ice / dynamic atmosphere experiments which use the atmosphere-model only; and 3) coupled ice-atmosphere model experiments.

5.4.1 *Dynamic Ice – Static Atmosphere Experiments*

5.4.1.1 SETUP OF ICE-ONLY MODEL EXPERIMENTS

Before proceeding to the coupled model experiments, three preliminary idealized experiments are performed with the ice cap model on its own, assuming static atmospheric conditions, to assess the degree to which DIC is in equilibrium with its present-day surface mass balances (MBs) and mass flux divergences (MFDs). These experiments use a symmetric ice dome, approximately the height and diameter of the DIC (i.e. with a diameter of ~ 150 km and a summit near 2000 m), as their initial starting points and make no assumption regarding the basal topography of the ice cap (i.e. it is assumed that bed elevations are zero everywhere). Assuming a flat bed helps to emphasize the impact of the assumed boundary conditions at the margins of the ice cap (fixed vs. free-flowing), before adding in the extra complication of basal topography. Model ice cap surface elevations are then integrated forward in time as per equation (9), allowing for:

- a) zero surface MBs and non-zero MFDs;
- b) non-zero MBs and zero MFDs; and
- c) non-zero MBs and non-zero MFDs.

Ice velocities are then diagnosed from the new surface elevations every 50 years, using equation (8).

For the MFD-only experiment, DIC ice velocity measurements (e.g. Cress and Wyness, 1961; Doake et al., 1976; Wolff and Doake, 1986; Dowdeswell et al., 2004; Burgess et al., 2005; Shepherd et al., 2007) were used to constrain the ice velocities computed with the model, and modeled velocities were then used to constrain model MFDs. The western part of the ice cap and the ice cap interior flow primarily by ice deformation, while southeast side outlet glacier flow is enhanced by basal motion so that velocities can be $\sim 7\times$ greater than northwest side ice velocities. To simulate this in the model, contrasting northwest-southeast ice viscosities and drag coefficients (in equations 8 and 10) were experimented with. Because very similar results could be produced with either equation (8) or (10), depending on the viscosities and drags chosen, and because ice velocities are

easily computed from equation (10) using a relaxation method, this equation was used in most of the model experiments.

Since bed elevations of the idealized ice dome used in these model experiments are prescribed to be zero everywhere, model MFDs for given ice velocities will be greater than actual Devon MFDs by a factor of 3 to 5 (since actual DIC ice thicknesses are $\sim 1/5$ to $1/3$ of the model ice thicknesses). Actual DIC ice thicknesses range from ~ 200 - 600 m along the transects depicted in Figures 5.5 and 5.6 (see Figure 5.8, derived from data from Dowdeswell et al., 2004). So that the balance between observed surface MBs and model MFDs in the experiments remain similar to that of Devon Ice Cap, model mass fluxes ($\bar{h}\bar{u}$) were constrained to realistic values by reducing \bar{u} by $1/4$. That is, ice viscosities were chosen which produced model ice velocities with magnitudes $\sim 1/4$ of those observed. Note that measured bed elevations are used in the fully coupled experiments later on.

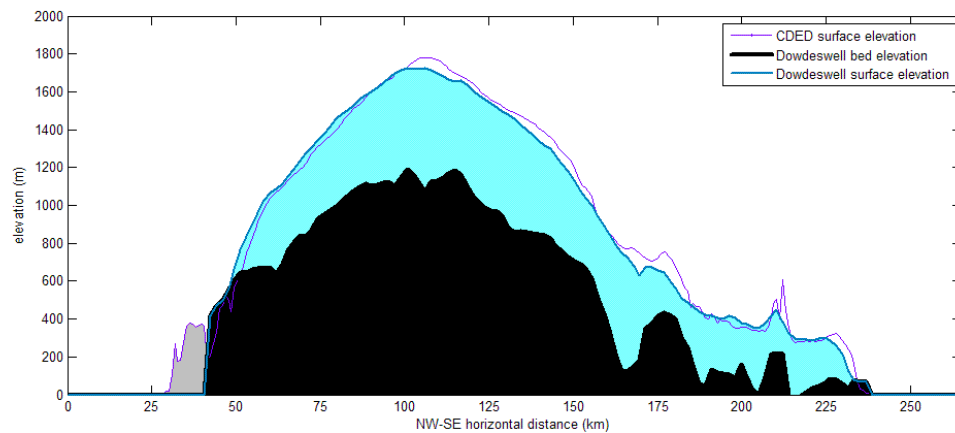


Figure 5.8. DIC ice thickness along a NW-SE transect passing through the center of the ice cap. 1 km - resolution surface and bed elevation data courtesy of Dowdeswell et al. (2004). For comparison, 500m-resolution 1959-1960 CDED surface elevations along the same transect are also plotted. The grey area on the left illustrates an area where CDED surface elevation data are available beyond the limit where the Dowdeswell et al. (2004) surface and bed elevation data end. The ice cap terminates at an elevation of ~ 600 m on its northwest side and at an elevation near sea level on its southeast side.

The MFD-only experiment was further divided into three cases:

- i) where both the northwest and southeast margins were assumed to be frozen to their beds and where ice mass was conserved;
- ii) where both margins were again assumed frozen to their beds, but where ice mass crossing the southeast margin was assumed lost from the ice cap (via glacier calving); and
- iii) where the northwest margin was assumed frozen to its bed but where the southeast margin was not, and where mass crossing the southeast margin was assumed lost from the ice cap (via glacier calving).

In experiments i)-iii), the kinematic viscosity in (10) was universally chosen as $\nu=4.0\times10^{+14} \text{ m}^2 \text{ s}^{-1}$. With such a viscosity, the ice model predicted initial equilibrium ice flow velocities with an order of magnitude of $<10^1 \text{ m yr}^{-1}$. This viscosity value is equivalent to an ice flow parameter of $\sim A=1.4\times10^{-18} \text{ kPa}^{-3} \text{ s}^{-1}$, where $(A=1/(2\rho\nu))$, which is appropriate for ice temperatures near -40°C (e.g. Paterson, 1994, p97). While DIC ice temperatures are warmer than this (e.g. Paterson and Clarke, 1978), recall that ice viscosities that generated reduced ice velocities were purposely chosen so that realistic DIC mass flux divergences could be reproduced in these experiments.

In experiments ii) and iii), to create a NW-SE contrast in ice flow, ice velocities were reduced to 80% of calculated values to the west of the 160km-mark (i.e. for ice lying above $\sim 600\text{m}$ elevation – see Figure 5.8). Ice velocities to the east of the 160km-mark were kept at 100% to simulate the faster flowing outlet glaciers in this area. Ice flow boundary conditions were chosen as $\bar{u}=0$ to simulate a margin frozen to its bed and $\partial\bar{u}/\partial x=0$ to simulate a margin across which ice travels freely (only to be lost to calving).

In the MB-only experiment, the NW and SE mass balance – elevation curves presented in Mair et al. (2005) were employed as the model MBs. In this experiment, the ice is assumed static and no ice velocities are modeled or used. A dome-shaped ice cap with an initial summit elevation of 1500 m is simply allowed to evolve for 5 ka under the prescribed MBs.

In the MB+MFD experiment, the MBs of Mair et al. (2005) were combined with time-evolving MFDs computed as in case iii) of the MFD-only experiment. Ice viscosities for the interior and western part of the ice cap were chosen as before, however for the eastern side of the ice cap ice viscosities were empirically decreased by a factor of 6.7. On both sides, as before, computed ice velocities were then reduced to 80% at elevations above $\sim 600\text{m}$. The reduction in east-side ice viscosity was found to be necessary in order to realistically quasi-balance the observed MBs.

5.4.1.2 RESULTS OF ICE-ONLY MODEL EXPERIMENTS

Results for the MFD-only experiments indicate that a symmetrical ice dome with an initial summit elevation of 2500 m will, after 10 ka, evolve a surface elevation profile that is very DIC-like under the conditions prescribed in case iii) (Figure 5.9i). These results indicate that a contrast in glacier flow (deformation-only vs. deformation+basal motion) together with a freely-calving, unfrozen southeast margin, have been historically important factors in the geometric evolution of DIC.

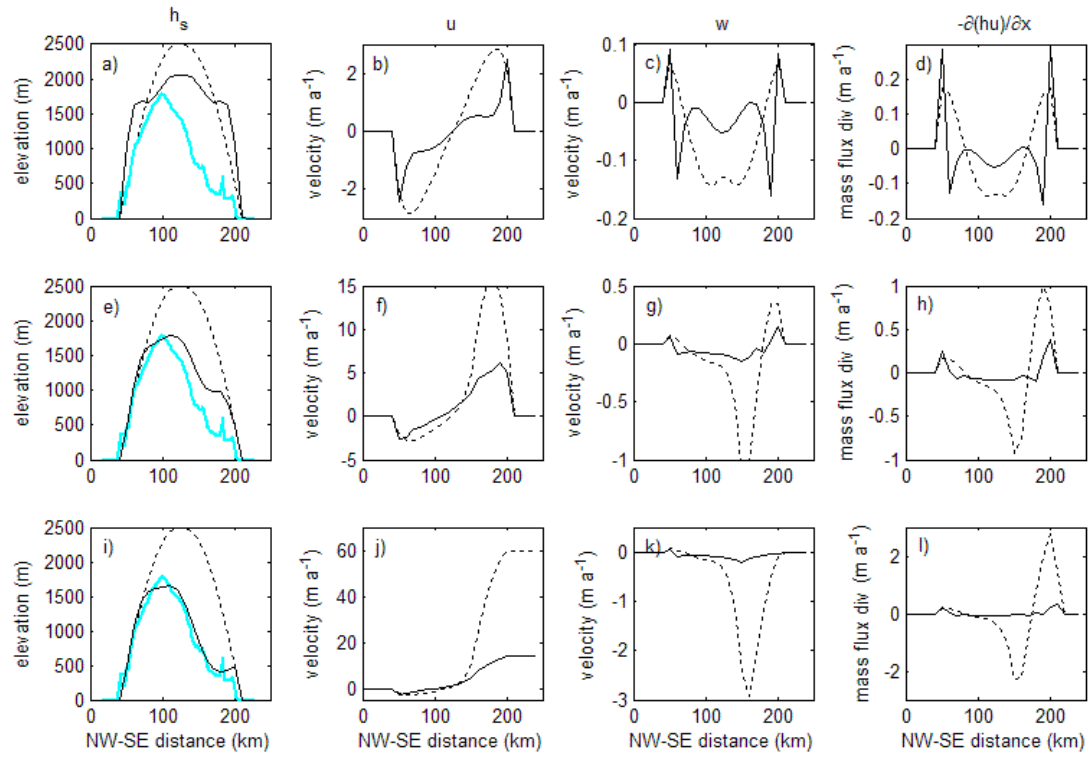


Figure 5.9. The three rows represent the three MFD-only ice experiments (Row 1 = case i); Row 2 = case ii); Row 3 = case iii)), while the columns display the surface elevations, horizontal velocities, vertical velocities, and mass flux divergences in each case. Dotted lines represent initial conditions and solid lines represent the solution after 10 ka. The blue line in the first column is a DIC NW-SE transect (from the CDED DEM), plotted for reference.

Results of the MB-only experiment show clearly that in the absence of mass flux divergences, the ice cap summit would continue to increase in elevation while the ice cap margins would significantly recede (Figure 5.10). Note that the final result presented in Figure 5.10 is in no way an equilibrium solution: ice surface elevations are still changing at 5 ka.

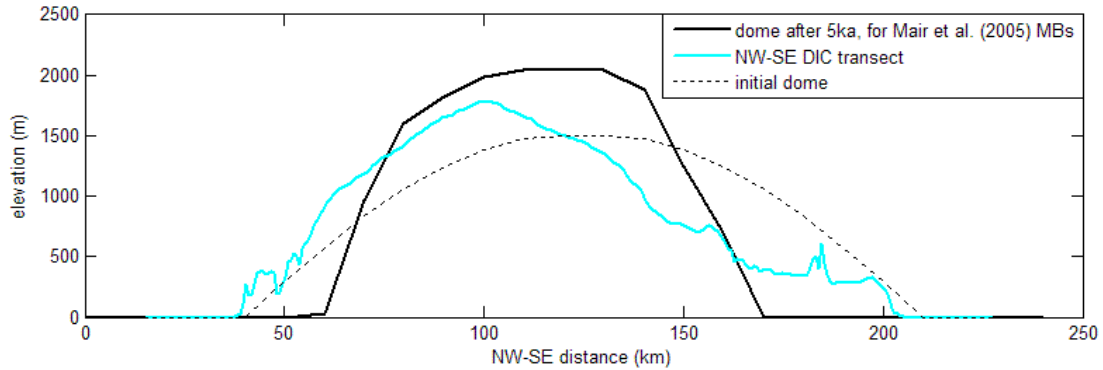


Figure 5.10. Modeled surface elevation in the MB-only experiment.

Results of the MB+MFD experiment, under fixed observed surface mass balances and time-evolving mass flux divergences, indicate that a dome-shaped ice cap with an initial summit elevation of 1850m evolves into a nearly equilibrium profile similar to that of DIC after approximately 2000 years. Note that although the centre DIC transect of figures 5.5 and 5.6 is displayed in all plots of the results for comparison purposes, in this case the resultant profile is more similar to that of the eastern transect.

The ice cap profile changes little after 2 ka in the MB+MFD experiment, except near the northwest summit (Figure 5.11) where it continues to increase in elevation and to bulge outwards at a rate of ~ 0.02 to 0.06 m yr^{-1} . This would indicate a slight disequilibrium between the MBs and the modeled MFDs in this location. Although the model experiment is admittedly highly idealized in nature, the northwest MB-MFD imbalance is not unrealistic given the advance of the northwest sector of the ice cap reported in Burgess and Sharp (2004) and the mass gains at high elevations in the northwest of the DIC reported by Shepherd et al. (2007). While the model thickening under-simulates the $\sim 0.20 \text{ m yr}^{-1}$ 1995-2000 A.D. thickening reported in Abdalati et al. (2004), it may be more representative of a longer-term average. For example, although they do not consider the northwest sector in their study, Burgess and Sharp (2008) report a $-0.01 \pm 0.05 \text{ m yr}^{-1}$ w.e. 40-year thickness change for the adjacent northern-sector accumulation zone of the DIC (where a slight thickening is still within the error bounds of their calculations).

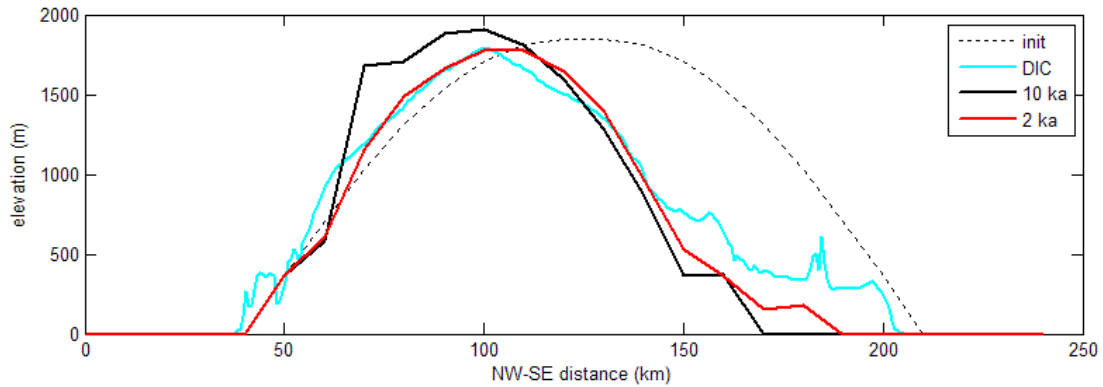


Figure 5.11. The evolution of a dome-shaped ice cap after 2 ka and 10 ka under fixed present-day Devon Ice Cap mass balances and time-evolving mass flux divergences: initial ice dome profile (dashed line), final ice profiles (red and black lines), and 2D transect through the Devon Ice Cap (light blue line). The “peak” on the northwest side of the ice cap is the result of fixing surface elevations at the next left grid-point to a value close to the initial value, given that the actual DIC terminates at ~600m elevation on this side of the ice cap. This forces the deforming ice to bulge upwards as it converges against the invisible “wall”, as in Figure 5.9a.

5.4.1.3 DISCUSSION OF ICE-ONLY MODEL EXPERIMENT RESULTS

The above experiments demonstrate a number of things:

1 – Even in the absence of basal topography, contrasting mass flux divergences on either side of the initial ice dome, which mimic the balance between present-day DIC surface mass balances and mass flux divergences, will eventually lead to an ice cap profile that is very similar to that of the DIC.

2 – Devon Ice Cap’s profile is presently close to equilibrium (except for a slight disequilibrium in the northwest). Its present-day asymmetric NW-SE profile represents an approximate balance between its mass flux divergences and surface mass balances.

3 – Present-day surface mass balances and mass flux divergences likely represent long-term averages for the DIC, at least for the last 2000 years and possibly for the last 10 ka, since the shape of the ice cap profile equilibrates under these conditions to one that is similar to that of the present-day DIC. If the present-day surface mass balances and mass flux divergences were not representative of the long-term averages, a different ice cap profile would have resulted in the MB+MFD experiment. This supports Koerner’s (1970) conclusion that the present accumulation pattern must have existed for several hundreds and possibly thousands of years.

In all the model experiments, it was assumed that the ice had mostly thinned to present-day thicknesses and extents by the Climatic Optimum (~8ka B.P. – a reasonable assumption given the findings of England et al., 2006), and a generic

ice dome the approximate height and width of the DIC was used as a starting point for the up to 10 ka runs. However, it can be supposed that any initial ice cap, under present-day DIC conditions, would eventually equilibrate to an ice cap profile similar to that of the present-day DIC.

However quickly or slowly the DIC reached its present-day profile, current surface mass balances and mass flux divergences appear to be in approximate equilibrium. The key factor to the MB-MFD equilibrium on the southeast side of the ice cap is the free calving and mass loss across the southeast margin. What key element would be required for an MB-MFD equilibrium on the northwest side of the ice cap? The answer may be related to ice-atmosphere feedbacks such as the orographic-precipitation feedback, which may have been a key factor in the slow continuing evolution of the ice cap's northwest profile.

5.4.2 Dynamic Atmosphere – Static Ice Experiments

Before proceeding to the coupled model experiments, preliminary experiments were also performed with the atmosphere model, assuming a static (non-flowing) DIC, to assess:

- 1) the degree to which the mean background air flow passes over as opposed to around the DIC;
- 2) the potential magnitude of the mechanical part of the glacier anticyclone feedback; and
- 3) the potential magnitude of the orographic-precipitation feedback.

5.4.2.1 2D ATMOSPHERE-ONLY MODEL EXPERIMENTS: SETUP AND RESULTS

To assess the degree to which the mean background air flow passes over as opposed to around the DIC, the atmosphere model (momentum equation only) was run under various mean background flow conditions, using a coarse 10km-resolution version of the CDED DIC surface elevations for the static model surface topography. Use of the coarser 10km-resolution (as opposed to the finer 1km-resolution) surface topography did not have a significant impact upon the model results in trial runs and greatly sped-up the model convergence time. This resolution was therefore adopted in the experiments below. Mean atmospheric flow directions were varied from southwest to northwest (i.e. a range of directions realistically possible for the vertical mean tropospheric flow over DIC) and speeds were varied from 5 to 10 m s⁻¹.

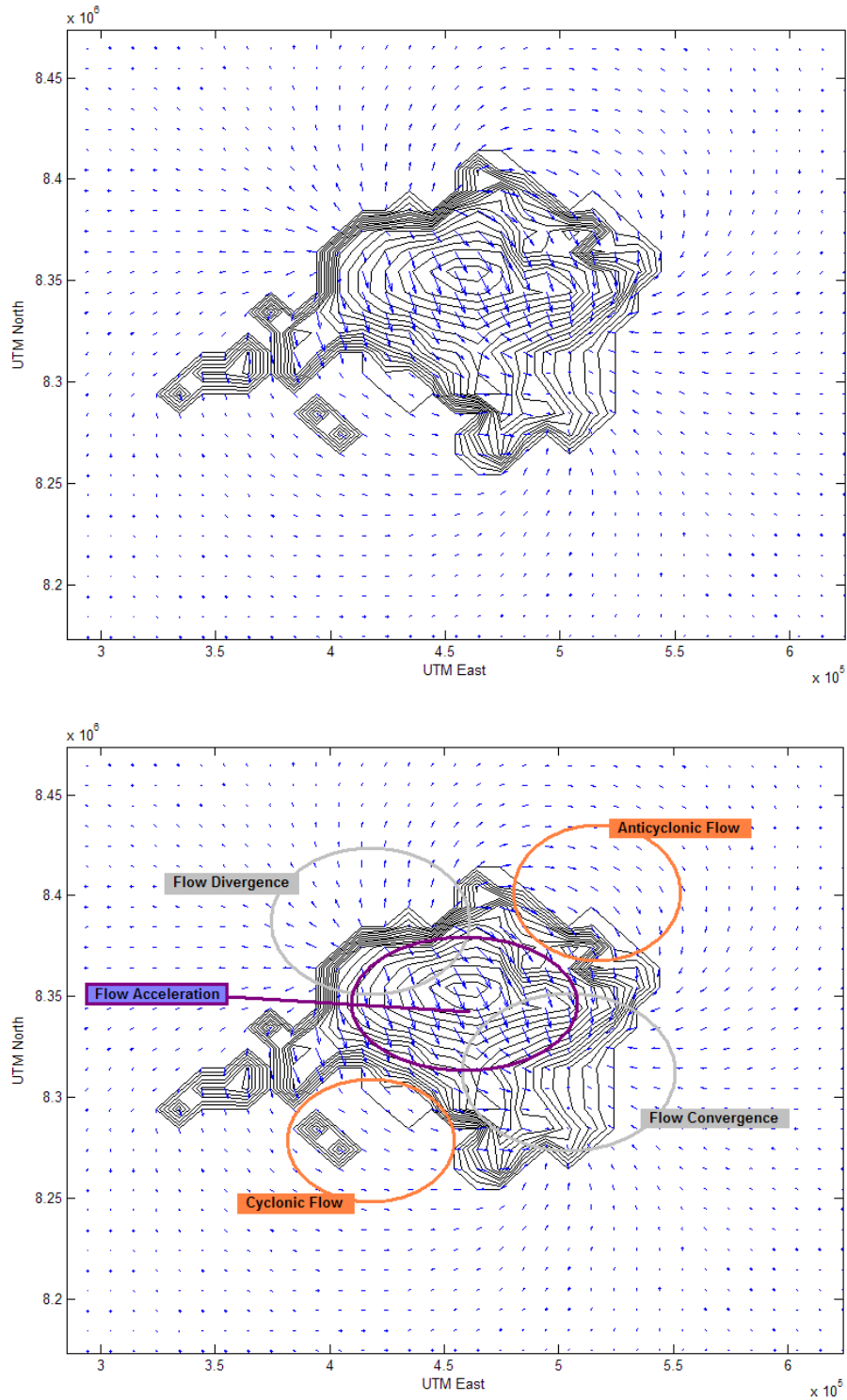


Figure 5.12. DIC anomalous, topographically-generated winds for a mean northwesterly flow of 25 km hr^{-1} (7 m s^{-1}). Top: without annotations. Bottom: with annotations indication areas of accelerated flow, flow divergence and convergence, and anticyclonic and cyclonic flow. The largest arrow over the ice cap summit = 1.0042 m s^{-1} .

The results of the 2D experiments demonstrated a number of things:

1 – Regardless of the direction of the mean background atmospheric flow, most of the air flows over the ice cap (Figure 5.12).

2 – As the air flows over the ice cap, it accelerates to create a zone of velocity divergence on the upstream flank of the ice cap and a zone of convergence on the downstream flank of the ice cap (Figure 5.12).

3 – A smaller amount of air is topographically-forced to flow around the ice cap (Figure 5.12).

4 – The magnitude of the anticyclonic flow of air around the north side of the ice cap is slightly greater than that of the cyclonic flow of air around the south side of the ice cap. Anticyclonic flow is always slightly greater than cyclonic flow in the northern hemisphere, for a given pressure gradient and Coriolis force, especially at sub-synoptic scales, due to a centrifugal force that develops in flows with strong curvature. The equilibrium balance between the pressure gradient, the Coriolis force, and the centrifugal force is called the gradient wind (e.g. Holton, 1979, p56-64).

The results of the 2D experiments (Figure 5.12) are similar to wind values and patterns that were produced during the observed hydraulic jump event observed for the DIC the week of February 19, 2008 (Figure 5.3b, lower panel). In both Figures 5.3b(lower) and 5.12 there is a visible acceleration of the flow over the ice cap, a divergence in the flow on the northwest side, a slight reversal and convergence in the flow on the southeast side, and a slightly greater acceleration of the anticyclonic flow around the north and northeast side of the ice cap than there is of the cyclonic flow around the southwest side (as a result of the centrifugal force associated with strong curvature of the flow).

5.4.2.2 DISCUSSION OF 2D ATMOSPHERE-ONLY MODEL RESULTS

Because the anomalous flow to the north of the DIC is greater than the flow to the south, the around-cap part of the topographically-generated airflow has a relative anticyclonic vorticity, $\zeta < 0$ (where $\zeta = \partial v / \partial x - \partial u / \partial y$; Holton, 1979, p83) which could serve to enhance any thermally-generated glacier anticyclone. Enhancing the ice cap's own anticyclonic circulation can in turn serve to restrict the influence of Baffin Bay lows upon the ice cap's mass balance near the summit (e.g. Koerner, 1979). Experiments with a double-thickness, double-radius DIC did not yield any significant change in the proportions of airflow over and around the ice cap, however (see section 5.4.2.3 for more about these proportions). For this reason, it is concluded that the contribution of this mechanism to the glacier anticyclone feedback, where DIC is concerned, is for the most part insignificant and that temperature plays the far greater role in the generation and erosion of the glacier anticyclone and any ice-atmosphere associated feedbacks.

5.4.2.3 1D ATMOSPHERE-ONLY MODEL EXPERIMENTS AND RESULTS

As in the 2D experiments, a similar 1D experiment, for a mean atmospheric height of $H \sim 8000$ m, a mean atmospheric flow of $U \sim 5$ m s⁻¹, and a DIC-sized dome for the static surface topography, resulted in a top-of-the troposphere height anomaly typical of low Froude Number ($Fr \equiv U^2/gH$) sub-critical flows (Figure 5.13a) and a topographically-generated acceleration of the air flow over the ice cap summit related to the Bernoulli effect (Figure 5.13b). Maximum values of η , u' , and w' produced by the mean winds passing over a sinusoidal ice cap ~ 2000 m high and 150 km wide (e.g. see the initial ice dome in Figure 5.11) are $\eta \sim -0.68$ m (0.0085% of H), $u' \sim +1.14$ m s⁻¹ (23% of U), and $w' \sim \pm 0.018$ m s⁻¹ (Figure 5.13c), where w' is the value calculated from the horizontal velocity divergence.

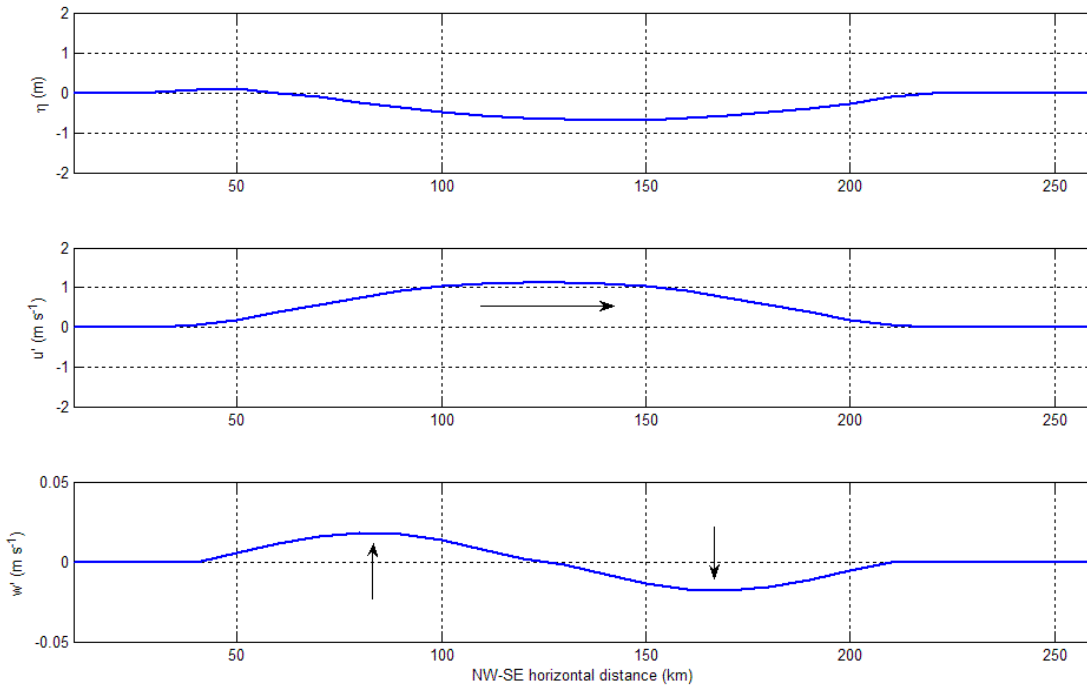


Figure 5.13. Anomalous atmospheric circulation induced by a mean 5 m s⁻¹ flow over a Devon-sized dome-shaped ice cap: a) anomalous tropospheric heights about 8000m; b) anomalous tropospheric layer-mean horizontal winds; and c) anomalous lower- to mid-tropospheric vertical winds.

Note that for equivalent background flows, the 1D ice-dome experiment produced greater-magnitude anomalous summit winds than did the 2D DIC experiment, because there is no option for part of the air flow to go around the obstacle in the 1D experiment. Thus, while a 7 m s⁻¹ background air flow in the 2D case produced values of $\eta \sim -0.87$ m and $u' \sim +1$ m s⁻¹, in the 1D case it produced values of $\eta \sim -1.3$ m and $u' \sim +1.6$ m s⁻¹ (and $w' \sim \pm 0.10$ m s⁻¹). A 5 m s⁻¹ background air

flow in the 1D case (Figure 5.13) produced values of η , u' , and w' closer to those generated by a background flow of 7 m s^{-1} in the 2D case.

5.4.2.4 DISCUSSION OF 1D ATMOSPHERE-ONLY MODEL RESULTS

For the vertical velocities described above, for a precipitation efficiency of 100%, and for a mean annual specific humidity of ~ 0.0003 to $0.0005 \text{ kg kg}^{-1}$ appropriate for the CHA (Peixoto and Oort, 1992, p165-168, p279-281), calculations using equation (7) indicate that as much as ~ 0.20 - 0.30 m yr^{-1} of additional ice-density-equivalent precipitation and accumulation, p' , can be generated on the upwind side of the ice dome. In reality, however, actual precipitation efficiencies are generally closer to 20% (e.g. Rogers, 1979, p175-177; Jiang, 2003, p309). A precipitation efficiency of 20% reduces the above estimate to $\sim 0.05 \text{ m yr}^{-1}$. On the other hand, if thermal calculations had been included in the simple model above, the dip in atmospheric heights caused by air passing over the ice cap would have been enhanced due to the cold surface temperatures and high atmospheric densities over the ice cap. This in turn would have served to enhance the horizontal winds over the ice cap, increasing the divergence on the upwind side of the ice cap, and consequently enhancing the anomalous vertical velocities and precipitation amounts in this location. Latent heat released during cloud condensation would also serve to enhance vertical winds and orographic precipitation amounts (Jiang, 2003). Thus, even though orographic precipitation amounts are over-estimated by the model under an assumption of 100% precipitation efficiency, they are also underestimated in the model under an assumption of 20% precipitation efficiency due to the neglect of atmospheric thermodynamics. Realistic precipitation efficiencies for the model in this study therefore lie between 20 and 100%.

For Devon Ice Cap, ice-density-equivalent snow accumulation rates on the northwest side are $\sim 0.20 \text{ m yr}^{-1}$ (as opposed to $\sim 0.45 \text{ m yr}^{-1}$ on the southeast side of the summit – from snowfall values given in $\text{g cm}^{-2} \text{ yr}^{-1}$ by Koerner, 1979). Orographically-generated precipitation amounts, although small, might therefore account for a significant percentage ($\geq 25\%$) of mean annual snowfall amounts on the upwind side of this particular ice cap. Additional accumulations of 0.05 - 0.10 m yr^{-1} could add hundreds of metres of ice to a (slowly deforming) ice cap if allowed to accumulate over thousands of years (since ice adjustment times are so much longer than atmospheric adjustment times – see section 5.1.2, final paragraph). Thus, although the orographic component to the precipitation on the northwest side of DIC is small, the significance of the orographic-precipitation *feedback* for northwestern DIC may yet be important over extended periods of time.

5.4.2.5 COUPLED ATMOSPHERE-(NON-FLOWING)ICE MODEL EXPERIMENTS: SETUP AND RESULTS

To illustrate the potential importance of the orographic-precipitation feedback over time, two experiments are conducted with the 1D version of the atmospheric

model. Both experiments neglect the impacts related to non-feedback-derived surface mass balances and mass flux divergences. That is, to model the changing ice topography in these experiments, a simplified mass continuity equation for the ice was used where $\partial e / \partial t = \partial h_s / \partial t = \dot{b} = p'$. In the first experiment, the vertical winds and the resultant p' calculated above (for a precipitation efficiency of 100%) are assumed to remain constant through time (i.e. they do not respond to the changing ice cap topography beneath). In the second experiment, vertical winds and the resultant p' are allowed to change with (i.e. respond to) the changing surface topography below: the atmospheric state is recalculated after every 50 years of surface accumulation. Note that where p' is negative (due to w' being negative), its value is set to zero. While a negative p' realistically simulates the suppression of precipitation on the lee side of the ice cap due to topographically-generated negative vertical winds (i.e. the rain shadow effect), this is not explored in the experiments in this study.

After 5000 years the initial dome-shaped ice cap in the first experiment evolves into an asymmetric profile similar to that of the DIC (in that it has a northwest-southeast asymmetry with a westward-shifted summit divide position), although with an exaggerated summit elevation (Figure 5.14a). In this experiment, the ice divide migrates ~50km to the northwest of its original position (Figure 5.14a). The actual present-day DIC summit is located ~20 km to the west of the bed summit (from the DEM data of Dowdeswell et al., 2004; see also Figure 5.8). It is possible that this displacement developed over time from the orographic precipitation effect, but could just as well be the result of contrasting ice flow on either side of the ice cap (see the experiments in section 5.4.1).

In the second experiment, where the computed vertical winds and p' are allowed to change as the ice cap topography beneath changes, a different ice cap profile is achieved after 5000 years (Figure 5.14b). The summit elevation in this case is not much higher than the initial ice dome elevation of 1500 m, but the westward displacement of the divide has doubled. The reason for this is that as the ice cap divide (summit) migrates windward in the model, so too do the horizontal wind divergences and convergences and, as a result, so too do the vertical wind patterns and the areas of enhanced or suppressed precipitation. As a result, the ice cap summit never reaches a final fixed location (which would then allow it to increase in elevation). Rather, the summit/divide continues to migrate upstream, with ice continuously added to upstream flanks.

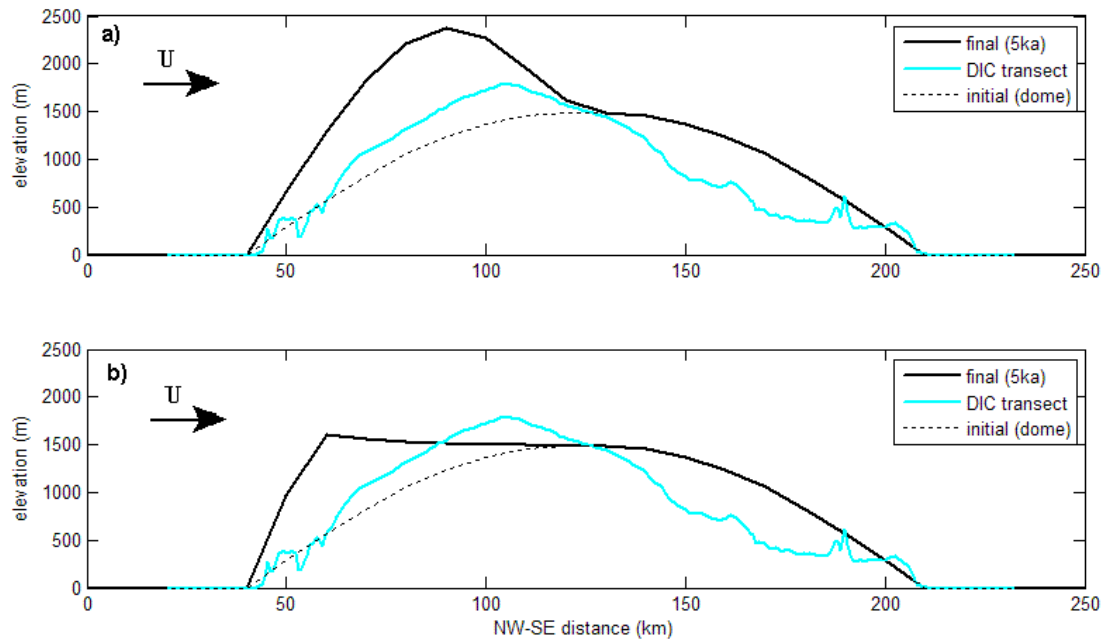


Figure 5.14. 5000-year evolution of a static ice cap under orographic precipitation only: a) no topographic - mass balance feedback; b) with the topographic – mass balance feedback. Initial ice profile (dashed line), final ice profile (solid black line), and 2D transect through the Devon Ice Cap (blue line).

5.4.2.6 DISCUSSION OF ATMOSPHERE-(NON-FLOWING)ICE MODEL RESULTS

The results obtained in the above experiments indicate that a time-dependent topographic – mass balance feedback has the potential to be an important factor in the evolution of an ice cap in the CHA. Orographically enhanced precipitation has the potential to be important to DIC’s annual snowfall accumulations on its northwest side, especially because Hell Gate polynya provides an upstream atmospheric moisture source (Figure 5.3). Model results indicate that the impact of the changing ice surface upon atmospheric circulation is also important to the resultant pattern of orographically enhanced/suppressed precipitation. It is therefore possible that the influence of the orographic-precipitation feedback may be contributing to an imbalance between long-term average surface MBs and ice cap MFDs in the northwest of the DIC. This now needs to be investigated further with coupled ice-atmosphere experiments which allow for a flow response in the ice cap.

5.4.3 Coupled Dynamic Atmosphere – Dynamic Ice Experiments

5.4.3.1 SETUP OF THE COUPLED ATMOSPHERE-ICE MODEL EXPERIMENTS

In this section, the potential role of orographically-generated and/or enhanced precipitation and, over the longer term, the orographic precipitation feedback, upon the evolution of the northwest side of the northwest-southeast DIC profile, is

examined in further detail. The aim is to investigate whether the orographic-precipitation feedback may have played a part in a long-term average MB-MFD imbalance on the northwest side of the ice cap, produced in the idealized ice-only experiments above. To this end, the ice and atmosphere models described above were coupled as described in section 5.3.3 so that orographic enhancement of precipitation, the response of the ice cap to this, and the mass balance – elevation feedback could be simulated in the model runs.

Two sets of model runs were conducted using the coupled model, which now uses the full version of equation (9):

- 1) for various combinations of DIC-appropriate mean atmospheric flows, specific humidities, and precipitation efficiencies; and
- 2) for a doubling of the mean atmospheric flow or a doubling of the specific humidity in the most realistic set of atmospheric flows, humidities, and precipitation efficiencies.

The first set of model runs was used to determine an appropriate set of atmospheric parameters (ϵ , q , U) which would allow the ice cap profile to reach an equilibrium solution or steady state over time. The second set of model runs was used to examine the impact of perturbing this equilibrium state by doubling the background atmospheric flow or by doubling the atmospheric humidity.

Because DIC observed surface accumulations and mass balances include the topographic precipitation effect, in these experiments (which seek the key to the MB-MFD imbalance on the northwest side of DIC) it was necessary to separate the time- and space-mean accumulation rate from the time- and space-varying component on the northwest side of the ice cap. To do this, the surface mass balance term in equation (9) was written as:

$$\dot{b} = (\bar{P} + p') - m \quad (11)$$

where \bar{P} represents the mean surface precipitation/accumulation, p' represents the transient precipitation/accumulation component, and m represents ice loss due to surface melt, runoff, and calving.

To separate \bar{P} and p' , it is assumed that the bulk of the curvature of the observed DIC mass balance versus elevation curves (Mair et al., 2005) is due to the orographic precipitation component. Arnold (2005) examined processes that impact the curvature of mass balance versus elevation curves and found that snow accumulation and air temperature can impact its form. He found that either colder or snowier than average conditions led to more greatly convex-upward shaped curves, similar to the DIC mass balance versus elevation curves (Figure 5.15, red curve). Here it is assumed that snowier than average conditions, produced via orographic enhancement of precipitation, are responsible for the bulk of the

curvature of the observed DIC mass balance versus elevation curves. While this ignores the possibility that temperature may have a significant influence as well, it is nevertheless of interest to examine the extent to which observed surface mass balances can be replicated under such an assumption.

Assuming $p' \sim 0$ near the base and at the summit of the ice cap (see Figure 5.14a – p' reaches a maximum in between these elevations), it is then possible to determine the mean precipitation and melt at these elevations from known surface accumulation and mass balance values. That is, \bar{P} will be approximately equal to the observed snowfall accumulation at these elevations (as given in Koerner, 1979), while m will be the difference between observed surface mass balances and \bar{P} (values derived from Koerner, 1979, and Mair et al., 2005). If it is further assumed that both \bar{P} and m vary linearly with elevation, values for these can then be calculated at all elevations between the ice cap base and summit. The combined total $\bar{P}-m$ versus elevation plot (Figure 5.15) retains some curvature with elevation (as a result of differences in the slopes of the assumed linear elevation-dependence of these two components). However, as stated above, the bulk of the curvature of the observed mass balance versus elevation curves on the northwest side of the DIC (Mair et al., 2005) is now assumed to be due to the orographic precipitation component.

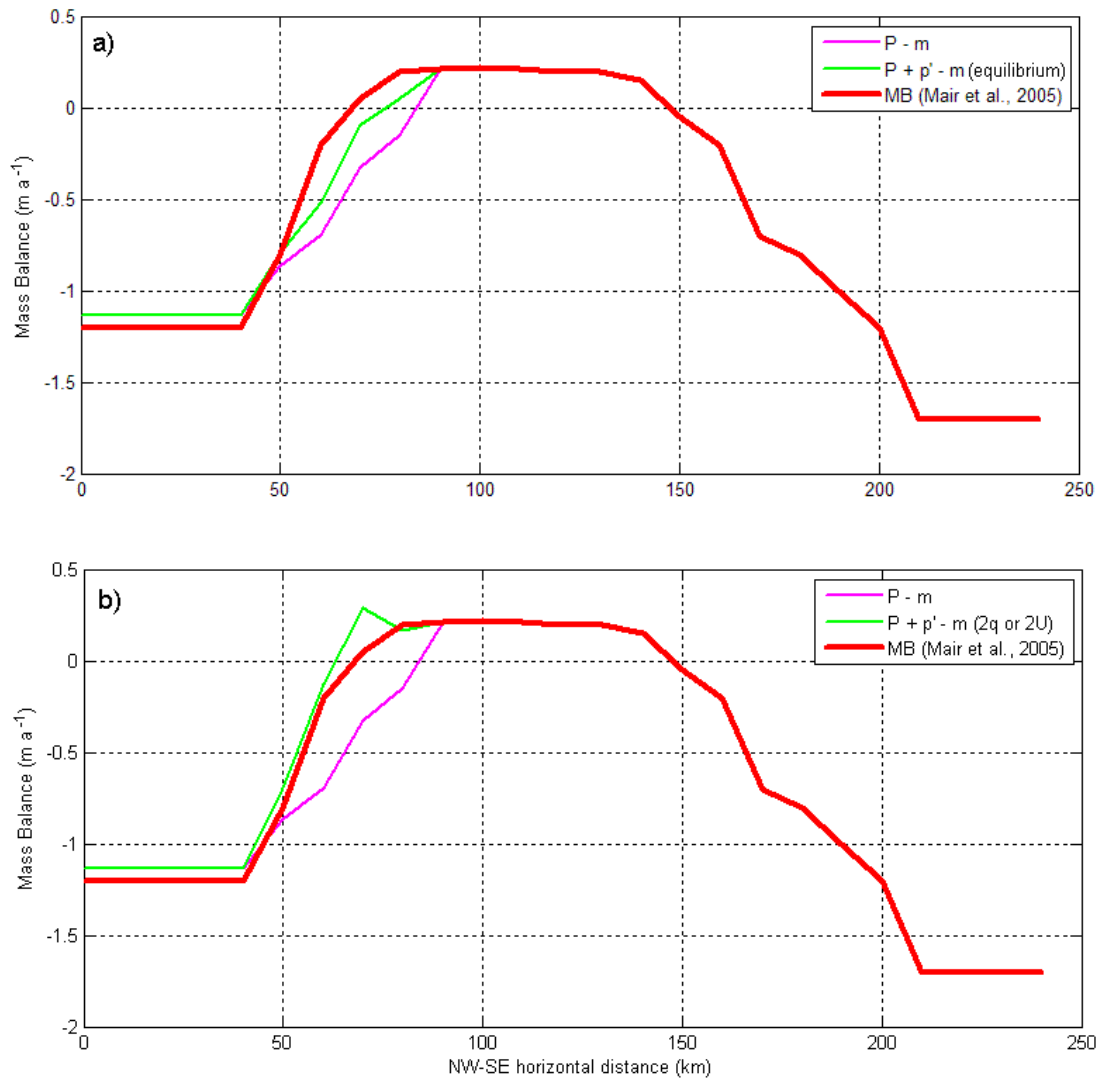


Figure 5.15. Modeled versus observed surface mass balances: a) for the equilibrium experiments; and b) for the 2×q and 2×U experiments. Note that whereas the mass balance curves presented in Mair et al. (2005) are plotted versus elevation, here they are plotted versus horizontal distance along the NW-SE ice cap transect, thus the slight differences in the shapes of the curves. For a description of the errors in the published mass balance curves (red line), see Mair et al. (2005).

As has been noted, the total observed mass balance is a time dependent term, composed of a mean value and a time-dependent transient component. While the transient component can be due to factors like orography and ice-atmosphere feedbacks, it is also related to externally-forced climate changes. In the model experiments below, to isolate the impact of the ice-atmosphere feedback and to ensure that atmospheric modifications arose solely from the ice cap topography and not from external climate changes, the experiments were conducted under constant background atmospheric conditions over periods of 10,000 years. It was assumed that the prescribed mean background atmospheric conditions were quasi-representative of the approximately stable Holocene climate of this region (see

section 5.4.1). Therefore, changes to the simulated atmosphere only arise from the mechanical interaction of the ice cap with the local mean atmospheric circulation. In addition, ice cap surface elevation changes were only related to the topographically enhanced precipitation and associated changes in mass flux divergences. Nevertheless, it is noted that although the impact of externally forced climate changes were neglected in this study, these will have had an impact upon evolving ice cap profiles.

Measured DIC bed elevations (Dowdeswell et al., 2004), interpolated to the 10km model grid, were used in the following coupled model experiments (as opposed to the flat bottom that was assumed for the model ice cap in section 5.4.1). Since realistic ice thicknesses were now being employed in the model calculations, no adjustments to the model mass flux divergences were necessary. Thus, ice viscosities were chosen so that observed surface ice velocities were simulated. Computed equilibrium model depth-averaged ice velocities (where the depth-averaged velocity in a deforming linearly viscous fluid is $\sim 75\%$ of the surface value) now peak at 7.8 m yr^{-1} on the northwest side of the ice cap, at the 70 km mark along the model transect. They equal zero at the ice cap summit, and are $\leq 40 \text{ m yr}^{-1}$ between the summit and the 140 km mark along the transect. They then accelerate to $>200 \text{ m yr}^{-1}$ at the southeastern margin. These velocities mimic measured ($\leq 10 \text{ m yr}^{-1}$) northwest DIC velocities and also the inSAR-derived velocity of 175 m yr^{-1} at the terminus of the glacier flowing into Croker Bay (Shepherd et al., 2007), although the chosen NW-SE transect does not actually end in Croker Bay but ends in an area of southeast glaciers that appear to be subject to periodic surging (Burgess and Sharp, 2008).

It should also be noted that in the fully coupled experiments below, ice surface elevations were smoothed with a low-pass filter every 2500 years, to remove small surface irregularities (e.g. see Figure 5.11). Because the atmospheric model is sensitive to surface topography, small surface irregularities can quickly grow into large, unstable irregularities over time.

5.4.3.2 RESULTS OF THE COUPLED MODEL EXPERIMENTS

In the first set of experiments, a mean atmospheric flow of $U = 5 \text{ m s}^{-1}$, a specific humidity of $q = 0.0004 \text{ kg kg}^{-1}$, and a precipitation efficiency of $\epsilon = 50\%$, resulted in an orographically-modified mass balance (Figure 5.15a – green line) and feedback on the northwest side of the DIC which allowed the model ice cap profile to reach an equilibrium over time that is similar to the present-day northwest DIC profile (Figure 5.16a). Just as the southeast side was found to reach a steady state under observed mass balances and modelled mass flux divergences after ~ 2000 years (see section 5.4.1), so too, now, does the northwest side. Turning off the orographic precipitation (setting it to zero at each time step – pink line, Figure 5.15a) resulted in a slow thinning of the ice cap northwest of the summit due to a slight imbalance between the surface mass balance and the mass flux divergence terms in equation (9). The result of this experiment is not

shown in Figure 5.16 because in this case the northwest part of the ice cap behaves in the same way as that already described for the rest of the ice cap.

It can be seen that the modeled mass balance curve for the northwest of the DIC, in the equilibrium case (Figure 5.15a – green line), lies below the measured mass balance curve (Figure 5.15a – red line). This would suggest that actual present-day mass balances (which are close to the long-term average – Koerner, 1970; see also section 5.4.1.3) are slightly too positive at high elevations on this side of the ice cap for an equilibrium state to exist.

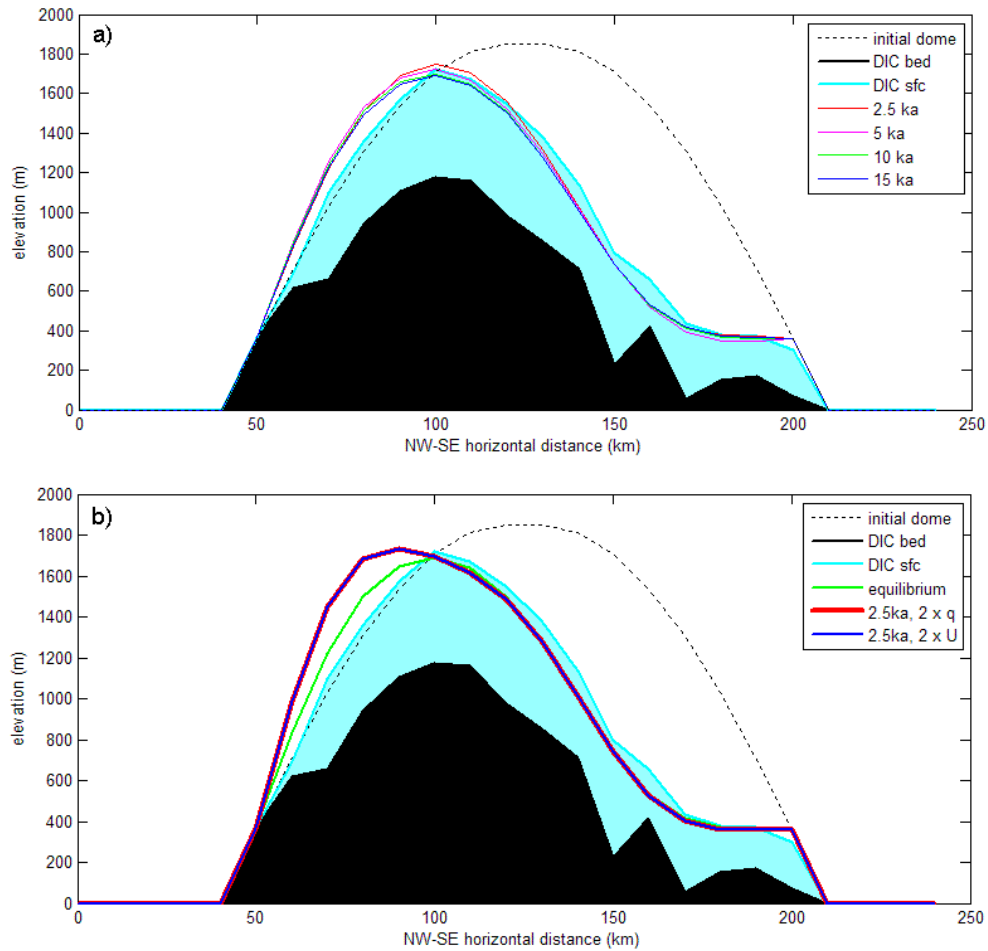


Figure 5.16. Results of the coupled ice-atmosphere model experiments: a) model runs to equilibrium; and b) doubled specific humidity and doubled background atmospheric flow experiments. Note that the double-q and double-U experiments yielded identical results because they had an identical effect upon the magnitude of the orographic precipitation. Thus, the red and dark blue curves in b) are plotted one on top of the other. The shaded black and light blue areas represents NW-SE cross-sections of the DIC bed and ice, respectively, taken from the 1km-resolution Dowdeswell et al. (2004) DEM and interpolated to the 10km model grid.

Doubling the annual mean specific humidity to $q=0.0008 \text{ kg kg}^{-1}$, or doubling the mean atmospheric background flow to $U = 10 \text{ m s}^{-1}$, disturbed the model

convergence towards equilibrium. Doubling q or U caused disequilibrium between the ice cap's mass balance and its mass flux divergence, which in turn caused ice thicknesses to begin increasing over time. This in turn triggered the orographic-precipitation feedback, which then served to accelerate the westward growth of the ice cap. Over a period of 2500 years, the ice cap thickened at a rate of $\sim 0.08 \text{ m yr}^{-1}$ (Figure 5.16b, red and dark blue lines) beyond the equilibrium profile determined above (Figure 5.16a – all lines, Figure 5.16b – green line).

Interestingly, in this case, the modeled surface mass balance curve for the northwest of the DIC (Figure 5.15b, green line) closely matches the measured surface mass balance curve (Figure 5.15b, red line). Time-averaged, high-elevation northwest-side mass balances might therefore have been experiencing a similar orographic enhancement and feedback, triggered by a Holocene increase in the availability of atmospheric moisture and/or an increase in the rate of orographic condensation/precipitation of this moisture.

5.4.3.3 DISCUSSION OF THE COUPLED MODEL RESULTS

While it is generally known that CHA values for q are less than 0.001 kg kg^{-1} (e.g. Peixoto and Oort, p279-280), that values for U are near 5 m s^{-1} (e.g. Peixoto and Oort, p153-154), and that general values for ϵ are between 20-100% (e.g. Rogers, 1979; Jiang, 2003), it is not known exactly what these values are for the DIC. The values chosen in the first set of experiments above are just one possible set which allow the northwest side of the ice cap to attain an equilibrium state over time. Nevertheless, regardless of the actual set of values chosen, the second experiment does show that a simple doubling of one of the chosen values can easily, as a result of the orographic effect and its associated mass balance – elevation feedback, lead to a northwest DIC MB-MFD imbalance similar to that which results when using actual observations to drive the model.

The model results suggest that the DIC profile reached an approximate steady state early on in the Holocene, where surface mass balances and mass flux divergences roughly cancelled each other out. This quasi-steady state may have then allowed a small ice-atmosphere orographic-precipitation feedback to become important in the continuing evolution of the ice cap's northwest profile.

5.5 SUMMARY AND CONCLUSIONS

The ice model experiments in section 5.4.1 examined the extent to which observed Devon Ice Cap surface mass balances and mass flux divergences were in equilibrium. Results indicated that while large imbalances between mass flux divergences and surface mass balances likely dominated early in the evolution of Devon Ice Cap, the present-day asymmetric profile has reached an approximate steady state, where surface mass balances and mass flux divergences roughly cancel each other out. A small imbalance between observed surface mass

balances and modeled mass flux divergences (which were constrained by measured ice velocities and ice thicknesses) exists for the northwest of the ice cap, however, allowing for a slow thickening of ~ 0.02 to 0.06 m yr^{-1} . This agrees with the calculations of Shepherd et al. (2007) and their observation that the northwest of DIC is slowly gaining mass. Shepherd et al. (2007) also point out that all other sectors of DIC are currently losing mass. This mass loss is recognized and represented in the model study of this chapter by allowing for the unrestricted flow of ice mass across the southeast margin and the loss (via runoff or calving) of any ice (melted or solid) that does cross the margin. It is this mass loss (runoff/calving) factor of the total surface mass balance which allows for the quasi-equilibrium of the ice cap profile on the southeast side of the ice cap in the model (and the recent thinning of the profile discussed in Shepherd et al., 2007, but not captured with the model in this study which used longer-term MB averages).

It was hypothesized that while the key factor to the MB-MFD equilibrium on the southeast side of the ice cap is the free calving and mass loss across the southeast margin, the key element which would be required for an MB-MFD equilibrium on the northwest side of the ice cap might be related to ice-atmosphere feedbacks such as the orographic-precipitation feedback. Longer-term (40 years and greater) mass gains may be a continuing or delayed dynamic response to historical climate conditions and positive mass balance associated with the LIA (e.g. Burgess et al., 2004; Colgan and Sharp, 2008). It is also possible that long-term Holocene-average surface mass balances were influenced by the mass balance – elevation feedback on the northwest side.

Observations (Figure 5.3) and experiments with a slab-type atmospheric model in section 5.4.2 (which examined the potential magnitude of the orographic precipitation component and also tested the potential impact of the orographic precipitation feedback over the long term) indicate that orographic precipitation amounts on the northwest side of the ice cap are likely not insignificant when compared to measured snowfall values. In the atmosphere - static ice experiments, the orographic precipitation feedback had a significant impact on millennial timescales. These results indicated that the quasi-steady state of the Devon Ice Cap (determined in section 5.4.1) could have allowed the ice-atmosphere orographic-precipitation feedback to become important in the continuing evolution of the ice cap's profile.

The results of coupled atmosphere-ice model runs in section 5.4.3 indicated that without orographic precipitation and the mass balance – elevation feedback there would be a slight thinning of the northwest part of the Devon Ice Cap in the model, similar to that observed for all other sectors of the ice cap. With orographic precipitation and the mass balance – elevation feedback, there is a thickening of $\sim 0.08 \text{ m yr}^{-1}$ of the northwest part of Devon Ice Cap if the background atmospheric flow, specific humidity, and precipitation efficiency are

chosen such that the current observed MB vs. elevation curves of Mair et al. (2005) are closely replicated in the model (for the northwest part of the ice cap).

With orographic precipitation and the mass balance – elevation feedback, to achieve an MB-MFD equilibrium on the northwest side of the ice cap, either the mean annual wind speeds from the northwest or the atmospheric specific humidity or the precipitation efficiency would have to be 50% of its present-day value (in the model). This suggests that the present-day northwest MB-MFD imbalance and mass gains would be smaller if orographic precipitation was absent and the mass balance – elevation feedback were inoperative. Although computed orographic precipitation amounts on the northwest side of the ice cap are small (representing ~20-25% of the total observed precipitation amounts), and while the ice cap is likely still responding to past climate conditions such as those from the Little Ice Age, the mass balance – elevation feedback is playing a role in the evolution of this ice mass.

With respect to the mechanical part of the glacier-anticyclone feedback, 2D atmospheric model experiments in section 5.4.2 indicate that the contribution of this mechanism to the glacier anticyclone feedback is small and that temperature must therefore play the far greater role in the generation and erosion of the glacier anticyclone and any ice-atmosphere feedbacks associated with it.

In conclusion, the numerical experiments in this study indicate that an ice-atmosphere elevation-precipitation feedback is playing a part in the observed high altitude mass gains of the northwestern DIC ice cap. While the impact of regional-scale ice caps, such as the Devon Ice Cap, upon atmospheric circulation patterns is minor due to generally weak mean atmospheric flows at high latitudes, they can still significantly alter their own evolution if the atmospheric effects are able to accumulate over a long period of time. Furthermore, once an ice cap reaches an approximate steady state between its surface mass balances and mass flux divergences, the ice-atmosphere topographic – mass balance feedback may become a primary factor in any further changes to its profile over time, supplementing changes in ice dynamics due to lagged responses to past climate events such as the LIA.

5.6 REFERENCES

Abdalati, W., W. Krabill, E. Frederick, S. Manizade, C. Martin, J. Sonntag, R. Swift, R. Thomas, J. Yungel, and R. Koerner, 2004: Elevation changes of ice caps in the Canadian Arctic Archipelago. *Journal of Geophysical Research*, **109**(F4), F04007, doi:10.1029/2003JF000045.

Abe-Ouchi, A., T. Segawa and F. Saito (2007): Climatic conditions for modelling the Northern Hemisphere ice sheets throughout the ice age cycle. *Climate of the Past*, **3**, 423–438.

Alt, B. T., 1978: Synoptic climate controls of mass-balance variations on Devon Island ice cap. *Arctic and Alpine Research*, **10**(1), 61-80.

Alt, B. T., 1987: Developing synoptic analogs for extreme mass balance conditions on Queen Elizabeth Island ice caps. *Journal of Climate and Applied Meteorology*, **26**(12), 1605-1623.

Arnold, N., 2005: Investigating the Sensitivity of Glacier Mass-Balance/Elevation Profiles to Changing Meteorological Conditions: Model Experiments for Haut Glacier D'Arolla, Valais, Switzerland. *Arctic, Antarctic, and Alpine Research*, **37**(2), 139-145.

Burgess, D. O., and M. J. Sharp, 2004: Recent changes in areal extent of the Devon Ice Cap, Nunavut, Canada. *Arctic, Antarctic, and Alpine Research*, **36**(2), 261-271.

Burgess, D. O., M. J. Sharp, D. W. F. Mair, J. A. Dowdeswell, and T. J. Benham,, 2005: Flow dynamics and iceberg calving rates of Devon Ice Cap, Nunavut, Canada. *Journal of Glaciology*, **51**(173), 219-230.

Burgess, D., and M. J. Sharp, 2008: Recent changes in thickness of the Devon Island ice cap, Canada. *Journal of Geophysical Research (Solid Earth)*, **113**, B07204, doi:10.1029/2007JB005238, 2008.

Colgan, W., and M. Sharp, 2008: Combined oceanic and atmospheric influences on net accumulation on Devon Ice Cap, Nunavut, Canada. *Journal of Glaciology*, **54**(184), 28-40.

Cress, P., and R. Wyness, 1961: The Devon Island expedition, observations of glacial movements. *Arctic*, **14** (4), 257-259.

Doake, C.S.M., M. Gorman, and W.S.B. Paterson, 1976: A further comparison of glacier velocities measured by radio-echo and survey methods. *Journal of Glaciology*, **17** (75), 35-38.

Dowdeswell, J. A., T. J. Benham, M. R. Gorman, D. Burgess and M. J. Sharp, 2004: Form and flow of the Devon Island Ice Cap, Canadian Arctic. *Journal of Geophysical Research*, **109**, F02002, doi:10.1029/2003JF000095.

Dyke, A. S., and V. K. Prest, 1987: Late Wisconsinan and Holocene history of the Laurentide Ice Sheet. *Géographie Physique et Quaternaire*, **41**, 237-264.

Dyke, A.S., 1999: Last Glacial Maximum and deglaciation of Devon Island, Arctic

Canada: support for an innuitian ice sheet. *Quaternary Science Reviews*, **18**, 393-420.

England, J., N. Atkinson, J. Bednarski, A. S. Dyke, D. A. Hodgson, C. Ó Cofaigh, 2006: The Innuitian Ice Sheet: configuration, dynamics and chronology. *Quaternary Science Reviews*, **25**, 689–703.

Gardner, A. S., and M. Sharp, 2007: Influence of the Arctic Circumpolar Vortex on the Mass Balance of Canadian High Arctic Glaciers. *Journal of Climate*, **20**, 4586-4598. DOI: 10.1175/JCLI4268.1

Garrett, C., 2004: Frictional processes in straits. *Deep-Sea Research II*, **51**, 393-410.

Glen, J.W., 1955: The creep of polycrystalline ice. *Proc. R. Soc. Lon. Ser-A*, **228** (1175), 519-538.

Goldsby, D. L., and D. L. Kohlstedt, 2001: Superplastic deformation of ice: experimental observations. *Journal of Geophysical Research*, **106**(B6), 11017-11030.

Grubišić, V., R. B. Smith, and C. Schär, 1995: The effect of bottom friction on shallow-water flow past an isolated obstacle. *Journal of the Atmospheric Sciences*, **52**(11), 1985-2005.

Holton, J. R., 1979: An Introduction to Dynamic Meteorology, 2nd Ed. Academic Press, New York.

Hubbard, A., 2000: The verification and significance of three approaches to longitudinal stresses in high-resolution models of glacier flow. *Geografiska Annalar*, **82 A** (2000), 4, 471-487.

Hulton, N. R. J. and D. E. Sugden, 1995: Modelling mass balance on former maritime ice caps: a Patagonian example. *Annals of Glaciology*, **21**, 304-310.

Jiang, Q., 2003: Moist dynamics and orographic precipitation. *Tellus*, **55A**, 301-316.

Koerner, R. M., 1966: Accumulation on the Devon Island ice cap, Northwest Territories, Canada. *Journal of Glaciology*, **6**(45), 383-392.

Koerner, R. M., 1970: The mass balance of the Devon Ice Cap, Northwest Territories, Canada 1961-66. *Journal of Glaciology*, **9**(57), 325-336.

Koerner, R. M., 1977: Devon Island Ice Cap: Core Stratigraphy and Paleoclimate. *Science*, **196**(4285), 15-18.

Koerner, R. M., 1979: Accumulation, ablation, and oxygen isotope variations on the Queen Elizabeth Island ice caps, Canada. *Journal of Glaciology*, **22**(86), 25-41.

Koerner, R.M., 1989: Queen Elizabeth Islands glaciers. *In: Quaternary Geology of Canada and Greenland* (R.J. Fulton, ed.), Geological Survey of Canada, Geology of Canada, no. 1, 464-477.

Koerner, R. M., and D. A. Fisher, 1990: A record of Holocene summer climate from a Canadian high-Arctic ice core. *Nature*, **343**, 630-631.

Koerner, R.M., 2002: Glaciers of North America – Glaciers of Canada, Glaciers of the Arctic Islands, Glaciers of the High Arctic Islands. *In: Satellite Image Atlas of Glaciers of the World* (R.S. Williams, Jr. and J.G. Ferrigno, eds.), U.S. Geological Survey Professional Paper 1386-J-1.

Koerner, R. M., 2005: Mass balance of glaciers in the Queen Elizabeth Islands, Nunavut, Canada. *Annals of Glaciology*, **42**(1), 417-423.

Kutzbach, J.E., P.J. Guetter, P.J. Behling, and R. Selin, 1993: Simulated climatic changes: results of the COHMAP climate-model experiments. *In: Global Climates since the Last Glacial Maximum* (Wright Jr., H.E., J.E. Kutzbach, T. Webb III, W.F. Ruddiman, F.A. Street-Perrott, and P.J. Bartlein, eds.). University of Minnesota Press, Minneapolis and London, 24-93.

Lindeman, M., and J. Oerlemans, 1987: Northern hemisphere ice sheets and planetary waves: a strong feedback mechanism. *International Journal of Climatology*, **7**(2), 109-117. doi:10.1002/joc.3370070202.

Mair, D., D. Burgess, and M. Sharp, 2003: Using shallow ice coring experiments and melt modelling to determine mass balance of Devon Ice Cap, Canada. *Geophysical Research Abstracts* (European Geophysical Society), **5**, 10575.

Mair, D., D. Burgess, and M. Sharp, 2005: 37-year mass balance of the Devon Island Ice Cap, Nunavut, Canada, determined by shallow ice coring and melt modelling. *Journal of Geophysical Research* (Earth Surface), **110**, F01011, doi:10.1029/2003JF000099.

Mangeney, A., F. Califano, and C. Castelnau, 1996: Isothermal flow of an anisotropic ice sheet in the vicinity of an ice divide. *Journal of Geophysical Research*, **101**, 28189-28204.

Mangeney, A., and F. Califano, 1998: The shallow-ice approximation for anisotropic ice: formulation and limits. *Journal of Geophysical Research*, **103**, 691-705.

Marshall, H. P., J. T. Harper, W. T. Pfeffer, and N. F. Humphrey, 2002: Depth-varying constitutive properties observed in an isothermal glacier. *Geophysical Research Letters*, **29**(23), 2146, doi:10.1029/2002GL015412.

Marshall, S. J., L. Tarasov, G. K. C. Clarke, and W. R. Peltier, 2000: Glaciological reconstruction of the Laurentide Ice Sheet: physical processes and modeling challenges. *Canadian Journal of Earth Sciences*, **37**, 769–793.

Marshall, S. J., T. S. James, and G. K. C. Clarke, 2002: North American Ice Sheet reconstructions at the Last Glacial Maximum. *Quaternary Science Reviews*, **21**, 175–192.

Marshall, S. J., M. J. Sharp, D. O. Burgess and F. S. Anslow, 2007: Near-surface-temperature lapse rates on the Prince of Wales Icefield, Ellesmere Island, Canada: implications for regional downscaling of temperature. *International Journal of Climatology*, **27**(3), 385-398. Published online in Wiley InterScience (www.interscience.wiley.com) DOI: 10.1002/joc.1396 .

NCAR Monthly Northern Hemispheric 72×19 Tropospheric Analyses, continuing from 1947. Dataset number ds085.1. National Center for Atmospheric Research (Data Support Section), Boulder, Colorado, U.S.A.

Paterson, W. S. B., R. M. Koerner, D. Fisher, S. I. Johnsen, H. B. Clausen, W. Dansgaard, P. Butcher, and H. Oeschger, 1977: An oxygen isotope climatic record from the Devon Island Ice Cap, Arctic Canada. *Nature*, **266**, 508-511.

Paterson, W.S.B. and G.K.C. Clarke, 1978: Comparison of theoretical and observed temperature profiles in Devon Island ice cap, Canada. *Geophys. J. R. astr. Soc.*, **55**, 615-632.

Peixoto, J.P., and A.H. Oort, 1992: Physics of Climate. American Institute of Physics, New York.

Pettit, E. C., and D. Waddington, 2003: Ice flow at low deviatoric stress. *Journal of Glaciology*, **49**(166), 359-369.

Purves, R. S., and N. R. J. Hulton, 2000: Experiments in linking regional climate, ice-sheet models and topography. *Journal of Quaternary Science*, **15**(4), 369–375.

Roe, G.H. and R.S. Lindzen, 2001: The mutual interaction between continental-scale ice sheets and atmospheric stationary waves. *Journal of Climate*, **14**, 1450-1465.

Rogers, R. R., 1979: A Short Course in Cloud Physics, 2nd Ed. Pergamon Press, Oxford.

Sanberg, J.A.M., and J. Oerlemans, 1983: Modeling of Pleistocene European ice sheets: the effect of upslope precipitation. *Geologie en Mijnbouw*, **62**, 267-273.

Shepherd, A., Z. Du, T. J. Benham, J. A. Dowdeswell, and E. M. Morris, 2007: Mass balance of Devon Ice Cap, Canadian Arctic. *Annals of Glaciology*, **46**, 249-254.

Wallace, J.M. and P.V. Hobbs, 1977: Atmospheric Science: An Introductory Survey. Academic Press Inc., New York.

Wolff, E.W., and C.S.M. Doake, 1986: Implications of the form of the flow law for vertical velocity and age-depth profiles in polar ice. *Journal of Glaciology*, **32** (112), 366-370.

Wolken, G. J., J. H. England and A. S. Dyke, 2008a: Changes in late Neoglacial perennial snow/ice extent and equilibrium-line altitudes in the Queen Elizabeth Islands, Arctic Canada. *Holocene*, **18**(4), 615-627.

Wolken, G. J., M. J. Sharp and J. H. England, 2008b: Changes in late Neoglacial climate inferred from former equilibrium-line altitudes in the Queen Elizabeth Islands, Arctic Canada. *Holocene*, **18**(4), 629-641.

6. Conclusions

While no large ice sheets exist in the Canadian High Arctic (CHA) today, many areas remain extensively glaciated and include ice caps hundreds to tens of thousands of square kilometres in size. These ice masses interact with the polar atmosphere, both by responding to climate changes and by modifying the regional climate. Because the cryosphere and the atmosphere evolve co-dependently (e.g. Oerlemans, 1986; Dowdeswell et al., 1995; Roe and Lindzen, 2001), feedbacks may develop between the two systems, both positive and negative, which can act to amplify or damp their mutual response to external perturbations.

In this thesis, the impact of two positive feedbacks between the cryosphere and the atmosphere were quantified and examined for CHA land ice systems, through a series of modeling experiments. Positive feedbacks are of interest because of their destabilizing nature – they produce continuing and amplified responses to perturbations and move a system away from its initial state. Amplifications to climate perturbations initiated by CHA land ice masses may or may not be important, when compared to sea ice – related amplifications. This thesis sought to partially fill in this gap in current understanding and to provide an initial foundation for future studies in this area.

The primary and secondary positive cryosphere-atmosphere feedbacks are, respectively (e.g. Abe-Ouchi et al., 2007): 1) the snow/ice-albedo feedback; and 2) the elevation - mass balance feedback. While snow and sea ice in the polar regions are the main factors in snow/ice-albedo feedback-related amplification of recent climate change in the Arctic, land ice masses may locally further amplify the changes in a significant way. Local amplification in Surface Air Temperature (SAT) changes as a result of the terrestrial ice-albedo feedback may accelerate changes in outlet glaciers, by impacting ice temperatures and thicknesses and eventually ice flow. Furthermore, while the elevation – mass balance feedback is generally considered to be of secondary importance to the snow/ice-albedo feedback in the co-evolution of ice sheets and the atmosphere, it is nevertheless worth quantifying for CHA ice caps to ascertain its magnitude and impact. The impacts of small amplifications may “accumulate” over time, so that what appears negligible on decadal time scales may become significant on centennial to millennial time scales. Although these two feedbacks interact with each other (i.e. are not independent of each other), in this thesis they were examined separately. To this end, the experiments in this thesis were designed to isolate the two ice-atmosphere feedbacks under investigation from each other as much as possible.

To assess whether changes in CHA terrestrial ice mass temperatures, mass fluxes, and geometries can be amplified by the local interactions of these ice masses with the overlying atmosphere, possibly leading to further accelerations in the observed changes, the following points were addressed in the thesis experiments:

- 1) The magnitude of the snow/ice-albedo feedback for a representative CHA outlet glacier was quantified and the contribution of the ice to the combined snow/ice feedback was examined (Chapter 2);
- 2) The implications of local snow/ice-albedo amplifications for the evolution of CHA land ice masses (via their marginal glaciers) was examined by exploring whether amplified Surface Air Temperature (SAT) and Mass Balance (MB) changes are important to their response times (Chapter 2);
- 3) The impact of local-regional SAT changes, both direct and indirect, both feedback-amplified and unamplified, upon the magnitude of internal and basal temperature anomalies within CHA land ice masses was investigated (Chapters 3 and 4); and
- 4) Although considered secondary to the snow/ice-albedo feedback, the impact of mass balance – elevation feedback amplifications of atmospheric moisture perturbations upon the post – Last Glacial Maximum (LGM) evolution of Devon Ice Cap was examined (Chapter 5).

These concerns formed the basis of the modeling experiments described in the four chapters of this thesis and the specific findings are described below.

6.1 KEY RESULTS AND CONCLUSIONS

6.1.1 *Chapter 2*

In Chapter 2, radiative perturbation experiments using a coupled atmosphere-surface energy-mass balance model were performed and a linear feedback analysis of the results was used to quantify the magnitude of the snow/ice-albedo feedback for a CHA glacier catchment (John Evans Glacier, Ellesmere Island).

The following results were obtained and conclusions drawn:

6.1.1.1 THE MAGNITUDE OF THE TERRESTRIAL SNOW/ICE-ALBEDO FEEDBACK

It was found that changes in area-averaged surface temperatures in the model are amplified by a factor of up to $1.9\times$ as a result of the terrestrial snow/ice-albedo feedback (depending on the type and sign of the radiative perturbation). Changes in vertically- and area-averaged air temperatures are amplified by a factor of up to $1.6\times$. Changes in area-averaged surface mass balances are amplified by a factor of up to $7.7\times$.

Non-area-averaged calculations of the feedback parameter indicated strong spatial variability in the magnitude of the snow/ice-albedo feedback. The highest amplifications of temperature and mass balance occurred near zones of high

surface albedo contrast: at the glacier margins, near the mean polar-day location of the snow – bare ice front, and near the snow – bare firn line at the peak melt season. This result supports the assertion of others that the snow/ice-albedo feedback is most effective at ice cap and ice sheet margins (e.g. Pritchard et al., 2008). In this study, in these locations, the amplification of surface temperature changes reached a factor of $5\times$ and greater.

Thus, a key finding of this study is that the magnitude of the terrestrial snow/ice-albedo feedback can locally exceed values computed for sea ice near zones of strong summer surface albedo contrast (e.g. in the vicinity of the ice margins). For comparison, Holland and Bitz (2003) found model-simulated polar warming in the Arctic to be 1.5 to 4.5 times the global mean warming, primarily due to sea ice – related feedbacks.

6.1.1.2 THE CONTRIBUTION OF TERRESTRIAL ICE

A second key finding of this study is that the presence of terrestrial ice can serve to significantly enhance the magnitude of the snow-albedo feedback (or combined snow/ice-albedo feedback) on decadal timescales and less. This is because the presence of terrestrial ice prolongs snow cover and therefore the effectiveness of the snow/ice-albedo feedback throughout the melt season. It also creates two additional zones of albedo contrast. In addition to the snow – bare ground zone of contrast, there are also the snow – bare ice and the snow – bare firn zones on contrast. Model results showed that because of this, the magnitude of the combined snow/ice-albedo feedback in terms of mean annual area-averaged surface and atmospheric temperatures can be nearly double that of the snow-albedo feedback on its own. Thus, while glaciers may lower the mean annual temperature of a valley, *changes* in mean annual SATs are amplified to a greater extent in glaciated valleys because glaciers act to prolong the operation and effectiveness of the snow-albedo feedback mechanism into the summer season. The contribution of terrestrial ice to the effectiveness of the snow/ice-albedo feedback on decadal timescales and less is therefore not locally negligible.

6.1.1.3 IMPLICATIONS FOR GLACIER RESPONSE TIME

Glacier response times, determined by dividing the mean glacier thickness by the surface mass balance at the glacier snout (Johannesson et al., 1989), are significantly affected by the amplification of mass balance changes via the snow/ice-albedo feedback, because amplification of mass balance changes is largest at the glacier margins. For example, while an unamplified decrease in surface mass balance of $2\times$ will halve the glacier response time, this same mass balance decrease amplified by $5\times$ will further reduce the glacier response time to $\sim 1/10^{\text{th}}$ of the original response time. Such amplified changes in response time will have significant implications for glaciers evolving under the present-day climate warming, leading to non-linear and accelerated changes in their flow, mass flux divergence, and geometry.

6.1.2 Chapter 3

In Chapter 3, the role of past SAT changes, both amplified by the snow/ice-albedo feedback and not, in the formation and modification of englacial temperature anomalies within ice cap and glacier accumulation zones was investigated. Specifically, this study examined whether differences in the amplitude of Little Ice Age (LIA) derived englacial temperature anomalies measured near the summits of a CHA glacier and of the Greenland Ice Sheet may be related to: 1) differing past snow/ice-albedo feedback amplifications of LIA SAT changes; and/or 2) variations in the diffusive smoothing of the englacial temperature anomaly due to the presence/absence of older SAT-derived anomalies of the opposite sign.

To this end, the snow/ice-albedo feedback amplifications of SAT changes computed in Chapter 2 were first used in a series of preliminary calculations. A 1D borehole ice temperature model was then used to simulate SAT-derived englacial temperature anomalies in a hypothetical ice cap. Time integrations were driven by the SAT temperature anomaly time series recovered from the GRIP borehole temperature profile (Dahl-Jensen et al., 1998).

The following results were obtained and conclusions drawn:

6.1.2.1 THE ROLE OF THE SNOW/ICE-ALBEDO FEEDBACK

The LIA-related englacial temperature anomaly calculated for White Glacier's boreholes (magnitude greater than -0.3°C ; Chapter 3) is more than $3\times$ that in the GRIP borehole (magnitude less than -0.1°C ; Dahl-Jensen et al., 1998). This is partly due to the difference in the original LIA-related SAT anomaly at these sites. The LIA-related SAT anomaly for the Greenland summit averaged $\sim -0.6^{\circ}\text{C}$ (derived from the GRIP borehole ice temperatures – Dahl-Jensen et al., 1998). On the other hand, the LIA-related SAT anomaly for the CHA was $\sim -1.0^{\circ}\text{C}$ to -1.5°C (derived from various proxy data – Overpeck et al., 1997; Wolken et al., 2008b), approximately double the decrease in SAT determined for the GRIP site for this same climate event.

Amplifications of area-averaged SAT changes as a result of the terrestrial snow/ice-albedo feedback averaged $\sim 1.3\times$ for negative perturbations to the incoming shortwave radiation (Chapter 2), while amplifications of area-averaged SAT changes as a result of the sea-ice-albedo feedback are $\sim 1.5\times$ and greater (Curry et al., 2001; Holland and Bitz, 2003). Simple calculations show that together, the terrestrial snow/ice-albedo feedback and the sea ice – albedo feedback amplifications of SAT changes can account for the differences between the LIA-related SAT anomalies inferred for the GRIP site and the CHA. An SAT change of -0.6°C becomes -0.9°C after amplification by the sea ice – albedo

feedback, and becomes -1.2°C after further amplification by the terrestrial snow/ice-albedo feedback.

6.1.2.2 THE ROLE OF THE THERMAL MEMORY OF THE ICE

The GRIP borehole LIA ice temperature anomaly constitutes a smaller percentage of the original GRIP SAT anomaly ($\sim 10\%$) than does the White Glacier ice temperature anomaly of its inferred LIA SAT-anomaly ($\sim 25\%$). Model experiments revealed that where positive englacial temperature anomalies, related to the Holocene Climatic Optimum (CO) and the Medieval Warm Period (MWP), exist within a borehole's thermal depth-profile, only 9-12% of the original LIA SAT-anomaly is preserved, as opposed to 19-26% where the CO/MWP signal is absent. Because the GRIP borehole, being deeper, contains signals associated with the CO and the MWP (Dahl-Jensen et al., 1998), where White Glacier does not (Blatter, 1987), it is likely that the negative GRIP LIA ice temperature anomaly has been more greatly eroded (or diffusively smoothed) over time via thermal diffusion processes from these older, positive anomalies.

Together the snow/ice-albedo feedback and the thermal memory of the ice can account for the differences in the LIA-related ice temperature anomalies of the White Glacier summit and GRIP boreholes. Additionally, they can account for the observed “subdued-ness” of the GRIP borehole LIA signal (e.g. Fischer et al., 1998; Barlow, 2001). Others have proposed various explanations for this observation (mostly related to atmospheric circulation patterns – e.g. Barlow, 2001), but the explanation may be much simpler as shown above.

6.1.3 Chapter 4

In Chapter 4, the role of past SAT changes, both direct and indirect, both feedback-amplified and not amplified, in the formation and maintenance of warm basal ice temperatures in the ablation zones of predominantly cold CHA glaciers was investigated. Specifically, this study examined the extent to which the warm basal ice temperatures of John Evans Glacier (JEG), inferred from stream chemistry (Skidmore and Sharp, 1999), dye tracing experiments (Bingham et al., 2003; Bingham et al., 2005) and via radio echo sounding (Copland and Sharp, 2001), are in equilibrium with its thermal boundary conditions (BCs). The implications of the results were then considered for other predominantly cold polythermal glaciers in the CHA (e.g. Laika Glacier: Blatter and Kappenberger, 1988; Blatter and Hutter, 1991; White Glacier: Blatter, 1987; Stagnation Glacier: Irvine-Fynn et al., 2006).

A 2D ice temperature model was used to simulate the internal ice temperatures of JEG along a longitudinal transect following a series of mass balance stakes from the summit to the snout. Equilibrium experiments were performed using SATs or measured 15-m ice-depth temperatures as the surface BC, and using the geothermal heat flux as the primary basal heat source. Time integrations were

performed using the SAT-anomaly time series derived from the GRIP borehole temperatures (Dahl-Jensen et al., 1998). Specific experiments involved CHA-appropriate LIA SAT anomalies (Overpeck et al., 1997; Wolken et al., 2008b), LIA ice thickness changes of up to 25%, LIA changes in the altitude of maximum surface refreezing corresponding with regional shifts in Equilibrium Line Altitude (ELA; as determined from trimlines – Wolken et al., 2008a), and post-LIA changes in supraglacial-subglacial meltwater production and flow.

The following results / conclusions were obtained:

6.1.3.1 THE EXTENT TO WHICH JEG BASAL ICE TEMPERATURES ARE IN EQUILIBRIUM WITH ITS THERMAL BCS

Equilibrium model experiments indicate that JEG's internal and basal temperature distribution in the upper part of the ablation zone is not in equilibrium with present-day SATs and ice thicknesses. Basal temperatures may or may not be in equilibrium over the lower part of the ablation zone, depending on the estimated magnitudes of additional basal heat fluxes related to sliding friction, basal refreezing and subglacial water flow and upon the degree of sliding-related upstream subsidence and advection of cold surface temperatures to the bed;

6.1.3.2 THE DIRECT INFLUENCE OF HISTORICAL SAT CHANGES

The *direct* result of past SAT changes has been to cool the ice and its bed, increasing the disequilibrium between JEG model results and present-day observations of warm basal temperatures in the ablation zone. In time-dependent model experiments involving historical SAT changes only, ice-bed interface temperatures were -0.2°C to -0.35°C cooler than equilibrium temperatures computed under present-day mean annual SATs (depending on the choice of bed material: solid bedrock or saturated sand);

6.1.3.3 THE INDIRECT INFLUENCE OF HISTORICAL SAT CHANGES

Time-dependent model experiments indicate that it is the *indirect* influence of past and continuing SAT changes that has been critical to the development and evolution of JEG's warm basal temperatures (i.e. via changes in ice thickness, surface refreezing, and supraglacial meltwater production and amounts reaching the bed).

Past greater ice thicknesses during the LIA are partially responsible for the inferred warm basal temperatures in the lower ablation zone of JEG. In model experiments involving ice thickness increases of up to 50% during the LIA, present-day ice-bed interface temperatures were 3.0°C to 4.5°C warmer than without the historical thickness increase (depending on whether the thickening and subsequent thinning were assumed to occur in a linear or ice-atmosphere feedback-related exponential fashion). Note that a 50% ice thickness increase

represents a maximum limiting case: trim lines in the JEG catchment indicate an LIA-related JEG thickening more like ~20-25%.

Latent heat released by surface refreezing during the LIA is also partially responsible for the elevated basal temperatures in the lower ablation zone of JEG. In model experiments where surface refreezing was included (via the application of measured 15-m ice depth temperatures), ice-bed interface temperatures in the ablation zone were ~3-4°C warmer than in experiments using SATs only as the surface thermal BC.

Post-LIA supraglacial meltwater reaching the glacier bed is the single most critical heat source responsible for the disequilibrium between present-day inferred warm ice bed temperatures and modeled equilibrium ice bed temperatures under present-day BC's, especially in the upper ablation zone of JEG. While it is likely that supraglacial meltwater fluxes have increased over the past 100 years to the currently observed amounts of $1\text{-}5\text{ m}^3\text{ s}^{-1}$, and that supraglacial meltwater production and the formation of active moulins have risen in elevation over time, it is sufficient that near-present-day amounts reached the bed of the upper ablation zone from ~1930AD onward. In such a case, regardless of whether significant amounts of supraglacial meltwater reached the bed during the LIA or not, model results indicate that present-day basal temperatures reach the pressure melting point (PMP) along the entire 8 km length of the glacier ablation zone.

6.1.4 Chapter 5

In chapter 5, the impact of mass balance – elevation feedback amplifications of atmospheric moisture perturbations on the evolution of Holocene CHA ice caps was examined. Specifically, this study focused on whether mass balance - elevation feedback amplifications were important to Devon Ice Cap's (DIC's) evolution throughout the Holocene and whether it may yet be involved in the mass gains observed in the northwest sector of the ice cap over the last ~40 years (Koerner, 1966; 1970; 1979; Mair et al., 2005; Shepherd et al., 2007).

To this end, a 1D linearly viscous Shallow Ice Equation (SIE) model was coupled to a 1D slab atmosphere model so that the mass balance – elevation feedback could be simulated in the model runs. Model surface mass balances (MBs) and mass flux divergences (MFDs) were constrained using present-day DIC observations (MBs: Mair et al., 2005; Koerner, 1966; 1970; 1979. MFDs (ice thickness and ice velocity): Burgess et al., 2005; Dowdeswell et al., 2004; Shepherd et al., 2007).

The following results / conclusions were obtained:

6.1.4.1 THE EXTENT TO WHICH DEVON ICE CAP'S OBSERVED MBs AND MFDs ARE IN EQUILIBRIUM

The results of uncoupled ice model runs, driven by observed MBs and MFDs, indicate that the 40-year mean measured MBs (Mair et al., 2005) are in equilibrium with measured MFDs on the southeast side of the ice cap (if calving is allowed for in the model), but not on the northwest side (where the ice continues to thicken at a rate of $\sim 0.05 \text{ m yr}^{-1}$ in the model). This concurs with observations of mass gains in the northwest sector of the ice cap (e.g. Shepherd et al., 2007).

6.1.4.2 THE IMPACT OF OROGRAPHIC PRECIPITATION AND THE MASS BALANCE – ELEVATION FEEDBACK

The results of coupled atmosphere-ice model runs, experimenting with MB variations on the northwest part of the ice cap, indicate that without orographic precipitation and the mass balance – elevation feedback there is a slight thinning of the northwest part of the Devon Ice Cap in the model, similar to that observed for all other sectors of the ice cap. With orographic precipitation and the mass balance – elevation feedback, there is a thickening of $\sim 0.08 \text{ m yr}^{-1}$ of the northwest part of Devon Ice Cap if the background atmospheric flow, specific humidity, and precipitation efficiency are chosen such that the current observed MB vs. elevation curves of Mair et al. (2005) are closely replicated in the model (for the northwest part of the ice cap).

With orographic precipitation and the mass balance – elevation feedback, to achieve an MB-MFD equilibrium on the northwest side of the ice cap, either the mean annual wind speeds from the northwest or the atmospheric specific humidity or the precipitation efficiency would have to be 50% of its present-day value (in the model). This suggests that the northwest MB-MFD imbalance and mass gains would be smaller if orographic precipitation was absent and the mass balance – elevation feedback were inoperative. Although computed orographic precipitation amounts on the northwest side of the ice cap are small (representing $\sim 20\text{-}25\%$ of the total observed precipitation amounts), and while the ice cap is likely still responding to past climate conditions such as those from the Little Ice Age, the mass balance – elevation feedback is playing a role in the evolution of this ice mass.

6.2 SUMMARY AND FUTURE INVESTIGATIONS

In summary, results of the series of modelling studies presented here confirms that ice-atmosphere interactions in the Canadian High Arctic are critical to the mass balance, ice temperature, flow dynamics, response time and evolution of glaciers in this region. A linear feedback analysis of model climate simulations for John Evans Glacier shows that the snow/ice-albedo feedback can locally significantly amplify surface temperature, air temperature, and surface mass balance changes on less than decadal timescales, and that the presence of glacier ice nearly doubles the effectiveness of the snow-albedo feedback in the model domain. Model

simulations of borehole temperatures in ice cap accumulation zones showed that although historical SAT changes (feedback-amplified or not) might be the direct cause of measured englacial temperature anomalies, they can also be the indirect cause of significantly-enhanced diffusive loss of the englacial climate signals. Ice temperature simulations for John Evans Glacier indicated that while the direct result of past SAT changes has been to cool the ice and its bed, the indirect result has been to create and maintain warm (pressure melting point) basal temperatures in the ablation zone (via ice thickness, surface melt and refreezing, and subglacial meltwater changes). Ice-atmosphere model simulations for Devon Ice Cap indicated that the imbalance between surface mass balances and mass flux divergences (and resultant mass gains) in the northwest sector of the ice cap would be smaller without orographic precipitation and the mass balance – elevation feedback, supporting the hypothesis that this feedback is playing a role in the evolution of the ice cap.

The model results in this thesis also indicate that the mass balance – elevation feedback plays a smaller, secondary role to the snow/ice-albedo feedback in the evolution of CHA ice caps. While the snow/ice-albedo feedback is locally significant on less than decadal time scales, with implications for the response time of the glacier, the mass balance – elevation feedback only becomes significant at greater than decadal timescales. This concurs with the conclusions presented in Abe-Ouchi et al. (2007), for large ice sheets.

Previously unexplored implications of the snow/ice-albedo and topographic – mass balance feedbacks further indicate that, individually, Arctic glaciers and ice caps are also capable of modifying their local and regional climates (via amplified air temperature changes and modification of local wind and precipitation patterns). As a result, the collective impact of these ice masses upon Arctic atmospheric circulation patterns will not be negligible.

To extend the results described in this thesis, future work should include further, more comprehensive, numerical modelling experiments and fieldwork and a more thorough incorporation of paleoenvironmental records. The magnitude of the snow/ice-albedo feedback should be verified for a land area containing a larger number of glaciers, before conclusively extending results to glaciated areas of the Canadian High Arctic as a whole. The significance of the topographic – mass balance feedback to Arctic ice caps and to the Arctic atmospheric circulation should be investigated with an expanded 3D coupled atmosphere-ice model. More extensive borehole drilling of High Arctic ice caps and glaciers is required to verify the model results of the Little Ice Age thermal experiments. Finally, a series of boreholes drilled into John Evans Glacier would be useful to verify the basal processes suggested by surface measurements and the modelling experiments.

6.3 REFERENCES

- Abe-Ouchi, A., T. Segawa and F. Saito, 2007: Climatic conditions for modelling the Northern Hemisphere ice sheets throughout the ice age cycle. *Climate of the Past*, **3**, 423–438.
- Barlow, L. K., 2001: The time period A.D. 1400-1980 in central Greenland ice cores in relation to the North Atlantic sector. *Climatic Change*, **48**(1), 101–119.
- Blatter, H., 1987: On the thermal regime of an Arctic valley glacier: a study of White Glacier, Axel Heiberg Island, N.W.T., Canada. *Journal of Glaciology*, **33**, 200-211.
- Blatter, H., and K. Hutter, 1991: Polythermal conditions in arctic glaciers. *Journal of Glaciology*, **37**, 261-269.
- Blatter, H., and G. Kappenberger, 1988: Mass balance and thermal regime of Laika Ice Cap, Coburg Island, N.W.T., Canada. *Journal of Glaciology*, **34**, 102-110.
- Bingham, R. G., P.W. Nienow and M. J. Sharp, 2003: Intra-annual and intraseasonal flow dynamics of a High Arctic polythermal valley glacier. *Annals of Glaciology*, **37**, 181-188.
- Bingham R. G., P. W. Nienow, M. J. Sharp and S. Boon, 2005: Subglacial drainage processes at a High Arctic polythermal valley glacier. *Journal of Glaciology*, **51**, 15–24.
- Burgess, D. O., and M. J. Sharp, 2004: Recent changes in areal extent of the Devon Ice Cap, Nunavut, Canada. *Arctic, Antarctic, and Alpine Research*, **36**(2), 261-271.
- Burgess, D. O., M. J. Sharp, D. W. F. Mair, J. A. Dowdeswell, and T. J. Benham,, 2005: Flow dynamics and iceberg calving rates of Devon Ice Cap, Nunavut, Canada. *Journal of Glaciology*, **51**(173), 219-230.
- Cess, R.D., and 32 others, 1991: Interpretation of snow-climate feedback as produced by 17 General Circulation Models. *Science*, **253**, 888-892.
- Copland, L. and Sharp, M. 2001: Mapping thermal and hydrological conditions beneath a polythermal glacier with radio-echo sounding. *Journal of Glaciology*, **47**(157), 232-242.

- Curry, J.A., J.L. Schramm, D. Petrovich, and J.O. Pinto, 2001: Application of SHEBA/FIRE data to evaluation of sea ice surface albedo parameterizations. *Journal of Geophysical Research*, **106**(D14), 15345-15355.
- Dahl-Jensen, D., K. Mosegaard, N. Gundestrup, G.D. Clow, S.J. Johnsen, A.W. Hansen, and N. Balling, 1998: Past temperatures directly from the Greenland Ice Sheet. *Science*, **282**, 268-271.
- Dowdeswell, J.A., R. Hodgkins, A.M. Nuttall, J.O. Hagen, and G.S. Hamilton. 1995. Mass balance change as a control on the frequency and occurrence of glacier surges in Svalbard, Norwegian High Arctic. *Geophysical Research Letters*, **22** (21), 2909-2912.
- Dowdeswell, J. A., T. J. Benham, M. R. Gorman, D. Burgess and M. J. Sharp, 2004: Form and flow of the Devon Island Ice Cap, Canadian Arctic. *Journal of Geophysical Research*, **109**, F02002, doi:10.1029/2003JF000095.
- Fischer, H., M. Werner, D. Wagenbach, M. Schwager, T. Thorsteinsson, F. Wilhelms, J. Kipfstuhl and S. Sommer, 1998: Little Ice Age clearly recorded in northern Greenland ice cores. *Geophysical Research Letters*, **25**(10), 1749-1752.
- Holland, M. M., and C. M. Bitz, 2003: Polar amplification of climate change in coupled models. *Climate Dynamics*, **21**, 221-232.
- Irvine-Fynn, T. D. L., B. J. Moorman, J. L. M. Williams and F. S. A. Walter, 2006: Seasonal changes in ground-penetrating radar signature observed at a polythermal glacier, Bylot Island, Canada. *Earth Surface Processes and Landforms*, **31**, 892-909.
doi: 10.1002/esp.1299 .
- Johannesson, T., C.F. Raymond, and E.D. Waddington, 1989: A simple method for determining the response time of glaciers. In: *Glacier Fluctuations and Climatic Change* (J. Oerlemans, ed.), Kluwer Academic Publishers, London, 343-352.
- Koerner, R. M., 1966: Accumulation on the Devon Island ice cap, Northwest Territories, Canada. *Journal of Glaciology*, **6**(45), 383-392.
- Koerner, R. M., 1970: The mass balance of the Devon Ice Cap, Northwest Territories, Canada 1961-66. *Journal of Glaciology*, **9**(57), 325-336.
- Koerner, R. M., 1979: Accumulation, ablation, and oxygen isotope variations on the Queen Elizabeth Island ice caps, Canada. *Journal of Glaciology*, **22**(86), 25-41.

Mair, D., D. Burgess, and M. Sharp, 2005: 37-year mass balance of the Devon Island Ice Cap, Nunavut, Canada, determined by shallow ice coring and melt modelling. *Journal of Geophysical Research* (Earth Surface), **110**, F01011, doi:10.1029/2003JF000099.

Oerlemans, J., 1986: Glaciers as indicators of a carbon dioxide warming. *Nature*, **320**, 607-609.

Overpeck, J., K. Hughen, D. Hardy, R. Bradley, R. Case, M. Douglas, B. Finney, K. Gajewski, G. Jacoby, A. Jennings, S. Lamoureux, A. Lasca, G. MacDonald, J. Moore,

M. Retelle, S. Smith, A. Wolfe, and G. Zielinski, 1997: Arctic Environmental Change of the Last Four Centuries. *Science*, **278**, 1251-1256.

DOI: 10.1126/science.278.5341.1251.

Pritchard, M. S., A. B. G. Bush and S. J. Marshall, 2008: Neglecting ice-atmosphere interactions underestimates ice sheet melt in millennial-scale deglaciation simulations. *Geophysical Research Letters*, **35**, L01503, doi: 10.1029/2007GL031738.

Roe, G.H. and R.S. Lindzen, 2001: The mutual interaction between continental-scale ice sheets and atmospheric stationary waves. *Journal of Climate*, **14**, 1450-1465.

Shepherd, A., Z. Du, T. J. Benham, J. A. Dowdeswell, and E. M. Morris, 2007: Mass balance of Devon Ice Cap, Canadian Arctic. *Annals of Glaciology*, **46**, 249-254.

Skidmore M. L., and Sharp M. J., 1999: Drainage system behaviour of a High-Arctic polythermal glacier. *Annals of Glaciology*, **28**, 209–215.

Wolken, G. J., J. H. England and A. S. Dyke, 2008a: Changes in late Neoglacial perennial snow/ice extent and equilibrium-line altitudes in the Queen Elizabeth Islands, Arctic Canada. *Holocene*, **18**(4), 615-627.

Wolken, G. J., M. J. Sharp and J. H. England, 2008b: Changes in late Neoglacial climate inferred from former equilibrium-line altitudes in the Queen Elizabeth Islands, Arctic Canada. *Holocene*, **18**(4), 629-641.